

Electrochemical Doping of Semiconducting Polymer Films with Controlled Morphologies

Von der Fakultät Chemie der Universität Stuttgart zur Erlangung der Würde eines

Doktors der Naturwissenschaften (Dr. rer. nat.)

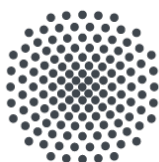
genehmigte Abhandlung

vorgelegt von

David Neußer

aus Aachen

Hauptberichterin:	Prof. Dr. Sabine Ludwigs
Mitberichter:	Prof. Dr. Joris van Slageren
Prüfungsvorsitzender:	Prof. Dr. Oliver Clemens
Tag der mündlichen Prüfung:	14.12.2022



Universität Stuttgart



Institut für Polymerchemie

Lehrstuhl für Struktur und Eigenschaften polymerer Materialien

2022

*Erkennest dann der Sterne Lauf,
Und wenn Natur dich unterweist,
Dann geht die Seelenkraft dir auf,
Wie spricht ein Geist zum andern Geist.*
- Johann Wolfgang von Goethe

Erklärung über die Eigenständigkeit der Dissertation

Ich versichere, dass ich die vorliegende Arbeit mit dem Titel

Electrochemical Doping of Semiconducting Polymer Films with Controlled Morphologies

selbständig verfasst und keine anderen als die angegebenen Quellen und Hilfsmittel benutzt habe; aus fremden Quellen entnommene Passagen und Gedanken sind als solche kenntlich gemacht.

Declaration of Authorship

I hereby certify that the dissertation entitled

Electrochemical Doping of Semiconducting Polymer Films with Controlled Morphologies

is my own work entirely except where otherwise indicated. Passages and ideas from other sources have been clearly indicated.

Datum, Ort

David Neußer

I. Danksagung

Diese Dissertation entstand am *Institut für Polymerchemie* der *Universität Stuttgart* am *Lehrstuhl für Struktur und Eigenschaften polymerer Materialien* im Zeitraum von Januar 2019 bis Oktober 2022. In diesem Zeitraum hatte ich das Glück viele Menschen kennenzulernen, die maßgeblich zum erfolgreichen Abschluss dieser Dissertation beigetragen haben. Dabei kann der fachliche und persönliche Beitrag Einiger nur schwer in knappen Sätzen wiedergegeben werden, dennoch möchte ich dies in den folgenden Zeilen versuchen.

An erster Stelle möchte ich mich bei *Prof. Dr. Sabine Ludwigs* bedanken, die meine wissenschaftliche Ausbildung von Beginn meiner Bachelorarbeit 2015 an, über die Masterarbeit 2018 bis hin zur Promotion maßgeblich geprägt hat. Besonders hervorzuheben ist hierbei die unkomplizierte Aufnahme in das Team, die Möglichkeit der Ausarbeitung eines Themas in einem interdisziplinären und relevanten Forschungsumfeld und die offenen fachlichen Diskussionen mit der Chance, eigene Ideen einzubinden. Die hervorragende Laborausstattung sowie die Möglichkeit an internationalen Fachkonferenzen teilzunehmen (insofern es die Pandemielage zuließ), bereicherten die Zeit meiner Promotion fachlich und persönlich.

Ich danke *Prof. Dr. Joris van Slageren* für die freundliche Übernahme des Mitberichts sowie für die Möglichkeit eines Forschungspraktikums in seiner Gruppe und spannenden Kooperationen in der darauffolgenden Zeit. Bei *Prof. Dr. Oliver Clemens* bedanke ich mich herzlich für die Übernahme des Prüfungsvorsitzes.

Da diese kumulative Dissertation ohne die erfolgreiche Zusammenarbeit mit unseren nationalen und internationalen Kooperationspartnern nicht möglich gewesen wäre, gilt meinen Co-Autoren mein besonderer Dank. Hierbei zu nennen sind von der Universität Stuttgart *Prof. Dr. Joris van Slageren*, *Dr. Michal Kern*, *Lea-Sophie Hornberger* und *Claudia Malacrida*. Von der Simon Fraser University in Vancouver *Prof. Dr. Loren G. Kaake*. Von der Universität zu Berlin und dem Helmholtz-Zentrum für Materialien und Energie *Prof. Dr. Norbert Koch* und *Dr. Thorsten Schultz*. Von der Monash University in Melbourne und dem Australian Synchrotron *Prof. Dr. Christopher R. McNeill*, *Dr. Wen Liang Tan* und *Dr. Lars Thomsen*. Sowie von der Universität Potsdam *Prof. Dr. Dieter Neher*, *Bowen Sun*, *Lorena Perdigón-Toro* und *Dr. Safa Shoaee*.

Ich danke allen ehemaligen und aktuellen Mitgliedern der Ludwigs Arbeitsgruppe, die mich auf meinem Weg begleitet und die Zeit meiner Promotion mit vielen schönen Erinnerungen bereichert haben. An vorderster Stelle zu erwähnen ist *Dr. Klaus Dirnberger*, dem ich für ein immer offenes Ohr bei sämtlichen Themen danke und *Beatrice Omiecienski* für den unermüdlichen Einsatz, den zuweilen kaum zu bewältigenden Organisationsapparat der Universität für uns zu ordnen.

Für die Unterstützung im Labor im Rahmen von Praktika und Abschlussarbeiten danke ich *Klaudia Opri, Sophia Botsch, Sally Eickmeyer, Maren Scheffler* und *Jan Jacobs*. Hervorheben möchte ich hier *David Moser*, der während seiner Masterarbeit, trotz schwieriger wissenschaftlicher Herausforderungen, nie die Motivation verlor. Außerdem danke ich *Lea-Sophie Hornberger*, mit der ich viel Zeit im Labor und die Erst-Autorenschaft einer der Publikationen dieser Dissertation teilen durfte.

Ich danke meinen Mitdoktoranden und Doktorandinnen *Dr. Yannic Groß, Dr. Kirsten Bruchlos, Dr. Matthias Wieland, Dr. David Gepperth, Carsten Dingler, Sherri Liu, Claudia Malacrida, Dr. Jochen Kuhlmann, Lukas Stein* und *Stephan Pflumm* für die schöne Zeit in und außerhalb der Uni. Individuell möchte ich mich bei *Claudia Malacrida* bedanken. Große Teile meines Wissens über die Elektrochemie durfte ich von ihr lernen und auch die schöne Zeit beim Besuch der Konferenz in Malaga wird mir immer positiv in Erinnerung bleiben. *Sherri Liu* danke ich für zahllose gemeinsame aufschlussreiche Stunden am AFM und SEM sowie für die geteilte Leidenschaft für gutes Essen und Tennis. Ich danke *Lukas Stein* für gelegentliche Einblicke in echte synthetische Laborarbeit und den Austausch über musikalische Themen. *Carsten Dingler* danke ich für kritische Diskussionen auf fachlicher Ebene, genauso wie für entspannte Momente außerhalb der Uni. Bei *Stephan Pflumm* bedanke ich mich für die Motivation und den Mut, es doch immer wieder in der Mensa zu probieren. *Julia Rumeny* danke ich für ihren ausgeprägten Sinn für Ordnung im Elektrochemielabor und die Bereitschaft sich schnell in neue Methoden und Setups einzuarbeiten. Für technische Angelegenheiten jeglicher Art danke ich *Philipp Sliskovic*.

Die lange Zeit des Studiums bestritt ich unter anderem mit *Dr. Tamara Schad, Dennis Schäfter, Johanna Dollinger* und *Marina Fuhrer*. Ich danke euch für die gemeinsame Bewältigung der Herausforderungen während des Studiums, die allein kaum zu schaffen gewesen wären, und die vielen unvergesslichen Momente während dieser Zeit.

Der abschließende Dank gilt meinen Eltern, die für mich gleichermaßen Vorbild und Rückhalt sind für ihre bedingungslose Unterstützung und meinem Bruder für den Ausgleich zum stressigen Alltag sowie dem ganzen Öcher Bus.

Table of Contents

I.	Danksagung	VII
II.	Abstract	XIII
III.	Kurzzusammenfassung	XV
IV.	Publication List	XVIII
V.	List of Abbreviations	XXI
1	Introduction	1
1.1	<i>Semiconducting Polymers for Organic Electronics Devices</i>	2
1.1.1	Conductivity and Charge Transport in Semiconducting Polymers	2
1.1.2	Chemical vs. Electrochemical Doping	8
1.2	<i>P3HT as Model System</i>	11
1.2.1	Synthesis	11
1.2.2	Semicrystalline Morphology in Thin Films	14
1.2.3	Advanced Electrochemistry and Coupled Spectroscopic Techniques	18
1.3	<i>From P3HT to State of the Art Donor-Acceptor Copolymers</i>	19
1.4	<i>Applications</i>	21
1.4.1	Organic Photovoltaics (OPV)	21
1.4.2	Storing Charge in Organic Electrochemical Devices	27
2	Aim of this Thesis	32
3	Part I: Conductivity-Tuning of P3HT Films by an Electrochemical Doping Approach	36
3.1	<i>High Conductivities of Disordered P3HT Films by an Electrochemical Doping Strategy</i>	36
3.1.1	Publication Data	36
3.1.2	Short Summary	37
3.1.3	Manuscript	38
3.1.4	Reprint Permission	49
3.2	<i>How Charge Trapping Affects the Conductivity of Electrochemically Doped Poly(3-hexylthiophene) Films</i>	50
3.2.1	Publication Data	50
3.2.2	Short Summary	51
3.2.3	Manuscript	52
3.2.4	Reprint Permission	60

4	Part II: Electrochemical Doping of state-of-the-art Materials	64
4.1	<i>Spectroelectrochemically Determined Energy Levels of PM6:Y6 Blends and their Relevance to Solar Cell Performance</i>	64
4.1.1	Publication Data	64
4.1.2	Short Summary	65
4.1.3	Manuscript	66
4.1.4	Reprint Permission	80
4.2	<i>Electrochemical Conductivity Tuning and its Structural Impact on Aligned Films of P(NDI2OD-T2)</i>	81
4.2.1	Publication Data	81
4.2.2	Short Summary	82
4.2.3	Manuscript	83
5	Summary and Outlook	94
6	References	101
7	Appendix	110
7.1	<i>SI to High Conductivities of Disordered P3HT Films by an Electrochemical Doping Strategy</i>	110
7.2	<i>SI to How Charge Trapping affects the Conductivity of Electrochemically Doped Poly(3-Hexylthiophene) Films</i>	126
7.3	<i>SI to Spectroelectrochemically Determined Energy Levels of PM6:Y6 Blends and their Relevance to Solar Cell Performance</i>	137

II. Abstract

The present cumulative thesis was focused on establishing electrochemical doping as a powerful doping method to transfer semiconducting polymer films into the conducting state in order to maximize their electronic conductivity. The doping process itself can be considered the key element in the field of organic semiconductors and its understanding is essential to prepare highly conducting polymer films that are of potential use in organic electronics devices. Apart from the doping process, the control of film morphology plays a decisive role when it comes to improving the electronic properties especially of conjugated polymers and depicts an equally important factor for successful applications. Therefore, the characterization of the interplay between electrochemical doping and film morphology was the central objective of this thesis.

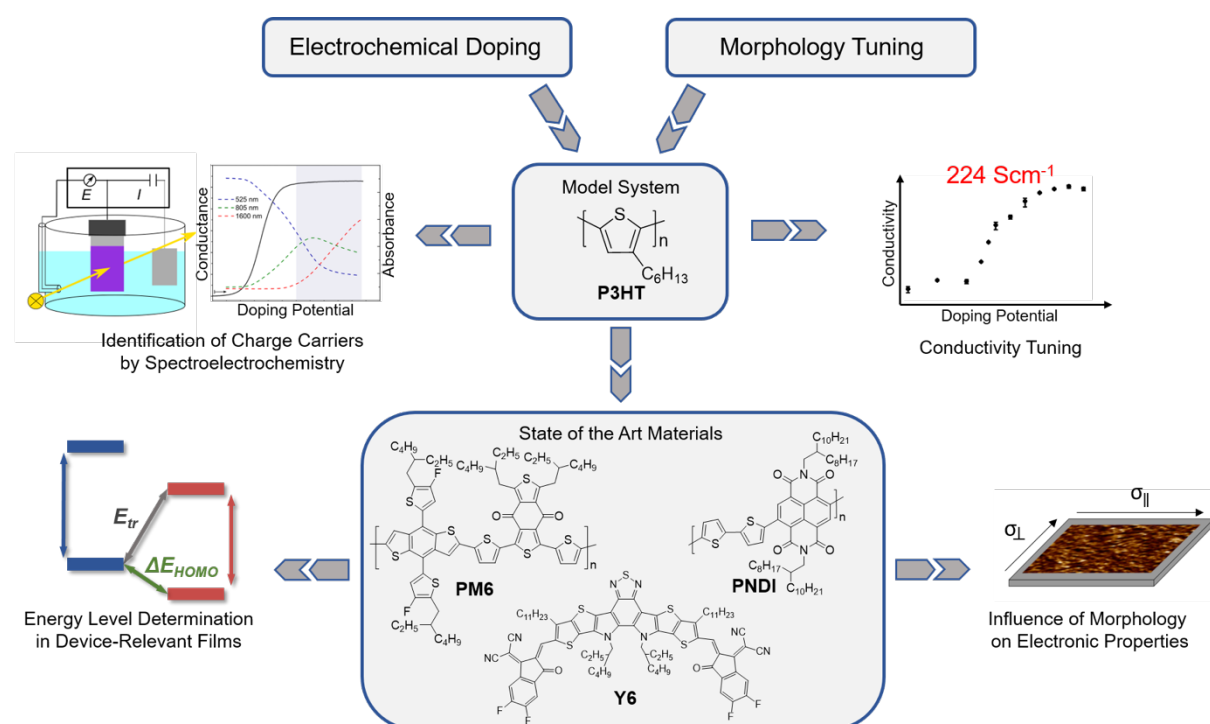


Figure I: Schematic overview of the main aspects of this thesis. This schematic contains parts that are adapted with permission from reference. [I] © 2020, ACS.

The first part of this work was covered by two publications in the context of electrochemical doping of films of poly(3-hexylthiophene) P3HT which acted as model system for conjugated polymers. Here, a fundamental knowledge was built to understand basic concepts of introducing charge carriers by an electrochemical doping approach that produced highly doped films in the presence of an electrolyte. Potential dependent regions of high conductivity and the responsible charge carriers were identified in electrolyte at first by *in situ* electrochemical techniques. Conducting films with fine-tuned charge carrier density were then transferred into the solid-state. To ensure a successful transition of the induced charged species into the solid-state, UV-vis and EPR spectroscopy was performed after doping. The

outcomes assisted in understanding the charge transport mechanism and allowed for a discussion of the differences arising from the results generated from poly(vinylphenylcarbazole), a classical redox polymer.

Besides the doping process, the influence of morphology was outlined by comparing semicrystalline morphologies of spin-coated regioregular P3HT films to fully amorphous films of regiorandom P3HT. The electrochemically doped P3HT films showed tunable conductivities over 6 orders of magnitude reaching up to 224 Scm^{-1} demonstrating the potential of our applied doping approach. [I] A second publication in this context was presented to strengthen the understanding of the electrochemical doping process of P3HT films and discuss occurring charge trapping effects. Here, the size and nature of the counterion in the electrolyte, which is necessary for counterbalancing of the induced charge carriers upon doping, was a central aspect. The reversibility of the electrochemical doping process was described in detail and links to the achievable solid-state conductivity in highly doped P3HT films were pointed out. Whereas ion size seemed to not have any direct influence, a clear connection could be drawn between a higher tendency for charge trapping and a decreased conductivity in the solid-state. [II]

The second part of this thesis was built on the fundamental expertise on electrochemical doping of P3HT films provided by the previous publications. A third paper was focused on the energy level determination of the state-of-the-art conjugated polymer PM6 and the non-fullerene acceptor Y6 in high-performance blend films for bulk heterojunction solar cells. The extensive knowledge on the occurring charged species in P3HT upon electrochemical doping was the starting point for a spectroelectrochemical approach which enabled us to identify charged species of PM6 and Y6. By locating the onsets of oxidation and reduction, the individual frontier orbital levels (HOMO and LUMO) were determined in blend films. One of the main questions concerned the impact of morphology (face-on vs. edge-on) on the blend energetics since both orientations showed significantly differing device performance. The calculated HOMO offset of the materials in the blend films proved to be 0.33 eV and was only marginally influenced by the different morphologies. Nevertheless, we discussed the difference in device performance within the scope of different interfacial molecular orientations, which are known to have influence on the non-radiative decay rate of the charge-transfer state. [III] Additionally, this part of the thesis contains a manuscript, that extends the electrochemical doping approach to the n-type conjugated polymer P(NDI2OD-T2). Here, we tried to take advantage of its high tendency for aggregation to produce films with aligned fiber morphologies which were electrochemically doped in the following. A main aspect was to understand the mechanism of charge transport in this n-type system when fine-tuning the doping levels and its overall impact on the resulting conductivities. Furthermore, the inherent process of integration of the counterions to counterbalance the induced charges during electrochemical doping was documented by *ex situ* GIWAXS. The structural response to ion integration definitely led to a decrease of order, but the former induced morphology (face-on or edge-on) was sustained to large proportions. [IV]

III. Kurzzusammenfassung

Die vorliegende kumulative Dissertation fokussiert sich darauf, die elektrochemische Dotierung als Methode zur Überführung von halbleitenden Polymeren in ihren leitfähigen Zustand zu etablieren. Hierbei bildet die Maximierung der elektronischen Leitfähigkeit eines der Hauptziele. Der Vorgang der Dotierung kann als einer der Schlüsselaspekte im Bereich der organischen Halbleiter gesehen werden und sein grundsätzliches Verständnis ist essenziell, um leitfähige Polymerfilme herzustellen, die von potenziellem Nutzen für Bauelemente der organischen Elektronik sein können. Neben dem Dotiervorgang spielt die Kontrolle der Morphologie eine entscheidende Rolle, um die elektronischen Eigenschaften, speziell im Fall von konjugierten Polymeren, zu verbessern. Die Steuerung der Morphologie wird daher als ebenso wichtig für erfolgreiche Anwendungen betrachtet. Aus diesen Gründen ist die Beschreibung der Wechselwirkung zwischen elektrochemischem Dotieren und Filmmorphologie eines der zentralen Ziele dieser Dissertation.

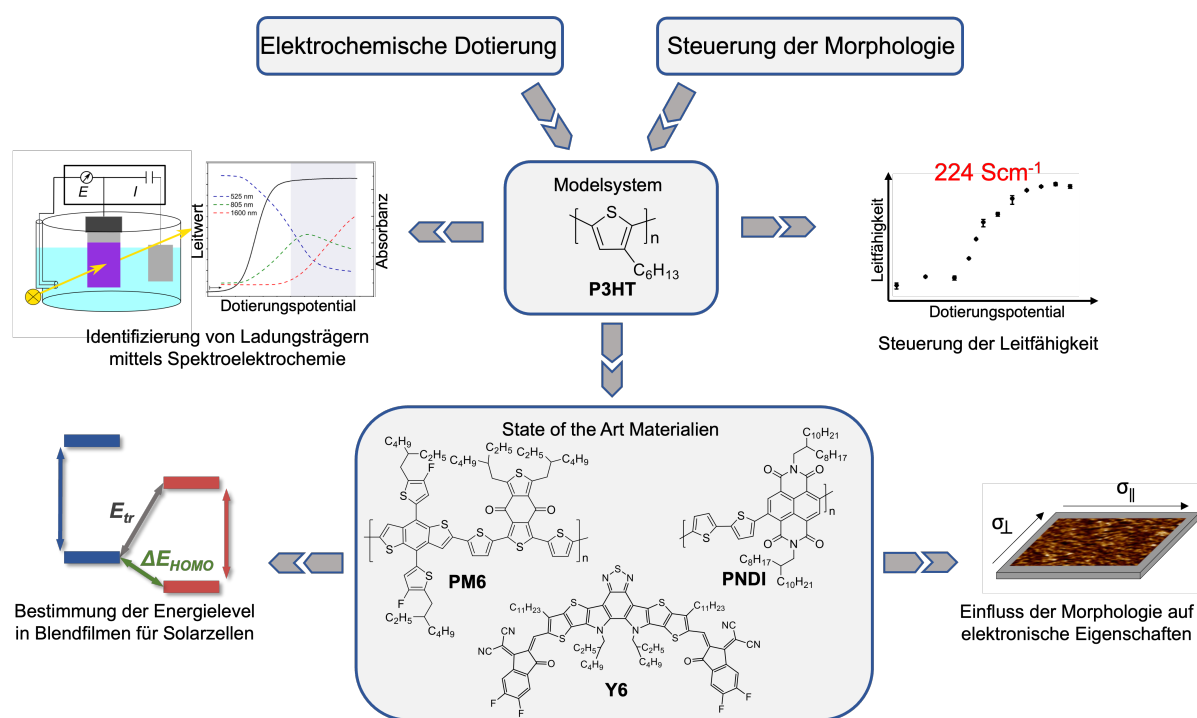


Abbildung I: Schematischer Überblick über die Hauptziele dieser Dissertation. Diese Abbildung enthält Teile die mit Erlaubnis aus Referenz [I] adaptiert wurden. © 2020, ACS.

Zwei Publikationen im Bereich der elektrochemischen Dotierung von Poly(3-hexylthiophen) (P3HT) Filmen bilden den ersten Abschnitt dieser Arbeit. Hierbei fungiert P3HT als Modellsystem für die Materialklasse der konjugierten Polymere. So konnte fundamentales Wissen aufgebaut werden, um die grundlegenden Vorgänge der Ladungsträgerinduzierung in P3HT Filmen mittels elektrochemischer Dotierung zu verstehen. Daraus konnte ein Ansatz entwickelt werden, der es ermöglicht, elektrochemisch dotierte leitfähige Filme in den festen Zustand zu überführen. Durch *in situ* Messungen

in Elektrolyt, wurden so zunächst potentialabhängige Regionen hoher Leitfähigkeit und dafür verantwortliche Ladungsträger identifiziert. In einem nächsten Schritt wurden die leitfähigen Filme mit eingestellter Ladungsträgerdichte in den festen Zustand überführt. Um einen erfolgreichen Transfer sicherzustellen, wurden die induzierten Ladungsträger mittels UV-vis und ESR Spektroskopie nach der Dotierung untersucht. Die Ergebnisse wurden genutzt, um Modelle des Ladungstransports zu diskutieren und ermöglichten einen Vergleich mit einem klassischen Redoxpolymer (Poly(vinylphenylcarbazol)).

Neben dem Dotiervorgang wurde auch der Einfluss der Morphologie untersucht, indem die teilkristalline Morphologie von regioregulärem P3HT mit vollständig amorphen Filmen aus regiorandom P3HT verglichen wurden. Elektrochemisch dotierte P3HT Filme zeigten Leitfähigkeiten bis zu 224 Scm^{-1} , die über 6 Größenordnungen steuerbar waren. Dieses Ergebnis demonstriert das Potential unseres Ansatzes. [I] Eine zweite Publikation in diesem Kontext diente dem tieferen Verständnis des Dotiervorgangs und rückte den Fokus auf Charge Trapping Effekte, die vor allem für konjugierte Polymere charakteristisch sind. Da dem Gegenion beim Kompensieren der induzierten Ladungsträger eine Schlüsselaufgabe zukommt, wurde der Einfluss von Größe und Art des Gegenions im Elektrolyten diskutiert. Die Reversibilität des elektrochemischen Dotiervorgangs wurde detailliert beschrieben und Verbindungen zur resultierenden Leitfähigkeit in dotierten P3HT Filmen herausgearbeitet. Dabei stellte sich heraus, dass die Größe des Gegenions keinen direkten Einfluss hat, jedoch eine höhere Tendenz zu Charge Trapping konkret mit niedrigeren Leitfähigkeiten im festen Zustand in Verbindung steht. [II]

Der zweite Teil dieser Dissertation baut auf der gewonnenen Expertise zu elektrochemischem Dotieren von P3HT Filmen auf. Eine dritte Publikation legte den Schwerpunkt auf die Bestimmung der Energielevel des State of the Art konjugierten Polymer PM6 und dem fullerenfreien Akzeptor Y6, die in Blendfilmen für organische Hochleistungssolarzellen eingesetzt werden. Speziell das umfassende Wissen über das Auftreten von geladenen Spezies in P3HT während dem elektrochemischen Dotieren diente hier als Ausgangspunkt. Mittels Spektroelektrochemie war es so möglich, geladene Spezies von PM6 und Y6 klar zu identifizieren. Über das Lokalisieren der Ansatzpunkte von Oxidation und Reduktion wurden die individuellen Grenzorbitalenergien (HOMO und LUMO) in Blendfilmen bestimmt. Eine der Hauptfragen betraf dabei den Einfluss von unterschiedlichen Morphologien (face-on vs. edge-on) auf die Energetik der Blends, da beide Orientierungen eine deutlich unterschiedliche Effizienz in der Solarzelle zeigten. Der berechnete HOMO Abstand der Materialien betrug 0.33 eV und wurde nur marginal durch die verschiedenen Morphologien beeinflusst. Daher wurde die unterschiedliche Effizienz in der Solarzelle im Rahmen von verschiedenen molekularen Grenzflächenorientierungen diskutiert, die nachweislich Einfluss auf die strahlungsfreie Zerfallrate von Ladungstransferkomplexen ausüben können. [III]

Zusätzlich verfügt der zweite Teil der Dissertation über ein Manuskript, das die elektrochemische Dotierung auf das n-halbleitende konjugierte Polymer P(NDI2OD-T2) ausweitet. Hier wurde die hohe Neigung des Materials zur Aggregation in Lösung und Film ausgenutzt, um Filme mit ausgerichteter Faserstruktur zu erzeugen, die im Anschluss dotiert wurden. Ein wichtiger Teil war hier das Verständnis des Ladungstransportmechanismus in diesem n-halbleitenden System. Dazu wurde der Dotierungsgrad gesteuert und sein Einfluss auf die resultierende Leitfähigkeit untersucht. Außerdem wurde der zugrundeliegende Vorgang der Integration von Gegenionen zum Ladungsausgleich näher betrachtet, indem zusätzliche *ex situ* GIWAXS Messungen durchgeführt wurden. Die strukturelle Antwort auf die Ionenaufnahme führte dabei zu einer Abnahme der Ordnung, dennoch wurde die ursprünglich induzierte Morphologie (face-on oder edge-on) zu großen Teilen erhalten. [IV]

IV. Publication List

- I. D. Neusser, C. Malacrida, M. Kern, Y. M. Gross, J. van Slageren and S. Ludwigs, High Conductivities of Disordered P3HT Films by an Electrochemical Doping Strategy, *Chem. Mater.*, 2020, **32**, 6003-6013.
IF: 9.8 (2021/2022)
- II. L.-S. Hornberger*, D. Neusser*, C. Malacrida, L. G. Kaake and S. Ludwigs, How Charge Trapping Affects the Conductivity of Electrochemically doped Poly(3-hexylthiophene) Films, *Appl. Phys. Lett.*, 2021, **119**, 163301.
*: authors contributed equally
IF: 3.8 (2022)
- III. D. Neusser, B. Sun, W. L. Tan, L. Thomsen, T. Schultz, L. Perdigón-Toro, N. Koch, S. Shoaee, C. R. McNeill, D. Neher and S. Ludwigs, Spectroelectrochemically Determined Energy Levels of PM6:Y6 Blends and their Relevance to Solar Cell Performance, *J. Mater. Chem. C*, 2022, **10**, 11565-11578.
Hot Paper + Cover Image
IF: 7.4 (2021/2022)
- IV. D. Neusser, W. L. Tan, L. Thomsen, C. R. McNeill and S. Ludwigs, Electrochemical Conductivity Tuning and its Structural Impact on Aligned Films of P(NDI2OD-T2), *manuscript in preparation*.

Publications beyond the scope of this thesis

- C. Rothe, D. Neusser, N. Hoppe, K. Dirnberger, W. Vogel, S. Gámez-Valenzuela, J. T. López Navarrete, B. Villacampa, M. Berroth, M. C. Ruiz Delgado and S. Ludwigs, Push–Pull Thiophene Chromophores for Electro-Optic Applications: From 1D Linear to β -Branched Structures, *Phys. Chem. Chem. Phys.*, 2020, **22**, 2283-2294.
- M. Kern, L. Tesi, D. Neusser, N. Rußegger, M. Winkler, A. Allgaier, Y. M. Gross, S. Bechler, H. S. Funk, L.-T. Chang, J. Schulze, S. Ludwigs and J. van Slageren, Hybrid Spintronic Materials from Conducting Polymers with Molecular Quantum Bits, *Adv. Funct. Mater.*, 2020, **31**, 2006882.

- P. Shiri, D. Neusser, C. Malacrida, S. Ludwigs and L. G. Kaake, Mixed Ion-Carrier Diffusion in Poly(3-hexyl thiophene)/Perchlorate Electrochemical Systems, *J. Phys. Chem. C*, 2021, **125**, 536–545.
- C. Beaumont, J. Turgeon, M. Idir, D. Neusser, R. Lapointe, S. Caron, W. Dupont, D. D’Astous, S. Shamsuddin, S. Hamza, E. Landry, S. Ludwigs and M. Leclerc, Water-Processable Self-Doped Conducting Polymers via Direct (Hetero)arylation Polymerization, *Macromolecules*, 2021, **54**, 5464–5472.
- S. Gámez-Valenzuela, D. Neusser, C. Benitez-Martin, F. Najera, J. A. Guadix, C. Moreno-Yruela, B. Villacampa, R. Ponce Ortiz, S. Ludwigs, R. Andreu and M. C. Ruiz Delgado, V-Shaped Pyranilidene/Triphenylamine-Based Chromophores with Enhanced Photophysical, Electrochemical and Nonlinear Optical Properties, *Mater. Adv.*, 2021, **2**, 4255-4263.
- F. Borrmann, T. Tsuda, O. Guskova, N. Kiriya, C. Hoffmann, D. Neusser, S. Ludwigs, U. Lappan, F. Simon, M. Geisler, B. Debnath, Y. Krupskaya, M. Al-Hussein and A. Kiriya, Charge-Compensated N-Doped π -Conjugated Polymers: Toward both Thermodynamic Stability of N-Doped States in Water and High Electron Conductivity, *Adv. Sci.*, 2022, 2203530.

Conference Contributions

Talk

- D. Neusser, C. Malacrida, M. Kern, J. van Slageren and S. Ludwigs, Ex situ Electrochemical Doping Study of P3HT Films, *2nd Symposium on Progress in Organic Optoelectronics & Energy Conversion*, Malaga, 12th – 13th December 2019.

Poster

- C. Malacrida, D. Neusser and S. Ludwigs, Electroactive Polymers, Exploring Conductivity Behaviors and Doping Methods, *Makromolekulares Kolloquium 2020*, Freiburg, 26th – 28th February 2020.
- D. Neusser, C. Malacrida, M. Kern, J. van Slageren and S. Ludwigs, Controlled Doping of Conjugated Polymers for Tuning of Conductivities for (Flexible) Electronics Applications, *Quantum Alliance Community Event Germany*, online, 11th November 2020.

- D. Neusser, L.-S. Hornberger, C. Malacrida, P. Shiri, L. G. Kaake and S. Ludwigs, Controlled Electrochemical Doping to Achieve High Conductivities of Poly(3-Hexylthiophene) Films, *NanoGe 2021*, Valencia (online), 12th March 2021.
- D. Neusser, L.-S. Hornberger, C. Malacrida, P. Shiri, L. G. Kaake and S. Ludwigs, Controlled Electrochemical Doping to Achieve High Conductivities of Poly(3-Hexylthiophene) Films, *Biennial Meeting of the GDCh Division of Macromolecular Chemistry 2021*, online, 13th – 14th September 2021.

V. List of Abbreviations

AFM	atomic force microscopy
BHJ	bulk heterojunction
CB	conduction band
Cbz	carbazole
CF	chloroform
CN	1-chloronaphthalene
ENDOR	electron nuclear double resonance
CV	cyclic voltammetry
DFT	density functional theory
EGOFET	electrolyte-gated organic field effect transistor
EPR	electron paramagnetic resonance
et al.	and others (et alii)
F4TCNQ	2,3,5,6-tetrafluoro-7,7,8,8-tetracyanoquinodimethane
Fc	ferrocene
GIWAXS	grazing incidence wide angle X-ray scattering
GRIM	Grignard metathesis
HOMO	highest occupied molecular orbital
HT, HH, TT	head-tail, head-head, tail-tail
ITIC	3,9-bis(2-methylene-(3-(1,1-dicyanomethylene)-indanone)-5,5,11,11-tetrakis(4-hexylphenyl)-dithieno[2,3-d:2',3'-d']-s-indaceno[1,2-b:5,6-b']dithiophene)
ITO	indium tin oxide
LUMO	lowest unoccupied molecular orbital
NDI	naphthalene-bis(dicarboximide)
NFA	non-fullerene acceptor
OPV	organic photovoltaics
OEET	organic electrochemical transistor

PA	polyacetylene
PBDTBDD	poly(benzodithiophene-benzo[1',2'-c:4',5'-c']dithiophene-4,8-dione)
PCBM	[6,6]-phenyl-C61-butyric acid methyl ester
PCPDTBT	Poly[2,6-(4,4-bis-(2-ethylhexyl)-4H-cyclopenta[2,1-b;3,4-b']dithiophene)-alt-4,7(2,1,3-benzothiadiazole)]
PDI	perylene-bis(dicarboximide)
PEDOT	poly(3,4-ethylenedioxythiophene)
PM6	Poly[(2,6-(4,8-bis(5-(2-ethylhexyl)-3-fluoro)thiophen-2-yl)-benzo[1,2b:4,5b']dithiophene))-alt-(5,5-(1',3'-di-2-thienyl-5',7'-bis(2-ethylhexyl)benzo[1',2'-c:4',5'-c']di-thiophene-4,8-dione)))]
P(NDI2OD-T2)	poly[(<i>N,N'</i> -bis(2-octyldecyl)-1,4,5,8-naphthalenedicarboximide)-2,6-diyl]- <i>alt</i> -5,5'-(2,2'-bithiophene)]
P(PDI2OD-T2)	poly[(<i>N,N'</i> -bis(2-octyldecyl)-3,4,9,10-perylenedicarboximide-(1,7&1,6)-diyl)- <i>alt</i> -5,5'-(2,2'-bithiophene)]
PPP	poly(p-phenylene)
PPy	polypyrrole
PSS	polystyrenesulfonate
PTS	poly(6-(thiophene-3-yl)hexane-1-sulfonate)
PTVE	poly(2,2,6,6-tetramethylpiperidine-4-yl-1-oxylvinylether)
PVPhCbz	poly(vinyl-phenylcarbazole)
PVTPA	poly(vinyltriphenylamine)
P3HT	poly(3-hexylthiophene)
TEMPO	(2,2,6,6-tetramethylpiperidin-1-yl)oxyl
TPA	triphenylamine
UPS	ultraviolet photoelectron spectroscopy
UV-vis	ultraviolet-visible light
VB	valence band

Y6

[2,2'-((2Z,2'Z)-((12,13-bis(2-ethylhexyl)-3,9-diundecyl-12,13-dihydro-[1,2,5]thiadiazolo[3,4e]thieno[2'',3':4',5']thieno[2',3':4,5]pyrrolo [3,2g]thieno[2',3':4,5]-thieno[3,2-b]indole-2,10-diyl)bis(methanylylidene))bis(5,6-difluoro-3-oxo-2,3-dihydro-1H-indene-2,1-diylidene))-dimalononitrile]

1 Introduction

The development of plastics in all its variety has shaped our modern society and has defined our way of living like hardly any industrial innovation within the last 100 years. As a consequence of the impact of this technology on every aspect of life, our age is often considered to be the age of plastics.^{1,2} The reason for the vast rise of plastic technology rests upon the properties of this material class which enables an implementation into the entire product range. The most vital properties being low-weight, high mechanical stability and accessible options for large scale processing techniques. In this way, different types of plastics became essential materials in fields like packaging, automotive parts, materials in constructions industry, parts for electronic devices and medical products. The increasing need for highly specialized materials drives the development of high-performance plastics that will allow for more and new applications in the future.

Especially in the field of electronic devices, polymeric materials that are electrically conducting offer the unique combination of flexibility and electrical conductivity, challenging traditional semiconductor materials based on silicon. The concept of flexible electronics fuels researchers and creates exciting new devices like flexible sensors that are necessary for electronic skin or wearable electronics as platforms that can connect biological systems with smartphones for example.^{3, 4} In a time where every new technology must play its part in reducing CO₂ emissions and conserve natural resources, organic materials might be one way to tackle these issues. Conducting polymeric materials are based on carbon which is an easily available and non-toxic element and can be synthesized in relatively low energy consuming processing steps. Although the progress on these organic semiconductors in the last years has been impressive, more work needs to be focused on finding new high-performance materials and understanding the way their properties influence the performance of the final device.

In this context this thesis offers new insights into fundamental processes in organic semiconductors like doping and the resulting conductivity, but also tries to understand the impact of nanoscale structure of organic semiconductors on the performance of the device.

1.1 Semiconducting Polymers for Organic Electronics Devices

Nowadays the field of electronic devices is still vastly dominated by metals and inorganic semiconductors like silicon. Starting from the processing steps, the production of for example highly crystalline silicon consumes significant amounts of energy and therefore has the potential to release lots of greenhouse gases. When produced in industry-relevant amounts, organic semiconductors can be processed via roll-to-roll approaches to coat big surface areas in very little time by simple and straightforward solution processing techniques at room temperature. This offers opportunities for energy saving right at the manufacturing step. In any case, organic semiconductors like semiconducting polymers combine electrical conductivity with low-weight, flexibility and good mechanical stability mentioning only the main advantages of this unique material class.

1.1.1 Conductivity and Charge Transport in Semiconducting Polymers

Conjugated Polymers

The groundbreaking research in the field of semiconducting conjugated polymers was acknowledged with the Nobel Prize for A. J. Heeger, A. G. MacDiarmid and H. Shirakawa for “*the discovery and development of electrically conductive polymers*” in the year 2000.^{5, 6} The main discovery that was awarded with this prize was the increase in conductivity of polyacetylene over several orders of magnitude when exposed to halogen vapor. This was the first time an organic covalent polymer reached a conductivity far beyond 100 Scm^{-1} (10^5 Scm^{-1} to be precise) approaching the conductivity of metals like silver (10^8 Scm^{-1}).⁷⁻⁹ Nevertheless, conducting films of polyacetylene have severe drawbacks mostly based on their limited stability. Postulated reasons for this lack of stability were structural defects within the polyacetylene chains causing an interruption of charge transport. These structural defects were faced by moving from polyenes to polyaromatic systems with increased chemical stability.¹⁰ The essential property allowing for electrical conductivity is the conjugated π -system on the backbone of the polymer leading to a unique electronic configuration. In this context, conjugation describes the presence of both localized σ -bonds and more delocalized π -bonds which are arranged in a strictly alternating fashion. Numerous examples of structural motives including polymers with aromatic monomers, have been introduced since, based on the simplest version of polyacetylene (see **Figure 1**).¹¹

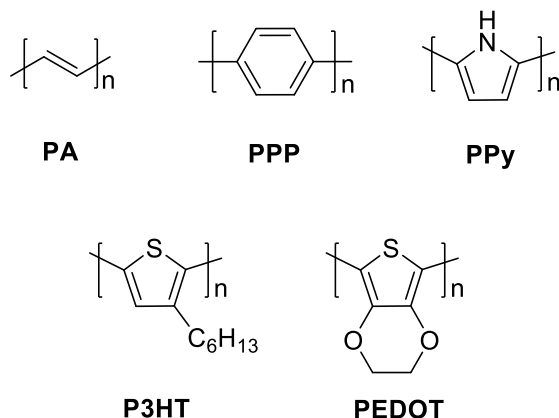


Figure 1: Chemical structures of exemplary conjugated polymers. Beginning with polyacetylene (PA), poly(p-phenylene) (PPP), polypyrrole (PPy), poly(3-hexylthiophene) (P3HT) and poly(3,4-ethylenedioxythiophene) (PEDOT).

Describing conjugated polymers as chains with identical bond lengths and completely delocalized π -electrons would make them a so-called synthetic metal. As experiments show, this is not the case. The bonds have an inherent difference in length which leads to alternating σ - and π -bonds along the polymer chain. The bond alternation is a direct consequence from Peierls instability which claims that systems with equal bond lengths and one unpaired electron per atom are unstable. The increase in stability of an alternating bond system is the result of a coupling between the wave function of the π -electrons and a vibration mode of the lattice (phonon). This arrangement leads to a division of the π -system into two bands (π and π^*). Each π -bond can hold two electrons leading to a completely filled π -band and an empty π^* -band, separated by a bandgap. This makes conjugated polymers semiconductors that show no or very low electric conductivity in the ground state.^{10, 12}

Regarding the orbital configuration of the carbon atoms along the backbone, a conjugated π -system is supported by a sp^2 -hybridization. Increasing the amount of adjacent carbon atoms in this sp^2 configuration, atomic orbitals merge into molecular orbitals which can ultimately be described as valence (filled π -band) and conduction band (empty π^* -band). The separating bandgap E_g is defined by two characteristic frontier orbitals which mark the upper and lower edge of the bandgap. The highest occupied molecular orbital (HOMO), meaning the energetic state with the highest energy that is still completely filled in the neutral state, is the top edge of the valence band. Its counterpart is the lowest unoccupied molecular orbital (LUMO), describing the bottom edge of the conduction band and the lowest energetic state that is completely empty in the neutral state (see **Figure 2**). The bandgap of polyacetylene for example lies in the range of 1.5 eV and hence does theoretically not allow for charge transport in its ground state.¹³

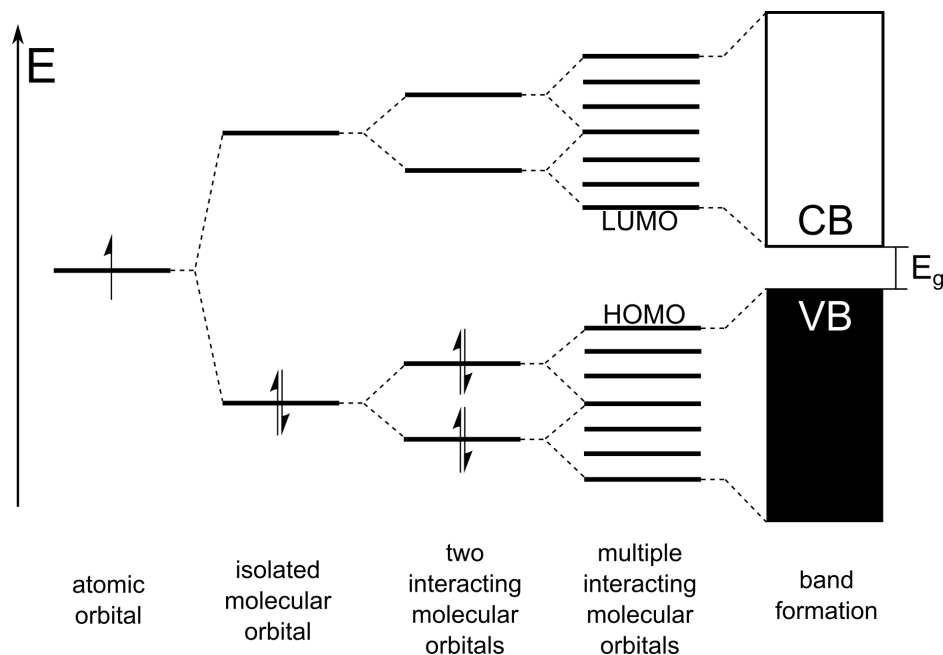


Figure 2: Evolution of a single isolated atomic orbital of a sp^2 hybridized carbon atom into a molecular orbital in for example ethylene. An increase in the number of interacting atoms and their orbitals leads to a band formation. The fully occupied valence band (VB) containing the highest occupied molecular orbital (HOMO) is separated by the band gap E_g from the unoccupied conduction band (CB), carrying the lowest unoccupied molecular orbital (LUMO). Adapted with permission from reference.¹⁰ © 2003, John Wiley and Sons.

To enable electronic conductivity conjugated polymers need to be doped. The doping process in conjugated polymers works fundamentally different compared to inorganic semiconductors, where atoms in the lattice are replaced by foreign atoms to create holes (p-type doping) or additional electrons (n-type doping) in the material. In the case of conducting polymers doping means an oxidation (p-type) or reduction (n-type) of the backbone itself. This redox reaction can be induced by different chemical or electrochemical approaches. Removing one electron from an aromatic conjugated polymer system (see **Figure 3**) creates a polaron that appears as radical cation on the backbone. A polaron is a quasiparticle with fermionic properties, including a spin of $\frac{1}{2}$ and the charge e and is connected to a localized geometrical relaxation. Here, the benzenoid bond configuration is being transferred into a quinoid-like form. Regarding the band model, this effect creates additional energetic states inside the bandgap. Further increasing of the doping level, leads to the removal of a second electron creating a bipolaron. A bipolaron is a spinless dication that carries the charge $2e$. It is created by the overlap of two polarons and is energetically favored over two separated polarons because the bond configuration around the quinoid bipolaron can relax back into its original benzenoid form. This interaction with the lattice generates enough energy to overcome the initial coulomb repulsion of converging two polarons of identical charge and spin. Similar to the polaronic states, bipolarons create additional states in the bandgap. Due to the fact that both charge carriers create different energetic states inside the bandgap,

different optical transitions are possible. This phenomenon can be used to spectroscopically detect both charged states. Besides that, while a polaron carries an electron spin a bipolaron is spinless offering further options to distinguish the two charge carriers.^{6, 13}

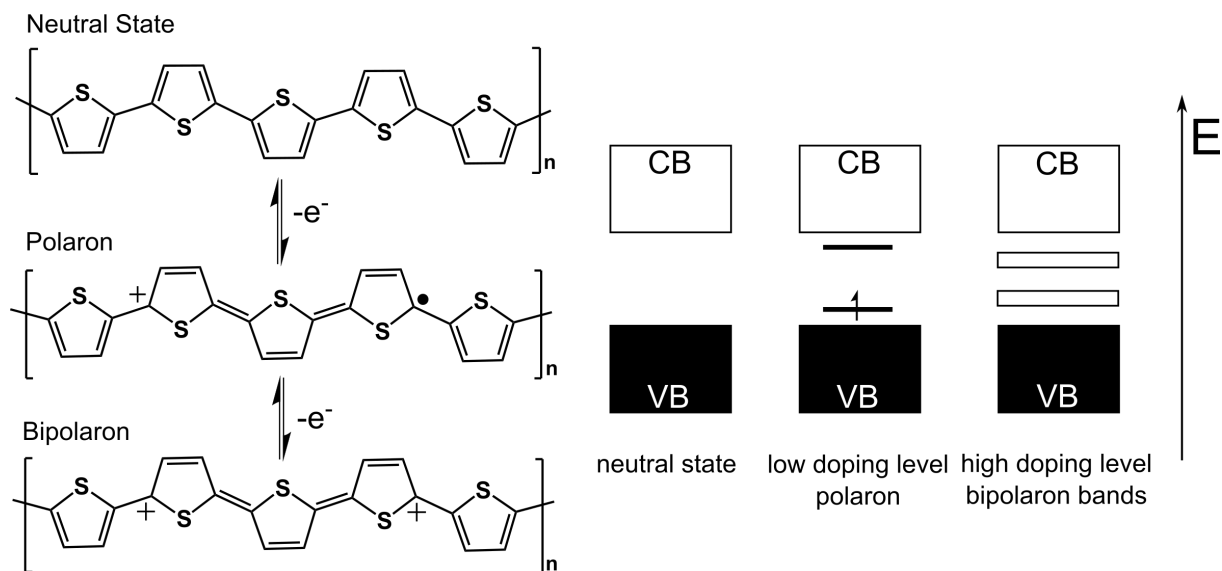


Figure 3: Schematic representation of the doping process of a polythiophene, when charging from neutral to polaron and bipolaron state (left side). The influence of doping on the band configuration of a conjugated polymer is displayed on the right. Additional states inside the band gap lead to an overall narrowing of the effective band gap. Adapted with permission from reference.¹³ © 1985, ACS.

At high doping levels, the bipolaron states can be described as bipolaron bands which reach deeper into the bandgap and are energetically further detached from the valence and conduction band compared to the polaron states. This can be explained by the increased lattice relaxation occurring around two charges compared to only one charge in a polaron. Another aspect that favors the creation of a bipolaron over two separated polarons is the higher stability caused by the strong shielding of a bipolaron with its corresponding counterions. Conductivity measurements of conjugated polymers in dependence of their doped state show that maximum conductivities can be found at high doping levels.¹⁴ One must add that a prerequisite of these findings is a high stability of doped states and no material degradation that could cause any loss of conductivity. At high doping levels the dominating charge carriers are found to be spinless, indicating the presence of mainly bipolarons. The bipolaron conduction at high doping levels is often described as bipolaron model and declares that highly mobile bipolarons provide for general charge propagation.^{12, 15-17} When strictly following the bipolaron model, charge transport mainly focuses on single chain propagation. This has been challenged by the knowledge of finite polymer chains which rarely exceeds a number of 50 monomer units per chain. Indeed, not the total length of polymer chain is decisive, it is the effective conjugation length of a chain segment that matters. Effective conjugation is often interrupted by material or morphology defects in an organic semiconductor which is naturally

more disordered and not perfectly crystalline. Hence, the key process determining the rate of charge transport is based on intra- and interchain hopping processes along and in-between polymer chains.¹⁵

Redox Polymers

Although doping of semiconducting conjugated polymers always involves a redox reaction either on the backbone or on tethered redox active sites, one can subdivide these materials regarding the way of charge propagation.¹⁸ In this context, redox polymers rely on electron hopping processes between localized redox sites which can be integrated into the chain or attached as side group to the backbone of the polymer.¹⁹ The high localization of charge on the respective redox sites is a decisive difference compared to previously described conjugated polymers which show a higher degree of charge delocalization among multiple repeating units. Concerning charge transport, conjugated polymers tend to show electron conduction via intra- and inter chain transport along conjugated backbones. Summing up, the way of charge propagation is strongly connected to the chemical structure of the polymer.^{15,20} In the following the focus will be put on characteristic structural motives, that are often used as redox active sites in redox polymers. As **Figure 4** displays, redox active centers can be for example covalently attached to a non-conjugated backbone or integrated into a fully conjugated backbone. The top row of **Figure 4** gives examples of redox polymers where redox active centers like triphenylamine (TPA),^{21,22} carbazole (Cbz)^{23,24} or a (2,2,6,6-tetramethylpiperidin-1-yl)oxyl (TEMPO) derivate^{25,26} are linked to a non-conjugated backbone. The bottom row gives two examples of conjugated redox polymers with redox active units like naphthalene-bis(dicarboximide) (NDI) and perylene-bis(dicarboximide) (PDI)²⁷ that are integrated into the conjugated backbone. Although there is a certain degree of charge delocalization in these examples, the strong localization of negative charge upon reaching the reduced states on the NDI-based units leads to an electronic behavior that can be described best in the context of a redox polymer.^{28,29}

When investigating the conductivity behavior of conducting polymer films and judging the impact of the induced charge carriers on the conductivity profile, a commonly used technique is coupling electrochemical experiments with *in situ* conductance measurements.³⁰ The conductivity in conducting polymers is tightly linked to the redox state of the material and relies on a trigger (doping) to switch from non-conducting to conducting state. Coupling electrochemical doping (CV) with additional sampling of the current flow between two combs of an interdigitated electrode, the conductance can be registered *in situ* while performing a classical CV experiment. The resulting potential dependent conductance profile can be used to localize regions of high conductance and correlate them to distinct doping levels (electrochemical potentials). The development of this method is mainly based on early works of Zotti and Wrighton.^{31,32}

When interpreting the results of *in situ* conductance experiments literature usually differentiates between two limiting cases. The conductance profile of conducting polymers typically appears in either a

sigmoidal shape with a plateau of high conductance at high potentials or a bell-shape profile with a local maximum at intermediate potentials and decreasing conductance at highest potentials. The first case with the plateau-shape conductance is typical for P3HT and follows the classical image of an organic semiconductor which switches from non-conductive to conductive upon the creation of charge carriers along its backbone. In general, this behavior follows the traditional bipolaron conduction model described earlier.^{13, 16} It is necessary to exactly control the applied potential window, since irreversible side reactions at high potentials or even material degradation might occur, leading to a sudden decrease of conductance at maximum potentials. The bell-shape conductance profile on the other hand is usually a characteristic phenomenon of redox polymers. The conductivity maximum is reached at an intermediate potential (half-charged level) and drops down significantly when further increasing the applied potential (increasing the doping level).³³⁻³⁵

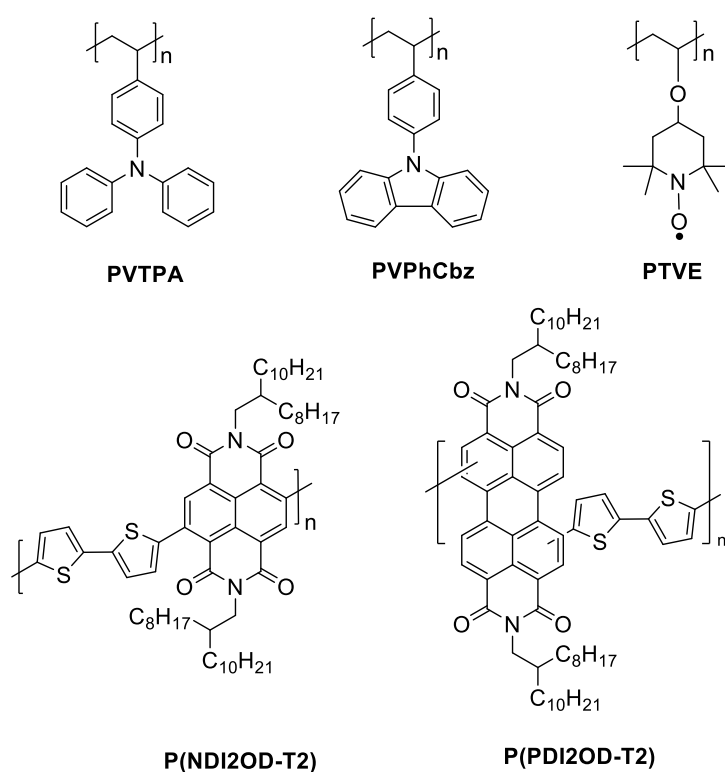


Figure 4: Chemical structures of examples of different redox polymers both with and without conjugated backbone. The top row showing redox active groups attached to the non-conjugated vinyl backbone in poly(vinyltriphenylamine) (PVTPA), poly(vinyl-phenylcarbazole) (PVPhCbz) and poly(2,2,6,6-tetramethylpiperidine-4-yl-1-oxylvinylether) (PTVE). Two examples for conjugated redox polymers P(NDI2OD-T2) and P(PDI2OD-T2) are given below.

The accepted explanation for the occurrence of a bell-shape conductivity profile is being provided by the mixed valence conductivity model.^{36, 37} Herein, charge transport is being described as hopping process between isoenergetic states of localized redox sites. The maximum conductivity is being reached

when roughly half of the redox sites are charged, offering the greatest amount of potential intermolecular hopping events. A further increase of potential leads to charging of all redox sites and the disappearance of potential hopping destinations. This results in a drop of conductivity recorded in the *in situ* conductance experiment at high potentials (high doping levels).

1.1.2 Chemical vs. Electrochemical Doping

As briefly described earlier, doping in inorganic semiconductors is usually based on the integration of foreign atoms into the crystal lattice of the crystalline semiconductor. This means dopants are often represented by single atoms with different electronic configuration. Since the doping process in organic semiconductors involves the addition of an electron to the LUMO of the semiconductor (n-type dopant) or the extraction of an electron from the semiconductor HOMO (p-type dopant), dopants used for organic semiconductors are molecules that are able to induce redox reactions. Atomic dopants are likely to diffuse if they are not covalently attached in a crystalline lattice structure and therefore avoided at all costs. Moving from atomic to molecular dopants, the tendency to diffuse is reduced and the stability of the doped state can be increased.^{38,39} The simple aspect of size, as a way to keep diffusion under control and increase the stability of doped organic semiconductors shows its impact especially in PEDOT:PSS, where poly(styrenesulfonate) is used as polymeric anion.^{40,41}

In general, dopant molecules can be a Brønsted or Lewis acid type of compound or a neutral small molecule with high electron affinity when acting as p-type dopants. The key property of all dopants is, their ability to donate or accept an electron in an electron transfer process. In this process no covalent bonds are broken or built to ensure a theoretical reversibility of the doping process. The interaction is of electronic nature without any chemical follow up reaction.^{38,39} To discuss further details of the molecular doping process, important differences between inorganic and organic semiconductor doping have to be pointed out. The most obvious difference is the amount of disorder on the nanoscale. Whereas inorganic materials often show nearly perfect symmetry and crystallinity, an organic semiconductor inherits a higher degree of disorder with structural defects leading to a substantial amount of electron hopping. Further, these structural defects give rise to charge trapping locations and can heavily influence the conductivity of the doped material.⁴²

This unique set of properties leads to two different configurations when organic semiconductors are molecularly doped. The straightforward situation is realized when the p-type dopant extracts one electron from the HOMO of the semiconductor into its LUMO. Following this process, each dopant molecule is entirely ionized and creates a free charge carrier in the organic semiconductor. This integer charge transfer leads to the formation of ion pairs. It needs to be underlined that the created charge carriers in the case of ion pairs are not locally bound but considered free charge carriers which are available for charge transport. The discovery of a very limited amount of actual free charge carriers

quickly brought the realization that the situation is more complex and the concept of the ion pair needs to be extended. The limited amount of free charge carriers is associated with a degree of charge transfer between dopant and organic semiconductor that is < 1 . That means integer charge transfer is not always the dominant process and that dopant and semiconductor can undergo more complicated electronic interactions.⁴³ These interactions are described by a charge transfer complexation which is a hybridization of the frontier orbitals of the dopant and the semiconductor. In these charge transfer complexes, a certain amount of charge is being transferred and shared. The concept of the ion pair can also integrate into the charge transfer complex idea where it marks the extreme case of complete charge transfer. Whether the doping process relies more on ion pair formation or charge transfer complexation cannot be declared in general but must be discussed for every dopant/semiconductor combination individually. The formation and amount of charge transfer complexes is highly relevant and needs to be taken into consideration when discussing the doping efficiency since it can decrease the amount of accessible free charge carriers significantly.^{38, 39}

For polythiophenes and especially P3HT the molecular p-type dopants FeCl_3 (Lewis acid) and F4TCNQ (neutral molecule) have been used extensively. Both molecules offer a high electron affinity that matches the ionization potential of P3HT to ensure charge transfer and the creation of doped P3HT.⁴⁴⁻⁴⁶ Besides the compatible electron affinity regarding the oxidation potential of P3HT, both molecules comprise another beneficial aspect regarding the processing aspect of the doping procedure. Both molecules can be brought into contact with P3HT either in solution or through the vapor phase.^{47, 48}

An alternative doping approach which completely avoids the limiting fact of finding a fitting dopant for an organic semiconductor, is electrochemical doping. Here, an electrochemical potential is applied at the oxidation/reduction potential of the semiconductor to induce the redox reaction and to create charge carriers in the material. Especially in transistor geometries it is important to draw a clear line between field-effect charging at the interface and electrochemical bulk doping. The difference becomes obvious when considering a conducting polymer film brought into contact with electrolyte in an electrochemical setup (see chapter 1.4.2) or transistor configuration (see **Figure 5**).

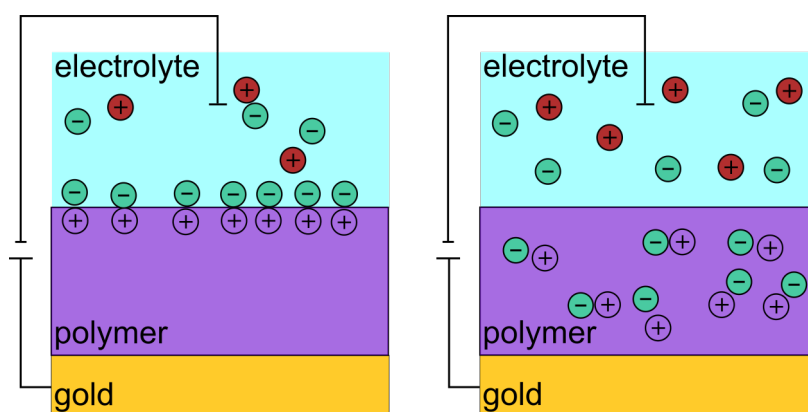


Figure 5: Schematic of classical field effect charging and electrochemical bulk doping in the geometry of an electrolyte-gated transistor configuration. In case of field effect charging, the charges are created and located at the interface between film and electrolyte (left side). Electrochemical bulk doping on the other hand charges the entire film and leads to an integration of counterions from the electrolyte to the bulk (right side). Adapted with permission from reference.⁴⁹ © 2007, ACS.

Upon applying electrochemical potentials below the oxidation potential of the conducting polymer, an electrostatic double layer is generated at the interface between electrolyte and polymer film. This creates a high density of negative counterions in close proximity to the film surface, which compensate the positive charge carriers near the surface inside the film. The applied voltage, or gate voltage is responsible for the formation of this field-induced capacitive double layer.

If the applied voltage reaches or exceeds the oxidation potential of the semiconducting polymer, electrochemical bulk doping sets in, creating positive charge carriers inside the bulk of the polymer film. To counterbalance the created charge carriers counterions (anions) from the electrolyte solution start to diffuse into the film. This leads to a situation where the film is electrically neutral to the outside, because every induced charge carrier is weakly bound to a counterion. The fact that the bulk of the film is charged and ions reach deep into the material is the distinct difference to the previously described field-induced charging of the double layer at the surface of the film. Although it has to be stated that the charging of the double layer occurs parallel to the doping of the bulk film. Theoretically, the process of electrochemical bulk doping is completely reversible since the integrated ions are moving electrostatically inside the film without the creation or disruption of chemical bonds. As already implied, local defects of the organic material can lead to charge traps, limiting the overall electrochemical reversibility of the entire process. One of the most outstanding features of electrochemical doping is the possibility to fine-tune the charge carrier density inside the bulk material by simply adjusting the applied voltage (doping voltage).^{49, 50}

1.2 P3HT as Model System

Among all conjugated polymers polythiophenes have quickly become one of the most promising material classes. Polythiophenes offer great advantages like good stability under ambient conditions and satisfying thermal stability.⁵¹ Since P3HT has shown to be the model polymer from the group of polythiophenes, numerous applications from transistors to solar cells have been realized with P3HT. A combination of simple synthetic accessibility, good charge transport properties and sufficient solubility in organic solvents, maintained by the introduction of the alkyl side-chains, are some of the reasons for the success of P3HT in the field of organic electronics.⁵²

1.2.1 Synthesis

Due to the attachment of the hexyl side chain on one side of the thiophene ring in 3-hexylthiophene, three regioisomers can be formed during the polymerization. The different options of linking two monomers result in 2,5' head-to-tail (HT), 2,2' head-to-head (HH) and 5,5' tail-to-tail (TT) regioisomers (see **Figure 6**).

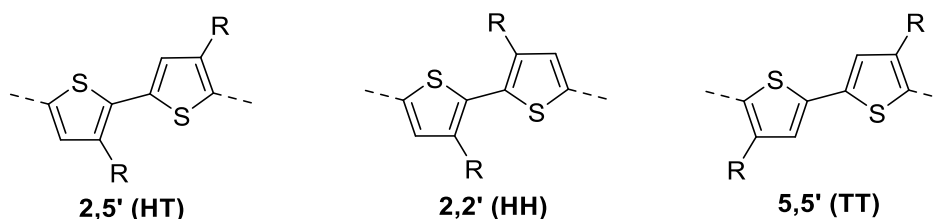


Figure 6: Chemical structure of different regioisomers of P3HT as a consequence of the position of the hexyl side chain. The isomers are 2,5' head-to-tail (HT), 2,2' head-to-head (HH) and 5,5' tail-to-tail (TT).

Only the strictly regioregular 2,5' (HT) configuration is favorable for electronic properties which rely fundamentally on self-organized morphologies with efficient π - π stacking to maximize the effective conjugation length. Especially the 2,2' (HH) linkage, found in regiorandom P3HT, is prone to high steric hindrance due to the alkyl side chains disturbing backbone ordering.⁵³ A deeper insight into morphology and its influence on the electronic properties will be given in later chapters. Different synthetic approaches have been presented to satisfy the demand for regioregular poly(3-alkylthiophenes) like P3HT. An exemplary synthetic route will be pointed out here which dates back to the work of McCullough. The very first synthetic route was invented by Loewe and McCullough in 1992⁵⁴ but due to the need of low temperatures, reducing the practicability, further developments were necessary. In 1999 Loewe published an improved synthesis based on an efficient and economical Grignard metathesis (GRIM) reaction, that excluded the need of cryogenic temperatures.⁵⁵

After the bromine is being exchanged with the magnesium Grignard reagent, a composition of 4:1 regarding the magnesium on position 5 versus 2 is being obtained via this route. Although this delivers an access of only 80 %, the final polymer contains about 99 % of 2,5' (HT) couplings (see **Figure 7**). This is being explained by a higher selectivity of the catalyst for the excess magnesium component during the polymerization.⁵⁵ The mechanism of the polymerization follows three characteristic steps that are postulated for Ni(II) catalyzed cross-coupling polymerizations being oxidative addition, transmetalation and reductive elimination arranged in a catalytic cycle. This polymerization type belongs to the chain-growth mechanisms and yields narrow polydispersities in the case of regioregular poly(3-alkylthiophenes).⁵⁶

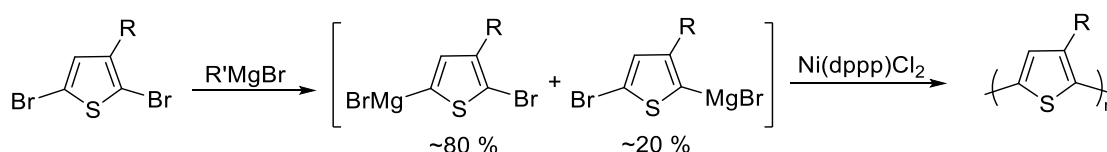


Figure 7: Synthetic route towards regioregular poly(3-alkylthiophenes) with narrow polydispersity following the Grignard metathesis reaction and subsequent Ni(II) catalyzed cross-coupling polymerization.

When generally considering the electrochemical properties of polythiophenes like P3HT an alternative synthetic approach to the common chemical synthesis needs to be outlined. A unique property of conducting polymers is the ability of their monomeric precursor units to be polymerized in an electrochemical way. In the case of P3HT this oxidative polymerization is being induced by the application of an external electrochemical potential that is strong enough to match the oxidation onset of the monomers to trigger an oxidative coupling. The so called electropolymerization is performed in electrochemical setups with monomers dissolved in the electrolyte solution and leads to a fast and effective deposition of a polymerized electroactive film on the electrode surface.

As far as the understanding of the electropolymerization goes, the mechanism is described by three consecutive steps. Initially, monomers are being oxidized at the electrode and immediately coupled to generate oligomers that are still soluble and start to concentrate within the diffusion layer close to the electrode. The second step is induced by nucleation and leads to a deposition of oligomers as a solid film on the surface of the electrode. The third stage of the mechanism is the polymerization in solid-state on the electrode surface, leading to increasing chain lengths and crosslinking reactions.^{15, 57}

At first, the mechanism of the electropolymerization has been described as a successive coupling of charged monomers to a growing chain. After dimerization the more easily oxidized dimers are immediately being oxidized and react with another monomer radical cation to form a trimer and so on.

The coupling of cations is followed by proton elimination to return to the aromatic oligomeric species.⁵⁸⁻⁶¹ This mechanism can be considered similar to a chain-growth polymerization in ionic polymerizations for example. A more widely accepted concept of electropolymerization reactions is based on the so-called oligomer approach and takes more complex processes into account which cannot be fully respected in the simplistic chain-growth model of Diaz.^{58, 59}

One of the central aspects which are highlighted in the oligomer approach (see **Figure 8**) is that properties and processes during the electropolymerization are heavily influenced by the chain length of the respective oligomeric species. One of these aspects is the overall reactivity. When the chain length of the oligomeric species increases, the reactivity is strongly decreasing. This has a direct consequence on the mechanism of the polymerization. Since the reactivity of charged radical monomeric species is immensely higher compared to longer oligomers, the dimerization between the radical monomer species dominates.^{62, 63} This makes a coupling reaction between a charged radical monomer and a charged oligomer highly unlikely and its probability further decreases with increasing chain length of the participating oligomeric species.

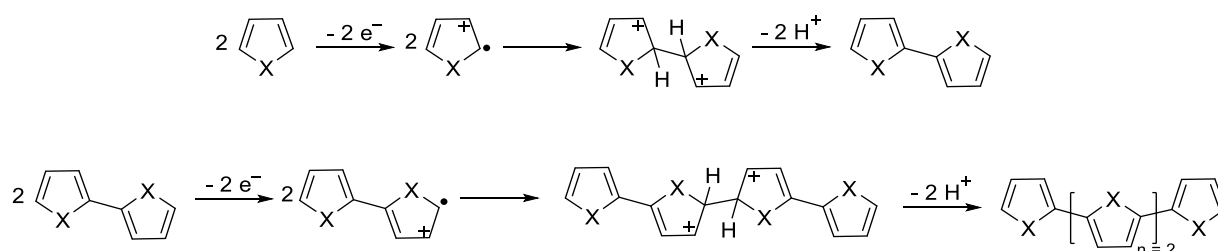


Figure 8: Postulated mechanism for the electropolymerization of polythiophenes following the concept of the oligomer approach. Monomers couple to form dimers which form tetramers and higher oligomers in consecutive steps. Adapted with permission from reference.¹⁵ © 2010, ACS.

Looking more closely on the coupling reaction it was discussed that besides the coupling rate, the proton elimination step of the resulting σ -dimer seems to be the rate determining step.^{64, 65} Since an increased conjugation length is beneficial for stabilizing the additional charge after coupling, the proton elimination becomes slower and only occurs efficiently when the applied oxidation potential sets an additional driving force. These two parameters (reactivity and rate of proton elimination) fuel the probability of coupling reactions between charged radical monomers and makes a permanent elongation of oligomers by a stepwise addition of a charged monomer unlikely. Here, a coupling of oligomeric species describes the mechanism best, leading to an oligomerization beginning with a dimerization, followed by the coupling of dimers into a tetramer and so on.^{15, 57}

1.2.2 Semicrystalline Morphology in Thin Films

In general, many of the properties that make P3HT and conducting polymers such a unique material class, are based on their semicrystalline character when processed in films for example. The central reason that is responsible for boosting the tendency to self-organize into ordered morphologies is the planar and rigid backbone, which is provided by the aromatic system. Nevertheless, the influence of the position, size and nature of the side groups attached to the backbone should not be neglected. For semicrystalline conducting polymers the image of folding chains that form crystalline lamellae alternating with unordered amorphous domains is the widely accepted image (see **Figure 9 a**).^{52, 66-68} The presence of amorphous domains in between lamellar sections highlights the need of a certain number of interconnected chains, allowing for hopping locations to support macroscopic charge transport. The lamellar structures have a strong desire to further aggregate and form hierarchical superstructures. The most prominent superstructures based on semicrystalline lamellae are fiber-like structures and radially symmetric spherulites. Upon simple and fast processing conditions like spin coating, the crystalline lamellae are randomly oriented and typically less-perfectly pronounced, due to the high nucleation density and fast crystallization time. On the molecular level the semicrystalline morphology typically forms two major configurations (edge-on and face-on) describing the chain orientation in respect to the surface plane of the substrate. In the case of edge-on the backbone and π - π stacking direction is oriented parallel to the substrate with the alkyl chains being in a perpendicular orientation, standing out of the substrate plane. In face-on configuration the backbone and alkyl chains are positioned parallel to the substrate with the π - π stacking direction oriented perpendicular to it (see **Figure 9 c**).

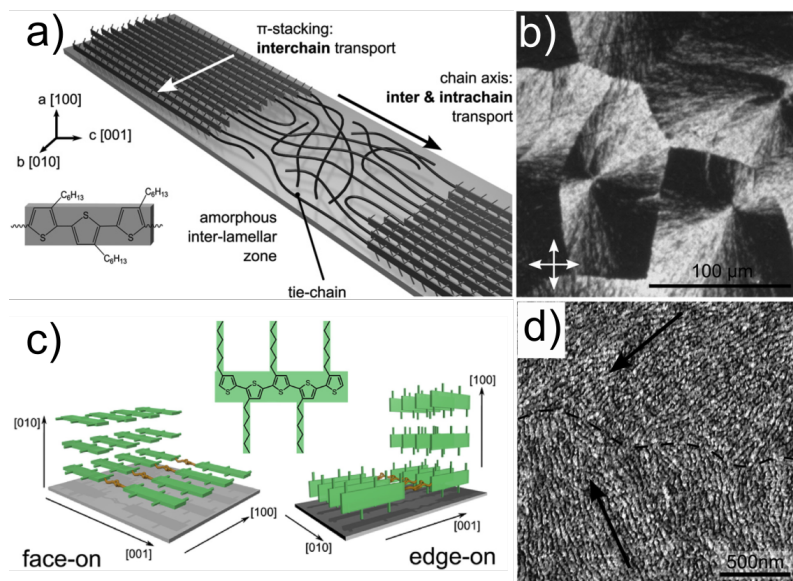


Figure 9: Schematic representation of the semicrystalline morphology of P3HT in a), consisting of crystalline lamellar regions and amorphous zones. Inter- and intrachain transport as possible ways of charge propagation are also indicated. The two main molecular orientations edge-on and face-on are shown in c). A polarized optical microscope image of P3HT spherulites in b) and corresponding AFM image in d) showing different orientations of the crystalline lamellae at the grain boundary. Adapted with permission from reference.⁶⁹ © 2012, John Wiley and Sons.

One powerful method to control and fine-tune the crystallization process is solvent vapor annealing. Here, films produced for example via spin coating are afterwards exposed to an atmosphere with controlled solvent vapor pressure. This leads to swelling of the film and induces a solubilized state where sufficient structural rearrangement is possible. By slowly reducing the solvent vapor pressure the crystallization process can be triggered and the nucleation density is drastically reduced. This allows for well-defined morphologies with highly ordered domains like spherulite structures as shown in **Figure 9** b) and d).^{69, 70}

The type and degree of crystallinity have a strong impact on the optical and electronic properties of conducting polymers. The close correlation between morphology and material properties is usually referred to as structure-property relationship. Therefore, the control over the crystallization process is the key to strengthen the desired properties of the neat material and transfer them into functional devices. In the case of P3HT the crystallinity in thin films can have a strong influence on the absorbance spectrum. In fact, the difference is resulting in film colors ranging from orange to purple and is already visible by eye.⁷¹ The strongest difference can be seen when comparing regiorandom and regioregular P3HT films.

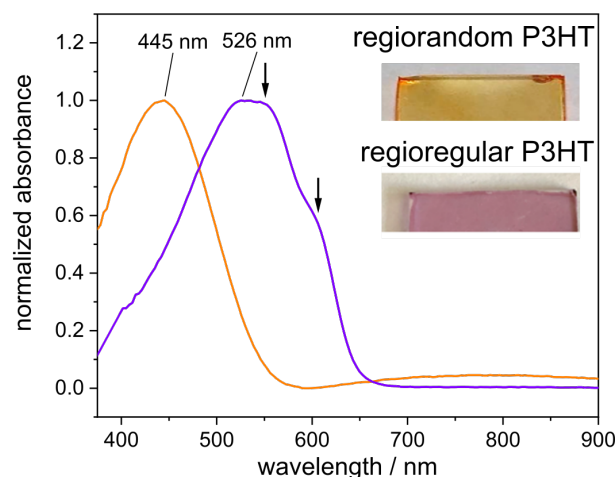


Figure 10: Absorbance spectra of films of regiorandom (orange) and regioregular (purple) P3HT are shown and characteristic points marked with black arrows. Additionally, images of the spincoated films are given to show the distinct color change.

The absorbance spectra of a regiorandom P3HT film shows a broad absorption without any additional features as a result of an entirely amorphous film. The random orientation of the attached side chains sterically hinders an efficient chain aggregation and leads to a nearly completely amorphous morphology in thin films. The film spectrum of regioregular P3HT on the other hand is significantly shifted to longer wavelengths and bears additional features and shoulders as indicated by the arrows in **Figure 10**.^{72, 73} The absorbance shoulders are vibronic features that are a direct consequence of strong chain aggregation in the film. Here, the high regioregularity allows for efficient chain ordering leading to a high amount of π - π stacking.⁷⁴ Besides regioregularity the molecular weight has a strong influence on the morphology as well and thus on the shape and position of the peaks in the absorption spectrum.⁷¹ Low molecular weight P3HT tends to form strongly defined fibers that can even be separated from each other for the lowest molecular weights. The low degree of interconnection between the fibers is one source of charge trapping effects and lowers electric performance. With increasing molar mass, the definition of the fibers is lost and an increasing amount of tie chains lead to higher overall interconnectivity between the fiber-like domains.^{66, 67} Regarding electric performance, it is clear that efficient charge transport relies on these interconnected domains, which essentially bridge the amorphous regions to areas of higher crystallinity enabling efficient charge transport. It is shown in literature that a high degree of π - π aggregation and short-range interconnectivity is of utmost importance for sufficient macroscopic electronic performance.⁶⁸ In particular, high crystallinity and long-range order might be the ideal condition for charge transport in semicrystalline polymers but even completely amorphous P3HT shows acceptable conductivities, questioning the importance of perfect long-range order and underlining the impact of short-range interconnectivity.^{24, 42, 75}

Not only the absorption properties are strongly influenced by the film morphology, electronic properties like the electrochemical behavior observed in cyclic voltammetry is heavily impacted by the morphology in films of P3HT.⁷⁶

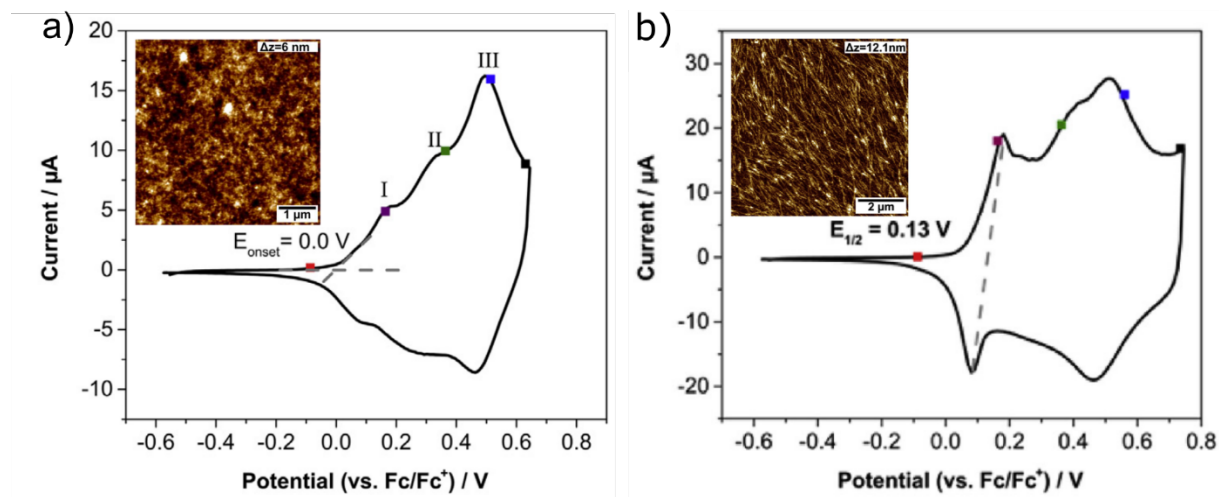


Figure 11: Cyclic voltammograms of films of P3HT in different morphologies are presented in a) and b). The cyclic voltammogram in a) is recorded from a simply spin coated film, whereas the result in b) was obtained with a P3HT film showing highly ordered spherulitic structures. The corresponding morphology is indicated by the inserted AFM images. Adapted with permission from reference.⁷⁶ © 2018, Elsevier.

At first sight, both CVs in **Figure 11** reveal the typical broad wave which is characteristic for conducting polymers like P3HT and is sourced in the polydisperse nature of the material. Different chain lengths can lead to different effective conjugation lengths which inherit a slightly different oxidation potential, resulting in an overlap of multiple redox processes. Nevertheless, when closely examining the shape of the redox wave several underlying subsignals can be distinguished. Different interpretations of these subsignals are present in literature and are mainly focused on the work of Trznadel and Sompka.⁷⁷ The early model of Trznadel et al. assigns signal I to the transition of the neutral state into radical cations in ordered domains whereas signal II is the corresponding signal of radical cations in disordered domains. Signal III describes the transition from radical cation into dication.^{78, 79} Whether signal III is truly induced by the oxidation step into the dication is questioned by the model of Skompka. Here, all three signals are assigned to the oxidation of the neutral state into the radical cation. The differentiating aspect is the degree of order and crystallinity of the domain in which the charge is induced. Signal I belongs to crystalline domains, II to quasi-ordered and III to disordered domains.^{80, 81} The degree of order imposes a direct influence on the average effective conjugation length in specific domains and therefore slightly shifts the oxidation potential of the respective species.⁸²⁻⁸⁴ By increasing the general amount of crystalline domains (for example by allowing for growth of spherulitic structures) the signal belonging to the oxidation of crystalline domains (subsignal I) can be drastically enlarged (see **Figure 11** b)). The

onset remains constant in both cases and is typically located at around 0 V (vs. Fc/Fc^+) for P3HT. Since the oxidation of crystalline domains of P3HT occurs first (located at the lowest electrochemical potentials), the contribution to the electrochemical onset mainly originates from these highly ordered regions.⁷⁶

1.2.3 Advanced Electrochemistry and Coupled Spectroscopic Techniques

Due to the broad waves in the cyclic voltammograms of conducting polymers like P3HT the signals of the oxidation of neutral into polaronic species and the second oxidation step of polaron into bipolaron is hard to identify from purely evaluating the electrochemical current response. As mentioned above, different effective conjugation lengths influenced by the overall film crystallinity further complicate the analysis of the participating charge carriers. Therefore, coupled electrochemical techniques have been introduced which combine a classical CV experiment with spectroscopic analysis methods like UV-vis or EPR (electron paramagnetic resonance) spectroscopy. Both techniques take advantage of differing properties between neutral, polaron and bipolaron species. In the case of UV-vis spectroscopy each charge carrier shows an individual fingerprint in the absorption spectrum, based on the unique optical transitions occurring upon radiation. EPR spectroscopy is a spectroscopic technique that is highly sensitive for unpaired electrons. In this way the transition from the EPR silent neutral state into the spin bearing polaron state can be followed.

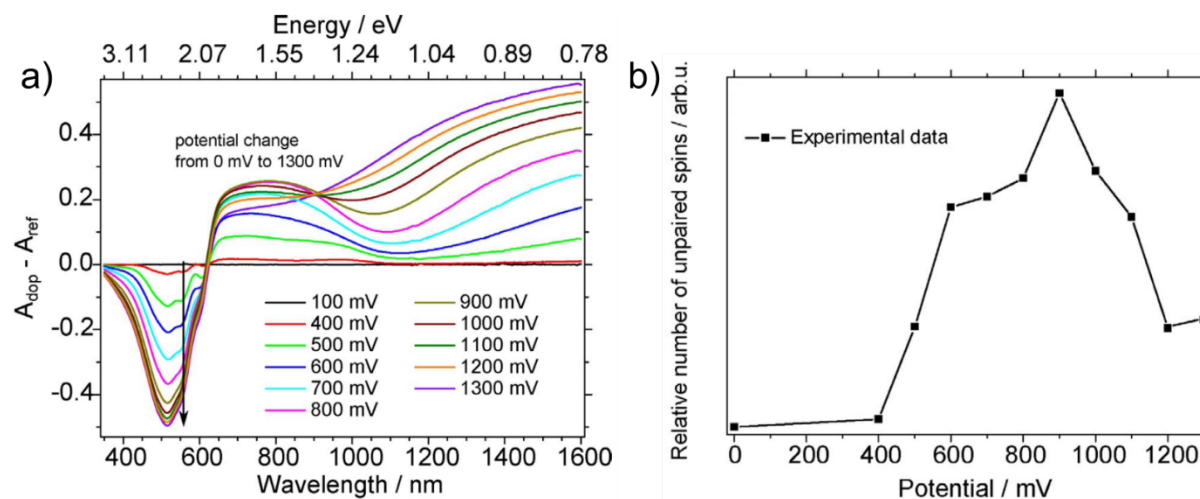


Figure 12: Results of a differential *in situ* spectroelectrochemistry experiment are shown in a) giving the characteristic absorption upon electrochemical charging. The data obtained from a cyclic voltammetry experiment coupled with *in situ* EPR are shown in b). The relative number of spins is being recorded during increasing the electrochemical potential. Adapted with permission from reference.⁸⁵ © 2016, John Wiley and Sons.

When describing the differential absorption behavior upon *in situ* charging in **Figure 12** a) the characteristic wavelengths of each species become clear. The absorption band of the neutral state is

located at around 500 nm which is significantly decreasing when the potential is increased in favor of a new band at around 700 nm. This intermediate band is usually assigned to the polaron in the literature. Shortly after the band at 700 nm rises the signal at high wavelengths increases at around 1500 nm. It is important to note that this band also keeps gaining intensity when the band at 700 nm is decreasing again at highest potentials. This is often interpreted as the characteristic transition into the bipolaron state.^{76, 81} This interpretation is being supported by the *in situ* recorded number of spins (**Figure 12 b**). At the beginning only few spins can be detected since the neutral state is spinless and EPR silent. After passing a distinct potential the number of spins increases and shows a maximum at intermediate potentials. This correlates to the position of maximum polaron concentration. Further increasing the potential across this point leads to a decrease of unpaired electrons explained by the transition into spinless bipolaron states.⁸⁵ The observation that still some spins are present at highest doping potentials might indicate the presence of mixed charge carriers throughout the experiment. Besides *in situ* coupled electrochemical experiments, EPR can provide more in depth understanding about the nature of the charge carriers in P3HT. Recent work by Neher et al. used advanced ENDOR spectroscopy on doped regioregular and regiorandom P3HT solutions.⁸⁶ ENDOR essentially detects the hyperfine coupling between electron spins and the nuclear spins of the protons on the polymer backbone. The coupling strength of the individual protons can be used to determine the amount of delocalization of the unpaired electron spin along the chain segment. Results show that regioregular P3HT allows for much higher delocalization of polaron spins of about 12 thiophene units compared to regiorandom P3HT with just about 6 thiophene units. This underlines the importance to understand the interplay between aggregation and crystallinity and the characteristics of the induced charge carriers in conducting polymers like P3HT. Further, interactions of different dopants with polaronic charge carriers in films of P3HT were recently presented by Behrends et al.⁸⁷ Here, EPR spectroscopy provided new insights on the influence of dopants like F4TCNQ and their impact on the delocalization of charge carriers on the P3HT backbone. Interactions between dopants and charge carriers, like locally bound pairs can limit the amount of free charge carriers in the film and therefore weaken the electrical conductivity. Although the interactions between charge carrier and dopant are usually not favorable in this case, approaches by van Slageren et al. try to exploit the interactions between polaronic charge carriers in a P3HT matrix and inserted spin bearing molecular quantum bits in a guest-host system.⁸⁸ By inducing spin bearing polaronic charge carriers in the P3HT matrix, these systems are investigated as a platform for spin-dependent charge transport and offer possibilities for an electrical readout of the polarization of the integrated quantum bits.

1.3 From P3HT to State of the Art Donor-Acceptor Copolymers

One of the most promising advantages of conjugated polymers is the possibility to fine-tune the electronic properties by different synthetic approaches. A change of the electronic structure has direct

consequences on the energy levels (HOMO and LUMO) and the band gap of the material. This allows for an exact adjustment of the position of the energy levels which is important for example when producing efficient solar cell devices. Although the combination of P3HT and fullerene acceptors dominated the field for some time, limiting factors like the small absorption range and the relatively high HOMO level of P3HT substantiated the need for new material development. In this case the family of copolymers offers a great variety of different comonomers leading to wider possibilities to fine-tune the electronic structure compared to classical conjugated polymers where researchers are limited to one single monomer. In the following **Figure 13** the two state-of-the-art copolymers PM6 and P(NDI2OD-T2) are to be presented in closer detail.^{89, 90}

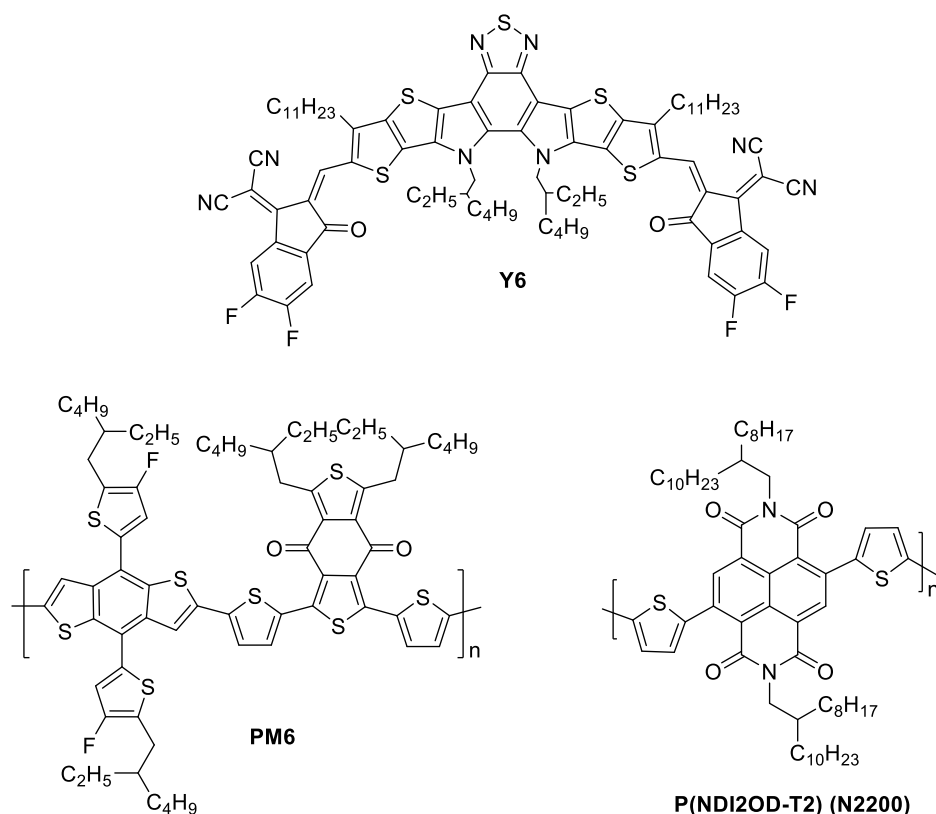


Figure 13: Chemical structures of the chosen state-of-the-art donor acceptor molecule Y6 as well as the donor acceptor copolymers PM6 and P(NDI2OD-T2).

PM6 short for (Poly[(2,6-(4,8-bis(5-(2-ethylhexyl)-3-fluoro)thiophen-2-yl)-benzo[1,2-b:4,5b']dithiophene))-alt-(5,5-(1',3'-di-2-thienyl-5',7'-bis(2-ethylhexyl)benzo[1',2'-c:4',5'-c']dithiophene-4,8-dione))) is a donor material developed in the context of donor-acceptor copolymers for photovoltaic applications. PM6 can be described as the fluorinated version of the copolymer PBDTBDD which was introduced in 2012 by Hou et al.⁹¹ The copolymer PBDTBDD combines the electron donating structure of benzodithiophene with the acceptor moiety benzo[1',2'-c:4',5'-c']di-thiophene-4,8-dione. Although BHJ solar cells from PBDTBDD and PC₆₁BM reached power conversion efficiencies around

6 %, the double fluorination of PBDTBDD turned out to be a key step in elevating the device performance. The resulting donor-acceptor copolymer PM6, presented in 2015 by Hou et al., showed significant improvements in device performance by increasing the power conversion efficiency by 30 % (BHJ cell with PC₇₁BM).⁸⁹ The attachment of two fluorine atoms influences the electronic structure of the material by lowering the HOMO which has direct consequences on parameters of the final device. Besides the impact of the fluorination on the electronic properties, an increase in overall polarity also influences the aggregation and packing behavior. PM6 shows strong aggregation and π - π stacking which plays a role also when it comes to mixing and phase separation with the respective acceptor component. The potential of PM6 as donor material has been presented in 2019 by Zou et al. where BHJ solar cells of the high-performance blend of PM6 and the non-fullerene acceptor Y6 delivered power conversion efficiencies over 15 %.⁹²

Another state-of-the-art material which counts to the much more limited group of n-type donor-acceptor copolymers is P(NDI2OD-T2). This copolymer based on naphthalene-bis(dicarboximide) (NDI) is also known as N2200 or P(NDI2OD-T2) short for poly((N,N9-bis(2-octyldodecyl)-naphthalene-1,4,5,8-bis(dicarboximide)-2,6-diyl)-alt-5,59-(2,29-bithiophene)) was first presented by Facchetti et al. in 2009 and still remains a benchmark system in the field of n-type semiconducting polymers.⁹⁰ P(NDI2OD-T2) caught attention due to its good solubility and high charge carrier mobilities in organic field effect transistors. Beyond transistor applications, it has also shown to be a promising acceptor material in organic solar cells giving power conversion efficiencies around 8 %.⁹³ A property of P(NDI2OD-T2) that is strongly pronounced is its tendency to aggregate in solution or thin films. The aggregation describes strong π - π interactions between several polymer chains or between segments of a single chain. The amount of aggregation can be tuned by choosing good or bad solvents or modifying the regioregularity of the polymer. Heavy aggregation in solution also imposes a certain order when deposited in thin films in this case. Techniques like blade coating can be used to take advantage of this pre-aggregation in solution and induce aligned fibers in thin films. Properties like charge transport have shown to be sensitive to the anisotropy in aligned films of P(NDI2OD-T2).^{94, 95}

1.4 Applications

1.4.1 Organic Photovoltaics (OPV)

The characteristic high extinction coefficient of conducting polymers like P3HT caught early attention for potential applications as light harvesting material in active layers of organic solar cells. Additional features of organic solar cells like large scale roll-to-roll processability on flexible and light-weight substrates (foils) are already in the focus of companies like Heliatek and infinityPV. These companies offer OPV devices on flexible foils for different demands to cover for example roofs or curved surfaces like wind power stations. Although aspects like efficiency and long-time stability need to be further

improved, these examples show the wide range of possibilities for industrial scale OPV in specific market niches. The field of photovoltaics is still dominated by silicon-based devices making up more than 95 % of all produced solar cell modules in 2020.⁹⁶ The average efficiency a commercial silicon-based solar cell module can reach is roughly located around 20 %. This value can be regarded as a target benchmark value which needs to be consistently achieved in any alternative solar cell approach to realize a commercial application at large scale. In the last 15 years organic solar cells have seen an impressive development increasing their efficiencies from around 5 % to now closely approaching the value of 20 % in research cell configurations (see **Figure 14**, orange filled circles).

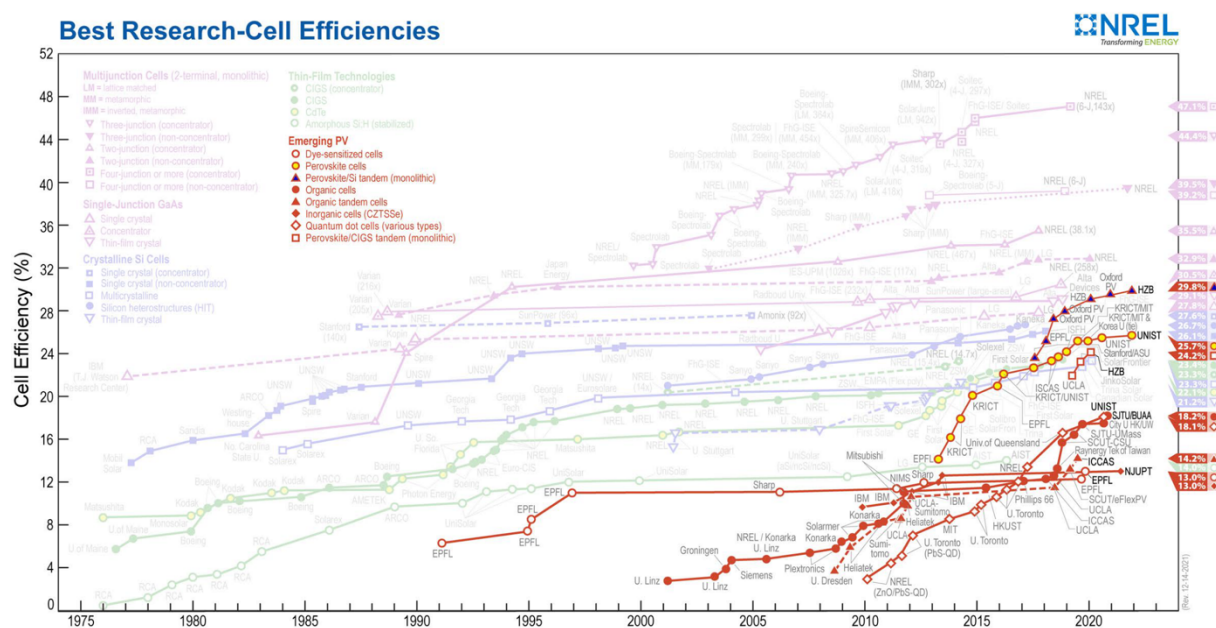


Figure 14: General overview over the progress of cell efficiencies of research cells based on different technical concepts and geometries. Specifically highlighted are the data points on emerging photovoltaic cells marked in orange, since they also contain organic solar cells (solid orange circles), outlining their strong surge up to 18 % efficiency in recent years. This plot is courtesy of the National Renewable Energy Laboratory, Golden, CO.⁹⁷

The typical buildup of organic solar cells consists of a transparent electrode with a thin layer of conducting oxide on top (e. g. ITO). This electrode is followed by two organic photoactive layers. One being a donor material with low ionization potential (high HOMO level) and the other an acceptor layer with high electron affinity (low LUMO level). These two layers are responsible for the efficient light harvest of the solar spectrum, charge generation and transport. The second electrode (e. g. Al) completes the classical OPV device.

The physical processes of charge generation in an organic solar cell are fundamentally different from its inorganic counterpart. When two doped inorganic semiconductors are combined and form a p-n junction, the carrier distribution at the interface creates a space charge region with a strong electric field.

Induced charge carriers diffuse to the interface where the electric field accelerates the charge carriers and leads to an accumulation on the other side of the p-n junction. Hence, the overall charge transport is governed by diffusion in the bulk and drift at the space charge region.

In an organic solar cell (see **Figure 15**), light with an energy that exceeds the band gap of the organic material is being absorbed (1). This creates a locally bound electron-hole pair in its equilibrium state (2) which is called exciton. In order to dissociate into separated charge carriers, the excitons need to diffuse (3) to the donor-acceptor interface which must be in close proximity for efficient exciton dissociation (4). The process competing with exciton diffusion is recombination and needs to be avoided to increase the overall efficiency of the device. The different work functions of the chosen electrodes induce an additional electric field assisting in the charge transport and charge carrier collection at the respective electrodes (5). The charge transport in an OPV is based on a strong interplay of drift and diffusion in the bulk and at the interface.⁹⁸⁻¹⁰⁰

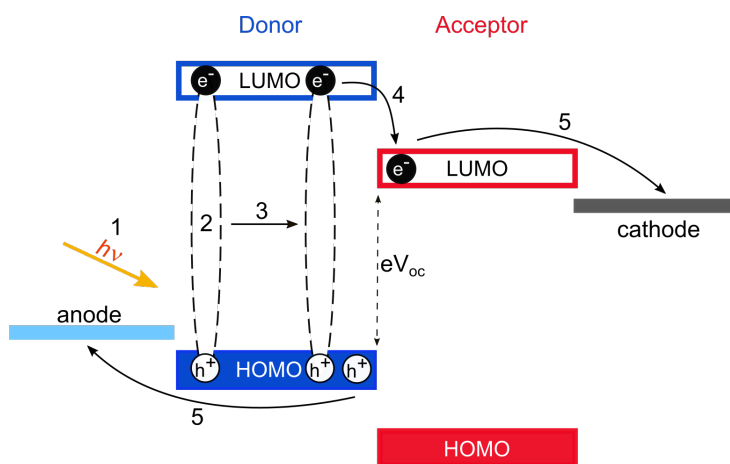


Figure 15: Schematic of the basic elements of an organic bulk heterojunction solar cell and the fundamental processes occurring during charge generation. The single steps are numbered as follows: 1) illumination by sun light; 2) creation of a locally bound exciton; 3) exciton diffusion to the donor acceptor interface; 4) charge separation into free charge carriers; 5) transport of the respective charge carriers to the individual electrodes. Adapted with permission from reference.⁹⁸ © 2008, RSC.

As described before, exciton dissociation at the donor-acceptor interface is the critical step during charge generation in the organic active layer. Therefore, research was focused on increasing the size of the interface between donor and acceptor layer. Since the exciton diffusion length is limited to around 10 nm, the impact of the morphology of the active layer is of highest importance.¹⁰¹⁻¹⁰³ The simplest arrangement of donor and acceptor layer is the planar heterojunction configuration. Although fabrication might be convenient for devices in this arrangement, the rather small donor-acceptor interface is not favoring efficient charge separation. In this context, a bulk heterojunction approach shows to be a more promising architecture and outperforms the traditional planar heterojunction due to its large donor-

acceptor interface (see **Figure 16** left). Therefore, the donor and acceptor materials can be either codeposited¹⁰⁴ or already blended in solution.^{105, 106} Aspects that need to be fulfilled in a bulk heterojunction is a self-assembly into phase-separated structures with a domain size between 10-20 nm. Only in regions of this domain size, a sufficient charge separation limited by the diffusion length of the exciton can be assured. Secondly, the phase separation needs to be well-defined to guarantee for charge pathways that connect the donor-acceptor interface to the respective electrode. In this way, charge carrier mobility is high enough to transport charges to the electrode before recombination deteriorates the device efficiency.^{103, 107}

The OPV device performance can be evaluated by different electrical parameters taken from the current density-voltage characteristics displayed in **Figure 16**. The graph shows the current density in the dark (dashed line) and under illumination (solid line). Under illumination, two characteristic parameters can be extracted, located on the intersections with the two axis which are the short-circuit current J_{SC} and the open-circuit voltage V_{OC} . The short-circuit current J_{SC} marks the highest generated photo current under illumination and is the result of the photo-to-electron conversion process in an ideal case. The open-circuit voltage V_{OC} at the intersection with the x-axis is derived from the effective transport gap (energy gap between HOMO of the donor and LUMO of the acceptor) of the chosen donor-acceptor pair.

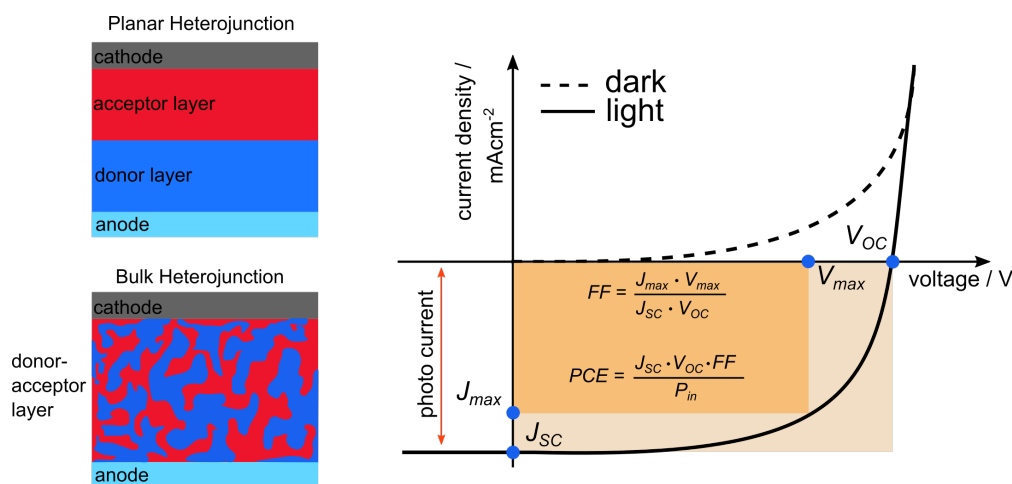


Figure 16: Schematic overview of the different geometries of a planar heterojunction and a bulk heterojunction, both containing a donor (blue) and acceptor (red) material. On the right a characteristic current density-voltage plot of an organic solar cell is presented, containing all important parameters to characterize the device performance in detail. Adapted with permission from reference.¹⁰⁸ © 2012, John Wiley and Sons.

Although the V_{OC} can be increased by decreasing the overall offset between the energy levels of the donor-acceptor pair, it is usually located between 0.3 and 0.5 eV to overcome the exciton binding energy to secure an efficient exciton diffusion at the interface. Having discussed J_{SC} and V_{OC} , a value calculated

from both of these parameters is the fill factor FF . It is a measure of the overall quality of the solar cell device and is influenced by parasitic resistances occurring mainly due to contact resistances inside the device. Especially when organic semiconductors are used, effects resulting from impurities and disorder can further decrease the device quality and affect the fill factor. The most relevant device parameter is the power conversion efficiency (PCE or η) which is the essential metric when judging the device performance. Generally spoken, the PCE specifies how much of the sun's power which is illuminating the device is actually converted into electrical power and can be very helpful in comparing different device architectures.⁹⁸⁻¹⁰⁰

Donor Materials for OPV

Different materials have proven their worth as donor layer in OPV devices.¹⁰⁰ Although there is a great variety of materials the following section will mainly focus on thiophene-based organic semiconductors and their derivatives. For many years, the model system of this material class has been P3HT (see **Figure 17**). Due to its semicrystalline character with high tendency for π - π stacking it fulfills the prerequisites for charge transport in combination with strong absorption properties.^{52, 109} In combination with PCBM, P3HT shows efficiencies up to 5 %, which led the OPV device development for many years.^{110, 111} Progress in the field of conjugated donor-acceptor copolymers introduced PCPDTBT and its derivatives to the solar cell community.^{112, 113} By replacing the central bridging atom by silicon, morphology and electronic properties could be further improved leading to efficiencies above 5 %.^{114, 115} Regarding polymer donors, the recently presented PM6^{89, 116, 117} and its modifications display impressive performance in the device giving power conversion efficiencies up to 18 %.¹¹⁸⁻¹²² Besides polymer donors, molecular or oligomer-based donor materials play an important role in OPV as well.^{57, 108, 123} In this case small molecules containing for example TPA units^{124, 125} or simple oligothiophenes like sexithiophene found their way into different organic electronics devices.¹²⁶⁻¹²⁸ Differences and challenges in the processing steps of these materials are to be considered, since small molecules are often deposited through the vapor phase and exhibit a high sensitivity to crystallize in the film.

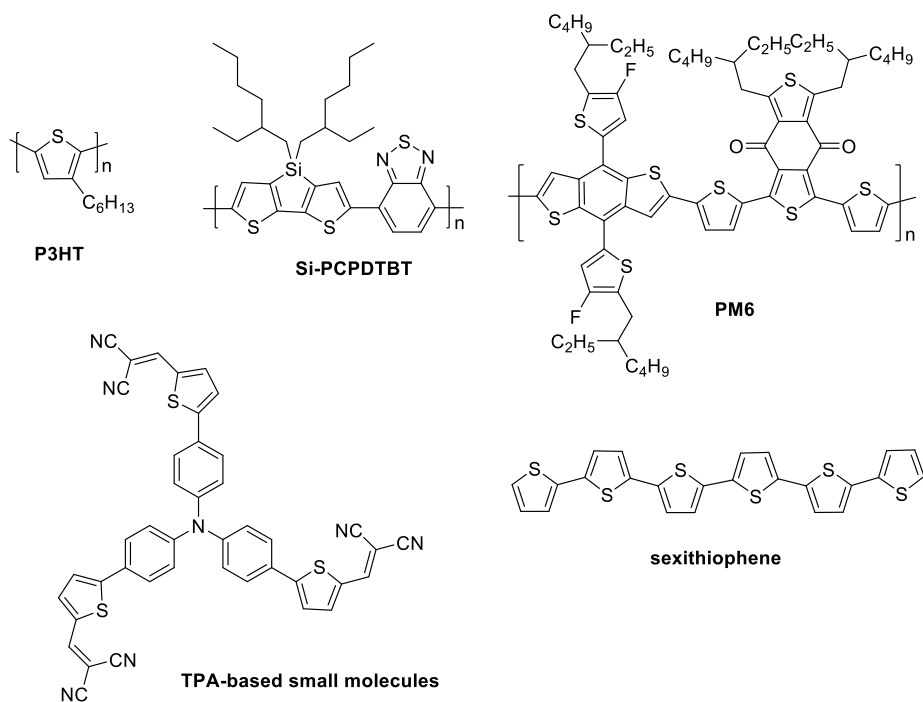


Figure 17: Chemical structures of a variety of commonly applied donor materials, containing the model system P3HT, two donor-acceptor copolymers (Si-PCPDTBT and PM6) and two small molecules. One TPA-based molecule following the concept of push-pull chromophores and one being the benchmark material sexithiophene.

Acceptor Materials for OPV

The most famous material class regarding acceptor layers are without any doubt fullerene acceptors which have been used extensively over the last decade.^{129, 130} Modified fullerenes like PCBM (see **Figure 18**) combine high electron affinity with good charge transport properties explaining their impact on the field in combination with various donors like for example P3HT.^{110, 111} Due to dimerization and degradation under illumination, fullerenes can struggle with stability in the photo-active layers.¹³¹ The integration of n-type semiconducting polymers can be presented as alternative to fullerene acceptors allowing for the construction of all-polymer solar cells. A widely studied n-type polymer is P(NDI2OD-T2) (N2200) which has been initially established as material for field-effect transistors where it shows impressive charge carrier mobilities.^{90, 132} A transfer into OPV devices together with a donor called J50 in the literature shows efficiencies of 8.27 %.⁹³ Recent advances presented non-fullerene acceptors (NFA) as the next generation of materials pushing efficiencies towards 20 %.¹³³⁻¹³⁶ Famous examples accelerating the field of NFAs in recent years are ITIC¹³⁷⁻¹⁴⁰ and Y6.¹⁴¹⁻¹⁴³ Especially Y6 needs to be mentioned which is often paired with PM6 in devices that deliver efficiencies around 16 %.^{92, 144, 145}

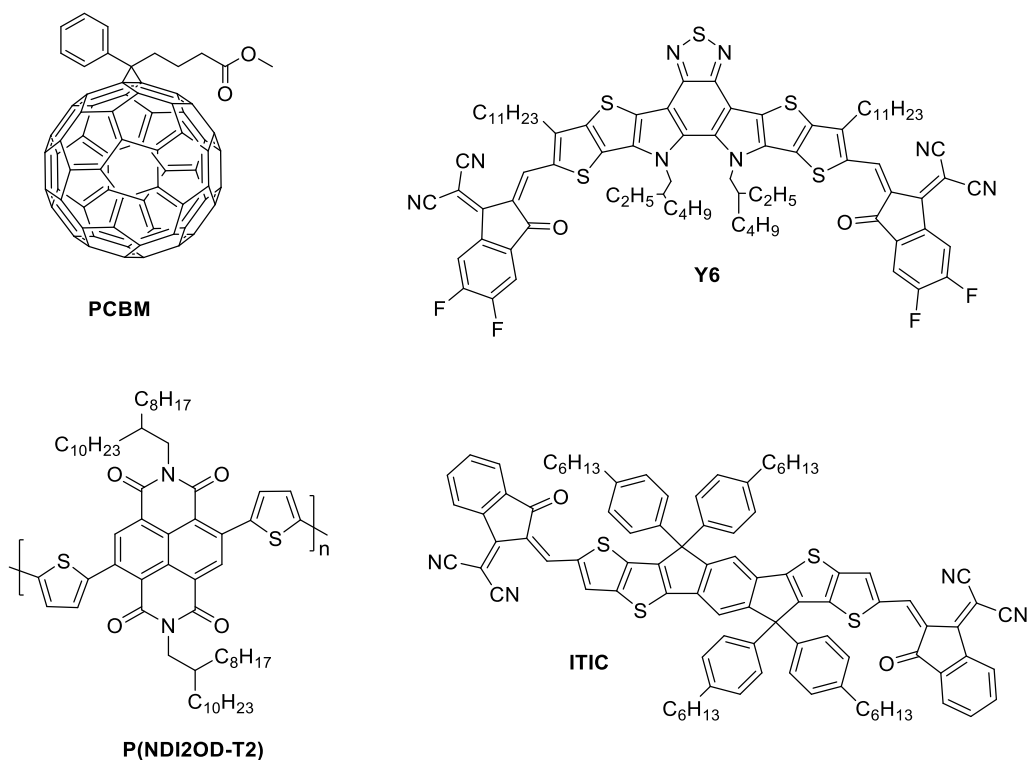


Figure 18: Chemical structures of frequently used acceptor materials in organic solar cells, showing the classical fullerene PCBM, a donor-acceptor copolymer P(NDI2OD-T2) and two of the recently presented non-fullerene acceptors Y6 and ITIC.

1.4.2 Storing Charge in Organic Electrochemical Devices

The two main ways of introducing charge carriers in a conducting polymer are chemical and electrochemical doping. Both basic concepts have been described in chapter 1.1.2 and act as theoretical background for the following section. Because this thesis is focused on the fundamental process of electrochemical doping, this section will present an example where this charge generation method is being applied in an organic electronics device. This will grant wider context and strengthen the overall impact of the performed studies presenting insights into devices that can profit from new findings in this research field.

An organic electronics device that relies on the fundamental process of electrochemical charge injection is the organic electrochemical transistor (OECT). In this transistor geometry ions start to migrate into the bulk of the organic semiconductor in the channel upon application of a gate voltage. The applied voltage controls the degree of electrochemical doping and the charge carrier density, regulating the overall conductivity inside the semiconductor channel. This device geometry and its working principle is decisively different from electrolyte-gated field effect transistors (EGOFET). Here, charges accumulate only on the surface and no bulk penetration of ions is being observed. In addition, in an

OECT, charge creation and storage occurs in an electronic and ionic way, explaining the high transconductance (relation between voltage input and current output) which is one of the striking characteristic properties of OECTs (see **Figure 19**).^{146, 147}

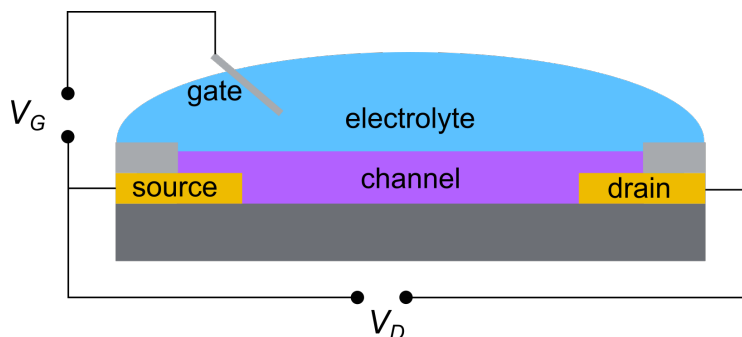


Figure 19: OECT device geometry consisting of a source, drain and gate electrode. In between source and drain the transistor channel is covered with the organic semiconductor film. Adapted with permission from reference.¹⁴⁶ © 2014, John Wiley and Sons.

The basic principle, that the conductivity inside a channel-like electrode structure covered with a semiconducting polymer in contact with electrolyte is tunable by an additional gate voltage was reported in 1984.³² In the neutral state the polymer behaves like an insulator turning the device into the “off” state. Increasing the gate voltage above the oxidation potential of the polymer, the conducting state is being reached, charges are created and compensated by ions from the electrolyte and the device changes into the “on” state. Only in the “on” state sufficient mobile charge carriers are present to allow for a current to flow. This type of operation mode is called accumulation mode, where the channel is being drained from charge carriers when no gate voltage is applied. The described operation mode can be realized with different kinds of conjugated polymers since most of them are in their neutral, non-conducting state when no voltage is applied. The accumulation mode is quite interesting because these devices are running on low power since they are usually in the “off” state and only turn “on” when the analyte reaches the interface. The working principle also influences the time response, meaning the switching time between “off” and “on” state which is limited by ion diffusion into the bulk film. In the case of OECTs switching times are usually significantly higher compared to OFET geometries where no real bulk doping occurs.¹⁴⁶ Knowledge on the diffusion process and effects like charge trapping that can interfere with ion integration and expulsion is therefore highly relevant and exhibits direct influence on the device relevant parameters.

The importance of ion migration in the bulk and its effect on the redox active polymer film has been recognized by different groups. Here, potential dependent GIWAXS measurements are a powerful tool to examine the degree and kind of structural reaction of the polymer film upon integration of counterions.¹⁴⁸⁻¹⁵⁰ In the case of P3HT the image provided by literature is quite clear. With an increasing

gate voltage, the alkyl spacing is increasing whereas the π - π stacking distance is decreasing. This trend implies that the integrated counterions reside between the alkyl chains and do not interfere with the π - π stacked motifs. The result underlines that a certain amount of order is being preserved even when ions accompanied by solvent molecules enter the bulk film. The structural change occurs simultaneously to a noticeable increase in effective charge carrier mobility.

A drawback of purely conjugated polymers in OECTs is their inherent hydrophobic character which can impact migration of naturally hydrated ions from the electrolyte into the bulk material in a negative way.¹⁵¹ Due to the fact that the working principle of an OECT demands for a combination of good ionic and electronic conductivity, the conjugated backbone can be modified with side groups like ionic groups or glycol chains to increase hydrophilicity.^{152, 153} In this context conjugated polyelectrolytes like poly(6-(thiophene-3-yl)hexane-1-sulfonate) (PTS) derived from classical P3HT and mixed systems like PEDOT:PSS have been established and presented as mixed conductor systems (see **Figure 20 a**). The sulfonate group attached to the hexyl side chain in PTS can be compensated with a tetrabutylammonium cation. The big and sterically demanding cation has the advantage of a reduced tendency to move under applied voltage and is therefore less likely to take part in the diffusion processes in the bulk film.¹⁵⁴ This effect can be pushed even further when moving to polymeric ions like poly(styrenesulfonate) (PSS).

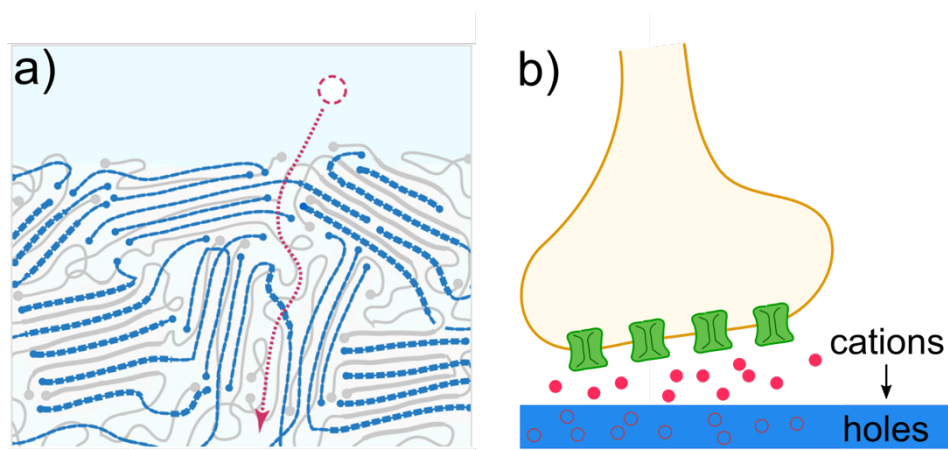


Figure 20: The interface between a PEDOT:PSS film and an ion containing electrolyte is shown in a). Possible migration ways for ion insertion are depicted in red. A schematic overview of a neuron that can be modified with OECTs to build a biosensor platform is presented in b). Adapted with permission from reference.¹⁵⁵ © 2013, ACS. Adapted with permission from reference.¹⁵⁶ © 2015, John Wiley and Sons.

In the case of the semiconducting polymer PEDOT:PSS, the OECT channel is doped with no additional gate voltage applied and a transfer to the “off” state (depleting the channel from charge carriers) is only obtained with an additional gate bias.¹⁵⁷ This operation mode is referred to as depletion mode. In the case of PEDOT:PSS it has been reported that electronic and ionic conductivity not only depends on the applied gate voltage but is strongly influenced by the water content and the swelling state of the film.

An exact control of the swelling state by tuning the water content is an interesting approach to fine-tune the ionic and electronic conductivity in PEDOT:PSS-based systems.¹⁵⁸

In contrast to typical inorganic semiconductors, polymer-based films lack the insulating oxide layer on the surface which behaves like a natural barrier, shielding the electrolyte from the bulk of the inorganic semiconductor. Without this barrier an interaction with for example biological systems becomes possible. The improved hydrophilicity and good ionic and electronic conductivity make conjugated polymers an interesting platform for implementation into biological interfaces. In this context, applications like biosensors or neural interfaces are of high interest. The low operating voltage enables functional devices in aqueous media and the high transconductance can facilitate the detection of even smallest signals in biological systems. In particular, the transmittance of signals in synapses of neurons in the human brain highly depends on the change in flux of ions. By integrating OECTs into synapses (see **Figure 20 b**)) artificial bioinspired platforms can be constructed which contribute to the development of different ways of communication between biological systems and machines.^{155, 156, 159}

2 Aim of this Thesis

To broaden the opportunities for the integration of semiconducting polymer films into a wide range of organic electronics devices, a high electronic conductivity is one of the key elements that demand the attention of researchers. In the case of semiconducting conjugated polymers this can only be realized by finding effective ways to transfer these materials into their conducting state, ideally in a controlled and stable way. Therefore, the main objective of this thesis is to understand the process of electrochemical doping on a fundamental level and exploit its inherent advantages to produce highly conducting polymer films with tunable conductivities. When it comes to electronic properties the doping process itself only covers one part of the issue. The ability to control the film morphology of conjugated polymers has a significant impact on the electronic performance and needs to be taken into account when trying to understand charge transport properties and play a major role when improving device relevant parameters. Hence, this thesis aims to understand the **interplay between electrochemical doping and film morphology** to identify essential aspects important for highly conducting polymer films.

In a first step a basic expertise on the process of electrochemical doping should be generated by reverting to the conjugated polymer P3HT. As one of the workhorses in the field of organic electronics, P3HT comes with a high data availability in literature and offers the possibility to build on the specific knowledge of our group. Here, electrochemical doping should be applied to induce charge carriers *in situ* in an electrochemical cell.

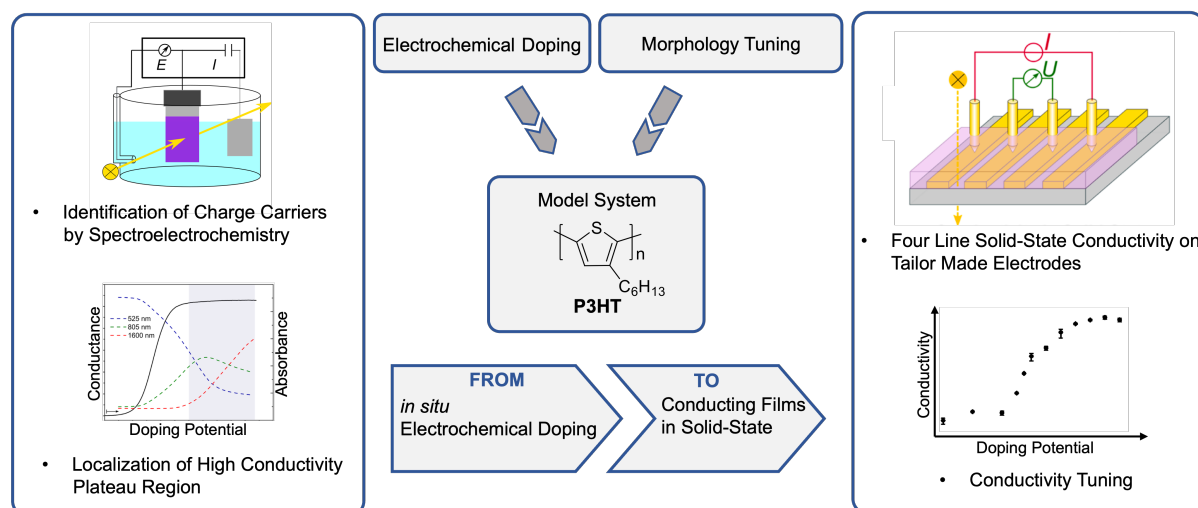


Figure 21: Schematic overview of the electrochemical doping study on P3HT films. This schematic contains parts that are adapted with permission from reference.²⁴ © 2020, ACS.

The identification of the charge carriers by different coupled spectroscopic methods depicts an important aspect to understand the conductivity behavior. Following the localization of potential dependent regions of high conductivity, the central issue of extracting the doped films from the electrochemical

cell should be realized. Measuring the conductivity of the doped films in the solid-state on tailor made four line electrodes is a central advantage of our approach. Besides defining the maximum conductivity, the possibility to **fine-tune the conductivity** in dependence of the doping level should be investigated. To improve the understanding of the charge transport model the results on P3HT are compared to a classical redox polymer PVPhCbz. Finally, the question of morphology is being concerned by comparing disordered semicrystalline morphologies of regioregular P3HT to completely amorphous films of regiorandom P3HT.

The electrochemical doping study on P3HT will be extended by focusing more strongly on the doping process itself and which factors can have direct consequences on the solid-state conductivity. Here, the choice of the counterbalancing ion within the electrolyte is in the center of attention. The general impact of **ion size** and nature on the electrochemical reversibility is to be assessed and characterized regarding their tendency for **charge trapping**.

Part two of this thesis should build on the gained expertise on electrochemical doping of P3HT to answer to challenges of current state-of-the-art materials. At first, the **analysis of the energy levels** of the conjugated polymer PM6 and the non-fullerene acceptor Y6 in device relevant blends is to be performed. The knowledge of emerging charged species upon electrochemical doping of P3HT films should be used as established expertise to identify and locate charged species of PM6 and Y6 when processed in blend films. By using spectroelectrochemistry as the method of choice spectral onsets should be used to calculate the resulting energy levels of the individual compounds in the blend films.

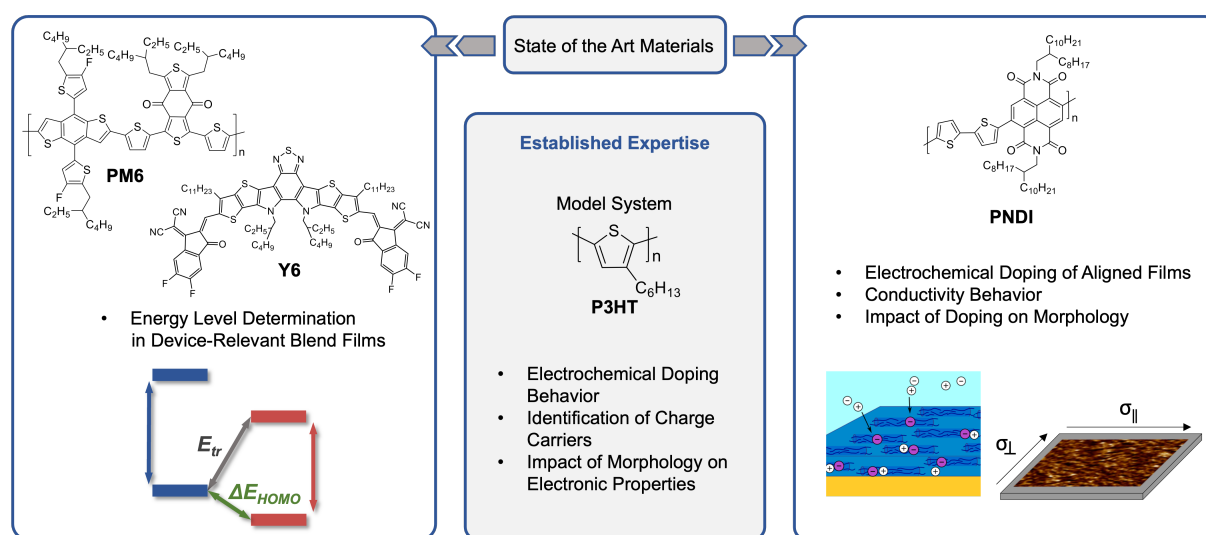


Figure 22: Schematic overview of the work on the state-of-the-art materials PM6:Y6 and P(NDI2OD-T2) both based on the established expertise on P3HT.

Additionally, specific interest concerns the **morphology of the blend films** and its potential influence on the energetics. This interest is based on results that show considerably differing solar cell performance regarding the open circuit voltage when comparing face-on to edge-on configurations.

An additional final aim of this thesis is to transfer the electrochemical doping approach, established with P3HT, to the benchmark n-type conjugated polymer P(NDI2OD-T2). Here, the unique urge of this material to strongly aggregate in solution and in films should be exploited to produce aligned films by blade coating which can be electrochemically doped. In this way, the influence of alignment on the tuning of the conductivity can be judged and compared to regularly spin coated films. The well-defined morphology of the aligned films further acts as platform to understand the **structural response** to certain electrochemical doping levels and conductivities. In this way, the characteristic integration of counterions into the bulk films can be followed and its interplay with defined morphologies characterized.

3 Part I: Conductivity-Tuning of P3HT Films by an Electrochemical Doping Approach

3.1 High Conductivities of Disordered P3HT Films by an Electrochemical Doping Strategy

3.1.1 Publication Data

Title: “High Conductivities of Disordered P3HT Films by an Electrochemical Doping Strategy”

Status: Full Paper, Publication July 10th, 2020

Journal: Chemistry of Materials, 2020, 32, 6003-6013

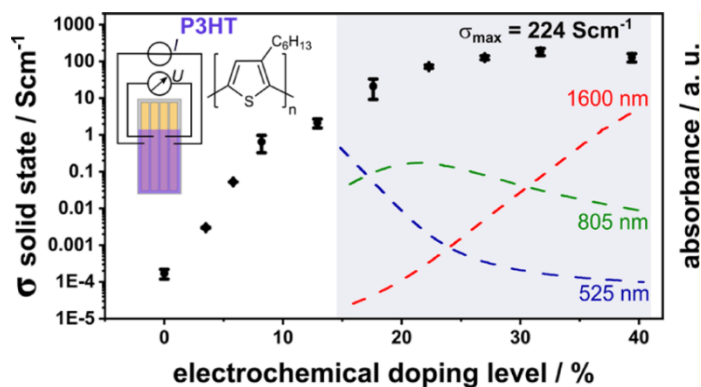
Publisher: American Chemical Society

DOI: 10.1021/acs.chemmater.0c01293

Authors: David Neusser, Claudia Malacrida, Michal Kern, Yannic M. Gross, Joris van Slageren and Sabine Ludwigs.

Contributions: D. Neusser executed all experiments and wrote the first version of the manuscript. M. Kern performed and interpreted the EPR measurements. The co-authors revised the first version of the manuscript. All work was supervised by S. Ludwigs.

Graphical Abstract (TOC)



3.1.2 Short Summary

Poly(3-hexylthiophene) represents one of the most studied conjugated polymers and is known as one of the workhorses in the organic electronics community. Its semiconducting nature gives rise to a conductivity that can be modified over multiple orders of magnitude upon doping. The doping process itself is usually conducted via chemical or electrochemical doping approaches. In the case of conjugated polymers doping describes a redox reaction on the polymer backbone that is initiated by either introducing redox agents (chemical doping) or by applying an electrochemical potential (electrochemical doping) to the film. This work describes the advantages of an *ex situ* electrochemical doping approach offering the opportunity to fine-tuning the doping level by applying a distinct electrochemical doping potential. The potential induces charge carriers inside the P3HT film compensated by counterions from the electrolyte leading to an increasing charge carrier density at high doping levels. For our films the rise in charge carrier density is accompanied by an increase in conductivity up to values of 224 Scm^{-1} . This value marks an increase in conductivity over 6 orders of magnitude compared to the undoped neutral state of our P3HT films. To identify the created charge carriers, we analyze the doped films by UV-vis and EPR spectroscopy. Both techniques confirm that *in situ* generated charge carriers can be successfully transferred into the solid-state under the inert conditions of our approach. Further, our results show that doped P3HT is present in mixed charged states over the entire plateau range where highest conductivities can be found. We interpret this result with the coexistence of polarons and bipolarons at all doping levels, where the relative amount of polarons is increasing from low to intermediate doping levels and then gradually consumed in favor of bipolaron states when going to highest doping levels. Finally, we compare the results on P3HT films with a typical redox polymer PVPhCbz that offers more insights into the conductivity behavior of a pure redox polymer system which is dominated by hopping transport and explained in the context of the mixed valence conductivity model. Assessing the influence of morphology, we are using simply spin coated films with rather disordered semicrystalline morphologies as well as completely amorphous films of regiorandom P3HT. Here, our highly conducting films fuel the question whether a high crystallinity with long range order can be denoted as a prerequisite for good conductivity in conjugated polymer films or rather short-range interconnectivity is the key for efficient charge transport.

3.1.3 Manuscript



pubs.acs.org/cm

Article

High Conductivities of Disordered P3HT Films by an Electrochemical Doping Strategy

David Neusser, Claudia Malacrida, Michal Kern, Yannic M. Gross, Joris van Slageren, and Sabine Ludwigs*

Cite This: *Chem. Mater.* 2020, 32, 6003–6013

Read Online

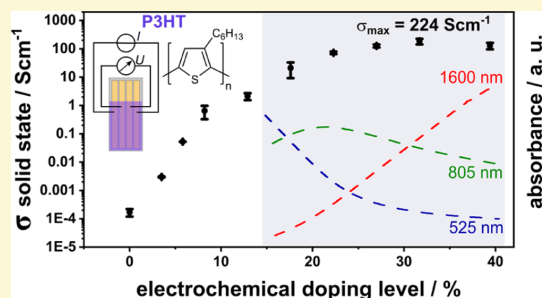
ACCESS |

Metrics & More

Article Recommendations

Supporting Information

ABSTRACT: In this work, we demonstrate that high solid-state conductivities of simply spin-coated poly(3-hexylthiophene) (P3HT) films can be obtained by means of an *ex situ* electrochemical doping strategy using 4-line electrodes. With increasing electrochemical doping potential, we find an increase in conductivity over 6 orders of magnitude, giving a maximum conductivity up to 224 S cm^{-1} with maximum hole densities of 10^{21} holes per cm^3 . Most intriguingly, highly conducting states are achieved over a very broad potential range from 0.4 to 0.8 V versus Fc/Fc⁺ in the doped state. The experiments are complemented by UV–vis–NIR absorption and electron paramagnetic resonance spectroscopy in the solid state as well as with *in situ* electrochemical measurements which confirm that the electrochemically generated doped species can be successfully transferred into the solid state. Our results suggest that for reaching high conducting states, P3HT has to be present in different redox states and that the plateau conductivity region should arise from the coexistence of overlapping polaron and bipolaron states. Comparisons to films of regiorandom P3HT and pure redox polymer systems based on diphenyl-3,3'-bicarbazyl are further presented, which highlight the role of mixed valence states in conducting polymers. Last but not least, the highly conducting films are simply spin-coated and therefore rather disordered, adding new aspects to the discussion whether high crystallinity is a prerequisite for achieving high conductivities in conjugated polymers.



1. INTRODUCTION

Conducting polymers (CPs) feature a unique set of properties such as low weight, processability from solution, and intrinsic electronic conductivity upon doping, explaining their successful integration in numerous applications in the field of organic electronics and electrochemical devices in the last years.^{1–3} Depending on their chemical nature, CPs can be divided into conjugated and redox polymers.⁴ In redox polymers, charge transport is governed by pure hopping transport between localized redox units that are in different oxidation states, following a well-accepted mixed valence conductivity model.^{5–8} Conjugated polymers on the other hand are based on long π -conjugated backbones that allow inter- and intrachain transport between the chains. Charge carriers go along with a geometrical deformation, delocalized over multiple repeating units and are hence usually referred to as polaron and bipolaron species.^{8–11} The existence of mixed conductivity mechanisms also in conjugated polymers, that is, treating the polymer as molecular redox systems has been, for example, proposed in the work of Heinze and co-workers.^{12–15}

Poly(3-hexylthiophene) (P3HT) is one of the most studied conjugated polymers and is often considered to be the workhorse in the field of organic electronics devices because

of a variety of realized applications.² Regioregular P3HT with high regioregularity can be assigned to the group of semicrystalline polymers, which—depending on the processing conditions—can be obtained in morphologies ranging from mainly amorphous films with short-range order to highly crystalline films with large-scale well-oriented domains. Techniques such as mechanical rubbing^{16–18} and controlled crystallization in solvent vapor atmospheres¹⁹ have been used for increasing crystallinity and improving orientation of the chains with respect to substrates in preferentially face-on and edge-on orientations to measure anisotropic charge transport.^{17,18,20}

The conductivity of pristine neutral CPs can be increased over several orders of magnitude by means of chemical or electrochemical doping. Regarding chemical doping approaches of polymer films, the dopant can either be directly

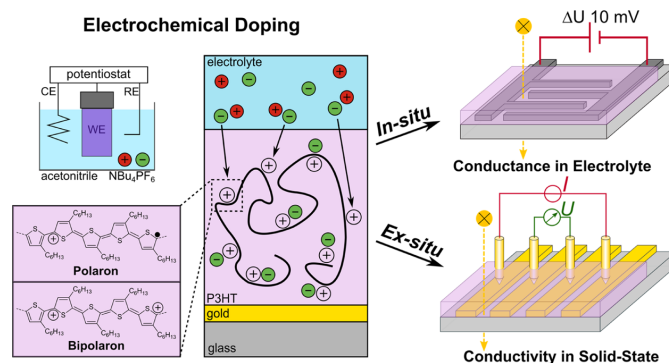
Received: March 26, 2020

Revised: June 29, 2020

Published: July 10, 2020



Scheme 1. Schematic Overview of an Electrochemical Bulk Doping Process in a Three-Electrode Geometry; This Doping Technique can be Coupled with *In Situ* Conductance and UV–Vis–NIR Spectroscopy Performed in Liquid Electrolyte (*In Situ*, Top) Inside the Electrochemical Cell and Further Allows for *Ex Situ* Measurements of Solid-State Bulk Conductivities in Combination with Spectroscopic Tools after Removing the Doped Films from the Electrochemical Cell (*Ex Situ*, Bottom)



mixed with the polymer in solution and then deposited as blend²¹ or sequentially added to as-cast films either through the vapor phase or by using dip- or spin-doping approaches.^{22–24} The advantage of the latter approach is that morphology optimization in terms of improving order and orientation can be conducted to the films before they are exposed to the dopant.^{25,26}

Because of matching energy levels, chemical redox dopants like FeCl_3 ,²⁷ 2,3,5,6-tetrafluoro-7,7,8,8-tetracyanoquinodimethane (F_4TCNQ),²⁸ and dodecaborane clusters²⁹ were presented as strong and efficient dopants for P3HT which has the highest occupied molecular orbital (HOMO) energy of -5.1 eV ³⁰ (when determined from an electrochemical oxidation onset of $\sim 0 \text{ V vs Fc/Fc}^+$, using the correction factor of 5.1 eV ³¹). Müller and co-workers provided a systematic conductivity comparison on using different solvents for spin-coating of P3HT films which were subsequently vapor-doped with F_4TCNQ .³² These results strongly suggest that high order in terms of crystallinity is necessary to obtain high conductivities.^{16,30,32} However, alternative theories proposed by Zozoulenko and co-workers hypothesize that only efficient π - π aggregation with a network of percolation paths seems to be essential for high electric performance and can outweigh the importance of perfect long-range crystalline order.^{33–35}

An outstanding feature of electrochemical doping is the possibility for precisely adjusting the redox doping potentials and therefore the induced doping levels and charge carrier densities in the polymer.^{36–38} Electrochemical measurements are typically performed in three-electrode setups and can be performed either statically or dynamically, providing the additional advantage of reversible doping and dedoping. The influence of the used supporting electrolyte, most commonly TBAPF_6 , is not to be underestimated because the doping process is accompanied by the incorporation of counterions from the electrolyte into the polymer film to stabilize the induced charge carriers on the conjugated moieties. Only if the counterions are able to penetrate the bulk polymer film and remain inside the film, acceptable stability of the doped states can be realized.^{12,37}

While fundamental electrochemistry of CPs is a mature field in the electrochemical literature, only recently its important experimental value has started to impact the polymer

electronics and materials science communities. New applications like organic electrochemical transistors (OECTs)^{39,40} and thermoelectric devices are nowadays hot topics in terms of energy conversion.^{41–43} Electrochemical doping represents the fundamental mechanism in OECTs,⁴⁴ where the charge density inside the semiconductor layer is varied to tune the strength of the drain currents occurring in the transistor channel.^{39,40,45,46}

It is essential to differentiate between a field effect-based charging (accumulation of charge carriers at the semiconductor–electrolyte interface) and an electrochemical doping of the bulk material with diffusion of ions into the semiconductor film. We refer to the literature which discusses differences in the working principles for devices built from P3HT.^{37,47,48} Berggren *et al.* used the OECT configuration to monitor thermoelectric performance of poly(3,4-ethylenedioxythiophene) as function of the doping level.^{49,50}

In this study, we present a new approach to fine-tuning solid-state conductivities by *ex situ* electrochemical bulk doping, which goes beyond classical *in situ* electrochemical approaches.^{5,51} *Ex situ* in this context means semiconducting films are first electrochemically doped, then taken out of the electrochemical cell, dried under inert conditions, and measured with 4-line probe conductivity measurements.

Maximum conductivities of regioregular P3HT films of as high as 224 S cm^{-1} are obtained in the solid state. Most importantly, the highly conducting state is achieved over a broad potential range, namely, from 0.4 to $0.8 \text{ V (vs Fc/Fc}^+)$. Intriguingly, the P3HT films are simply spin-coated, that means, have not been further ordered or oriented. Comparisons to regiorandom P3HT films with conductivities up to 10 S cm^{-1} are included to discuss the role of disorder in the films.

This manuscript is organized as follows: In the first step, we explore the electrochemical doping behavior employing cyclic voltammetry (CV) coupled with *in situ* conductance and *in situ* UV–vis–NIR spectroscopy in the electrolyte (see Scheme 1, top). This set of experiments allows us to systematically identify regions of highest conductivities and additionally assign the generated redox species which are responsible for the charge transport.

We then present our new 4-band electrode design which on the one hand allows to perform electrochemical doping in the

electrolyte and on the other hand enables obtaining reliable conductivities in the solid state after doping by 4-line conductivity measurements (see Scheme 1, bottom). The conductivity measurements are complemented with UV–vis–NIR and electron paramagnetic resonance (EPR) spectroscopy. Our experiments show that species that are generated *in situ* in the electrochemical measurements can be fully transferred to the solid state and suggest that the presence of P3HT in different redox states is needed for highly conducting states.

The role of mixed charge carrier species for achieving high conductivities is discussed by a comparison to electrochemically cross-linked vinyl polymer films containing redox-active bis(phenylcarbazole) (BCbz) moieties which are prone to mixed valence conductivity.^{8,52}

2. RESULTS AND DISCUSSION

2.1. In Situ CV Studies of P3HT Films. First, a basic electrochemical characterization was performed to reveal the nature of the charge carriers upon electrochemical doping in the oxidative region from -0.2 up to 0.9 V. We refrained from exploring higher doping potentials to avoid irreversible side reactions in the polymer film which can occur at extreme oxidation potentials.⁵³

The CV is, as typical for conjugated polymer films, quite broad without distinct peaks (see Figure 1a) which can be attributed to the oxidation of multiple overlapping redox states.^{12,54} The oxidation onset is around 0 V which results in a HOMO level of -5.1 eV.³⁰ Because of the absence of a strong redox wave between 0.11 and 0.13 V, the spin-coated P3HT films can be regarded as mainly disordered.³⁰ The nearly complete absence of an absorption shoulder at 610 nm, which is characteristic for a vibrational fine structure of aggregated and crystalline P3HT films,^{55,56} further indicates that our films can be specified as rather disordered. The low crystallinity of our films becomes even more clear when comparing the CV and spectroelectrochemistry data to results of completely amorphous films of regiorandom P3HT (see Figure S2).

The *in situ* spectroscopy data in Figure 1b provide a deeper insight into the conduction mechanism by giving information about the generated charged species when increasing the potential. In the case of P3HT, three characteristic absorption spectra can be identified: a neutral, a first oxidation state, and a second oxidation state. With respect to well-accepted literature, these spectra can be assigned to the neutral species, polarons, and bipolarons.^{51,57,58} The neutral P3HT film shows a distinct absorption band at 525 nm, and no further signals at higher wavelengths (inset in Figure 1).

Above the oxidation onset of 0 V, the absorption band of the neutral species starts to decrease in favor of an intermediate band at 805 nm. A broad absorption in the wavelength region of 1600 nm starts to develop above 0.3 V, when the band at 805 nm has already reached substantial intensity. The 805 nm band reaches its maximum at an oxidation potential of 0.5 V and starts to decrease again when going to potentials beyond 0.5 V. In contrast, the broad signal at 1600 nm constantly increases up to the maximum oxidation potential of 0.86 V. In agreement with the traditional literature, the band at 805 nm can be assigned mainly to polaronic species, whereas the broad absorption above 1600 nm is rather correlated to bipolarons at high doping levels.^{51,57,59} Comparison with *in situ* EPR spectroelectrochemistry data supports this assignment.⁵¹ Recent literature by Zozoulenko *et al.* uses density functional

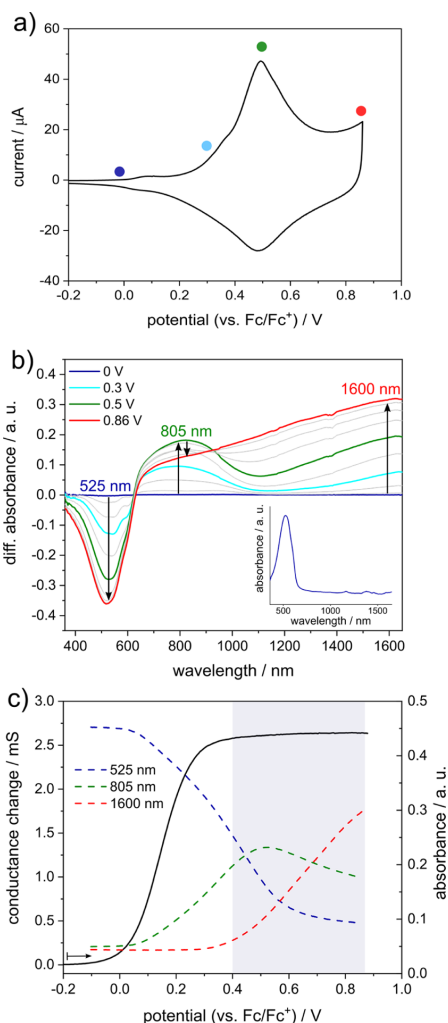


Figure 1. *In situ* electrochemical studies of a P3HT film spin-coated from CHCl_3 solution. (a) CV measured in 0.1 M TBAPF₆/MeCN at 20 mV s⁻¹ on an interdigitated Pt electrode, (b) correlating *in situ* UV–vis–NIR spectra at the given potentials. The neutral spectrum of P3HT is inserted in the bottom right corner. (c) Changes of the *in situ* conductance measured in 0.1 M TBAPF₆/MeCN at 10 mV s⁻¹ on an interdigitated Pt electrode (forward scan) and evolution of the absorption maxima at 525 , 805 , and 1600 nm corresponding to the characteristic species in the forward scan from (b). The complete *in situ* spectroelectrochemistry and *in situ* conductance data are given in the Supporting Information.

theory (DFT) calculations to give evidence that both polarons and bipolarons give rise to two absorption maxima, meaning polarons also contribute to a certain degree to the absorption at wavelengths above 1600 nm and bipolarons absorb also to some extent around 800 nm.¹¹

Especially in the case of oligomeric species, literature further discusses the existence of σ -dimers, π -dimers, and polaron pairs as alternative charged species.^{38,60–62} Regarding our obtained data, we do not see clear evidence for the existence of other

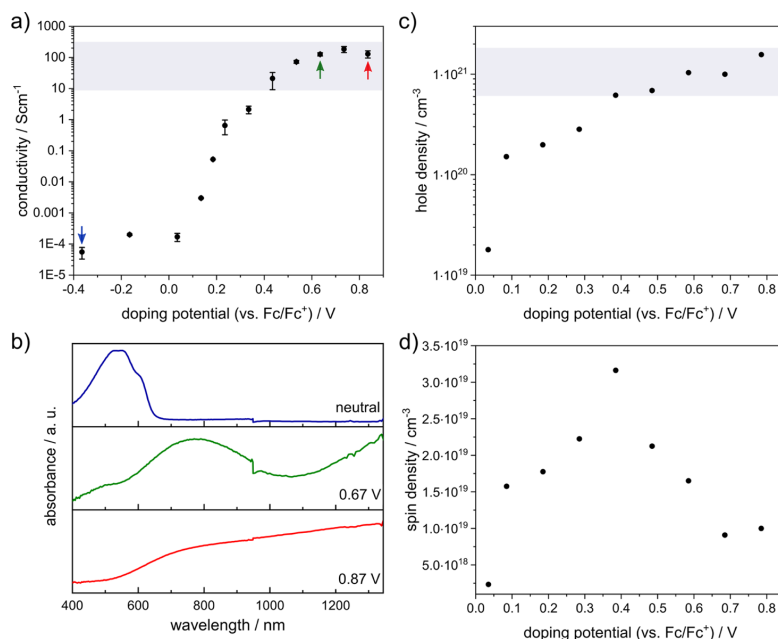


Figure 2. *Ex situ*-measured solid-state conductivities (a) and corresponding UV-vis-NIR spectra at three selected doping potentials (b) of electrochemically doped P3HT films on 4-line electrodes (an extended UV-vis-NIR spectrum up to 2200 nm can be found in Figure S8). (c) Calculation of the corresponding hole density is based on the evaluation of the injected charge during the potentiostatic doping process performed on Au-coated Kapton. (d) Spin densities calculated from EPR measurements from potentiostatically doped films on Au-coated Kapton.

species, which might be because of the high molecular weight and polydispersity of the P3HT that we used ($M_n = 46.6$ kg mol⁻¹, PDI = 2.4).

The obtained conductance change (Figure 1c black) appears in a sigmoidal shape starting from a region of lower conductance for P3HT in its neutral state, where conductance remains low until the onset of the cyclic voltammogram is reached. The emerging doping process is accompanied by a strong increase in the conductance until a plateau-like region is entered at an oxidation potential of ~0.3 V. This plateau of high conductance is fully developed when potentials of 0.4 V are reached. By reversing the potential sweep direction, the film can once again be brought into the neutral state with low conductance proving the reversibility of the doping experiment (see Figure S3 for backward cycle of the conductance change).

As the absorption band evolution of the differently charged species implies, the plateau of highest conductance suggests the presence of differently charged species. Below 0.3 V—during the steep increase of conductance—there seem to be mainly neutral and polaron species present. The strong increase of the absorption at 1600 nm (which is around the beginning of the plateau at ~0.3 V) further suggests the point where there is considerable formation of bipolarons, suggesting their importance in highly conducting states. This agrees with *in situ* EPR spectroscopy from Enengl *et al.*⁵¹ Literature reports evidence that mixed valence states involving bipolarons tend to be highly conductive compared to mixed valence states containing only neutral and polaron species.⁷ In view of the substantial conductance at potentials where bipolaron concentration should still be low, a conduction mechanism

that is exclusively based on bipolarons^{9,63} is therefore unlikely. We refer to Heinze *et al.* for further discussions of this topic.¹²

Interestingly, our data show the existence of the neutral species up to 0.8 V, implying a broad potential range where we seem to have mixed charge transport between neutral/polaron and polaron/bipolaron redox couples. These findings agree well with recent DFT-studies from Zozoulenko *et al.*, suggesting a coexistence of differently charged species over the whole applied potential range.¹¹

2.2. *Ex Situ* Studies of Electrochemically Doped P3HT Films.

2.2.1. *Ex Situ*-Measured Solid-State Conductivities.

Although all previously presented experiments were performed *in situ* employing a dynamic potential sweep to investigate the oxidation (doping) behavior of the P3HT films on interdigitated electrodes, the following experiments were conducted using new tailor-made 4-line gold electrodes. These 4-line electrodes allow for the application of defined potentials to the polymer film by electrochemical doping in the electrochemical cell and can furthermore be used straightaway to measure reliable conductivities in the dry solid state. P3HT films were deposited by spin-coating onto the 4-line electrodes and then potentiostatically charged at defined oxidation potentials. During potentiostatic charging, the current was recorded until it approached zero, indicating a completed oxidation process. Respective current-time graphs are provided in Figure S4. The electrochemically doped films were then removed from the electrolyte, and solid-state conductivity measurements were conducted.

An important feature of our procedure is that the entire experiment is performed under the inert conditions of a glovebox with short times between potentiostatic charging in

the electrochemical cell and measurement of the conductivity in solid state. This setup excludes harmful influences of humidity on electronic conductivity that occur when moisture from the air comes in contact with highly doped polymer films.⁶⁴ The line-based electrode geometry helps to reduce contact issues especially in samples with low conductivities. Reference measurements in a traditional 4-point probe geometry gave similar conductivity values.

Because maintaining the counterions from the electrolyte inside the film is crucial to securing the obtained highly doped state, the samples are not washed after doping and removal from the electrochemical cell. This procedure does not impact the electronic conductivity measurements because even when ions from the electrolyte are still on the sample, electronic conductivity is dominant.⁶⁴

Washing of the doped samples turned out to reduce the conductivity by at least 1 order of magnitude in our experimental procedure. This can be explained by the fact that the counterions are washed away which leads to dedoping and hence less charge carriers in the highly doped samples. This might be the reason for only low conductivities of electrochemically doped P3HT and polythiophene films reported in the literature so far.^{65,66}

Figure 2a presents the results of the *ex situ*-measured solid-state conductivity measurements as function of the applied electrochemical doping potential. The conductivity data clearly show a sigmoidal shape with an extended plateau of high conductivity from 0.4 to 0.85 V. This trend is comparable to the obtained conductance change in the *in situ* experiment given in Figure 2c. The measured conductivity values are independent of the channel length of the 4-line electrodes and independent from the film thickness of the deposited P3HT film (see Figure S5).

At low doping potentials, before reaching a doping potential of ~ 0.05 V, the conductivities are rather low in the range of 10^{-4} S cm^{-1} . Above 0.05 V, a strong increase of conductivity by over 6 orders of magnitude is observed. The conductivity becomes rather constant at doping potentials above 0.4 V with conductivities ranging from above 10 up to 220 S cm^{-1} . Maximum conductivities of 224 S cm^{-1} are reached which are impressive values when compared to literature of chemically doped samples.

For the system P3HT/ F_4TCNQ , published conductivities peak in the region of 48 S cm^{-1} for films doped through the vapor phase.⁶⁷ FeCl_3 doping gave high conductivities of up to 63 S cm^{-1} for blade-coated P3HT films.¹⁶ Only strongly oriented films of P3HT provided conductivities in the same order of magnitude with measured values of 250 and 570 S cm^{-1} by exploiting techniques like small-molecule epitaxy⁶⁸ or high-temperature rubbing,¹⁶ respectively. Also Müller and co-workers suggested that high conductivities are achievable only with high crystallinities and order.^{16,32,67} Our reported high conductivities over the broad doping potential range are however obtained by a simple spin-coating procedure from toluene solution. The rather disordered nature of the films is proven by atomic force microscopy (AFM) (Figure S6) and absorption spectroscopy in the neutral state; see discussion below. The influence of many amorphous regions in regioregular P3HT films on the resulting conductivity is further evidenced by measurements on completely amorphous films of regiorandom P3HT (see Figure S7). These experiments delivered conductivities of up to 10 S cm^{-1} , which is 2

orders of magnitude higher than reported for chemically doped regiorandom P3HT films by Müller *et al.*³²

The conductivities of the regiorandom P3HT films are overall 1 order of magnitude lower compared to the regioregular P3HT films, Figure S7, which fits to findings in literature.³² For completely amorphous films, these values are still very impressive and underline the success of our *ex situ* doping strategy, implying that high crystallinity with perfect long-range orientation is not a prerequisite to achieving high conductivities in semicrystalline polymer films. Although a certain degree of crystallinity seems favorable, good short-range order with efficient π - π aggregation is of higher importance regarding electronic properties. This goes more in line with predictions from theoretical studies from Zozoulenko and co-workers who show that only efficient π - π aggregation with a network of percolation paths seems to be essential for good electric performance.³³⁻³⁵

Possibly, the rather low crystallinity of the films might be also favorable for incorporation and securing counterions to stabilize the doped states.³⁷ Counterion incorporation has also strong impact on the film morphology because upon electrochemical doping, the counterions also take solvent molecules with them into the films.^{30,37} This process is always accompanied by swelling of the entire polymer film.⁵⁵ The higher the doping potential the more ions need to be incorporated into the film to counterbalance the (bi)polarons in the film and the more dominant swelling effects become therefore. Furthermore large amounts of counterion incorporation in the charged polymer films can influence the charge transport in a negative way *via* the so-called Coulomb scattering.³² The Coulomb potential of a counterion in this case can act as a trap for charge carriers in its close distance leading to weaker electronic properties.⁶⁹

In this context, our finding of a conductivity plateau in the potential region from 0.4 to 0.8 V (highlighted area in gray in Figure 2a) is even more significant. Our method allows to obtain high conductivities already at low doping levels where the counterion incorporation and swelling should still be low and less destructive for the film morphology than using high potentials and high doping levels. In the literature, it has also been shown that the tuning of doping levels is extremely important to optimize the thermoelectric performance in CP materials.⁵⁰

2.2.2. Discussion of Nature of Charged Species in the Highly Conducting Films. To characterize the highly conducting states further, *ex situ* UV-vis-NIR (on 4-line gold substrates) and EPR spectra (on gold-coated Kapton foil substrates) were recorded in the solid state. The absorption spectra in Figure 2 show a neutral P3HT film and two films after electrochemical doping: one at the beginning of the conductivity plateau region (0.67 V) and one at the highest doping level (0.87 V). The spectrum of the neutral P3HT film (Figure 2b, blue) shows one characteristic broad band at around 540 nm with a weak shoulder at 610 nm, suggesting rather low crystallinity similar to the *in situ* measurements.¹⁷

The spectrum obtained after doping at 0.67 V (Figure 2b, green) shows the presence of the neutral species at 540 nm, a broad band at 780 nm, and a broader signal at 1200 nm and higher. The spectrum of the film doped at 0.87 V has no evidence of the neutral band but shows a very broad absorption over the whole wavelength range above 600 nm. When overlaying these spectra with the *in situ* spectra from *in situ* spectroelectrochemistry, one can deduce that films doped

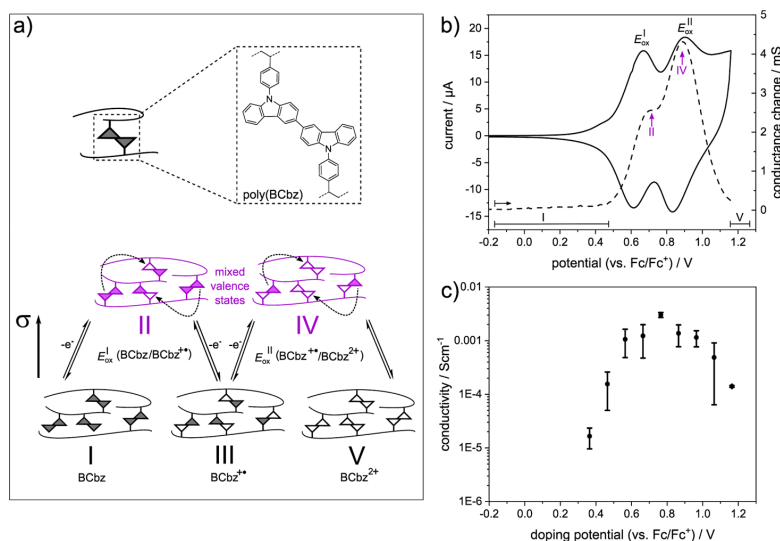


Figure 3. (a) Model of the chemical structure of a poly(BCbz) redox polymer film together with a sketch of mixed valence conductivity. (b) *In situ* conductance measurement (dotted black line, right axis, forward scan) with underlying cyclic voltammogram (solid black line, left axis) of poly(BCbz) measured in TBAPF₆/MeCN 0.1 M at 20 mV s⁻¹ on an interdigitated Pt electrode. (c) Results of *ex situ*-measured solid-state conductivities of potentiostatically doped poly(BCbz) films on 4-line gold electrodes.

at 0.67 V contain polarons, bipolarons, and a certain amount of neutral species, while the 0.87 V doped film seems to contain essentially just polarons and bipolarons.

All observed bands are in accordance with the detected bands in the *in situ* experiments, leading to the conclusion that the doped states obtained upon electrochemical doping are stable in the solid state. It should be highlighted that mixed charged states containing neutral, polaron, and bipolaron could be successfully transferred from solution to the solid state. This is in stark contrast to earlier reports in the literature.⁶⁵ We have to stress that keeping the samples in the doped states is absolutely necessary, that means, washing and humidity should be avoided.

The discussion of the nature of the generated doped states can be extended by taking the charge carrier density into account; in this case, the hole density in Figure 2c. The injected charge during the electrochemical doping process of P3HT films on gold-coated Kapton substrates was extracted by integrating the area under the recorded current–time graphs (see Figure S9 for current–time graphs). The evolution of the hole density in dependence of the doping potential follows the expected trend with a constant increase of injected charge from low to high doping potentials. The highest charge carrier density achieved by our doping technique is in the order of 10²¹ holes per cm³ which is comparable to the maximum hole densities presented for P3HT films in the literature, proving the reliability of our approach.^{39,40,65}

The potentiostatically doped films on Kapton were further studied by EPR spectroscopy to track the dependence of the polaron concentration as a function of applied doping potential. This is possible because the ions which are integrated for charge compensation are EPR silent, so that purely, the P3HT doping can be followed. Experimentally, the films had to be cut and sealed in an EPR tube under inert conditions and subsequently investigated by means of EPR

spectroscopy. The resulting spectra are displayed in Figure S10. There was no observable dependence of *g*-factor and linewidth on the orientation of the film with respect to the applied magnetic field, further suggesting the amorphous nature of the sample (Figure S11). At doping potentials below ~0 V, that means, in the neutral state, no EPR signal can be detected because no unpaired electrons are present in the films.

First, EPR spectra could be obtained above ~0 V which suggests the creation of polarons on the P3HT chains. The extracted change of the *g*-factor (Figure S10) with doping potential is small but significant, whereas the linewidth (Figure S10) shows a considerable increase. The linewidth increase can be interpreted as increased lifetime broadening because of (dipolar) interactions between polarons.

The double integral of the EPR spectrum is proportional to the number of spins and can be used to investigate the creation and conversion of polarons in P3HT in more depth. Figure 2d shows the spin density as a function of the doping potential.

The total amount of spins in Figure 2d shows a strong increase beyond 0 V and displays a maximum at doping potentials of ~0.4 V. Increasing the doping potential above 0.4 V leads to a decrease of the total amount of spins. This is consistent with EPR-active polaronic states turning into EPR-silent bipolaronic charge carriers at higher doping levels, and we interpret our results in this manner.^{51,66,70} However, a significant amount of spins and therefore polarons remain in the system even for the highest doping potential which means that polarons are present over the doping potential range from 0.1 to 0.8 V. The direct comparison with *in situ* EPR spectroelectrochemistry shows identical trends, suggesting that also the EPR measurements qualitatively prove that all *in situ* electrochemically doped species can in principle be transferred to the solid state.⁵¹ It should be noted that doped samples for quantitative EPR measurements are highly sensitive and the

sample preparation, involving cutting and sealing of the samples into a tube, can lead to loss of charge carriers and hence an underestimation of the total amount of spins in the EPR. This can explain the discrepancy of 1 order of magnitude between injected charge carriers (measured from potentiostatic measurements in the electrochemical cell) and detected spins in the EPR measurements (measured *ex situ*).

In conclusion, our experimental evidence with conductivity, UV–vis–NIR, and EPR spectra as a function of the doping potential in the solid state supports a coexistence of at least two different redox species over the plateau of high conductivity that depending on the doping potential leans more toward polarons or bipolarons.

From the data, it is also possible to calculate the amount of thiophene-repeating units and the resulting charge per repeating unit. Regarding an intermediate doping potential of 0.4 V with the highest amount of spins, ~ 0.15 charges per thiophene unit can be calculated. This corresponds roughly to one charge per five to six thiophene units, which correlates to the established picture of a polaron in P3HT. For the highest doping potential of 0.8 V, about 0.39 charges per thiophene unit can be obtained. This is close to two charges per five thiophene units, which could be explained by bipolaronic species. At these highest doping states, a maximum doping level of around 40% can be deduced (see conductivity as function of doping level in Figure S12).⁵¹

2.2.3. Comparison to Pure Redox Polymer Systems with Mixed Valence Conductivity. To set the presented results on electrochemically doped P3HT films in a wider context, the doping behavior of a more localized redox polymer system was examined. The idea was to demonstrate the conductivity behavior for a polymer system that shows pure intermolecular hopping transport because of localized redox centers. As redox centers, we chose bis(phenylcarbazole) which can be reversibly transferred from a neutral *via* a radical cation into a dication species; this is analogous to tetraphenylbenzidine species.^{8,52}

For this purpose, the redox polymer poly(vinylphenylcarbazole) (PVPhCbz) was spin-coated from solution and transferred into an electrochemical three-electrode setup. Upon oxidation, the carbazole-active pendants generate dimeric bis(phenylcarbazole) (poly(BCbz)) units (Figure S13 for mechanism). This dimerization behavior simultaneously leads to a crosslinking of the entire polymer film, whereas the cross-link points are the redox-active BCbz units (Figure 3a). The procedure is motivated by our earlier research on triphenylamine-bearing polymers which can be easily dimerized by electrochemical oxidation into dimeric redox species based on tetraphenylbenzidine units.^{8,52,71,72}

The created BCbz units are electroactive and can undergo a twofold oxidation from neutral to BCbz^{•+} radical cation into the BCbz²⁺ dication state. The cyclic voltammogram of an electrochemically cross-linked PVPhCbz film—hereafter referred to as poly(BCbz)—(Figure 3b solid black) is therefore characterized by two chemically reversible peaks with half-wave potentials of 0.63 V for the neutral/radical cation couple (BCbz/BCbz^{•+}) and 0.86 V for the radical cation/dication couple (BCbz^{•+}/BCbz²⁺), respectively.

The *in situ* conductance data of the poly(BCbz) film registered during the forward scan of the CV measurement (see Figure 3b dotted black line) gives a bell-shaped profile with a maximum at 0.89 V and a shoulder at 0.67 V; see Figure S14 for complete *in situ* conductance data with forward and backward scans. Both the peak maximum and the shoulder are

located close to the half-wave potentials of the first and the second peak in the CV which can be explained by a mixed valence conductivity model in accordance to the literature.^{5–7} Figure 3a shows a sketch of this model: in the neutral and fully oxidized state, no low conductance is obtained (states I and V), whereas the maxima of conductance are observed around the half-wave potentials when the highest amount of isoenergetic states between which hopping can take place is present (states II and IV). Interestingly, the first conductance regime, associated to hopping between neutral BCbz and the BCbz^{•+} radical cation species (state II) is lower in intensity with respect to the second conductance regime with BCbz^{•+} and BCbz²⁺ species (state IV).

Because the redox waves for the first and second oxidation are very close to each other (no baseline separation), the pure presence of BCbz^{•+} radical cations (state III) is not visible. This would in principle also correspond to a low to nonconducting state. The two close oxidation potentials however lead to a merging of the conductance into a broader peak or “bell-shape” profile. In agreement with the literature, in this redox system, high conductance can only be realized when the electroactive units are present in different states of oxidation.^{8,52}

The *ex situ*-doping approach used for P3HT was also pursued with the poly(BCbz) films. The solid-state conductivity as a function of different doping potentials of electrochemically doped poly(BCbz) films is presented in Figure 3c.

Above a threshold voltage of ~ 0.34 V which corresponds to the onset potential of the oxidation in the *in situ* experiments, the conductivity strongly increases over 3 orders of magnitude. The highest measured conductivity of up to $3.4 \times 10^{-3} \text{ S cm}^{-1}$ is achieved at a doping potential of 0.75 V. A further increase of the doping potential leads to a decrease of the conductivity values as expected from the *in situ* measurements. Poly(BCbz) films therefore feature a bell-shape conductivity trend, where highest conductivities are only detected in a very narrow potential window. While the conductivity is decreasing at high potentials, it is still higher than what would be expected from the *in situ* conductance profile in Figure 3b. The partial decrease of the conductivity in comparison to the *in situ* measurements (Figure 3b) might be explained by dedoping effects upon transferring the electrochemically generated doped state into the solid state. We observed that the counterions are leaving the polymer films significantly more compared to P3HT films when transferring the film from the electrolyte into the solid state. This phenomenon will be the subject of further studies and becomes particularly crucial when structural information is targeted, for example, by transmission electron microscopy.²⁵

Taking these data into account, a model for charge transport in the P3HT films might be proposed: The plateau conductivity with very high conductivities over a broad doping range might be explained as a consequence of many underlying conductivity maxima. Because of different chain lengths in a conjugated and polydisperse polymer like P3HT, a distribution in effective conjugation lengths seems intuitive. One could say that the P3HT polymer consists of sections of different effective conjugation lengths which could themselves be regarded as extended, delocalized redox systems varying in length. These extended redox systems would then have only slightly different oxidation potentials: A superposition of these multiple oxidized states with mixed charged species could be a

good explanation of the extended region of high conductivity, also taking into account the broad CV curves. The lack of clear isosbestic points in the *in situ* spectra underlines this statement.

3. CONCLUSIONS

In the presented work, we analyze the conductivity behavior of electrochemically doped P3HT films starting from dynamic *in situ* experiments in electrolyte. *In situ* conductance measurements show a sigmoidal conductance behavior with a plateau region of high conductance. *In situ* spectroelectrochemistry experiments conclude that at least two differently charged species are present over the entire doping potential range applied.

Proceeding from these results, solid-state conductivities of electrochemically doped P3HT films were recorded establishing a potentiostatic *ex situ*-doping approach. Reliable solid-state conductivities correlate with the *in situ* conductance change, confirming a successful transfer from *in situ* to *ex situ*. Maximum conductivities of up to 224 S cm^{-1} in highly doped states with maximum hole densities of 10^{21} holes per cm^3 for a P3HT film with low crystallinity are a highlight of this survey. Even completely amorphous films of regiorandom P3HT provide impressive conductivities, as high as 10 S cm^{-1} , questioning the importance of high crystallinity and perfect long-range order to obtain highly conducting films. The high conductivity follows theories suggesting that efficient π - π aggregation containing only a short-range order is sufficient to achieve high bulk conductivities in CPs.

Our UV-vis-NIR and EPR data support the presence of mixed charged species suggested from the *in situ* experiments also for the solid state. Both first and second oxidized states (polaron and bipolaron) are coexisting even at the highest doping levels.

Finally, a comparison to a short and localized redox system from the family of redox polymers is pursued. Cross-linked films of poly(BCbz) show a bell-shaped *in situ* conductance profile with localized but merging conductance maxima. Similar trends can be extracted from the *ex situ* solid-state conductivity measurements with peak conductivities of up to $3.4 \times 10^{-3} \text{ S cm}^{-1}$ at intermediate doping levels.

Summarizing, the large versatility of electrochemical redox doping for both conjugated and redox polymers is demonstrated in a potentiostatic *ex situ* doping approach to generate highly CP films with tunable charge carrier densities that can be implemented in *ex situ* device applications. This study outlines the importance of identifying doping potential-dependent regions of conductivity for a successful implementation of CPs in organic electronic devices such as OECTs, batteries, or applications in the field of thermoelectrics. The role of intermolecular interactions and semicrystalline morphologies together with counterbalancing incorporated charges will be subject of further studies to increase conductivities.

4. EXPERIMENTAL SECTION

4.1. Materials. P3HT (regioregular: $M_n = 46.6 \text{ kg mol}^{-1}$, PDI = 2.4, regioregularity of 95%; regiorandom: $M_n = 15.9 \text{ kg mol}^{-1}$, PDI = 2.4) was purchased from Merck and used without further purification. Solvents (chloroform, toluene, and acetonitrile) were purchased from Sigma-Aldrich (p. a. grade) and used as received. Poly(vinylphenylcarbazole) (PVPhCbz, $M_n = 2.3 \text{ kg mol}^{-1}$, PDI = 2.4) was synthesized according to literature procedures.^{73–76}

4.2. Thin-Film Preparation. Thin films of P3HT with different thicknesses (10–80 nm) were processed from solutions in chloroform or toluene prepared in a glovebox at concentrations ranging from 3 to 8 g L^{-1} . All solutions were stirred overnight at elevated temperatures ($40 \text{ }^\circ\text{C}$ for chloroform and $60 \text{ }^\circ\text{C}$ for toluene) to ensure complete dissolution. Films were spin-coated on pre-cleaned substrates (subsequent ultrasonication in acetone and isopropanol) in a dry nitrogen atmosphere.

4.3. *In Situ* Conductance Measurements. For *in situ* conductance experiments, films of P3HT (thickness 30 nm) were spin-coated (CHCl_3 , 3 g L^{-1} , 2500 rpm for 120 s, 5000 rpm for 15 s) on interdigitated platinum electrodes on glass substrates with a gap distance of $5 \mu\text{m}$. Measurements were performed in an electrochemically gated transistor setup under argon atmosphere using a scan rate of 10 mV s^{-1} and 0.1 M tetra-*n*-butylammonium hexafluorophosphate (TBAPF₆, electrochemical grade, Sigma-Aldrich) in acetonitrile (MeCN) as the electrolyte. An additional bias of 10 mV was applied between the individual combs of the interdigitated electrode leading to a measured current that is converted into the conductance at a certain potential. All potentials were referenced against the redox couple Fc/Fc^+ , added as the internal standard (after the measurement). The experiments were conducted by a commercial solution using a Metrohm PGSTAT101 potentiostat and a DropSens $\mu\text{STAT400}$ as the second potentiostat, connected to two resistors (Heka) to separate the signals in order to allow simultaneous measurement of CV and *in situ* conductance. Because background currents cannot be neglected in this configuration, we focus on discussing conductance trends and not absolute values in this study. Therefore, *in situ* conductance data are given as conductance changes related to the conductance of the material in the neutral state.

4.4. 4-Line Probe Conductivity. Custom-made 4-line gold electrodes with a channel width of 1 cm and a channel length of $100 \mu\text{m}$ were evaporated on glass substrates and subsequently coated by spin coating from P3HT solutions (toluene, 3 g L^{-1} , 2000 rpm for 120 s, 5000 rpm for 15 s, and thickness 10 nm). The individual samples were electrochemically doped by potentiostatically charging in a three-electrode setup in standard electrolyte (TBAPF₆/MeCN 0.1 M) controlled by a Metrohm PGSTAT101 potentiostat. Doped samples were removed from the electrochemical setup, and solid-state conductivity measurements were conducted by a Keithley 2636 system source meter, operated by a self-written LabView program. The entire procedure was performed under inert conditions.

4.5. *In Situ* Spectroelectrochemical Measurements. The spectroelectrochemical experiments were performed on the same electrode geometry as used for the *in situ* conductance measurements. Films of P3HT were processed *via* spin coating (CHCl_3 , 5 g L^{-1} , 1500 rpm for 120 s, 5000 rpm for 15 s, and thickness 50 nm) on interdigitated platinum electrodes on glass substrates. To allow for the detection of UV-vis-NIR data, the electrochemical cell (TBAPF₆/MeCN 0.1 M at 10 mV s^{-1}) was positioned in the beam path and the electrochemical setup was connected to a spectrometer *via* optical fibers. The *in situ* absorption spectra were recorded by a modular Zeiss spectrometer system (diode array) equipped with MCS611 2.2 and MCS621visII detectors and a CLH600 halogen lamp.

4.6. EPR Spectroscopy. Samples for EPR spectroscopy were prepared on custom-made gold coated Kapton foil (500 HN, DuPont) substrates. Films of P3HT were spin-coated (CHCl_3 , 8 g L^{-1} , 1250 rpm for 120 s, 5000 rpm for 15 s, and thickness 80 nm) on the foil substrates and electrochemically doped in a three-electrode setup using a Metrohm PGSTAT101 potentiostat and standard electrolyte (TBAPF₆/MeCN 0.1 M) under argon atmosphere. Subsequently, films were transferred into EPR tubes (under inert conditions) and analyzed in the EPR spectrometer. EPR measurements were performed on a Bruker EMX X-Band spectrometer in a Bruker ER4102ST cavity. For all measurements, the microwave frequency was $\sim 9.47 \text{ GHz}$ and the microwave power 5 mW. The magnetic field was modulated at 100 kHz with 1 Gauss amplitude. The measured spectra were fitted using the EasySpin package for MATLAB.⁷⁷ After obtaining the fit parameters (*g*-value, linewidth), the simulated spectra were doubly integrated to obtain the relative

numbers of spins. To obtain the absolute numbers of spins, the double integrals were compared to a calibration curve previously obtained from a concentration series of the 2,2-diphenyl-1-picrylhydrazyl (DPPH) radical.

■ ASSOCIATED CONTENT

Supporting Information

The Supporting Information is available free of charge at <https://pubs.acs.org/doi/10.1021/acs.chemmater.0c01293>.

Further *in situ* spectroelectrochemical data and conductivity for RR and regiorandom P3HT as well as PVPhCbz, EPR-data, and AFM morphology (PDF)

■ AUTHOR INFORMATION

Corresponding Author

Sabine Ludwigs – IPOC—Functional Polymers, Institute of Polymer Chemistry, University of Stuttgart, 70569 Stuttgart, Germany; orcid.org/0000-0002-6717-8538; Email: sabine.ludwigs@ipoc.uni-stuttgart.de

Authors

David Neusser – IPOC—Functional Polymers, Institute of Polymer Chemistry, University of Stuttgart, 70569 Stuttgart, Germany

Claudia Malacrida – IPOC—Functional Polymers, Institute of Polymer Chemistry, University of Stuttgart, 70569 Stuttgart, Germany

Michal Kern – Institute of Physical Chemistry, University of Stuttgart, 70569 Stuttgart, Germany

Yannic M. Gross – IPOC—Functional Polymers, Institute of Polymer Chemistry, University of Stuttgart, 70569 Stuttgart, Germany

Joris van Slageren – Institute of Physical Chemistry, University of Stuttgart, 70569 Stuttgart, Germany

Complete contact information is available at: <https://pubs.acs.org/doi/10.1021/acs.chemmater.0c01293>

Notes

The authors declare no competing financial interest.

■ ACKNOWLEDGMENTS

The authors thank the IQST at the University of Stuttgart for funding through the Carl Zeiss Foundation, and the Deutsche Forschungsgemeinschaft (DFG) for funding within the CRC-1333 (project 358283783). The project was supported by Philipp Sliskovic and Dr. Klaus Dirnberger regarding the synthesis of PVPhCbz which is highly acknowledged.

■ REFERENCES

- Swager, T. M. 50th Anniversary Perspective: Conducting/Semiconducting Conjugated Polymers. A Personal Perspective on the Past and the Future. *Macromolecules* **2017**, *50*, 4867–4886.
- P3HT Revisited—From Molecular Scale to Solar Cell Devices*; Ludwigs, S., Ed.; Springer Berlin Heidelberg: Berlin, Heidelberg, 2014; Vol. 265.
- Reynolds, J. R.; Thompson, B. C.; Skotheim, T. A. *Handbook of Conducting Polymers*, 4th ed.; CRC Press: Boca Raton, 2019.
- Gracia, R.; Mecerreyes, D. Polymers with Redox Properties: Materials for Batteries, Biosensors and more. *Polym. Chem.* **2013**, *4*, 2206–2214.
- Salinas, G.; Frontana-Urbe, B. A. Analysis of Conjugated Polymers Conductivity by *in situ* Electrochemical-Conductance Method. *ChemElectroChem* **2019**, *6*, 4105–4117.

- Ofer, D.; Crooks, R. M.; Wrighton, M. S. Potential Dependence of the Conductivity of Highly Oxidized Olythiophenes, Polypyrroles, and Polyaniline: Finite Windows of High Conductivity. *J. Am. Chem. Soc.* **1990**, *112*, 7869–7879.

- Zotti, G.; Schiavon, G. Spin and Spinless Conductivity in Polypyrrole. Evidence for mixed-valence Conduction. *Chem. Mater.* **1991**, *3*, 62–65.

- Yurchenko, O.; Heinze, J.; Ludwigs, S. Electrochemically Induced Formation of Independent Conductivity Regimes in Polymeric Tetraphenylbenzidine Systems. *Chemphyschem* **2010**, *11*, 1637–1640.

- Brédas, J. L.; Street, G. B. Polarons, Bipolarons, and Solitons in Conducting Polymers. *Acc. Chem. Res.* **1985**, *18*, 309–315.

- Salzner, U. Electronic Structure of Conducting Organic Polymers: Insights from time-dependent Density Functional Theory. *Wiley Interdiscip. Rev.: Comput. Mol. Sci.* **2014**, *4*, 601–622.

- Zozoulenko, I.; Singh, A.; Singh, S. K.; Gueskine, V.; Crispin, X.; Berggren, M. Polarons, Bipolarons, and Absorption Spectroscopy of PEDOT. *ACS Appl. Polym. Mater.* **2019**, *1*, 83–94.

- Heinze, J.; Frontana-Urbe, B. A.; Ludwigs, S. Electrochemistry of Conducting Polymers—Persistent Models and new Concepts. *Chem. Rev.* **2010**, *110*, 4724–4771.

- Chidsey, C. E. D.; Murray, R. W. Redox Capacity and Direct Current Electron Conductivity in Electroactive Materials. *J. Phys. Chem.* **1986**, *90*, 1479–1484.

- Kaufman, F. B.; Schroeder, A. H.; Engler, E. M.; Kramer, S. R.; Chambers, J. Q. Ion and Electron Transport in Stable, Electroactive Tetrathiafulvalene Polymer Coated Electrodes. *J. Am. Chem. Soc.* **1980**, *102*, 483–488.

- Heinze, J.; Tschuncky, P. *The Oligomer Approach*; Müllen, K., Wegner, G., Eds.; VCH-Wiley: Weinheim, 1998.

- Vijayakumar, V.; Zhong, Y.; Untilova, V.; Bahri, M.; Herrmann, L.; Biniek, L.; Leclerc, N.; Brinkmann, M. Bringing Conducting Polymers to High Order: Toward Conductivities beyond 10^5 S cm^{-1} and Thermoelectric Power Factors of $2 \text{ mW m}^{-1} \text{ K}^{-2}$. *Adv. Energy Mater.* **2019**, *9*, 1900266.

- Hartmann, L.; Tremel, K.; Uttiya, S.; Crossland, E.; Ludwigs, S.; Kayunkid, N.; Vergnat, C.; Brinkmann, M. 2D Versus 3D Crystalline Order in Thin Films of Regioregular Poly(3-hexylthiophene) Oriented by Mechanical Rubbing and Epitaxy. *Adv. Funct. Mater.* **2011**, *21*, 4047–4057.

- Tremel, K. Morphology of P3HT in Thin Films in Relation to Optical and Electrical Properties. In *P3HT Revisited—From Molecular Scale to Solar Cell Devices*; Ludwigs, S., Ed.; Springer Berlin Heidelberg: Berlin, Heidelberg, 2014; Vol. 265.

- Crossland, E. J. W.; Tremel, K.; Fischer, F.; Rahimi, K.; Reiter, G.; Steiner, U.; Ludwigs, S. Anisotropic Charge Transport in Spherulitic Poly(3-hexylthiophene) Films. *Adv. Mater.* **2012**, *24*, 839–844.

- Meredig, B.; Salleo, A.; Gee, R. Ordering of Poly(3-hexylthiophene) Nanocrystallites on the Basis of Substrate Surface Energy. *ACS Nano* **2009**, *3*, 2881–2886.

- Kiefer, D.; Kroon, R.; Hofmann, A. I.; Sun, H.; Liu, X.; Giovannitti, A.; Stegerer, D.; Cano, A.; Hynynen, J.; Yu, L.; et al. Double Doping of Conjugated Polymers with Monomer Molecular Dopants. *Nat. Mater.* **2019**, *18*, 149–155.

- Jacobs, I. E.; Aasen, E. W.; Oliveira, J. L.; Fonseca, T. N.; Roehling, J. D.; Li, J.; Zhang, G.; Augustine, M. P.; Mascal, M.; Moulé, A. J. Comparison of Solution-mixed and Sequentially Processed P3HT:F4TCNQ Films: Effect of Doping-induced Aggregation on Film Morphology. *J. Mater. Chem. C* **2016**, *4*, 3454–3466.

- Reinold, P.; Bruchlos, K.; Ludwigs, S. Simultaneous Doping and Crosslinking of Polythiophene Films. *Polym. Chem.* **2017**, *8*, 7351–7359.


- Jacobs, I. E.; Moulé, A. J. Controlling Molecular Doping in Organic Semiconductors. *Adv. Mater.* **2017**, *29*, 1703063.


- Gross, Y. M.; Trefz, D.; Dingler, C.; Bauer, D.; Vijayakumar, V.; Untilova, V.; Biniek, L.; Brinkmann, M.; Ludwigs, S. From Isotropic

- to Anisotropic Conductivities in P(NDI2OD-T 2) by (Electro-)Chemical Doping Strategies. *Chem. Mater.* **2019**, *31*, 3542–3555.
- (26) Dingler, C.; Dimberger, K.; Ludwigs, S. Semiconducting Polymer Spherulites-From Fundamentals to Polymer Electronics. *Macromol. Rapid Commun.* **2019**, *40*, 1800601.
- (27) Kratochvil, B.; Long, R. Iron(III)-(II) couple in acetonitrile. Oxidation of thiocyanate by iron(III). *Anal. Chem.* **1970**, *42*, 43–46.
- (28) Rainbolt, J. E.; Koech, P. K.; Polikarpov, E.; Swensen, J. S.; Cosimbescu, L.; Von Ruden, A.; Wang, L.; Sapochak, L. S.; Padmaperuma, A. B.; Gaspar, D. J. Synthesis and Characterization of P-type Conductivity Dopant 2-(3-(adamantan-1-yl)propyl)-3,5,6-trifluoro-7,7,8,8-tetracyanoquinodimethane. *J. Mater. Chem. C* **2013**, *1*, 1876–1884.
- (29) Aubry, T. J.; Winchell, K. J.; Salamat, C. Z.; Basile, V. M.; Lindemuth, J. R.; Stauber, J. M.; Axtell, J. C.; Kubena, R. M.; Phan, M. D.; Bird, M. J.; Spokoyny, A. M.; Tolbert, S. H.; Schwartz, B. J. Tunable Dopants with Intrinsic Counterion Separation Reveal the Effects of Electron Affinity on Dopant Intercalation and Free Carrier Production in Sequentially Doped Conjugated Polymer Films. *Adv. Funct. Mater.* **2020**, *30*, 2001800.
- (30) Bruchlos, K.; Trefz, D.; Hamidi-Sakr, A.; Brinkmann, M.; Heinze, J.; Ruff, A.; Ludwigs, S. Poly(3-hexylthiophene) Revisited – Influence of Film Deposition on the Electrochemical Behaviour and Energy Levels. *Electrochim. Acta* **2018**, *269*, 299–311.
- (31) Cardona, C. M.; Li, W.; Kaifer, A. E.; Stockdale, D.; Bazan, G. C. Electrochemical Considerations for Determining Absolute Frontier Orbital Energy Levels of Conjugated Polymers for Solar Cell Applications. *Adv. Mater.* **2011**, *23*, 2367–2371.
- (32) Hynynen, J.; Kiefer, D.; Yu, L.; Kroon, R.; Munir, R.; Amassian, A.; Kemerink, M.; Müller, C. Enhanced Electrical Conductivity of Molecularly p-Doped Poly(3-hexylthiophene) through Understanding the Correlation with Solid-State Order. *Macromolecules* **2017**, *50*, 8140–8148.
- (33) Rolland, N.; Franco-Gonzalez, J. F.; Volpi, R.; Linares, M.; Zozoulenko, I. V. Understanding morphology-mobility dependence in PEDOT:Tos. *Phys. Rev. Mater.* **2018**, *2*, 045605.
- (34) Noriega, R.; Rivnay, J.; Vandewal, K.; Koch, F. P. V.; Stingelin, N.; Smith, P.; Toney, M. F.; Salleo, A. A general Relationship Between Disorder, Aggregation and Charge Transport in Conjugated Polymers. *Nat. Mater.* **2013**, *12*, 1038–1044.
- (35) Wang, S.; Fabiano, S.; Himmelberger, S.; Puzinas, S.; Crispin, X.; Salleo, A.; Berggren, M. Experimental Evidence that Short-range Intermolecular Aggregation is Sufficient for Efficient Charge Transport in Conjugated Polymers. *Proc. Natl. Acad. Sci. U.S.A.* **2015**, *112*, 10599–10604.
- (36) Yuen, J. D.; Dhoot, A. S.; Namdas, E. B.; Coates, N. E.; Heeney, M.; McCulloch, I.; Moses, D.; Heeger, A. J. Electrochemical Doping in Electrolyte-Gated Polymer Transistors. *J. Am. Chem. Soc.* **2007**, *129*, 14367–14371.
- (37) Rawlings, D.; Thomas, E. M.; Segalman, R. A.; Chabiny, M. L. Controlling the Doping Mechanism in Poly(3-hexylthiophene) Thin-Film Transistors with Polymeric Ionic Liquid Dielectrics. *Chem. Mater.* **2019**, *31*, 8820–8829.
- (38) Shomura, R.; Sugiyasu, K.; Yasuda, T.; Sato, A.; Takeuchi, M. Electrochemical Generation and Spectroscopic Characterization of Charge Carriers within Isolated Planar Polythiophene. *Macromolecules* **2012**, *45*, 3759–3771.
- (39) Thomas, E. M.; Brady, M. A.; Nakayama, H.; Popere, B. C.; Segalman, R. A.; Chabiny, M. L. X-Ray Scattering Reveals Ion-Induced Microstructural Changes During Electrochemical Gating of Poly(3-Hexylthiophene). *Adv. Funct. Mater.* **2018**, *28*, 1803687.
- (40) Wang, S.; Ha, M.; Manno, M.; Frisbie, C. D.; Leighton, C. Hopping Transport and the Hall effect Near the Insulator-Metal Transition in Electrochemically Gated Poly(3-hexylthiophene) Transistors. *Nat. Commun.* **2012**, *3*, 1210.
- (41) Glauddell, A. M.; Cochran, J. E.; Patel, S. N.; Chabiny, M. L. Impact of the Doping Method on Conductivity and Thermopower in Semiconducting Polythiophenes. *Adv. Energy Mater.* **2015**, *5*, 1401072.
- (42) Hamidi-Sakr, A.; Biniek, L.; Bantignies, J.-L.; Maurin, D.; Herrmann, L.; Leclerc, N.; Lévêque, P.; Vijayakumar, V.; Zimmermann, N.; Brinkmann, M. A Versatile Method to Fabricate Highly In-Plane Aligned Conducting Polymer Films with Anisotropic Charge Transport and Thermoelectric Properties: The Key Role of Alkyl Side Chain Layers on the Doping Mechanism. *Adv. Funct. Mater.* **2017**, *27*, 1700173.
- (43) Zhang, Q.; Sun, Y.; Xu, W.; Zhu, D. What To Expect from Conducting Polymers on the Playground of Thermoelectricity: Lessons Learned from Four High-Mobility Polymeric Semiconductors. *Macromolecules* **2014**, *47*, 609–615.
- (44) Laiho, A.; Herlogsson, L.; Forchheimer, R.; Crispin, X.; Berggren, M. Controlling the Dimensionality of Charge Transport in Organic Thin-Film Transistors. *Proc. Natl. Acad. Sci. U.S.A.* **2011**, *108*, 15069–15073.
- (45) Zanettini, S.; Chaumy, G.; Chávez, P.; Leclerc, N.; Etrillard, C.; Leconte, B.; Chevrier, F.; Dayen, J.-F.; Doudin, B. High Conductivity Organic Thin Films for Spintronics: The Interface Resistance Bottleneck. *J. Phys.: Condens. Matter* **2015**, *27*, 462001.
- (46) Sun, H.; Gerasimov, J.; Berggren, M.; Fabiano, S. N-Type Organic Electrochemical Transistors: Materials and Challenges. *J. Mater. Chem. C* **2018**, *6*, 11778–11784.
- (47) Flagg, L. Q.; Giridharagopal, R.; Guo, J.; Ginger, D. S. Anion-Dependent Doping and Charge Transport in Organic Electrochemical Transistors. *Chem. Mater.* **2018**, *30*, 5380–5389.
- (48) Toss, H.; Suspène, C.; Piro, B.; Yassar, A.; Crispin, X.; Kergoat, L.; Pham, M.-C.; Berggren, M. On the Mode of Operation in Electrolyte-Gated Thin Film Transistors Based on Different Substituted Polythiophenes. *Org. Electron.* **2014**, *15*, 2420–2427.
- (49) Bubnova, O.; Berggren, M.; Crispin, X. Tuning the Thermoelectric Properties of Conducting Polymers in an Electrochemical Transistor. *J. Am. Chem. Soc.* **2012**, *134*, 16456–16459.
- (50) Bubnova, O.; Khan, Z. U.; Malti, A.; Braun, S.; Fahlman, M.; Berggren, M.; Crispin, X. Optimization of the Thermoelectric Figure of Merit in the Conducting Polymer Poly(3,4-ethylenedioxythiophene). *Nat. Mater.* **2011**, *10*, 429–433.
- (51) Enengl, C.; Enengl, S.; Pluczyk, S.; Havlicek, M.; Lapkowski, M.; Neugebauer, H.; Ehrenfreund, E. Doping-Induced Absorption Bands in P3HT: Polarons and Bipolarons. *Chemphyschem* **2016**, *17*, 3836–3844.
- (52) Yurchenko, O.; Freytag, D.; Zur Borg, L.; Zentel, R.; Heinze, J.; Ludwigs, S. Electrochemically Induced Reversible and Irreversible Coupling of Triarylaminines. *J. Phys. Chem. B* **2012**, *116*, 30–39.
- (53) Krische, B.; Zagorska, M. Overoxidation in Conducting Polymers. *Synth. Met.* **1989**, *28*, 257–262.
- (54) Wieland, M.; Malacrida, C.; Yu, Q.; Schlewitz, C.; Scapinello, L.; Penoni, A.; Ludwigs, S. Conductance and Spectroscopic Mapping of EDOT Polymer Films upon Electrochemical Doping. *Flexible Printed Electron.* **2020**, *5*, 014016.
- (55) Scholes, D. T.; Yee, P. Y.; Lindemuth, J. R.; Kang, H.; Onorato, J.; Ghosh, R.; Luscombe, C. K.; Spano, F. C.; Tolbert, S. H.; Schwartz, B. J. The Effects of Crystallinity on Charge Transport and the Structure of Sequentially Processed F 4 TCNQ-Doped Conjugated Polymer Films. *Adv. Funct. Mater.* **2017**, *27*, 1702654.
- (56) Yamagata, H.; Spano, F. C. Interplay Between Intrachain and Interchain Interactions in Semiconducting Polymer Assemblies: The HJ-Aggregate Model. *J. Chem. Phys.* **2012**, *136*, 184901.
- (57) Skompska, M.; Szkurlat, A. The Influence of the Structural Defects and Microscopic Aggregation of Poly(3-alkylthiophenes) on Electrochemical and Optical Properties of the Polymer Films: Discussion of an Origin of Redox Peaks in the Cyclic Voltammograms. *Electrochim. Acta* **2001**, *46*, 4007–4015.
- (58) Havinga, E. E.; Mutsaers, C. M. J.; Jennekens, L. W. Absorption Properties of Alkoxy-Substituted Thiénylene-Vinylene Oligomers as a Function of the Doping Level. *Chem. Mater.* **1996**, *8*, 769–776.
- (59) Yamamoto, J.; Furukawa, Y. Electronic and Vibrational Spectra of Positive Polarons and Bipolarons in Regioregular Poly(3-

- hexylthiophene) Doped with Ferric Chloride. *J. Phys. Chem. B* **2015**, *119*, 4788–4794.
- (60) van Haare, J. A. E. H.; Havinga, E. E.; van Dongen, J. L. J.; Janssen, R. A. J.; Cornil, J.; Brédas, J.-L. Redox States of Long Oligothiophenes: Two Polarons on a Single Chain. *Chem.—Eur. J.* **1998**, *4*, 1509–1522.
- (61) Rana, D.; Donfack, P.; Jovanov, V.; Wagner, V.; Materny, A. Ultrafast Polaron-Pair Dynamics in a Poly(3-hexylthiophene-2,5-diyl) Device Influenced by a Static Electric Field: Insights into Electric-Field-Related Charge Loss. *Phys. Chem. Chem. Phys.* **2019**, *21*, 21236–21248.
- (62) Baeuerle, P.; Segelbacher, U.; Maier, A.; Mehring, M. Electronic Structure of Mono- and Dimeric Cation Radicals in End-Capped Oligothiophenes. *J. Am. Chem. Soc.* **1993**, *115*, 10217–10223.
- (63) Bredas, J. L. Bipolarons in Doped Conjugated Polymers: A Critical Comparison Between Theoretical Results and Experimental Data. *Mol. Cryst. Liq. Cryst.* **1985**, *118*, 49–56.
- (64) Wieland, M.; Dingler, C.; Merkle, R.; Maier, J.; Ludwigs, S. Humidity-Controlled Water Uptake and Conductivities in Ion and Electron Mixed Conducting Polythiophene Films. *ACS Appl. Mater. Interfaces* **2020**, *12*, 6742–6751.
- (65) Harris, J. K.; Neelamraju, B.; Ratcliff, E. L. Intersystem Subpopulation Charge Transfer and Conformational Relaxation Preceding in Situ Conductivity in Electrochemically Doped Poly(3-hexylthiophene) Electrodes. *Chem. Mater.* **2019**, *31*, 6870–6879.
- (66) Kaneto, K.; Hayashi, S.; Ura, S.; Yoshino, K. ESR and Transport Studies in Electrochemically Doped Polythiophene Film. *J. Phys. Soc. Jpn.* **1985**, *54*, 1146–1153.
- (67) Lim, E.; Peterson, K. A.; Su, G. M.; Chabinye, M. L. Thermoelectric Properties of Poly(3-hexylthiophene) (P3HT) Doped with 2,3,5,6-Tetrafluoro-7,7,8,8-tetracyanoquinodimethane (F 4 TCNQ) by Vapor-Phase Infiltration. *Chem. Mater.* **2018**, *30*, 998–1010.
- (68) Qu, S.; Yao, Q.; Wang, L.; Chen, Z.; Xu, K.; Zeng, H.; Shi, W.; Zhang, T.; Uher, C.; Chen, L. Highly Anisotropic P3HT Films with Enhanced Thermoelectric Performance via Organic Small Molecule Epitaxy. *NPG Asia Mater.* **2016**, *8*, No. e292.
- (69) Zuo, G.; Li, Z.; Andersson, O.; Abdalla, H.; Wang, E.; Kemerink, M. Molecular Doping and Trap Filling in Organic Semiconductor Host–Guest Systems. *J. Phys. Chem. C* **2017**, *121*, 7767–7775.
- (70) Volkov, A. V.; Singh, S. K.; Stavrinidou, E.; Gabrielsson, R.; Franco-Gonzalez, J. F.; Cruce, A.; Chen, W. M.; Simon, D. T.; Berggren, M.; Zozoulenko, I. V. Spectroelectrochemistry and Nature of Charge Carriers in Self-Doped Conducting Polymer. *Adv. Electron. Mater.* **2017**, *3*, 1700096.
- (71) Blanchard, P.; Malacrida, C.; Cabanetos, C.; Roncali, J.; Ludwigs, S. Triphenylamine and some of its Derivatives as versatile Building Blocks for Organic Electronic Applications. *Polym. Int.* **2019**, *68*, 589–606.
- (72) Malacrida, C.; Habibi, A. H.; Gámez-Valenzuela, S.; Lenko, I.; Marqués, P. S.; Labrunie, A.; Grolleau, J.; López Navarrete, J. T.; Ruiz Delgado, M. C.; Cabanetos, C.; et al. Impact of the Replacement of a Triphenylamine by a Diphenylmethylamine Unit on the Electrochemical Behavior of Pentaerythritol-Based Push-Pull Tetramers. *ChemElectroChem* **2019**, *6*, 4215–4228.
- (73) Monnier, F.; Taillefer, M. Katalytische C-C-, C-N- und C-O-Ullmann-Kupplungen. *Angew. Chem.* **2009**, *121*, 7088–7105.
- (74) McKeown, N. B.; Badriya, S.; Helliwell, M.; Shkunov, M. The Synthesis of Robust, Polymeric Hole-Transport Materials from Oligoarylamine Substituted Styrenes. *J. Mater. Chem.* **2007**, *17*, 2088–2094.
- (75) Behl, M.; Hattemer, E.; Brehmer, M.; Zentel, R. Tailored Semiconducting Polymers: Living Radical Polymerization and NLO-Functionalization of Triphenylamines. *Macromol. Chem. Phys.* **2002**, *203*, 503–510.
- (76) Shi, H.-p.; Xu, L.; Cheng, Y.; He, J.-y.; Dai, J.-x.; Xing, L.-w.; Chen, B.-q.; Fang, L. Experimental and Theoretical Study of three new Benzothiazole-fused Carbazole Derivatives. *Spectrochim. Acta, Part A* **2011**, *81*, 730–738.
- (77) Stoll, S.; Schweiger, A. EasySpin, a Comprehensive Software Package for Spectral Simulation and Analysis in EPR. *J. Magn. Reson.* **2006**, *178*, 42–55.

3.1.4 Reprint Permission

HomeHelp ▾Email SupportSign inCreate Account



High Conductivities of Disordered P3HT Films by an Electrochemical Doping Strategy
Author: David Neusser, Claudia Malacrida, Michal Kern, et al
Publication: Chemistry of Materials
Publisher: American Chemical Society
Date: Jul 1, 2020
Copyright © 2020, American Chemical Society

PERMISSION/LICENSE IS GRANTED FOR YOUR ORDER AT NO CHARGE

This type of permission/license, instead of the standard Terms and Conditions, is sent to you because no fee is being charged for your order. Please note the following:

- Permission is granted for your request in both print and electronic formats, and translations.
- If figures and/or tables were requested, they may be adapted or used in part.
- Please print this page for your records and send a copy of it to your publisher/graduate school.
- Appropriate credit for the requested material should be given as follows: "Reprinted (adapted) with permission from {COMPLETE REFERENCE CITATION}. Copyright {YEAR} American Chemical Society." Insert appropriate information in place of the capitalized words.
- One-time permission is granted only for the use specified in your RightsLink request. No additional uses are granted (such as derivative works or other editions). For any uses, please submit a new request.

If credit is given to another source for the material you requested from RightsLink, permission must be obtained from that source.

[BACK](#) CLOSE WINDOW

3.2 How Charge Trapping Affects the Conductivity of Electrochemically Doped Poly(3-hexylthiophene) Films

3.2.1 Publication Data

Title: “How Charge Trapping Affects the Conductivity of Electrochemically Doped Poly(3-hexylthiophene) Films”

Status: Full Paper, Publication October 19th, 2021

Journal: Applied Physics Letters, 2021, 119, 163301

Publisher: AIP Publishing

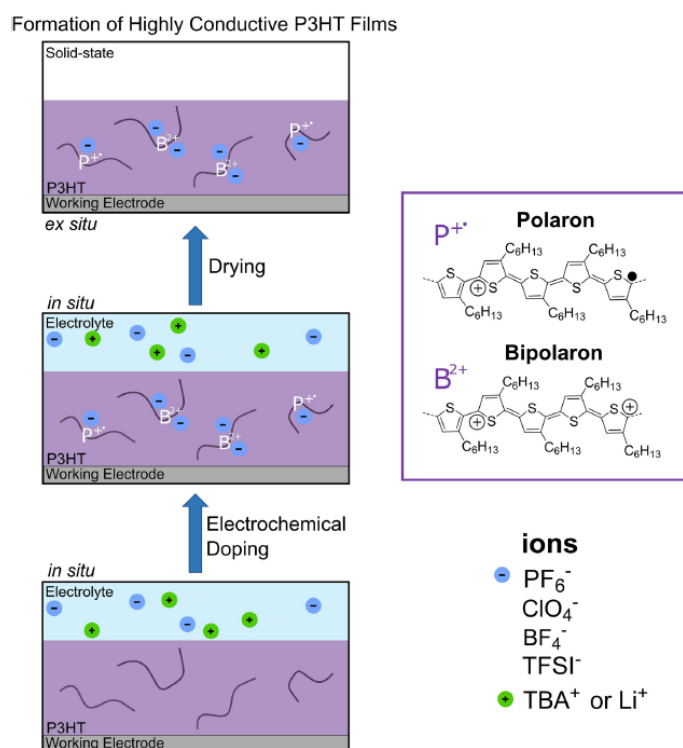
DOI: 10.1063/5.0056484

Authors: Lea-Sophie Hornberger*, David Neusser*, Claudia Malacrida, Loren G. Kaake and Sabine Ludwigs.

*authors contributed equally

Contributions: D. Neusser performed the experiments on TBAPF₆ and LiClO₄. L.-S. Hornberger executed the experiments on LiTFSI and TBABF₄. D. Neusser wrote the first version of the manuscript and L.-S. Hornberger designed the figures. The co-authors interpreted the results and revised the first version of the manuscript. All work was done under supervision of S. Ludwigs.

Scheme



3.2.2 Short Summary

To extend the fundamental understanding of the electrochemical doping process of P3HT films an in-depth electrochemical study is performed to draw conclusions between the doping process and the resulting solid-state conductivity. The process of ion integration to counterbalance the induced charge carriers upon application of the electrochemical doping potential is the essential step of electrochemical bulk doping. Additionally, the transfer of the highly doped films from the electrolyte into the solid-state can only be realized in an efficient way if the included counterions remain inside the film to avoid the loss of charge carriers. This work also focuses on charge trapping effects, which are typically charges and ions that remain in the film after electrochemical cycling. These aspects show that the impact of the counterion inside the electrolyte is of highest importance when trying to precisely tune the doping level and improve the electrochemical doping process in P3HT films.

Therefore, an electrochemical study of P3HT films is reported using electrolytes based on TBAPF₆, LiClO₄, LiTFSI and TBABF₄. Since P3HT is a p-type material we mainly focus on the anions that are supposed to enter the films in order to compensate for the created positive charge carriers in the P3HT films. Results show that TBAPF₆ and LiClO₄ overall outperform LiTFSI and TBABF₄ regarding electrochemical reversibility and solid-state conductivity. TFSI⁻ and especially the BF₄⁻ anion show significantly stronger charge trapping effects and low reversibility in combination with an induced loss of redox active material (P3HT) on the electrode surface. Our results imply that the higher amount of charge trapping harms the conductivity since trapped and immobile charges disturb efficient charge transport. A simple connection between ion size and electrochemical reversibility or conductivity could not be drawn. Although it is not the ion size our results show that conductivity values strongly depend on the choice of ion and that overall low electrochemical reversibility and strong charge trapping lead to lower conductivity values in electrochemically doped P3HT films.

3.2.3 Manuscript

How charge trapping affects the conductivity of electrochemically doped poly(3-hexylthiophene) films

Cite as: Appl. Phys. Lett. **119**, 163301 (2021); <https://doi.org/10.1063/5.0056484>
Submitted: 11 May 2021 • Accepted: 01 October 2021 • Published Online: 19 October 2021

Lea-Sophie Hornberger, David Neusser, Claudia Malacrida, et al.

COLLECTIONS

Paper published as part of the special topic on [Organic and Hybrid Thermoelectrics](#)



View Online



Export Citation



CrossMark

ARTICLES YOU MAY BE INTERESTED IN

[Design of experiment optimization of aligned polymer thermoelectrics doped by ion-exchange](#)

Applied Physics Letters **119**, 111903 (2021); <https://doi.org/10.1063/5.0055886>

[Carrier-carrier Coulomb interactions reduce power factor in organic thermoelectrics](#)

Applied Physics Letters **119**, 143301 (2021); <https://doi.org/10.1063/5.0071208>

[Doping-related broadening of the density of states governs integer-charge transfer in P3HT](#)

Applied Physics Letters **118**, 203301 (2021); <https://doi.org/10.1063/5.0052592>



1 qubit

Shorten Setup Time
Auto-Calibration
More Qubits

Fully-integrated
Quantum Control Stacks
Ultrastable DC to 18.5 GHz
Synchronized <<1 ns
Ultralow noise



100s qubits

[visit our website >](#)

How charge trapping affects the conductivity of electrochemically doped poly(3-hexylthiophene) films

Cite as: Appl. Phys. Lett. **119**, 163301 (2021); doi: [10.1063/5.0056484](https://doi.org/10.1063/5.0056484)

Submitted: 11 May 2021 · Accepted: 1 October 2021 ·

Published Online: 19 October 2021



Lea-Sophie Hornberger,¹ David Neusser,¹ Claudia Malacrida,¹ Loren C. Kaake,²  and Sabine Ludwigs^{1,a)} 

AFFILIATIONS

¹IPOC-Functional Polymers, Institute of Polymer Chemistry, and Center for Integrated Quantum Science and Technology (IQST), University of Stuttgart, Pfaffenwaldring 55, 70569 Stuttgart, Germany

²Department of Chemistry, Simon Fraser University, Burnaby British Columbia V5A 1S6, Canada

Note: This paper is part of the APL Special Collection on Organic and Hybrid Thermoelectrics.

a) Author to whom correspondence should be addressed: sabine.ludwigs@ipoc.uni-stuttgart.de

ABSTRACT

Electrochemical doping is an elegant method of controlling the doping level and charge carrier densities of conjugated polymer films and enhancing their thermoelectric figure of merit. Applying this doping technique to films of poly(3-hexylthiophene) (P3HT) results in conductivities with values as high as 200 S/cm. The stability of the doped films in the solid state can be probed by UV-vis-NIR spectroscopy. We found that the choice of the conducting salt in the liquid electrolyte exerts a strong influence over the conductivity. Using TBAPF₆ and LiClO₄ provides highest conductivities for P3HT films, while LiTFSI and TBABF₄ show overall lower performance. This effect is also reflected in cyclic voltammetry measurements coupled with *in situ* spectroscopy. Overall lower reversibility upon multiplex cycling in LiTFSI and TBABF₄ electrolytes suggests strong charge trapping effects, which one might attribute to a considerable fraction of charges (holes/ions) remaining in the films after charge/discharge cycles. The salts with stronger charge irreversibility in the electrochemistry experiments show the poorer solid state conductivities. Our conclusion is that one should carefully choose the electrolyte to ensure good percolation pathways and delocalized charge transport throughout doped films.

Published under an exclusive license by AIP Publishing. <https://doi.org/10.1063/5.0056484>

The control over charge density in semiconducting polymers and thermoelectric materials still presents a focal point for the development of new organic electronic devices.^{1,2} Specifically in thermoelectric applications, a strong dependence between conductivity and Seebeck coefficient (thermopower) has been established, shifting attention to the precise tuning of doping processes as a means of controlling thin film conductivity.^{3–6}

Doping of organic semiconductors can be done either by chemical or electrochemical doping. Chemical doping is based on small molecular dopants that act as oxidizing or reducing agents, donating or withdrawing electrons from the conducting polymer.⁷ Molecules like FeCl₃^{8,9} and F4TCNQ^{10–12} are popular dopants for oxidizing poly(3-hexylthiophene) (P3HT) films. The efficiency of this doping technique is governed by the way that the dopant is brought into contact with the organic semiconductor, for example, sequential solution doping^{13,14} or vapor phase doping.¹⁵ Alternatively, electrochemical doping can be performed in the presence of solid or liquid electrolytes.

An applied voltage leads to a modification of the charge carrier density in the material compensated by an incorporation of counterions from the surrounding electrolyte to ensure charge neutrality.^{16–19} While electrochemistry of conducting polymers is nearly as old as the field itself, electrochemical doping has received renewed attention from the organic electronics communities in the field of organic electrochemical transistors.^{20–23} Of specific interest is the role of morphology and ion choice in the electronic conductivity and process of ion incorporation.

In the case of chemical doping, the inherent electrochemical potential of the doping bounds the maximum extent of doping. As a result, the manipulation of the electronic conductivity is difficult as is the stability of the material. To combat these challenges, electrochemistry can be applied.^{24,25} Electrochemical doping approaches facilitate the exact tuning of the charge carrier density, and the resulting conductivity in the solid state can be simply adjusted by the electrochemical doping potential.^{17,24,25} We have recently shown that regioregular P3HT films can reach conductivities as high as 224 S/cm after

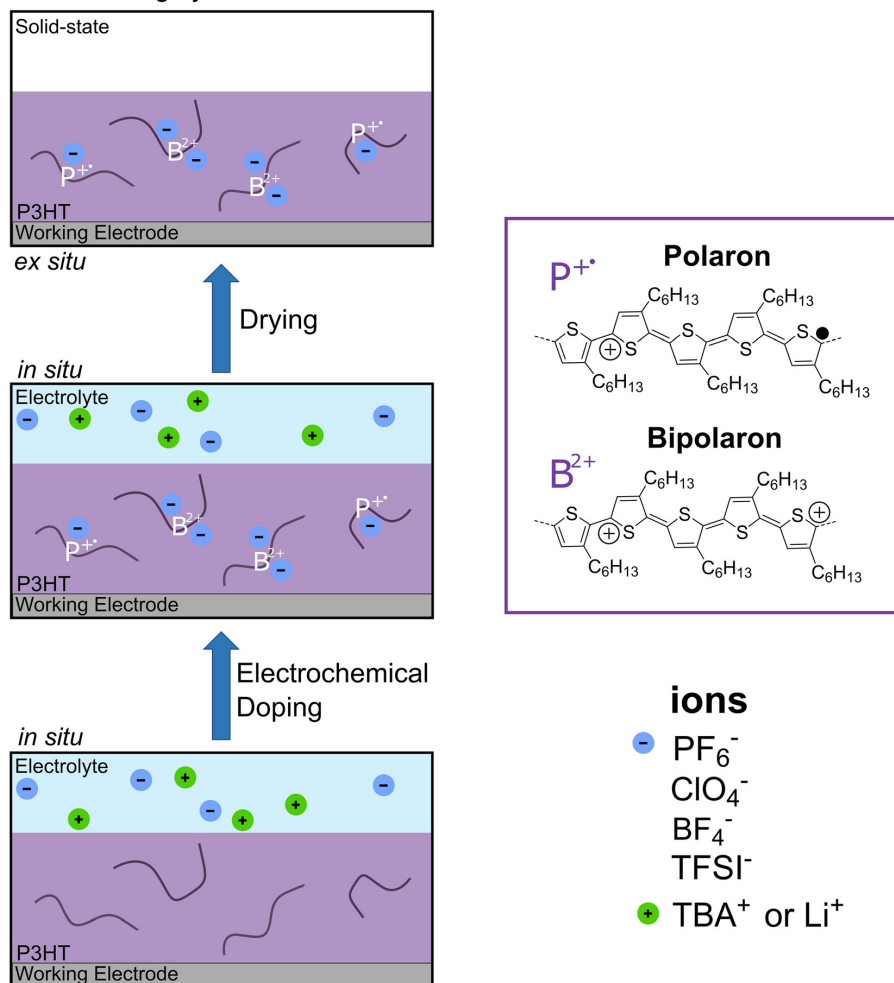
electrochemical doping using TBAPF₆/acetonitrile electrolytes.¹⁷ As mentioned before, charge neutrality is maintained by the movement of counterions from the electrolyte into the polymer film. Understanding this process begins with the drift-diffusion equation. Because the film is overall charge neutral, the drift term does not play a role, making counterion diffusion²⁶ the appropriate model in the absence of phase changes within the polymer film.^{22,27} The diffusion rate was suggested to vary with the ion size, polarizability, and applied potential using the Vogel–Tammann–Fulcher equation.²⁶ However, the generality of this approach remains an open question. In the context of thermoelectric

devices, the structure property relationship governing the electronic conductivity is of greater interest.

In this contribution, we go deeper in these charge compensation issues. We systematically study *in situ* electrochemical doping of P3HT films using different electrolytes, namely, LiClO₄, LiTFSI, TBAPF₆, and TBABF₄, and combine these results with conductivity measurements, which are probed *ex situ* as function of potentiostatically applied doping potential and doping electrolyte, Scheme 1.

We performed cyclic voltammetry on ITO electrodes in parallel with *in situ* spectroscopy to gain insight into the nature of the charge

Formation of Highly Conductive P3HT Films



SCHEME 1. Schematic overview of the electrochemical doping process using a three electrode setup. Charges are injected from the working electrode into the P3HT films with generation of polarons or bipolarons, which are counterbalanced by ions from the electrolyte.

carrying species upon changing the doping potential. Figure 1(a) shows a typical CV of a 10 nm spin-coated P3HT film in LiClO₄/acetonitrile with a rather broad redox wave without distinct shoulders.^{28,29} The broad shape is caused by multiple overlapping redox states with different conjugation lengths. The low intensity of the shoulder at around 0.1 V, which is characteristic for crystalline domains, indicates rather low crystallinity.^{30,31} The onset of oxidation of all measured electrolytes, including TBAPF₆, TBABF₄, and LiTFSI, is approximately 0 V, which corresponds to a HOMO level of -5.1 eV (using the correction factor of 5.1 eV with respect to the Fc/Fc⁺ redox couple).³² This is the typical HOMO level of regioregular P3HT films, also accepted in the literature.^{17,31}

Figure 1(b) shows the absorption spectra taken in parallel to the forward scan of the CV. It is typical to observe a transition from a neutral species (N) via a singly charged polaron species (P) to a doubly charged bipolaron (B) species upon increasing the potential. In the neutral state, there is a strong absorption band at 520 nm, which decreases upon increasing the potential, as shown in the bottom of Fig. 1(a) by tracking the intensity change in this band.^{17,18,30} Features at 846 and 1317 nm start increasing at the onset of the oxidation of 0 V. The characteristic peak at 846 nm is attributed to polarons and has its maximum of intensity at 0.5 V vs Fc/Fc⁺ and decreases when applying higher potentials.^{17,18,30,33} The strong absorption feature at 1317 nm is ascribed to bipolaronic species since more polarons are converted into bipolarons with the increasing potential, this is clearly visible from the intensity trends in Fig. 1(a).^{17,18,30} The spectrum taken at 0.73 V shows almost no neutral and a dominating amount of bipolaronic charges. Still some absorption intensity for the polaron can be detected, which means that even at high potentials, both polarons and bipolarons are present. This progression of the spectra is similar to the electrolyte system TBAPF₆/acetonitrile,¹⁷ and the spectral changes for LiTFSI/acetonitrile and TBABF₄/acetonitrile are also comparable (see Fig. S1). All of the used electrolytes seem to allow for the creation of the same charged species in P3HT films, namely, polarons and bipolarons.

The absorbance spectra of P3HT, however, show differences in terms of their reversibility when the electrolyte is changed. In Fig. 1(c), we relate the absorbance of the peak belonging to neutral P3HT at 520 nm after different cycles to the absorbance before any CV was performed. In the presence of LiClO₄ and TBAPF₆, the results imply completely reversible spectral changes. In the case of LiTFSI and TBABF₄, the absorbance decreases significantly upon cycling (TBABF₄ loses absorbance up to 19% after five cycles, for LiTFSI 15%) indicating incomplete discharge processes.

This outcome is supported by examining the CV curves in terms of doping efficiency,²⁴ which is essentially a measure of the electrochemical reversibility of the film. It is determined by relating the injected charge during the oxidation (charging) to the released charge in the reduction (discharging). This undoping to doping relation as function of cycle number is given in Fig. 1(c). LiClO₄ leads the chart with its undoping/doping ratio of around 85% with TBAPF₆ being approximately equivalent with up to 78%. For LiClO₄ and TBAPF₆, the undoping/doping ratio is constant after the first cycle. First cycle effects are very typical in electrochemical experiments, and therefore, it is common practice to disregard the first cycle and focus on the following reversible cycles.²⁸

TBABF₄ and LiTFSI on the other hand only have undoping/doping ratios of 62% and 68%, respectively. These data strongly suggest

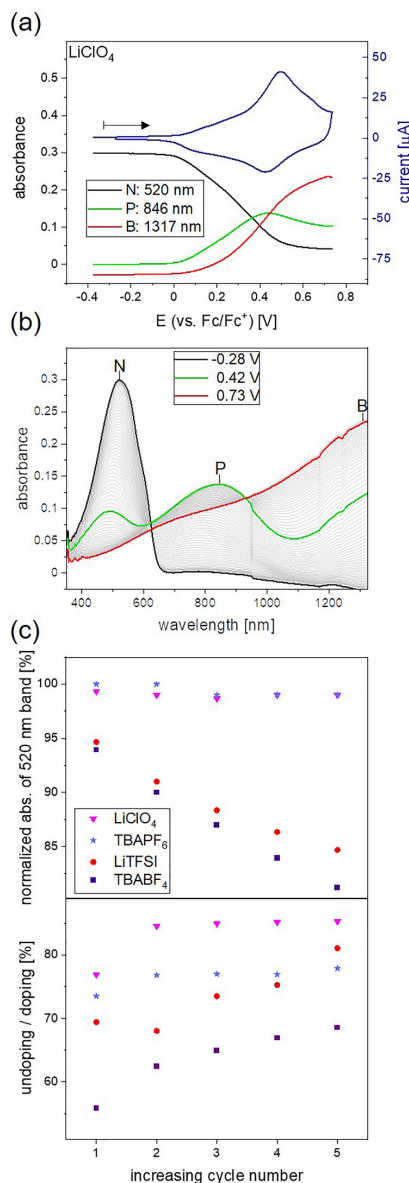


FIG. 1. (a) and (b) *in situ* spectroelectrochemistry measurement of a P3HT film in 0.1 M LiClO₄/acetonitrile. Absorption maxima of the individual species are marked as N (neutral), P (polaron), and B (bipolaron). (a) CV in combination with the spectral development upon doping for three characteristic wavelengths together with *in situ* recorded absorbance during the second charge cycle in (b). (c) Absorbance at 520 nm as function of cycle number as a percentage of the absorbance before any CV was performed (top graph) and as undoping/doping ratio as function of cycle number (bottom graph).

that the electrochemical charging and discharging is not reversible for these two salts, which indicates a loss of redox active material upon cycling. This might have several reasons, including film degradation, rearrangement in the chemical structure, σ -dimer formation as well as charge or ion trapping effects during charging and discharging.²⁸ Charge trapping has been addressed both in the organic field effect transistor literature^{26,34} and in the electrochemical literature.^{28,35,36} From an electrochemical perspective, we exemplarily refer to the research of Hillman *et al.*^{34,37,38} They found significant charge trapping for electropolymerized poly(3,4-ethylenedioxythiophene) films, when they did subsequent p- and n-doping cycles. In the CVs, this can be recognized by pre-waves upon oxidation and reduction from the neutral state. Hillman *et al.* describe such effects as ions bound to holes, which stay trapped in the film upon p-doping and so the following dedoping process is incomplete. These immobile ion/hole pairs are being isolated in a matrix of undoped polymer having no way to exchange electrons or eject ions. Besides immobile hole/ion pairs, the literature also discusses the formation of localized charges like σ -dimers, which do not contribute to the sum of mobile charge carriers either.²⁸ The literature on such trapping phenomena is dominated by research on electropolymerized films, where typically both anions and cations from the electrolyte play a role. The situation is different from solution-cast films as prepared here, which might cause higher enthalpic barriers to ion transport compared to electropolymerized films and, therefore, have different ion diffusion coefficients.¹⁹

Regarding choice of ions, working in aqueous electrolytes, Ginger *et al.* reported that the ion choice has an impact on the solvation as smaller ions being solvated by more solvent molecules than bigger ions that are barely solvated.²⁷ While water is a polar protic solvent, we use acetonitrile, which is as well polar but aprotic, with a dielectric constant of $\epsilon_r = 36$.³⁹ Referring to the research from Tsierkezos and

Philippopoulos,⁴⁰ polar aprotic solvents, like MeCN, have high dipole moments but do not strongly coordinate anions. Depending on the ion size and their amount of surface charge, differing degrees of solvation are reported. For the anions employed in our study, we suggest, therefore, also low degrees of solvation, the anions enter the films rather “naked.”^{38,41,42} However, it is well known that acetonitrile is dragged into the films as well.^{28,43,44}

One might expect a strong correlation between the amount of trapped charges and ion size. Large ions should disrupt film morphology more strongly, and one should expect more charge trapping.^{22,24} However, our observations suggest that the phenomenon is more subtle. UV-vis-NIR spectroelectrochemistry results show that LiClO_4 and TBAPF_6 seem to be good conducting salts. Their van der Waals volumes according to calculations from Ue *et al.* for the naked anions are 57 \AA^3 for ClO_4^- and 68 \AA^3 for PF_6^- .⁴⁵ In our results, both LiTFSI and TBABF_4 are correlated with lower charge reversibility. TFSI is the biggest anion investigated with a van der Waals volume of 216 \AA^3 .⁴⁵ BF_4^- with its 49 \AA^3 is the smallest with regard to the naked anions.⁴⁵ Therefore, a simple correlation between ion size and charge trapping effects in acetonitrile is not supported by our results.

A further method of choice when gathering information about ion movement from electrochemical measurements is scan rate dependent CV studies. Therefore, thin films of regioregular P3HT were first cycled for eight cycles at a scan rate of 20 mV/s. This was performed as a pre-condition step for all measurements in every electrolyte. Afterward, the same sample was measured for three cycles at each scan rate beginning from the lowest to the highest in the range of 20–500 mV/s. Results for LiClO_4 as well as LiTFSI are shown in Fig. 2(a).

With an increase in scan rates, the broad shape of the redox signal of P3HT does not change, although the oxidation wave shifts subtly toward higher potentials and the reduction wave shifts subtly to

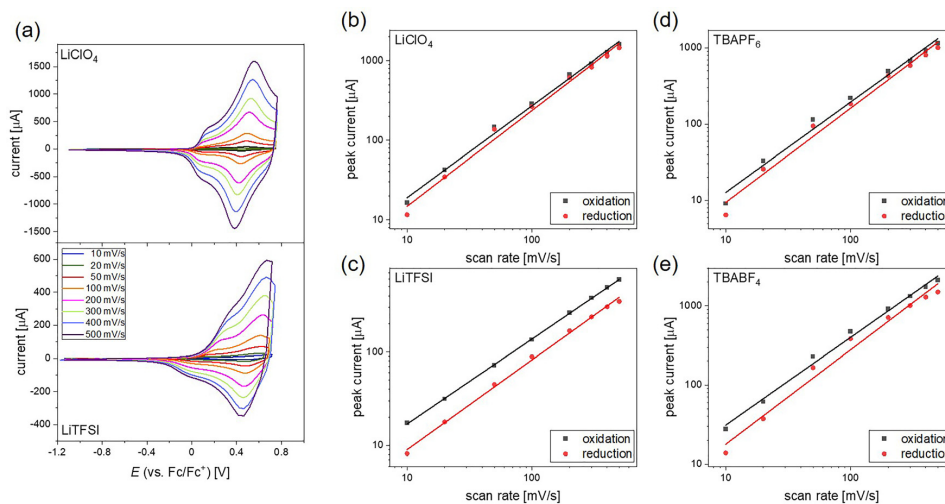


FIG. 2. (a) Scan rate dependent CV measurements of 50 nm thin P3HT films on gold, with Pt counter and Ag/AgCl reference electrodes. Electrolytes contained 0.1 M salt (LiClO_4 or LiTFSI) in acetonitrile. Each sample was preconditioned by cycling 8 times with a scan rate of 20 mV/s. Then, CVs were cycled starting from the slowest scan rate. (b) to (e) Peak currents are further examined as a function of the scan rate for LiClO_4 (b), LiTFSI (c), TBAPF_6 (d), and TBABF_4 (e).

lower potentials. An important observation is that the peak currents increase linearly with the scan rate. This is different than the Randles–Sevcik model which predicts a square root relationship. The square root dependence is the result of assuming that the sample is infinitely thick, a good approximation when dealing with the diffusion of redox active species in solution. However, a film of P3HT cannot be assumed to be infinitely thick at low scan rates because a meaningful amount of charge will be present throughout the film volume. As discussed previously, diffusion with a sample of finite thickness produces a linear increase in peak current with a scan rate.²⁶

With respect to the observed peak shift, this often is interpreted as indicating a kinetically limited process.⁴⁶ In addition to diffusion limitations, this can be caused by Ohmic drops that cannot be compensated. A peak separation of 57 mV between oxidation and reduction maximum at RT is a characteristic value marking chemically and electrochemically reversible redox processes following the Nernst equation.^{47,48} If the peak separation is similar but greater than 57 mV and increasing with scan rate, the system is referred to as a quasi-reversible system. The CVs in LiClO_4 and TBAPF_6 systems reveal quasi-reversible behavior [Figs. 2(a) and S3(b)] with peak separations

below 100 mV for scan rates up to 100 mV/s. Compared to that LiTFSI and TBABF_4 systems [Figs. 2(a) and S3(a)] are more irreversible, because even for the slow scan rates the peak separation already exceeds 100 mV.

For deeper examination, the intensity of the current peak maxima was plotted over the scan rate for the oxidative and reductive scanning direction for all of the investigated electrolytes [see Figs. 2(b)–2(e)]. Linear fits of these peak currents for anodic (oxidation) and cathodic (reduction) scanning directions were made including all measurement points. It is known that in the case of thin-film diffusion, the slope of peak current vs scan rate is independent of the diffusion constant for slow scan rates.⁴⁹ Instead, it is related to the number of redox sites per square area participating in the CV measurement. The increasing deviation between oxidation and reduction fits when going from TBAPF_6 and LiClO_4 to TBABF_4 and LiTFSI suggests higher degrees of trapped charges inside the films. These results indicate again that LiClO_4 and TBAPF_6 in acetonitrile are more suitable electrolytes for the P3HT film system.

As a final step the influence of the different anions on the resulting solid state conductivity was investigated, Scheme 1. Films of

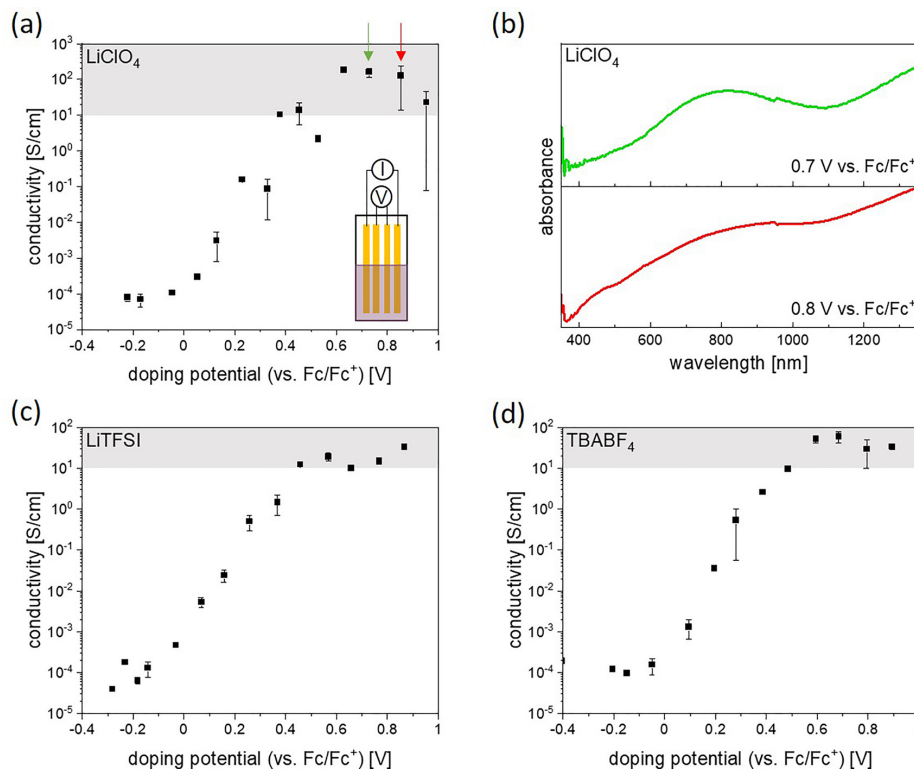


FIG. 3. (a), (c), and (d) Solid state conductivity of P3HT films on four-line electrodes (channel length $100\ \mu\text{m}$) after doping potentiostatically for 30 s in the electrochemical setup. Plateau regions of high conductivity are highlighted in gray. Arrows in (a) indicate the chosen potentials for the solid state spectroscopy of LiClO_4 in (b) on four-line electrodes (channel length $800\ \mu\text{m}$).

regioregular P3HT on tailor-made four line electrodes were doped for 30 s inside the electrochemical setup until the current reaches close to zero ensuring complete doping. Current-time graphs are added in Figs. S4–S6 as well as hole densities, Fig. S7, calculated from the current-time plots by integrating the area under the curves with values ranging between 10^{21} and 10^{22} holes per cm^3 for all investigated electrolytes. Conductivities were measured after drying the doped films.¹⁷ Figure 3 summarizes the measured conductivity values obtained by doping in the different conducting salts. The conductivity rises upon doping with higher potentials with the onset of conductivity located around the onset of the corresponding CVs. All curves are described by a sigmoidal shape with a plateau of high conductivity (highlighted in gray are conductivities above 10 S/cm).

TBAPF₆ as standard electrolyte reaches conductivity values up to 224 S/cm (published earlier).¹⁷ Conductivities of samples doped in LiClO₄ are in a similar range and reach up to 193 S/cm [Fig. 3(a)]. Highest conductivities of LiTFSI with 37 S/cm [Fig. 3(c)] and TBABF₄ [Fig. 3(d)], attaining 80 S/cm, are almost one order of magnitude lower. *Ex situ* UV-vis-NIR measurements were also conducted on the samples. In the measurements, 4-line electrodes with 800 μm instead of 100 μm channel length are used to ensure that enough light from the spectrometer can pass the channel. Arrows in Fig. 3(a) mark the chosen potentials of the spectroscopy as shown in Fig. 3(b), being both located in the highly conducting plateau region.

Doping in LiClO₄ at 0.7 V vs Fc/Fc⁺ leads to polaronic and bipolaronic species. The peak at 800 nm, which is assigned to be mainly polaronic absorption,^{17,18,30} is clearly visible, as well as a bipolaronic signal at wavelengths above. Doping at a higher potential of 0.8 V vs Fc/Fc⁺ leads to more bipolaronic contribution at the expense of the polaron. Solid state spectroscopy data of LiTFSI and TBABF₄ are given in the supplementary material (Fig. S8); both systems behave similar. Doping at 0.7 V vs Fc/Fc⁺ potential gives rise to dominant polaron species throughout the films. Doping at 0.8 V vs Fc/Fc⁺, on the other hand, seems to be strongly inhomogeneous: Depending on the measurement spot, the ratio of polarons and bipolarons seems to vary strongly (see Fig. S8). This suggests that electrochemical doping with LiTFSI and TBABF₄ is less good and points to inhomogeneities.⁵⁰

In summary, we used electrochemical doping to produce highly conducting thin films of P3HT and studied the film properties using CV and UV-vis-NIR spectroscopy. The outcome for the *ex situ* investigation of solid state conductivity can be linked to the *in situ* electrochemistry results. The irreversibilities in redox performance could be explained in the context of loss of redox-active material and charges (holes/ions) being trapped within the film. This is directly correlated with lower values of the maximum conductivity, indicating that the choice of counterion seems to be critical for achieving highest conductivities and ensuring good percolation and delocalized charge transport throughout the samples. Our experiments illustrate that TBAPF₆ and LiClO₄ are the most suitable conducting salts for electrochemically doping P3HT films in acetonitrile. Interestingly, these observations do not follow any simple trends related to ion size. As a solvent acetonitrile is not likely to coordinate anions, and as such, van der Waals radius is a reasonable measure of the ion size. Further work will be aimed at discovering the additional factors regarding the structure property relationship of counterbalancing anions in conducting polymers to stabilize high charge carrier densities enhancing their thermoelectric properties.

See the supplementary material for the experimental details, further *in situ* investigations, including spectroelectrochemistry of TBABF₄ and LiTFSI as well as scan rate dependent measurements in TBABF₄ and TBAPF₆. Additionally, current-time graphs of doping for the *ex situ* investigations, calculated hole densities, and solid state UV-vis-NIR spectroscopy measurements after doping in LiTFSI and TBABF₄ are given.

This work was supported by a project funded by the Carl Zeiss Foundation and the Deutsche Forschungsgemeinschaft (DFG) for funding within the CRC-1333 (Project No. 358283783). L.G.K. acknowledges funding from the National Science and Engineering Research Council of Canada (NSERC, No. RGPIN-2015-05981) under the Discovery Grants program and the NSERC Green Electronics Network.

AUTHOR DECLARATIONS

Author Contributions

L.-S.H. and D.N. contributed equally to this work.

DATA AVAILABILITY

The data that support the findings of this study are available from the corresponding author upon reasonable request.

REFERENCES

- K. A. Peterson, E. M. Thomas, and M. L. Chabiny, *Annu. Rev. Mater. Res.* **50**, 551 (2020).
- T. M. Swager, *Macromolecules* **50**, 4867 (2017).
- O. Bubnova, Z. U. Khan, A. Malti, S. Braun, M. Fahlmann, M. Berggren, and X. Crispin, *Nat. Mater.* **10**, 429 (2011).
- R. Kroon, D. A. Mengistie, D. Kiefer, J. Hynynen, J. D. Ryan, L. Yu, and C. Müller, *Chem. Soc. Rev.* **45**, 6147 (2016).
- A. M. Glaudell, J. E. Cochran, S. N. Patel, and M. L. Chabiny, *Adv. Energy Mater.* **5**, 1401072 (2015).
- V. Vijayakumar, Y. Zhong, V. Untilova, M. Bahri, L. Herrmann, L. Biniek, N. Leclerc, and M. Brinkmann, *Adv. Energy Mater.* **19**, 1900266 (2019).
- I. E. Jacobs and A. J. Moulé, *Adv. Mater.* **29**, 1703063 (2017).
- C. Malacrida, Y. Lu, K. Dirnberger, S. Gámez-Valenzuela, M. C. Ruiz Delgado, and S. Ludwigs, *J. Mater. Chem. C* **8**, 15393 (2020).
- J. Yamamoto and Y. Furukawa, *J. Phys. Chem. B* **119**, 4788 (2015).
- A. Hamidi-Sakr, L. Biniek, J.-L. Bantignies, D. Maurin, L. Herrmann, N. Leclerc, P. Lévêque, V. Vijayakumar, N. Zimmermann, and M. Brinkmann, *Adv. Funct. Mater.* **27**, 1700173 (2017).
- P. Reinold, K. Bruchlos, and S. Ludwigs, *Polym. Chem.* **8**, 7351 (2017).
- J. Hynynen, D. Kiefer, L. Yu, R. Kroon, R. Munir, A. Amassian, M. Kemerink, and C. Müller, *Macromolecules* **50**, 8140 (2017).
- I. E. Jacobs, E. W. Aasen, J. L. Oliveira, T. N. Fonseca, J. D. Roehling, J. Li, G. Zhang, M. P. Augustine, M. Mascal, and A. J. Moulé, *J. Mater. Chem. C* **4**, 3454 (2016).
- D. T. Scholes, S. A. Hawks, P. Y. Yee, H. Wu, J. R. Lindemuth, S. H. Tolbert, and B. J. Schwartz, *J. Phys. Chem. Lett.* **6**, 4786 (2015).
- E. Lim, K. A. Peterson, G. M. Su, and M. L. Chabiny, *Chem. Mater.* **30**, 998 (2018).
- O. Bubnova, M. Berggren, and X. Crispin, *J. Am. Chem. Soc.* **134**, 16456 (2012).
- D. Neusser, C. Malacrida, M. Kern, Y. M. Gross, J. van Slageren, and S. Ludwigs, *Chem. Mater.* **32**, 6003 (2020).
- C. Enengl, S. Enengl, S. Pluczyk, M. Havlicek, M. Lapkowski, H. Neugebauer, and E. Ehrenfreund, *ChemPhysChem* **17**, 3836 (2016).
- J. K. Harris and E. L. Ratcliff, *J. Mater. Chem. C* **8**, 13319 (2020).
- X. Wu, Q. Liu, A. Surendran, S. E. Bottle, P. Sonar, and W. L. Leong, *Adv. Electron. Mater.* **7**, 2000701 (2021).

- ²¹Y. Xu, H. Sun, A. Liu, H.-H. Zhu, W. Li, Y.-F. Lin, and Y.-Y. Noh, *Adv. Mater.* **30**, e1801830 (2018).
- ²²C. G. Bischak, L. Q. Flagg, K. Yan, T. Rehman, D. W. Davies, R. J. Quezada, J. W. Onorato, C. K. Luscombe, Y. Diao, C.-Z. Li, and D. S. Ginger, *J. Am. Chem. Soc.* **142**, 7434 (2020).
- ²³J. Rivnay, S. Inal, A. Salleo, R. M. Owens, M. Berggren, and G. G. Malliaras, *Nat. Rev. Mater.* **3**, 17086 (2018).
- ²⁴W. T. Choi and A. J. Bard, *J. Phys. Chem. C* **124**, 3439 (2020).
- ²⁵J. D. Yuen, A. S. Dhoot, E. B. Namdas, N. E. Coates, M. Heeney, I. McCulloch, D. Moses, and A. J. Heeger, *J. Am. Chem. Soc.* **129**, 14367 (2007).
- ²⁶P. Shiri, D. Neusser, C. Malacrida, S. Ludwigs, and L. G. Kaake, *J. Phys. Chem. C* **125**, 536 (2021).
- ²⁷L. Q. Flagg, R. Giridharagopal, J. Guo, and D. S. Ginger, *Chem. Mater.* **30**, 5380 (2018).
- ²⁸J. Heinze, B. A. Frontana-Urbe, and S. Ludwigs, *Chem. Rev.* **110**, 4724 (2010).
- ²⁹M. Wieland, C. Malacrida, Q. Yu, C. Schlewitz, L. Scapinello, A. Penoni, and S. Ludwigs, *Flexible Printed Electron.* **5**(1), 014016 (2020).
- ³⁰M. Skompska and A. Szurlat, *Electrochim. Acta* **46**, 4007 (2001).
- ³¹K. Bruchlos, D. Trefz, A. Hamidi-Sakr, M. Brinkmann, J. Heinze, A. Ruff, and S. Ludwigs, *Electrochim. Acta* **269**, 299 (2018).
- ³²C. M. Cardona, W. Li, A. E. Kaifer, D. Stockdale, and G. C. Bazan, *Adv. Mater.* **23**, 2367 (2011).
- ³³I. Zozoulenko, A. Singh, S. K. Singh, V. Gueskine, X. Crispin, and M. Berggren, *ACS Appl. Polym. Mater.* **1**, 83 (2019).
- ³⁴H. Sirringhaus, *Adv. Mater.* **21**, 3859 (2009).
- ³⁵J. Arias-Pardilla, W. Walker, F. Wudl, and T. F. Otero, *J. Phys. Chem. B* **114**, 12777 (2010).
- ³⁶A. R. Hillman, S. J. Daisley, and S. Bruckenstein, *Electrochim. Acta* **53**, 3763 (2008).
- ³⁷L. G. Kaake, P. F. Barbara, and X.-Y. Zhu, *J. Phys. Chem. Lett.* **1**, 628 (2010).
- ³⁸A. R. Hillman, S. J. Daisley, and S. Bruckenstein, *Electrochem. Commun.* **9**, 1316 (2007).
- ³⁹C. Zhong, Y. Deng, W. Hu, J. Qiao, L. Zhang, and J. Zhang, *Chem. Soc. Rev.* **44**, 7484 (2015).
- ⁴⁰N. G. Tserkezos and A. I. Philippopoulos, *Fluid Phase Equilib.* **277**, 20 (2009).
- ⁴¹V. Carlier, M. Skompska, and C. Buess-Herman, *Electroanal. Chem.* **456**, 139 (1998).
- ⁴²E. Sezer, M. Skompska, and J. Heinze, *Electrochim. Acta* **53**, 4958 (2008).
- ⁴³T. F. Otero and I. Boyano, *J. Phys. Chem. B* **107**, 6730 (2003).
- ⁴⁴T. F. Otero, H. Grande, and J. Rodriguez, *Electrochim. Acta* **41**, 1863 (1996).
- ⁴⁵M. Ue, A. Murakami, and S. Nakamura, *J. Electrochem. Soc.* **149**, A1385 (2002).
- ⁴⁶J. Gasiorowski, A. I. Mardare, N. S. Sariciftci, and A. W. Hassel, *J. Electroanal. Chem.* **691**, 77 (2013).
- ⁴⁷J. M. Savéant and C. Costentin, *Elements of Molecular and Biomolecular Electrochemistry: An Electrochemical Approach to Electron Transfer Chemistry* (Wiley, Hoboken, NJ, 2019).
- ⁴⁸A. J. Bard and L. R. Faulkner, *Electrochemical Methods: Fundamentals and Applications* (Wiley, Hoboken, NJ, 2001).
- ⁴⁹K. Aoki, K. Tokuda, and H. Matsuda, *J. Electroanal. Chem.* **146**, 417 (1983).
- ⁵⁰R. Giridharagopal, L. Q. Flagg, J. S. Harrison, M. E. Ziffer, J. Onorato, C. K. Luscombe, and D. S. Ginger, *Nat. Mater.* **16**, 737 (2017).

3.2.4 Reprint Permission

RightsLink Printable License

30.07.22, 17:37

AIP PUBLISHING LICENSE TERMS AND CONDITIONS

Jul 30, 2022

This Agreement between University of Stuttgart -- David Neusser ("You") and AIP Publishing ("AIP Publishing") consists of your license details and the terms and conditions provided by AIP Publishing and Copyright Clearance Center.

License Number	5358841033665
License date	Jul 30, 2022
Licensed Content Publisher	AIP Publishing
Licensed Content Publication	Applied Physics Letters
Licensed Content Title	How charge trapping affects the conductivity of electrochemically doped poly(3-hexylthiophene) films
Licensed Content Author	Lea-Sophie Hornberger, David Neusser, Claudia Malacrida, et al
Licensed Content Date	Oct 18, 2021
Licensed Content Volume	119
Licensed Content Issue	16
Type of Use	Thesis/Dissertation

Requestor type Author (original article)

Format Print and electronic

Portion Excerpt (> 800 words)

Will you be translating? No

Title Electrochemical Doping of Semiconducting Polymer Films in Controlled Morphologies

Institution name University of Stuttgart

Expected presentation date Oct 2022

Order reference number 2

Portions complete reprint

Requestor Location
University of Stuttgart
Pfaffenwaldring 55
Stuttgart, 70569
Germany
Attn: University of Stuttgart

Total 0.00 EUR

Terms and Conditions

AIP Publishing -- Terms and Conditions: Permissions Uses

AIP Publishing hereby grants to you the non-exclusive right and license to use and/or

distribute the Material according to the use specified in your order, on a one-time basis, for the specified term, with a maximum distribution equal to the number that you have ordered. Any links or other content accompanying the Material are not the subject of this license.

1. You agree to include the following copyright and permission notice with the reproduction of the Material: "Reprinted from [FULL CITATION], with the permission of AIP Publishing." For an article, the credit line and permission notice must be printed on the first page of the article or book chapter. For photographs, covers, or tables, the notice may appear with the Material, in a footnote, or in the reference list.
2. If you have licensed reuse of a figure, photograph, cover, or table, it is your responsibility to ensure that the material is original to AIP Publishing and does not contain the copyright of another entity, and that the copyright notice of the figure, photograph, cover, or table does not indicate that it was reprinted by AIP Publishing, with permission, from another source. Under no circumstances does AIP Publishing purport or intend to grant permission to reuse material to which it does not hold appropriate rights.
You may not alter or modify the Material in any manner. You may translate the Material into another language only if you have licensed translation rights. You may not use the Material for promotional purposes.
3. The foregoing license shall not take effect unless and until AIP Publishing or its agent, Copyright Clearance Center, receives the Payment in accordance with Copyright Clearance Center Billing and Payment Terms and Conditions, which are incorporated herein by reference.
4. AIP Publishing or Copyright Clearance Center may, within two business days of granting this license, revoke the license for any reason whatsoever, with a full refund payable to you. Should you violate the terms of this license at any time, AIP Publishing, or Copyright Clearance Center may revoke the license with no refund to you. Notice of such revocation will be made using the contact information provided by you. Failure to receive such notice will not nullify the revocation.
5. AIP Publishing makes no representations or warranties with respect to the Material. You agree to indemnify and hold harmless AIP Publishing, and their officers, directors, employees or agents from and against any and all claims arising out of your use of the Material other than as specifically authorized herein.
6. The permission granted herein is personal to you and is not transferable or assignable without the prior written permission of AIP Publishing. This license may not be amended except in a writing signed by the party to be charged.
7. If purchase orders, acknowledgments or check endorsements are issued on any forms containing terms and conditions which are inconsistent with these provisions, such inconsistent terms and conditions shall be of no force and effect. This document, including the CCC Billing and Payment Terms and Conditions, shall be the entire agreement between the parties relating to the subject matter hereof.

This Agreement shall be governed by and construed in accordance with the laws of the State of New York. Both parties hereby submit to the jurisdiction of the courts of New York County for purposes of resolving any disputes that may arise hereunder.

V1.2

Questions? customercare@copyright.com or +1-855-239-3415 (toll free in the US) or +1-978-646-2777.

4 Part II: Electrochemical Doping of state-of-the-art Materials

4.1 Spectroelectrochemically Determined Energy Levels of PM6:Y6 Blends and their Relevance to Solar Cell Performance

4.1.1 Publication Data

Title: “Spectroelectrochemically Determined Energy Levels of PM6:Y6 Blends and their Relevance to Solar Cell Performance”

Status: Full Paper, Publication August 3rd, 2022

Journal: Journal of Materials Chemistry C, 2022, 10, 11565-11578

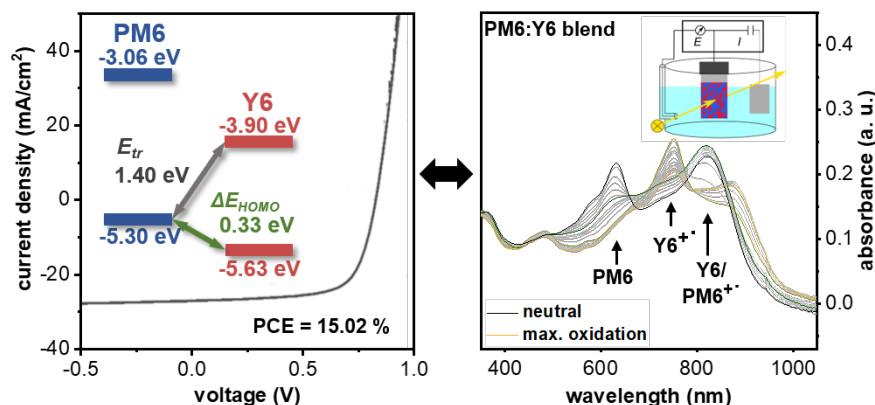
Publisher: RSC Publishing

DOI: 10.1039/d2tc01918c

Authors: David Neusser, Bowen Sun, Wen Liang Tan, Lars Thomsen, Thorsten Schultz, Lorena Perdigón-Toro, Norbert Koch, Safa Shoaee, Christopher R. McNeill, Dieter Neher and Sabine Ludwigs.

Contributions: Spectroelectrochemistry and the calculation of related energy levels was done by D. Neusser. GIWAXS and NEXAFS experiments were performed and interpreted by W. L. Tan, L. Thomsen and C. R. McNeill. UPS experiments were conducted and interpreted by T. Schultz and N. Koch. All data related to the presented solar cells were executed and evaluated by B. Sun, L. Perdigón-Toro, S. Shoaee and D. Neher. D. Neusser wrote the first version of the manuscript. All co-authors revised the first version of the manuscript. The project was supervised by S. Ludwigs and D. Neher.

Graphical Abstract (TOC)



4.1.2 Short Summary

The deep understanding of electrochemical doping of P3HT films drawn from the previous work is fundamental to perform an exact analysis of frontier orbital energies of new materials for organic electronics. This third publication is centered on the energy level determination of blend films of the state-of-the-art conjugated polymer PM6 and the non-fullerene acceptor Y6. Bulk heterojunction solar cells based on active layer blends of PM6:Y6 have shown impressive performance. Device performance, especially the open circuit voltage, strongly depends on the used processing solvent which in this case leads to either face-on or edge-on orientations in the blend films (obtained from GIWAXS). We use a spectroelectrochemical approach to identify spectral onsets for the determination of HOMO and LUMO levels of the individual compounds in the blend films to understand the influence of different morphologies on the energetics of the blend films. A major advantage of our method is the detection of the redox onsets of the individual compounds in the blend films by their unique spectral fingerprint. The exact declaration of the charged species upon electrochemical doping could not be done without the extensive work on electrochemical doping and identification of charge carriers in P3HT presented in the previous chapters.

The HOMO offset of both compounds in the blend films is located at 0.33 eV and is barely influenced by the morphological orientation as our measurements imply. We explain the strong difference in open circuit voltage in the context of different interfacial molecular orientations, which are able to significantly influence the non-radiative decay rate of the induced charge transfer state. To set our results in context, we performed UPS measurements confirming our HOMO offset calculated from electrochemistry when measured from blend films. Hence, varying values for HOMO offsets are obtained when comparing results derived from measurements on single compounds to results from blend films underlining the importance of gathering data from device relevant blend films instead of neat compound films.

4.1.3 Manuscript

Journal of
Materials Chemistry C

PAPER

View Article Online
View Journal | View IssueCite this: *J. Mater. Chem. C*, 2022,
10, 11565Spectroelectrochemically determined energy
levels of PM6:Y6 blends and their relevance to
solar cell performance†David Neusser,^a Bowen Sun,^b Wen Liang Tan,^c Lars Thomsen,^d
Thorsten Schultz,^e Lorena Perdigón-Toro,^f Norbert Koch,^g Safa Shoaee,^d
Christopher R. McNeill,^c Dieter Neher,^h and Sabine Ludwigs^{i,a}

Recent advances in organic solar cell performance have been mainly driven forward by combining high-performance p-type donor–acceptor copolymers (e.g. **PM6**) and non-fullerene small molecule acceptors (e.g. **Y6**) as bulk-heterojunction layers. A general observation in such devices is that the device performance, e.g., the open-circuit voltage, is strongly dependent on the processing solvent. While the morphology is a typically named key parameter, the energetics of donor–acceptor blends are equally important, but less straightforward to access in the active multicomponent layer. Here, we propose to use spectral onsets during electrochemical cycling in a systematic spectroelectrochemical study of blend films to access the redox behavior and the frontier orbital energy levels of the individual compounds. Our study reveals that the highest occupied molecular orbital offset (ΔE_{HOMO}) in **PM6:Y6** blends is ~ 0.3 eV, which is comparable to the binding energy of **Y6** excitons and therefore implies a nearly zero driving force for the dissociation of **Y6** excitons. Switching the **PM6** orientation in the blend films from face-on to edge-on in bulk has only a minor influence on the positions of the energy levels, but shows significant differences in the open circuit voltage of the device. We explain this phenomenon by the different interfacial molecular orientations, which are known to affect the non-radiative decay rate of the charge-transfer state. We compare our results to ultraviolet photoelectron spectroscopy data, which shows distinct differences in the HOMO offsets in the **PM6:Y6** blend compared to neat films. This highlights the necessity to measure the energy levels of the individual compounds in device-relevant blend films.

Received 9th May 2022,
Accepted 16th July 2022

DOI: 10.1039/d2tc01918c

rsc.li/materials-c

Introduction

The material class of organic semiconductors has seen significant advances in recent years due to their wide range of applications in the field of organic electronics and optoelectronics^{1,2} including organic solar cells (OSCs).^{3–5} The typically high extinction coefficients and the possibility to tune optical properties via the design of chemical structures strengthen the interest in developing and optimizing new materials for OSCs. Within the photoactive layer, bulk-heterojunction solar cells (BHJs) combine an electron donor material (D) and an electron acceptor material (A) to maximize the harvest of the solar spectrum and allow for an efficient charge generation and separation at the D/A-interface.^{6,7} To improve the efficiency regarding light absorption and charge generation, both components need to be tuned in terms of energy level matching. Here, a balance between a reduction of the energy loss during charge transfer and a large enough highest occupied molecular orbital offset (ΔE_{HOMO}) to drive exciton dissociation needs to be found.⁸ This aspect demonstrates that it is crucial to

^a IPOC – Functional Polymers, Institute of Polymer Chemistry, and Center for Integrated Quantum Science and Technology (IQST), University of Stuttgart, Germany. E-mail: sabine.ludwigs@ipoc.uni-stuttgart.de

^b Optoelectronics of Disordered Semiconductors, Institute of Physics and Astronomy, University of Potsdam, Germany

^c Department of Materials Science and Engineering, Monash University, Wellington Road, Clayton, Victoria, 3800, Australia

^d Australian Synchrotron, ANSTO, 800 Blackburn Road, Clayton, Victoria 3168, Australia

^e Helmholtz-Zentrum Berlin für Materialien und Energie GmbH, 12489, Berlin, Germany

^f Soft Matter Physics and Optoelectronics, Institute of Physics and Astronomy, University of Potsdam, Germany. E-mail: neher@uni-potsdam.de

^g Institut für Physik und IRIS Adlerhof, Humboldt Universität zu Berlin, 12489 Berlin, Germany

† Electronic supplementary information (ESI) available. See DOI: <https://doi.org/10.1039/d2tc01918c>

have a profound knowledge of the energy levels to achieve efficient devices. There are multiple methods available to determine the energy levels including cyclic voltammetry (CV), ultraviolet photoelectron spectroscopy (UPS) or scanning tunneling spectroscopy. Serious discussions have unfolded about when it is reasonable to compare resulting energy levels from different experimental methods and when different data sources can be problematic. For example, it is quite common to combine the HOMO level derived from cyclic voltammetry or UPS with the optical bandgap to determine the lowest unoccupied molecular orbital (LUMO) level energy, which is, however, inappropriate because of the large exciton binding energy of organic materials.^{9–11} Additionally, measurements on neat materials may not be suitable to explain the energetic properties of material blends.^{12,13} Microstructural order and morphology can be very unique in blends and therefore influence device-relevant parameters in a strong manner. Simply evaluating measurements on neat materials and translating them to material blends can therefore be a problematic approach. This work will deliver more insights into energy level determination in blend films and hence add more details to the prevailing discussions.

Due to its striking performance in solar cells, the present work is focused on thin films of the non-fullerene acceptor (NFA) molecule **Y6**¹⁴ (2,2'-(2Z,2'Z)-((12,13-bis(2-ethylhexyl)-3,9-diundecyl-12,13-dihydro-[1,2,5]thiadiazolo[3,4e]thieno[2'',3'':4',5']-thieno[2',3':4,5]pyrrolo[3,2-g]thieno[2',3':4,5]-thieno[3,2-b]indole-2,10-diyl)bis(methanylylidene))bis(5,6-difluoro-3-oxo-2,3-dihydro-1H-

indene-2,1-diylidene))-dimalononitrile), the conjugated donor polymer **PM6** (poly[(2,6-(4,8-bis(5-(2-ethylhexyl-3-fluoro)thiophen-2-yl)-benzo[1,2-*b*:4,5*b'*]dithiophene)-*alt*-(5,5-(1',3'-di-2-thienyl-5',7'-bis(2-ethylhexyl)benzo[1',2'-*c*:4',5'-*c'*]di-thiophene-4,8-dione)))])) and their blends **PM6:Y6** (see Fig. 1 for chemical structures).

One of the main achievements in the development of these high-performance materials was to tune the energy levels and shift the acceptor absorption to a region above 800 nm^{15–17} (see Fig. 1(c) for the normalized absorbance spectrum). This way some of the limitations of previous state-of-the-art fullerene-based acceptor materials which had struggled for example with thermal and photochemical stability could be addressed.¹⁸ The blue shift of the absorption peak of **Y6** in the blend compared to that in the neat film is a commonly observed phenomenon. The position of this peak is influenced by the degree of aggregation and by the intermolecular arrangements in the solid state of **Y6**.¹⁹ The exact decomposition of the absorption spectrum of **Y6** in solution, neat film and blend in the contributions of different aggregates and non-aggregated molecules is the subject of ongoing further investigations and beyond the scope of this work.

The acceptor **Y6** is designed following the well-established internal electronic push-pull character with alternating electron donating and withdrawing groups,^{20–22} leading to an internal A-DA'D-A structure. The electron deficient core in the center is realized by a benzothiadiazole moiety surrounded by two planar arms which are slightly tilted because of the steric demands of the alkyl chains attached to the center.^{14,23}

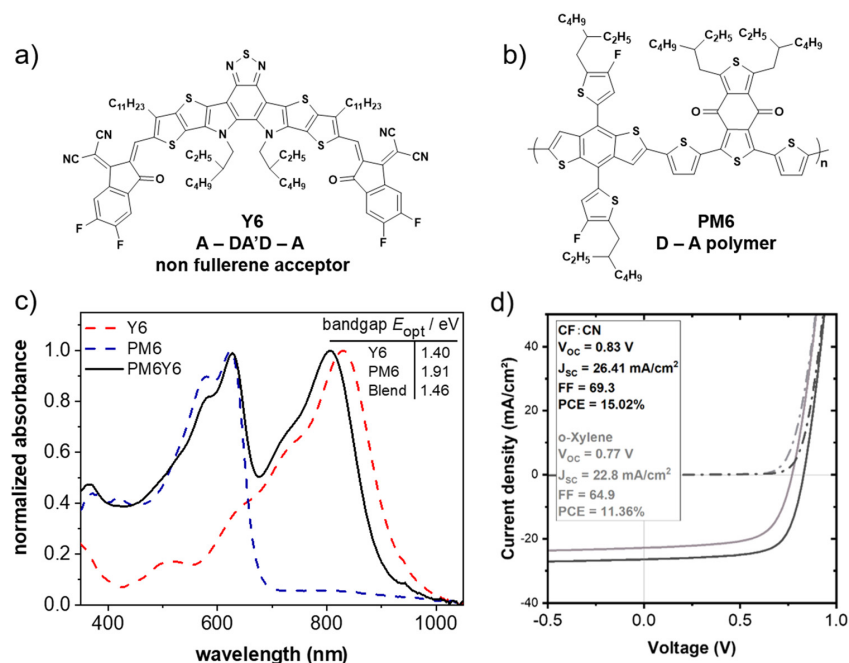


Fig. 1 Chemical structures of (a) **Y6** and (b) **PM6**. The corresponding UV-vis absorption spectra in thin films processed from CF:CN (chloroform + 0.5 v% chloronaphthalene) are given in (c) showing **Y6** in red, **PM6** in blue and a blend of **PM6:Y6** (1 : 1.2 wt%) in black. The device characteristics of **PM6:Y6** BHJ solar cells processed from CF:CN (black line) and *o*-xylene (grey line) are presented in (d).

The exact attachment position and length of the alkyl chains were carefully adjusted and not only modify the solubility properties but also influence the packing structure and performance of the final devices.²⁴

PM6 belongs to the thriving family of D/A copolymers based on polythiophenes.^{25–27} Poly(3-hexylthiophene) (P3HT) being one of the most prominent polythiophenes is still considered to be a work horse in organic electronics applications.^{12,28–30} Latest developments in the field of D/A copolymers present the introduction of halogen atoms, especially fluorine, to be one of the structural modifications that dramatically improves the properties of donor materials based on polythiophenes. The D/A copolymer **PM6** carries a benzodithiophene donor unit which allows for the attachment of two fluorine atoms per unit. These groups shift down the HOMO level and are therefore an effective approach for increasing the transport gap (E_T) which has a direct positive influence on the V_{OC} and increases the power conversion efficiency of the solar cell. Besides the energetic aspects, the fluorine atoms increase the tendency to aggregate and π - π stack by inducing a stronger dipole moment and improve the crystallinity favoring charge transport properties in general.^{26,31} **PM6**'s large bandgap leads to an absorption spectrum that perfectly complements the absorption spectrum of **Y6**. When processed in blends, the **PM6:Y6** absorption spectrum covers a large part of the solar spectrum from around 350–1000 nm (see Fig. 1(c)), making these two materials a promising match for BHJ solar cells.

When fabricated into BHJ solar cells, the **PM6:Y6** blends deliver an impressive power conversion efficiency of 15.7%, which is among the highest achieved in BHJ devices.^{14,32} This has been attributed to the negligible barrier for charge separation^{33–35} combined with a low density of traps.³⁶ Devices relying on **PM6**, **Y6** or slightly modified versions of them currently reach efficiencies of up to 19% and above^{37,38} when fabricated in more complex layers, *e.g.*, in ternary blends.^{39–44} The phase separation between the donor and acceptor plays a crucial role in efficient charge separation (exciton diffusion length is usually around 20 nm^{45,46}) and is influenced by the miscibility between **PM6** and **Y6** on the one hand. On the other hand, the properties of the chosen processing solvent and the processing method itself significantly impact the drying kinetics during film formation and therefore can influence the blend morphology. This D/A pairing shows suitable miscibility and interaction parameters for a favorable phase separation, which is beneficial for charge generation.³¹

Despite these advancements, there is an ongoing debate regarding the driving force of free charge generation in **PM6:Y6**. For fullerene-based OSCs, it is commonly accepted in the community that the HOMO energy offset of the frontier orbitals at the D/A heterojunction must be at least 300 meV to guarantee efficient exciton dissociation.^{47,48} Several recent papers reported efficient charge generation in NFA-based devices with HOMO offsets as small as 50 to 100 meV.^{49,50} The original paper on **PM6:Y6** reported a HOMO offset of only 0.09 eV, based on CV scans on neat films of the two components.¹⁴ On the other hand, recent measurements of the ionization energy and electron affinity of neat layers with photoelectron spectroscopy suggested a HOMO offset as large as 0.7 eV.³⁵ Table S1 (ESI[†]) provides an overview of the reported

HOMO and LUMO energy levels on neat films and on **PM6:Y6** blends from the literature. We notice a rather large variation of the energy values for the donor polymer **PM6**, while the scatter of data for **Y6** is much smaller. This may indicate a large effect of the morphology but also of the chosen method on the polymer energetics. Only a few studies concerned the HOMO and LUMO levels of the blend and reported slightly different values as for neat layers; however, none of the studies provided the HOMO offsets and transport in the actual blend.

In this study, we prepared representative **PM6:Y6** BHJ solar cells from two different solvent systems, namely CF:CN (chloroform + 0.5 v% chloronaphthalene) and *o*-xylene. The strong impact of the processing solvent on the active layer morphology has been reported in the literature^{25–27} and by choosing CF:CN and *o*-xylene as different processing solvents we induce two opposing orientations in the bulk of the active layer. As Fig. 1(d) demonstrates, the two orientations have a significant influence on the device performance.

PM6:Y6 solar cells produced from CF:CN give an open circuit potential (V_{OC}) of 0.83 V, a fill factor (FF) of 69.3% and a short circuit current (J_{SC}) of 26.4 mA cm⁻², with an overall efficiency of 15.02%, matching the literature results.¹⁴ Switching the processing solvent to *o*-xylene decreases all photovoltaic parameters, most importantly the V_{OC} which decreases to 0.77 V and the J_{SC} which is 22.8 mA cm⁻². Overall, the efficiency drops to 11.36%. We have confirmed the difference in the J_{SC} by measuring the photovoltaic external quantum efficiency (EQE_{PV}) spectra (see Fig. S1, ESI[†]). Here, the *o*-xylene coated blend displayed a lower photoresponse over the entire spectral range. Also, the integrated photocurrents from the EQE spectra matched the measured J_{SC} within a 5% error margin, highlighting the consistency of the results. Given that both blends yield a fairly small voltage dependence on the light-induced current near short circuit conditions, we rule out inefficient charge extraction as a possible source of a lower J_{SC} , as this loss displays a strong field dependence. More likely, the lower J_{SC} comes from less efficient exciton dissociation or the trapping of photogenerated charge on non-percolated domains. Regarding the V_{OC} , a central question to be answered in this work is whether the lower value for the *o*-xylene coated sample can be explained by changes of the energy levels of **PM6** and **Y6** induced by the opposing morphology in the blend or if other aspects must be taken into consideration. Therefore, we utilize a spectroelectrochemical method to determine frontier orbital energies of individual components in **PM6:Y6** blend films with different morphologies. The morphology of the blend films will be discussed in detail at first to define the starting point of all the following experiments. The results will be compared to experimental evidence from UPS measurements and discussed regarding device performance in the final section.

Results and discussion

1. Morphology characterization

As a first step we have studied the morphology of the blend films by a combination of grazing-incidence wide-angle X-ray

scattering (GIWAXS) and near-edge X-ray absorption fine-structure (NEXAFS) spectroscopy (see Fig. 2).

We prepared neat and blend films from two different solvent systems resulting in two different orientations of **PM6** in the bulk. GIWAXS data collected at critical angles show that the films spin coated from CF:CN exhibit a dominant face-on orientation in the bulk for both neat **PM6** films and blend films with **Y6**, marked by an intense in-plane (IP) lamellar (100) peak at around 0.3 \AA^{-1} and an out-of-plane (OOP) π - π stacking peak at around 1.7 \AA^{-1} . A minority edge-on orientation is also observed in both neat and blend films as marked by the OOP lamellar (100) peak and IP π - π stacking peak. This matches studies on GIWAXS analysis and peak assignment of neat and blend films of **PM6:Y6** processed from different solvents currently present in the literature.^{8,14,51} From surface-sensitive NEXAFS spectroscopy investigations, an edge-on orientation is found on the surface of the CF:CN-processed films (the average tilt angle of the conjugated backbone is $\langle \alpha \rangle = 64 \pm 1^\circ$). This observation is consistent with the GIWAXS data collected at an angle of incidence below the critical angle which probes surface microstructure, where the ratio of OOP to IP π - π stacking peak intensity decreases with a shallower incident angle (see Fig. S2, ESI[†]). The existence of different orientations regarding bulk and surface and the strong dependence of morphology on the processing parameters have already been reported for other conjugated polymers like N2200.^{52–54} Processing of **PM6** films

and blends of **PM6:Y6** from *o*-xylene solutions leads to edge-on orientation throughout the bulk, visible from the weak IP lamellar (100) peak and the corresponding strong OOP (100) signal, Fig. 2(b). The surface shows an edge-on orientation as well, with an average tilt angle of the conjugated backbone of $\langle \alpha \rangle = 65 \pm 1^\circ$. In general, the choice of solvent in combination with the processing method has a strong impact on the resulting morphology in the blends. Alternative processing methods like slot-die coating offering different drying kinetics are found in the literature and prove to show how orientations can differ using similar solvents as we do.⁵⁵ Regarding **Y6**, it has a high tendency to pack with a face-on orientation when processed from different processing solvents.^{14,24,56–59} Here, the literature also gives examples of how small changes on the side groups of **Y6** can impact the morphology although solution and processing parameters are kept constant.⁶⁰ These results underline the importance of the chosen solvent for film preparation since the influence on the morphology and orientation in the film is strong and decides whether there is face-on, edge-on or mixed orientations.^{25–27,59,61} This difference in morphological orientation of **PM6** in **PM6:Y6** films fabricated with CF:CN and *o*-xylene is reflected in the device performances (see Fig. 1(d) for the corresponding current density–voltage (*J*-*V*) characteristics and the Experimental section for the fabrication conditions). Compared to the device with the active layer prepared from CF:CN solution, the blend coated from *o*-xylene yields a

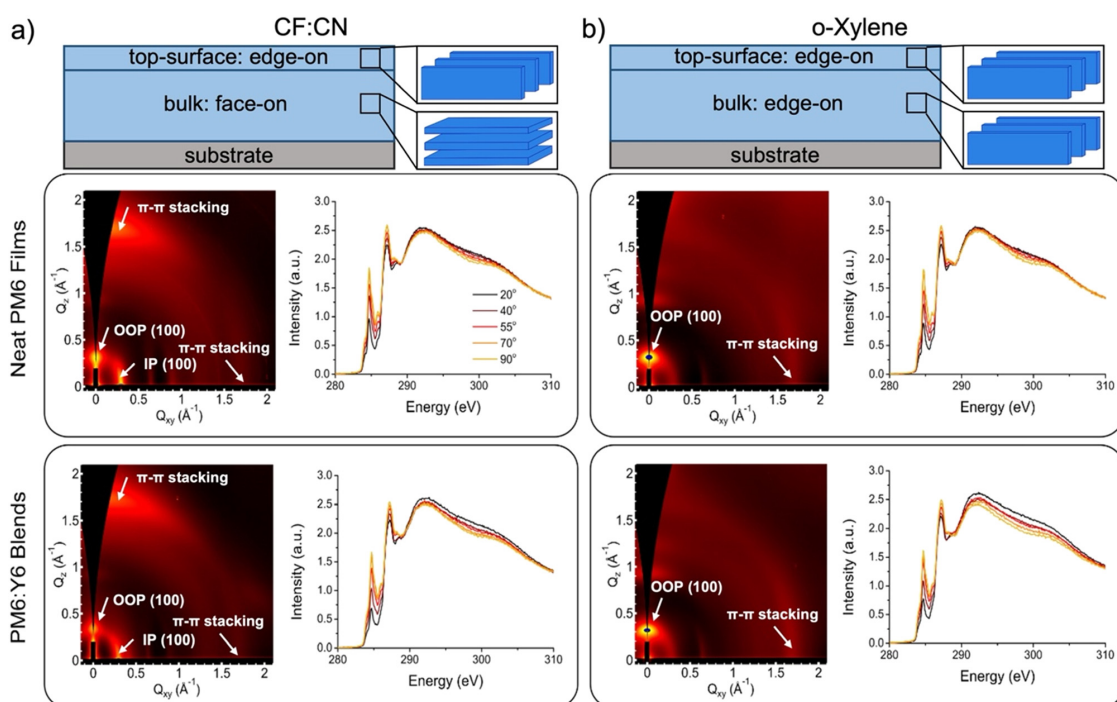


Fig. 2 Morphology of neat **PM6** films and **PM6:Y6** blend films (1: 1.2 wt%) spin coated from two different solvent systems: (a) CF + 0.5 v% CN and (b) *o*-xylene. Sketches of the top-surface and bulk morphologies of **PM6** as obtained from GIWAXS (bulk) and angle-resolved NEXAFS (top-surface). GIWAXS patterns were plotted on different color scales to properly illustrate all scattering features.

considerably smaller power conversion efficiency, which is mainly due to a lower V_{OC} . Possible reasons for this will be discussed below.

In addition, the NEXAFS results show that the film surface in the blend is enriched with **PM6** (~70–80% **PM6**, see Fig. S3, ESI†). This result is important because the HOMO levels of **PM6** from UPS can differ compared to results from cyclic voltammetry. Since UPS is a surface sensitive method, surface morphology should definitely be considered. The impact of the different morphological orientations on the resulting energy levels of the frontier orbitals of both **PM6** and **Y6** in the blend films is the subject of the following experiments.

2. Energy level determination by *in situ* spectroelectrochemistry

The next paragraph presents an in-depth electrochemical analysis by coupling cyclic voltammetry and *in situ* UV-vis spectroscopy to identify onsets of oxidation and reduction which will be the foundation for the energy level determination.⁶² An onset calculation purely based on cyclic voltammetry always suffers from a certain inaccuracy. In general, there is no thermodynamic foundation for an electrochemical onset potential which can vary due to kinetic effects (diffusion of ions into the film) and experimental aspects like background current and chosen electrolyte.¹² In particular, cyclic voltammetry of conjugated polythiophenes like **PM6** with its inherent broad redox waves offers much potential for errors when using the onset which is one of the reasons for the high deviations in the HOMO energies from a CV in the literature (see Table S1, ESI†). Additionally, a significant variation in the overall CV quality can be found in the literature, regarding the electrochemical reversibility and the avoidance of charge trapping effects, which unfortunately questions some of the published data. Whilst it does not rule out the general problem of onsets (definition of the threshold value) entirely, our approach excludes errors arising from the electrochemical experiment by focusing on the spectroscopic response of the material to the applied electrochemical potential, from now on referred to as the spectral onset.

Since most charged species have an individual spectral fingerprint (see Table 1), this elegant method allows for a more exact interpretation of the electrochemical processes. To discuss and disentangle multiple overlapping redox processes especially in the context of possible second oxidation steps (creating double charged species) the data from the CV are completed with the *in situ* spectral information discussed in the next section. A transfer from the neutral to charged form is usually accompanied by a significant change in the UV-vis spectrum, so the onset of spectral change can be used to determine HOMO/LUMO energies. The importance of *in situ* UV-vis techniques has already been proven in the literature, describing film formation kinetics and analyzing the influence of the processing solvent and conditions on parameters like aggregation, phase separation and crystallinity in blends of **PM6** and different NFAs. In this way morphology tuning of the BHJ active layers by annealing can be documented and

Table 1 Characteristic absorption maxima of neutral and charged states of neat **Y6** and **PM6** films. The arrows indicate oxidation and reduction steps

	Y6 ^{-•}	← Y6	→ Y6 ^{+•}	→ Y6 ²⁺
Wavelength/nm	380	830	750	890
	PM6 ^{-•}	← PM6	→ PM6 ^{+•}	→ PM6 ²⁺
Wavelength/nm	850, 1000	580, 625	830	890

modified towards increasing the performance of the final device.^{63,64}

Regarding the characterization of blend films our approach offers an additional advantage. The characteristic spectral response of each material allows us to discriminate between the two components in the blend and identify their individual contributions to the result. This means our technique helps us to differentiate between the redox states of the individual components, *e.g.*, whether the second redox wave in the CV scan corresponds to a differently charged state of component A or if it is the actual onset of component B.

In order to avoid errors in the onset determination, the redox behavior of **Y6** and **PM6** and spectral characteristics of the charged species all need to be understood individually. Before moving on to the complex electrochemical behavior of **PM6:Y6** blend films, it is fundamental to understand the redox properties of neat **Y6** and **PM6** films first. The knowledge on the spectral characteristics of the neat compounds and the blends can also be of great help for other spectroscopic methods like photo-induced absorption (PIA) or transient absorption spectroscopy (TAS). Cyclic voltammograms of the neat material and blend films are presented in Fig. 3 and 4, giving separate CVs for oxidation and reduction cycles to avoid the charge trapping effects. The presented data in the following section are produced with films processed from CF:CN solutions. The corresponding results of films from *o*-xylene are found in the ESI† (see Fig. S4 and S5).

2.1 HOMO determination

Y6. The electrochemical behavior of the **Y6** acceptor films shows sharp and defined peaks in the CV for the oxidation, shown in Fig. 3(a). The oxidation displays an intense wave at 0.92 V with an additional subsignal at 1.04 V. The reduction half-waves are less pronounced showing a weak wave at around 0.8 V. The spectral evolution during the charge half cycle of the oxidation (middle column) and the peak trends of significant absorption bands which are characteristic for the individual redox species (right column) is presented in Fig. 3.

The characteristic UV-vis spectrum of a neutral **Y6** film is shown in Fig. 1(c) and 3(a) in purple color at -0.37 V. When increasing the electrochemical potential, the absorption intensity at 830 nm (neutral band) decreases and a new band develops at 750 nm (red spectrum in Fig. 3(a)). The new band can be assigned to the first oxidized state (polaron). From the spectral evolution of the neutral species at 830 nm and the polaron species at 750 nm, the spectral onset can be determined *via* the tangent method (highlighted in Fig. 3(a), right

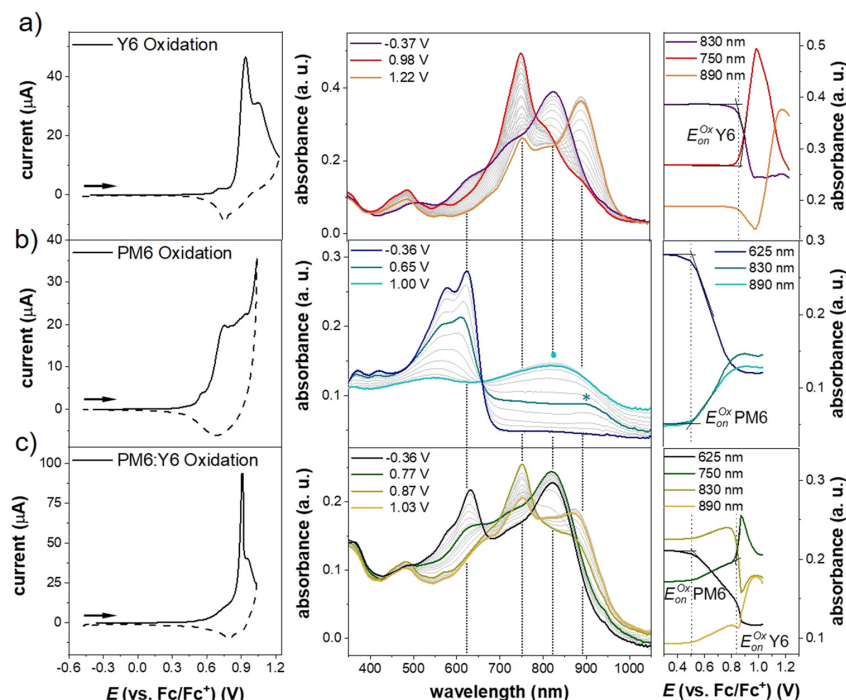


Fig. 3 *In situ* CV measurements coupled with UV-vis spectroscopy of (a) neat **Y6**, (b) neat **PM6** and (c) a blend of **PM6**:**Y6** (1:1.2 wt%) films, spin coated from CF:CN (0.5 wt%) solutions. CVs are given on the left (the forward half-cycle is highlighted as a solid line), the spectra of the forward charge half-cycle of the oxidation are presented in the center, completed with peak trends of significant bands on the right side. The peak trends are used for the determination of the spectral onsets which are indicated by dotted lines and obtained via using tangents. Underlying CVs (1st cycles) are measured in 0.1 M TBAPF₆/MeCN at 20 mV s⁻¹ on ITO substrates.

graph). In the case of **Y6** this gives a value of 0.84 V. This onset value will be the basis for the calculation of the HOMO energy of neat **Y6** films and amounts to -5.64 eV. For the sharp and well-defined wave in the CV, the onset from CV at ~ 0.85 V (determined by the tangent method) is located quite close to our spectral onset.

Increasing the potential above 1 V, another change in the spectrum becomes visible for **Y6**. The intensity at 750 nm decreases in favor of a new characteristic peak at 890 nm which we assign to the second oxidized state of **Y6** (yellow spectrum at 1.22 V in Fig. 3(a)). The potential of this spectral change fits to the previously observed signal in the CV at 1.04 V, which can now be assigned to the second oxidation step.

PM6. Moving from the small molecule **Y6** to the conjugated donor polymer **PM6** distinct differences in the electrochemical behavior are present. In particular the oxidation in Fig. 3(b) shows the typical broad wave which is characteristic for poly-disperse materials like polythiophenes and has been extensively studied for P3HT.^{12,65} In contrast to **Y6**, the backward half cycle of **PM6** can be observed as well, transferring the created oxidized species upon charging back into the neutral form.

Regarding neat **PM6** films the absorption spectrum of a neutral film is shown in Fig. 1 and 3(b) in dark blue at -0.36 V. The rather well-defined peak at 625 nm (neutral band)

decreases in intensity when extending the potential to positive values. The spectrum of the charged **PM6** film now shows a broad absorption around 830 nm with a shoulder at 890 nm. The spectral evolution displays an isosbestic point at 660 nm, indicating a clear transition from the neutral species into the oxidized form. From earlier studies on P3HT we suspect a coexistence of both polaronic and bipolaronic forms at high potentials, since the spectral evolution upon electrochemical doping is similar to polythiophenes like P3HT.^{12,30,66} Although the absorption shoulder at 890 nm (marked by a teal colored star) might be a feature of the polaron, exact assignment remains difficult due to identical and overlapping bands from both charged species at 830 nm (marked by a blue dot). The extracted spectral onset of the oxidation of neat **PM6** is found at 0.50 V which amounts to a HOMO of -5.30 eV. Here, the onset of the CV is located at 0.55 V which is at least 0.05 V further into the direction of positive potentials, caused by the broadening of the obtained CV wave and increased difficulties in finding the correct onset. The same problem also occurs in the CVs from the blend films. This underlines the significant advantage of our method relying on a combination of CV and spectral onset determination.

PM6:Y6 blend. Knowing the electrochemical characteristics of neat **Y6** and **PM6** films enables the experimental data on

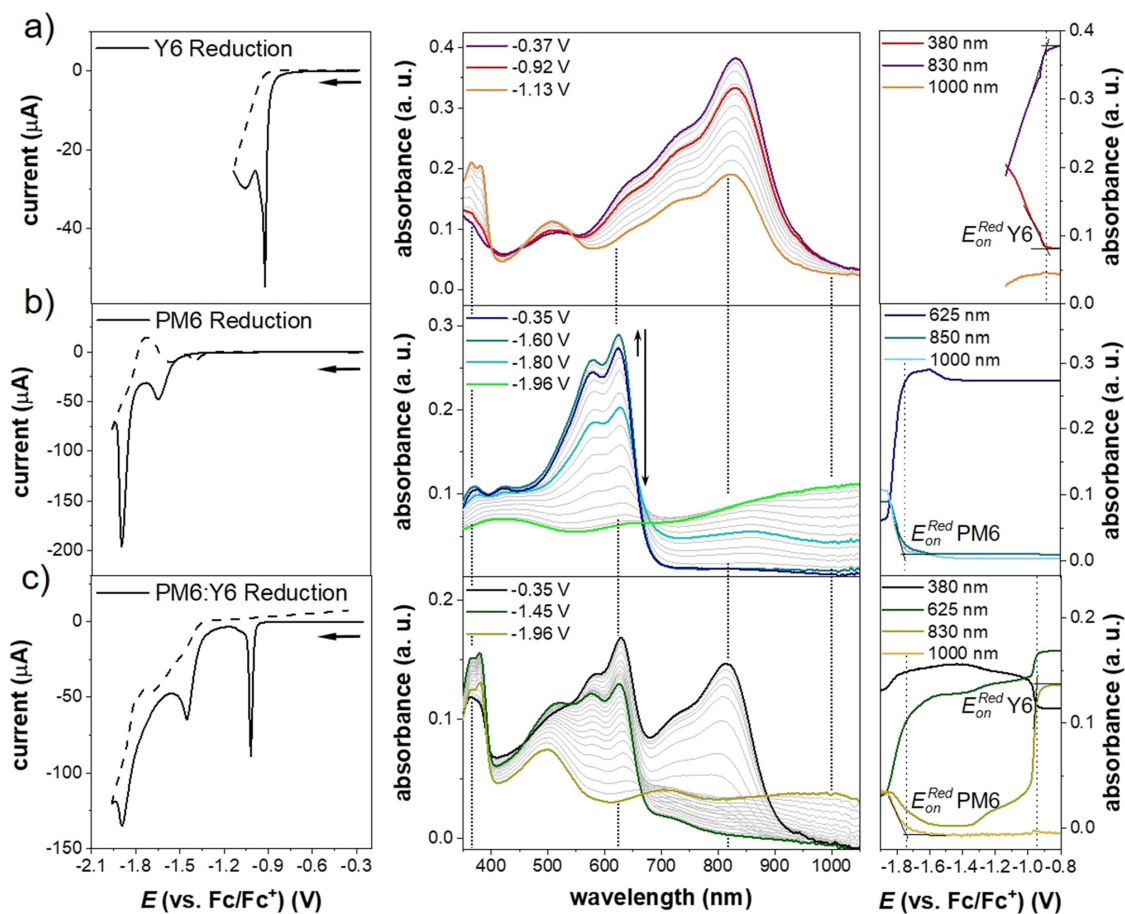


Fig. 4 *In situ* CV measurements coupled with UV-vis spectroscopy of (a) neat **Y6**, (b) neat **PM6** and (c) a blend of **PM6:Y6** (1: 1.2 wt%) films, spin coated from CF:CN (0.5 wt%) solutions. CVs are given on the left (the forward half-cycle is highlighted as a solid line), the spectra of the forward charge half-cycle of the reduction are presented in the center, completed with peak trends of significant bands on the right side. The peak trends are used for the determination of the spectral onsets which are indicated by dotted lines and obtained via using tangents. Underlying CVs (1st cycles) are measured in 0.1 M TBAPF₆/MeCN at 20 mV s⁻¹ on ITO substrates.

PM6:Y6 blends to be interpreted. In general, all the previously described waves and signals can be found in the CVs of the blend films as well. The oxidation in Fig. 3(c) shows a broad underlying wave with a sharp signal at 0.92 V which can be attributed to the oxidation of **Y6**. The broad signal underneath can be assigned to the oxidation of **PM6**.

Following the neat material films, the spectral evolution of the **PM6:Y6** blend film is considered. As already described in Fig. 1, the absorption of the neutral state of the blend film in Fig. 3(c) (black spectrum at -0.36 V) is almost a superposition of both neutral absorption bands of **Y6** and **PM6** with minor shifts occurring probably caused by different packing orders in the blend. This superposition of bands basically applies for the entire doping process and is highlighted by the vertical lines connecting characteristic bands in the neat material and blend films. The spectral onsets of the individual compounds in the blend are found at 0.50 V for **PM6** resulting in a HOMO of

-5.30 eV (identical with the neat film) and at 0.83 V for **Y6** with a HOMO of -5.63 eV.

For the presented films spin coated from CF:CN only a slight difference in the spectral onset of the oxidation between neat material and blend films can be found in the case of **Y6**, which can hardly be considered significant.

2.2 LUMO determination

Y6. The analysis of the spectral evolution of the reduction and the following extraction of spectral onsets for determining the LUMO levels are carried out accordingly.

The CV upon the reduction of **Y6** shows a quite sharp wave at -0.92 V, which is more pronounced compared to the oxidation behavior. In both cases (oxidation and reduction) in Fig. 3(a) and 4(a) the backward half cycles seem to be less pronounced which questions the electrochemical reversibility at first sight. It is important to mention that these CVs were

taken on thin films which are insoluble in the electrolyte in the pristine state. Experiments showed that the solubility properties of **Y6** change when charged species of **Y6** are being created. After completing the forward half cycle, the fully charged films start to dissolve into the electrolyte leading to a critical loss of electroactive material on the working electrode. As a result, the backward half cycles are weakly pronounced in the case of **Y6** oxidation or not visible at all in the case of reduction.

The displayed spectral evolution of the reduction of neat **Y6** films in Fig. 4(a) shows a decrease of the neutral band at 830 nm and a distinct increase at the low wavelength region of the spectrum around 380 nm. The isosbestic points clearly indicate a transition of the neutral state into a reduced form with a characteristic absorption band at 380 nm. The spectral onset of the reduction is located at -0.88 V which yields a LUMO of -3.92 eV.

PM6. The reduction of **PM6** shows two separated waves in the CV at -1.65 V and -1.89 V.

The spectral evolution of neat **PM6** films shows a unique behavior in the reduction. Upon decreasing the electrochemical potential, the absorption intensity of the neutral band (625 nm) seems to increase at first (spectra from dark blue at -0.35 V to teal color at -1.60 V). This increase of absorption intensity appears at the same potential as the first reduction peak observed in the CV. This is an indication that the **PM6** film is slightly oxidized under ambient conditions prior to the experiment. The induced charges – probably originating from the exposure to oxygen – are re-extracted leading to the first reduction signal at around 1.65 V. This is accompanied by an increase of absorbance of the neutral band when the film reaches its fully neutral state. Only after the fully neutral state is reached and the potential is further decreased the typical bleaching of the neutral band is observed together with a broad increase of absorption above 800 nm. Additionally, a weak shoulder can be seen around 900 nm which might be a signature of the negative polaron. A supposed band overlap and the coexistence of different charged species at the same time, which is typical for polythiophenes, make the exact interpretation of this feature difficult.^{30,67} The characteristic absorption of the fully reduced state found at potentials around -1.9 V fits to the second, only relevant, reduction peak in the

CV which now completes the description of two reduction peaks in the CV data. Using the spectral onset of this second reduction a value of -1.75 V can be extracted which leads to a LUMO of -3.05 eV for **PM6**.

PM6:Y6 blend. The CV of the reduction of the blend films in Fig. 4(c) displays three individual signals; one sharp wave (-1.02 V) which can be attributed to the reduction of **Y6** and two broader signals (-1.45 V and -1.90 V) which can be seen at similar potentials in the reduction of the neat **PM6** film. Evaluating the spectral onsets of the single compounds in the blend film results in a value of -1.74 V for **PM6** which yields a LUMO of -3.06 eV and a value of -0.9 V for **Y6** corresponding to a LUMO of -3.90 eV. Compared to the results of the neat films a shift of 0.02 V to a lower potential was found for **Y6** with respect to the blend. The observed shift of the spectral onset of **PM6** is only 0.01 V and therefore not significant.

2.3 Comparison of energy levels, HOMO offsets and transport gaps

All HOMO and LUMO levels of the neat material films and of the individual compounds inside the blend films (as obtained from the spectral onsets) are summarized in Fig. 5.

The determined frontier orbital energies of **PM6** and **Y6** neat films processed from CF:CN are positioned at -5.30 eV/ -3.05 eV (HOMO/LUMO **PM6**) and at -5.64 eV/ -3.92 eV (HOMO/LUMO **Y6**). The resulting electrochemical band gaps for **PM6** are found to be 2.25 eV and 1.72 eV for **Y6**. The HOMO offset of the two components calculated from the neat films is obtained at 0.34 eV. Compared to the results of the blend prepared from CF:CN, the energy levels of **PM6** (-5.30 eV/ -3.06 eV) and **Y6** (-5.63 eV/ -3.90 eV) are located at rather identical values. The blend shows a HOMO offset of 0.33 eV and a transport gap of 1.40 eV. The results for the neat films processed from *o*-xylene show slight changes in the energy levels. Our experiments yield energy levels of -5.33 eV/ -2.96 eV (HOMO/LUMO **PM6**) and -5.59 eV/ -3.95 eV (HOMO/LUMO **Y6**). This has a direct influence on the HOMO offset which shrinks to 0.26 eV. In the blend processed from *o*-xylene the HOMO/LUMO levels slightly differ from that of the neat films and are located at -5.31 eV/ -3.07 eV (HOMO/LUMO **PM6**) and at -5.66 eV/ -3.88 eV (HOMO/LUMO **Y6**). This correlates to a

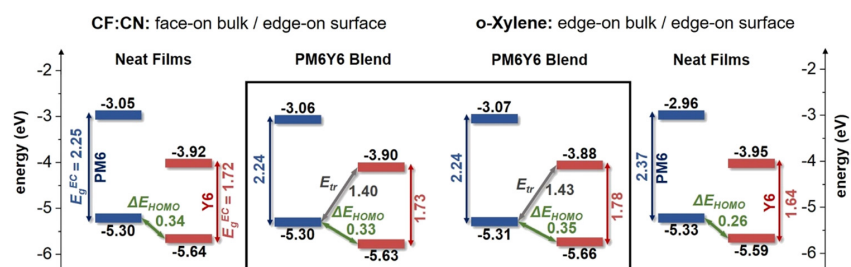


Fig. 5 Deduced HOMO/LUMO energy levels from the spectral onsets (Fig. 2 and 3) for films of neat **PM6**, neat **Y6** and the individual compounds in the blend films of **PM6**:**Y6** (1:1.2 wt%) processed from the two solvent systems CF:CN and *o*-xylene. The potentials were transformed to the Fermi scale using the correction factor of -4.8 eV. Electrochemical band gaps E_{EC} of the individual compounds are given as well as HOMO offsets ΔE_{HOMO} and transport gaps E_T .

HOMO offset of 0.35 eV and a transport gap of 1.43 eV. The calculated energy levels from the spectral onsets for the blend films show a HOMO offset (ΔE_{HOMO}) which is consistently positioned between 0.33 and 0.35 eV.

Comparing textures, in the blend prepared from the CF:CN solution (face-on orientation in bulk), the offset is 0.33 eV, whereas the offset slightly increases to 0.35 eV in the case of blends from *o*-xylene solutions (in edge-on orientation in bulk). The calculated effective transport gap of 1.4 eV for blend films processed from CF:CN (face-on orientation) is also slightly smaller than for blends from *o*-xylene solution (edge-on orientation) with an effective transport gap of 1.43 eV.

When comparing the HOMO offset in the neat films with the results of the blend films, differences regarding the solvent systems become visible. While the HOMO offsets remain rather constant for CF:CN films, an increase in the HOMO offset for films prepared from *o*-xylene solutions is registered. Our study therefore clearly shows that the impact of morphology and molecular orientation on device relevant parameters like HOMO offset and effective transport gaps is small but measurable. In particular, for the investigated materials **Y6** and **PM6**, the results from the spectroelectrochemical experiments lead to the conclusion that blending both components give measurable differences in the energy levels.

The occupied energy levels of the films (HOMO) prepared from different processing solvents (CF:CN and *o*-xylene) were further measured using ultraviolet photoelectron spectroscopy (UPS). Being a highly surface sensitive technique, UPS results are only influenced by the properties of the top surface of the films and cannot take differing bulk morphologies into account. Since films from CF:CN and *o*-xylene show identical surface orientations with edge-on orientation (see Fig. 2) no difference within the experimental error was measurable, as expected. The UPS spectra of neat **PM6** and **Y6** films as well as the **PM6:Y6** blend processed from CF:CN are shown in Fig. 6; the spectra of blends from other processing solvents are shown in the ESI† (see Fig. S6).

The secondary electron cut-off (SECO) spectra in Fig. 6(a) are used to calculate the work function of the material and give energies of -4.48 eV for **PM6**, -4.59 eV for **Y6** and -4.54 eV for the **PM6:Y6** blend. Adding the work function to the HOMO onsets extracted from the valence band spectra in Fig. 6(b) yields the ionization energy of the respective components. The onset used to calculate the binding energy of neat **PM6** is rather broad (blue line in Fig. 6(b)), while the HOMO of **Y6** has a more distinct onset. For binding energies, we extract 0.66 eV for **PM6** and 1.09 eV for **Y6**. This results in ionization energies of the neat films (HOMO levels) of **PM6** of -5.14 eV and of **Y6** of -5.68 eV (HOMO offset 0.54 eV), in good agreement with the other values reported in the literature from photoelectron spectroscopy on neat layers (see Table S1 in the ESI†).

The **Y6** HOMO from UPS at -5.68 eV agrees quite well with the value from the spectral onsets in the *in situ* CV measurements, while the UPS HOMO of **PM6** is shifted by about 0.15 eV to -5.14 eV. This is in line with previously reported data.³⁶ The reason for this is not clear yet, but we emphasize here that the

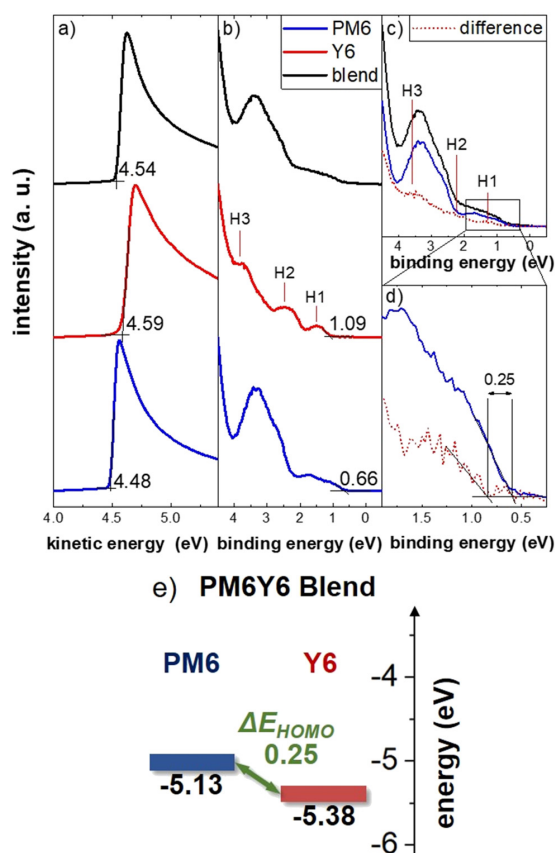


Fig. 6 (a) Secondary electron cut-off (SECO) and (b) valence band spectra of neat **PM6**, neat **Y6** and **PM6:Y6** (1:1.2 wt%) blend films prepared from CF:CN (0.5 wt%). (c) Subtraction of the **PM6** valence band spectrum (scaled) from the **PM6:Y6** blend spectrum. The residual intensity resembles a broadened **Y6** valence band spectrum, as indicated by the HOMO features labeled H1, H2 and H3. (d) Zoom into the valence band onset region marked in (c), yielding a HOMO offset between **PM6** and **Y6** in the blend of 0.25 eV, significantly smaller than the HOMO offset of the neat films (0.54 eV). Extracted energy levels and HOMO offset (ΔE_{HOMO}) for the blend film are displayed below in (e).

ionization energy from UPS is very sensitive to the electrostatics at the surface, which will most likely be different in neat and blend films.⁹¹ Therefore, we point out that experiments on neat films have to be taken with caution when they are used to explain the energetics of blend films. To actually access the HOMO energies of the individual components in blend films, we subtract the (scaled) reference valence band spectrum of neat **PM6** from the blend spectrum (see Fig. 6(c)). The residual intensity resembles the spectral shape of neat **Y6**, as indicated by the three features labeled H1, H2 and H3. A broadening is observed, which can be caused by the intermixing of the two molecules and the concomitant disorder.^{68,69} A zoom into the HOMO onset region is shown in Fig. 6(d) and yields HOMO energies of -5.13 eV and -5.38 eV for **PM6** and **Y6**, respectively. This corresponds to a HOMO offset of 0.25 eV between the two

materials, significantly smaller than the HOMO offset determined from the pristine films and in good agreement with the CV and UV-vis results. The difference in the absolute values compared to the CV/UV-vis results could be caused by different electrostatic interactions, *e.g.*, dipole, quadrupole or higher order moments, polarization and screening effects *etc.*, as has been demonstrated before.^{70–72}

3. Discussion of solar cell performance

With the transport gaps of the neat components and the blends at hand, we now turn to the performance of our **PM6:Y6** blend in solar cells. As pointed out earlier, it was proposed that the **PM6:Y6** blend exhibits a small barrier for free charge generation. Other groups argued that **Y6**-based solar devices function efficiently because of a very low or even vanishing exciton binding energy, E_b , of the **Y6** singlet exciton. For example, a recent self-consistent quantum mechanics/embedded charge study predicted the energy of **Y6** S_1 (*ca.* 2 eV) to lie 0.1 eV above that of the charge separated state (1.9 eV). There is, indeed, experimental evidence for direct free charge generation in **Y6** solid films.^{73,74} Our spectroelectrochemistry data put the electrochemical band gap of **Y6** in neat films at 1.72 eV (CF:CN) and 1.64 eV (*o*-xylene, see Fig. 5). This is up to 0.17 eV larger than the mean HOMO–LUMO gap from conventional CV (see Table S1, ESI[†]), but compares very well with the gap of 1.7 V determined by photoelectron spectroscopy in the literature.³⁵ The **Y6** band gap is slightly higher in the blend with 1.73 eV from CF:CN and 1.78 eV from *o*-xylene and consistent with a slight blue shift in absorption, indicating a slightly more distorted structure. On the other hand, we determined the energy of the **Y6** singlet energy by the intersection between the normalized absorption and PL of the blend to be 1.42 ± 0.02 eV (see Fig. S7, ESI[†]). This yields a **Y6** exciton binding energy at 0.33 ± 0.05 eV. This is in the same range as the HOMO offset in the blend, suggesting that the driving force for free charge formation by exciton dissociation is nearly zero. This contrasts the efficient free charge generation of the blend. A similar scenario has been

reported by Wu *et al.* where it was suggested that the formation of free charges is driven by entropy.³⁶ This is because an electron–hole pair in the charge separated state has many more options to distribute in the blend volume than when it is bound in an exciton or in a charge transfer state.⁷⁵ However, our own recent studies showed a pronounced decrease of the free carrier density with temperature,⁷⁶ which questions a strong contribution by entropy-driven processes. An alternative approach is to consider the presence of sub-bandgap states not accessible by our spectroscopy.^{77–79} Such states will be able to situate the free electron–hole pair at energies well below the singlet exciton of **Y6**.

We finally address the reason for the significantly lower V_{OC} of the device prepared from *o*-xylene (0.77 V vs. 0.83 V for the CF:CN). According to Fig. 5, the fundamental transport gaps are 1.43 eV and 1.40 eV for the blend prepared from *o*-xylene and CF:CN, respectively, showing the inverse trend. However, the relation between V_{OC} and the fundamental gap is not straight forward. In general, the V_{OC} of a device is given by the radiative voltage limit reduced by the non-radiative voltage loss: $V_{OC} = V_{OC}^{rad} - \Delta V_{OC}^{nr}$. The radiative V_{OC} limit is mainly determined by the ratio of the short circuit current, J_{SC} , and the radiative dark current, $J_{0,rad}$, the latter being proportional to the convolution of the external photovoltaic quantum efficiency (EQE_{PV}) of the device and the blackbody photon flux (ϕ_{BB}) over photon energy:⁸⁰ $qV_{OC}^{rad} = k_B T \ln(J_{SC}/J_{0,rad})$ where $J_{0,rad} = q \int EQE_{PV}(E) \phi_{BB}(E) dE$.

Here, the transport gap may enter indirectly *via* the onset of the EQE_{PV} spectrum. However, it has been shown before that the low energy tail of **PM6:Y6** EQE_{PV} is entirely determined by the **Y6** singlet exciton, which has a very similar energy for the two blends.⁸¹ As a consequence, the band-edge of the EQE spectra in Fig. 7(a) overlaps almost completely, yielding nearly the same V_{OC}^{rad} for the two devices (Table S2, ESI[†]). Therefore, the difference in V_{OC} of the two devices must be entirely caused by the non-radiative losses (ΔV_{OC}^{nr}). To confirm this, we measured the external electroluminescence quantum yield (ELQY), which

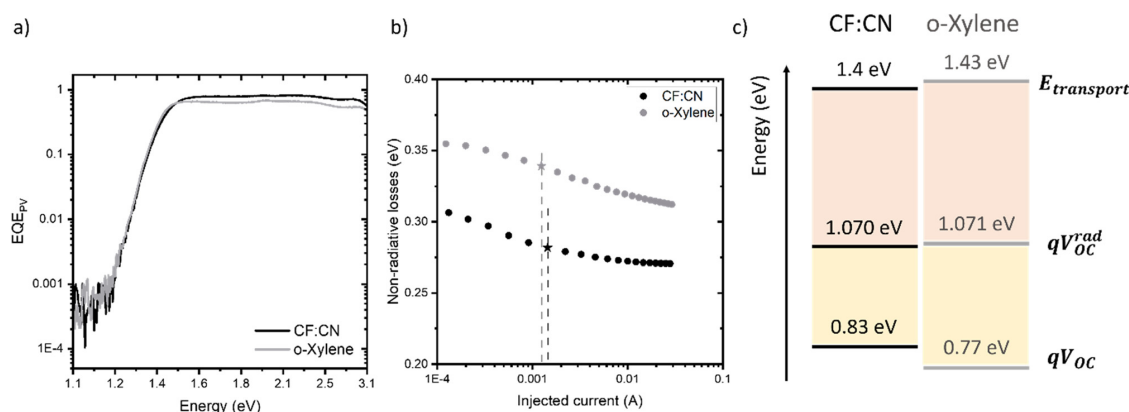


Fig. 7 EQE_{PV} (a), non-radiative voltage loss as a function of injected current (b), and schematic of relevant energy losses (c) of **PM6:Y6** devices fabricated in CF:CN (black) and *o*-xylene (grey). The dashed lines in (b) indicate when the injected current equals short-circuit current at 1 sun.

is related to ΔV_{OC}^{rad} via $q\Delta V_{OC}^{rad} = -k_B T \ln(ELQY)$ (see Fig. S8 in the ESI† for the emission spectra). This measurement revealed an almost 10 times lower ELQY for the device prepared from *o*-xylene (see Fig. 6(b) and Table S2, ESI† for the values). It has been shown that the ELQY of the **PM6:Y6** blend is limited by the non-radiative decay properties of the CT state.⁸¹ In organic solar cells, the predominant non-radiative decay pathway of the CT state is through vibronic coupling to the ground state.^{82,83} There is experimental and theoretical evidence that this process is significantly affected by the interfacial molecular orientation.^{84,85} Our results suggest that this is the determining factor also in our **PM6:Y6** devices.

Conclusions

In summary, this work presents an absorption spectroscopy assisted, spectroelectrochemical approach to determine the frontier orbital energies of **PM6** and **Y6** in blend films. A central advantage of our technique is the detection of the energy levels of the individual compounds inside the blend films and therefore examines influences arising from blending both materials. By preparing solar cells from two solvent systems resulting in two opposing bulk morphologies we investigated the influence of morphology on the energetics in blend films of the model system **PM6:Y6**.

Our results provided the HOMO/LUMO levels for **PM6** of -5.30 eV/ -3.06 eV and for **Y6** of -5.63 eV/ -3.90 eV in blend films processed from CF:CN (face-on morphology in bulk). Respective results for blend films processed from *o*-xylene (edge-on in bulk) delivered the HOMO/LUMO levels for **PM6** of -5.31 eV/ -3.07 eV and for **Y6** of -5.66 eV/ -3.88 eV. Interestingly, these values differ only slightly from the corresponding energies of the neat layers. Our data show that the effect of the different morphologies in the two blends on the energy levels is measurable but too small to explain the distinct difference in device performance. From our spectroelectrochemical measurements, we could determine the HOMO offsets and the transport gaps to be 0.33 eV and 1.4 eV for films from CF:CN and 0.35 eV and 1.43 eV for films from *o*-xylene, respectively. The HOMO offset was confirmed by UPS measurements on the blend, which yielded a value of 0.25 eV. Notably, the UPS measurements on the neat layers would suggest a HOMO offset of 0.54 eV, indicating that a comparison with neat material films must be taken with care. Finally, we determined the S_1 binding energy of the CF:CN coated **Y6** to be 0.33 eV, very similar to the HOMO offset. This suggests that an additional driving force exists for free charge generation. This study exemplifies the importance of precisely determining energy levels in blend films to generate device relevant information.

Experimental

Materials

PM6 ($M_n \sim 100$ kg mol⁻¹, PDI ~ 2.3) and **Y6** (1451.94 g mol⁻¹) were both purchased from 1-Material and used without further

purification. All used solvents were purchased from Sigma-Aldrich and used as received.

Film preparation and treatment

Thin films of neat **PM6**, neat **Y6** and a blend of **PM6:Y6** (1:1.2 wt%) were spin-coated from CF:CN (0.5 wt%) and *o*-xylene to obtain ~ 30 nm thick films on ITO substrates. The solutions were stirred at elevated temperatures (40 °C for CF:CN and 70 °C for *o*-xylene) to guarantee good solution quality before spin coating under a dry nitrogen atmosphere. All ITO substrates were previously cleaned by ultrasonication in isopropanol and acetone. The samples fabricated with CF:CN were annealed for 10 min at 110 °C under a dry nitrogen atmosphere right after the deposition of the active layer. For the samples fabricated with *o*-xylene, the active layer solution and substrate were heated up to 100 °C and 110 °C, respectively, prior to spin coating. The deposition of an active layer was conducted with hot solution and hot substrate.

Device geometry

All **PM6:Y6** devices were prepared in the same conventional structure (ITO/PEDOT:PSS/**PM6:Y6**/PDINO/Ag). Patterned ITO substrates (Psiotec, UK) were sonicated in Hellmanex, deionized water, acetone, and isopropanol for 20 min, 20 min, 10 min and 10 min, respectively. The cleaned ITO substrates were then treated with O₂ plasma (200 W, 4 min). Filtered (through 0.2 μ m PA filter) PEDOT:PSS (Clevios, AL4083) was spin coated on the plasma treated ITO substrates at 5000 rpm for 30 s under ambient conditions to form the hole transport layer. The PEDOT:PSS layer was then thermally annealed at 150 °C for 25 min. The rest of the fabrication was conducted in a glovebox. The **PM6:Y6** active layers made with CF:CN (0.5 wt%) and *o*-xylene were prepared, deposited, and treated on the top of the PEDOT:PSS layer exactly as described in the film preparation and treatment section. After the deposition and treatment of the active layer, a thin layer of PDINO (~ 10 nm) was spin coated on the top of the active layer to form the electron transport layer. Silver was then thermally evaporated through a patterned mask on the top of the PDINO layer to complete the devices with a pixel area of 0.06 cm².

Electrochemical measurements

Cyclic voltammograms were recorded in an electrochemical three-electrode setup under inert conditions. ITO substrates were used as working electrodes against a Pt counter electrode. An AgCl covered Ag wire was used as a pseudo reference electrode in 0.1 M TBAPF₆ (electrochemical grade) in MeCN as the standard electrolyte. All potentials were referenced against the Fc/Fc⁺ redox couple (added after the measurements) as the internal standard. The experiments were carried out on a PGSTAT204 potentiostat from Metrohm. The working electrodes were positioned in the beam path of a UV-vis spectrometer to collect the *in situ* spectral data. The modular diode array spectrometer system from Zeiss was provided with an MCS621 vis II detector and a CLH600 F halogen lamp.

Grazing-incidence wide-angle X-ray scattering (GIWAXS)

GIWAXS measurements were performed at the SAXS/WAXS beamline at the Australian Synchrotron.⁸⁶ A photon energy of 15 keV was used with 2D scattering patterns recorded using a Pilatus 2M detector. The sample-to-detector-distance was 742 mm calibrated using a silver behenate reference standard. The sample and detector were enclosed in a vacuum chamber to suppress air scatter. Scattering patterns were measured as a function of the angle of incidence, with the bulk-sensitive data acquired with an angle of incidence near the critical angle that maximized scattering intensity from the sample, and the surface-sensitive data acquired below the critical angle. The experimentally determined critical angles range from 0.105° to 0.13°. The difference in these apparent critical angles is within the acceptable range of error, which is defined by the resolution of incident angle alignment with a value of 0.02°. Data reduction and analysis were performed using a modified version of NIKA,⁸⁷ implemented in Igor Pro.

Near-edge X-ray absorption fine-structure (NEXAFS) spectroscopy

NEXAFS measurements were performed under high vacuum conditions at the Soft X-ray beamline at the Australian Synchrotron.⁸⁸ Data were acquired in the partial electron yield (PEY) mode whereby X-ray absorption was detected *via* the measurement of the energetic photons that were ejected from the sample that were detected by a channeltron detector. Data were calibrated and normalized using the so-called “stable monitor method” that uses an upstream gold mesh to monitor the beam intensity whose response is calibrated by measuring the signal at the sample position with a photodiode. Data analysis was performed in QANT,⁸⁹ with further details of data analysis procedures provided elsewhere.⁹⁰

Ultraviolet photoelectron spectroscopy (UPS)

All samples were transferred to a UHV system with a base pressure of 10⁻¹⁰ mbar without air exposure. A HIS 13 helium discharge lamp from ScientaOmicron equipped with a monochromator was used for excitation, yielding a reduced UV flux and therefore minimum degradation of the samples. The kinetic energy of the emitted photoelectrons was measured using a Specs Phoibos 100 hemispherical analyzer and pass energies of 5 eV or 2 eV for the valence band or the secondary electron cut-off (SECO) spectra, respectively. A bias of -10 V was applied between the sample and the analyzer during SECO measurements. The binding energy axis was calibrated by measuring the Fermi-edge of a polycrystalline gold sample and setting its center to 0 eV. The resolution of the setup in this configuration was 0.15 eV as determined from the width of the Fermi-edge.

Conflicts of interest

There are no conflicts to declare.

Acknowledgements

D. N. and S. L. thank the IQST at the University of Stuttgart for funding through the Carl Zeiss Foundation. B. S. and S. S. acknowledge funding by the Alexander von Humboldt Foundation (Sofja Kovalewskaja-Award), and L. P. T., N. K. and D. N. by DFG (HIOS Projektnummer 182087777 – SFB 951). This work was performed in part at the Soft X-ray and SAXS/WAXS beamlines at the Australian Synchrotron, part of ANSTO.

References

- 1 T. M. Swager, *Macromolecules*, 2017, **50**, 4867–4886.
- 2 O. Inganas, *Adv. Mater.*, 2018, **30**, 1800388.
- 3 *P3HT Revisited - From Molecular Scale to Solar Cell Devices*, ed. S. Ludwigs, Springer, Berlin, Heidelberg, 2014.
- 4 K. A. Mazzio and C. K. Luscombe, *Chem. Soc. Rev.*, 2015, **44**, 78–90.
- 5 B. Kippelen and J.-L. Brédas, *Energy Environ. Sci.*, 2009, **2**, 251.
- 6 O. Doat, B. H. Barboza, A. Batagin-Neto, D. Bégué and R. C. Hiorns, *Polym. Int.*, 2021, **71**, 6–25.
- 7 A. Facchetti, *Chem. Mater.*, 2010, **23**, 733–758.
- 8 J. Wu, Y. Meng, X. Guo, L. Zhu, F. Liu and M. Zhang, *J. Mater. Chem. A*, 2019, **7**, 16190–16196.
- 9 C. M. Cardona, W. Li, A. E. Kaifer, D. Stockdale and G. C. Bazan, *Adv. Mater.*, 2011, **23**, 2367–2371.
- 10 J. Sworakowski, J. Lipiński and K. Janus, *Org. Electron.*, 2016, **33**, 300–310.
- 11 R. E. M. Willems, C. H. L. Weijtens, X. de Vries, R. Coehoorn and R. A. J. Janssen, *Adv. Energy Mater.*, 2019, **9**, 1803677.
- 12 K. Bruchlos, D. Trefz, A. Hamidi-Sakr, M. Brinkmann, J. Heinze, A. Ruff and S. Ludwigs, *Electrochim. Acta*, 2018, **269**, 299–311.
- 13 M. Schwarze, W. Tress, B. Beyer, F. Gao, R. Scholz, C. Poelking, K. Ortstein, A. A. Günther, D. Kasemann, D. Andrienko and K. Leo, *Science*, 2016, **352**, 1446–1449.
- 14 J. Yuan, Y. Zhang, L. Zhou, G. Zhang, H.-L. Yip, T.-K. Lau, X. Lu, C. Zhu, H. Peng, P. A. Johnson, M. Leclerc, Y. Cao, J. Ulanski, Y. Li and Y. Zou, *Joule*, 2019, **3**, 1140–1151.
- 15 C. Yan, S. Barlow, Z. Wang, H. Yan, A. K. Y. Jen, S. R. Marder and X. Zhan, *Nat. Rev. Mater.*, 2018, **3**, 18003.
- 16 L. Zhu, M. Zhang, W. Zhong, S. Leng, G. Zhou, Y. Zou, X. Su, H. Ding, P. Gu, F. Liu and Y. Zhang, *Energy Environ. Sci.*, 2021, **14**, 4341–4357.
- 17 A. Wadsworth, M. Moser, A. Marks, M. S. Little, N. Gasparini, C. J. Brabec, D. Baran and I. McCulloch, *Chem. Soc. Rev.*, 2019, **48**, 1596–1625.
- 18 A. Distler, T. Sauermann, H.-J. Egelhaaf, S. Rodman, D. Waller, K.-S. Cheon, M. Lee and D. M. Guldi, *Adv. Energy Mater.*, 2014, **4**, 1300693.
- 19 G. Zhang, X. K. Chen, J. Xiao, P. C. Y. Chow, M. Ren, G. Kupgan, X. Jiao, C. C. S. Chan, X. Du, R. Xia, Z. Chen, J. Yuan, Y. Zhang, S. Zhang, Y. Liu, Y. Zou, H. Yan, K. S. Wong, V. Coropceanu, N. Li, C. J. Brabec, J. L. Bredas, H. L. Yip and Y. Cao, *Nat. Commun.*, 2020, **11**, 3943.

- 20 A. Mishra and P. Bauerle, *Angew. Chem., Int. Ed.*, 2012, **51**, 2020–2067.
- 21 J. Roncali, P. Leriche and P. Blanchard, *Adv. Mater.*, 2014, **26**, 3821–3838.
- 22 C. Malacrida, A. H. Habibi, S. Gámez-Valenzuela, I. Lenko, P. S. Marqués, A. Labrunie, J. Grolleau, J. T. López Navarrete, M. C. Ruiz Delgado, C. Cabanetos, P. Blanchard and S. Ludwigs, *ChemElectroChem*, 2019, **6**, 4215–4228.
- 23 Q. Wei, W. Liu, M. Leclerc, J. Yuan, H. Chen and Y. Zou, *Sci. China: Chem.*, 2020, **63**, 1352–1366.
- 24 K. Jiang, Q. Wei, J. Y. L. Lai, Z. Peng, H. K. Kim, J. Yuan, L. Ye, H. Ade, Y. Zou and H. Yan, *Joule*, 2019, **3**, 3020–3033.
- 25 M. Zhang, X. Guo, W. Ma, H. Ade and J. Hou, *Adv. Mater.*, 2015, **27**, 4655–4660.
- 26 Q. Fan, T. Liu, W. Gao, Y. Xiao, J. Wu, W. Su, X. Guo, X. Lu, C. Yang, H. Yan, M. Zhang and Y. Li, *J. Mater. Chem. A*, 2019, **7**, 15404–15410.
- 27 X. Xu, L. Yu, H. Yan, R. Li and Q. Peng, *Energy Environ. Sci.*, 2020, **13**, 4381–4388.
- 28 K. Tremel and S. Ludwigs, in *P3HT Revisited – From Molecular Scale To Solar Cell Devices*, ed. S. Ludwigs, Springer, Berlin, Heidelberg, 2014, vol. 265, pp. 39–82.
- 29 E. J. Crossland, K. Tremel, F. Fischer, K. Rahimi, G. Reiter, U. Steiner and S. Ludwigs, *Adv. Mater.*, 2012, **24**, 839–844.
- 30 D. Neusser, C. Malacrida, M. Kern, Y. M. Gross, J. van Slageren and S. Ludwigs, *Chem. Mater.*, 2020, **32**, 6003–6013.
- 31 R. Ma, G. Li, D. Li, T. Liu, Z. Luo, G. Zhang, M. Zhang, Z. Wang, S. Luo, T. Yang, F. Liu, H. Yan and B. Tang, *Sol. RRL*, 2020, **4**, 2000250.
- 32 Q. Guo, Q. Guo, Y. Geng, A. Tang, M. Zhang, M. Du, X. Sun and E. Zhou, *Mater. Chem. Front.*, 2021, **5**, 3257–3280.
- 33 L. Perdigon-Toro, H. Zhang, A. Markina, J. Yuan, S. M. Hosseini, C. M. Wolff, G. Zuo, M. Stolterfoht, Y. Zou, F. Gao, D. Andrienko, S. Shoaee and D. Neher, *Adv. Mater.*, 2020, **32**, e1906763.
- 34 Z. Tu, G. Han and Y. Yi, *J. Phys. Chem. Lett.*, 2020, **11**, 2585–2591.
- 35 S. Karuthedath, J. Gorenflot, Y. Firdaus, N. Chaturvedi, C. S. P. De Castro, G. T. Harrison, J. I. Khan, A. Markina, A. H. Balawi, T. A. D. Pena, W. Liu, R. Z. Liang, A. Sharma, S. H. K. Paleti, W. Zhang, Y. Lin, E. Alarousu, S. Lopatin, D. H. Anjum, P. M. Beaujuge, S. De Wolf, I. McCulloch, T. D. Anthopoulos, D. Baran, D. Andrienko and F. Laquai, *Nat. Mater.*, 2021, **20**, 378–384.
- 36 J. Wu, J. Lee, Y.-C. Chin, H. Yao, H. Cha, J. Luke, J. Hou, J.-S. Kim and J. R. Durrant, *Energy Environ. Sci.*, 2020, **13**, 2422–2430.
- 37 Y. Cui, Y. Xu, H. Yao, P. Bi, L. Hong, J. Zhang, Y. Zu, T. Zhang, J. Qin, J. Ren, Z. Chen, C. He, X. Hao, Z. Wei and J. Hou, *Adv. Mater.*, 2021, **33**, e2102420.
- 38 K. Chong, X. Xu, H. Meng, J. Xue, L. Yu, W. Ma and Q. Peng, *Adv. Mater.*, 2022, e2109516, DOI: [10.1002/adma.202109516](https://doi.org/10.1002/adma.202109516).
- 39 X. Ma, A. Zeng, J. Gao, Z. Hu, C. Xu, J. H. Son, S. Y. Jeong, C. Zhang, M. Li, K. Wang, H. Yan, Z. Ma, Y. Wang, H. Y. Woo and F. Zhang, *Natl. Sci. Rev.*, 2021, **8**, nwaa305.
- 40 W. Peng, Y. Lin, S. Y. Jeong, Z. Genene, A. Magomedov, H. Y. Woo, C. Chen, W. Wahyudi, Q. Tao, J. Deng, Y. Han, V. Getautis, W. Zhu, T. D. Anthopoulos and E. Wang, *Nano Energy*, 2022, **92**, 106681.
- 41 X. Wang, Q. Sun, J. Gao, X. Ma, J. H. Son, S. Y. Jeong, Z. Hu, L. Niu, H. Y. Woo, J. Zhang and F. Zhang, *Solar RRL*, 2021, **5**, 2100007.
- 42 J. Wu, G. Li, J. Fang, X. Guo, L. Zhu, B. Guo, Y. Wang, G. Zhang, L. Arunagiri, F. Liu, H. Yan, M. Zhang and Y. Li, *Nat. Commun.*, 2020, **11**, 4612.
- 43 M. Zhang, L. Zhu, G. Zhou, T. Hao, C. Qiu, Z. Zhao, Q. Hu, B. W. Larson, H. Zhu, Z. Ma, Z. Tang, W. Feng, Y. Zhang, T. P. Russell and F. Liu, *Nat. Commun.*, 2021, **12**, 309.
- 44 Y. Zhang, K. Liu, J. Huang, X. Xia, J. Cao, G. Zhao, P. W. K. Fong, Y. Zhu, F. Yan, Y. Yang, X. Lu and G. Li, *Nat. Commun.*, 2021, **12**, 4815.
- 45 P. E. Shaw, A. Ruseckas and I. D. W. Samuel, *Adv. Mater.*, 2008, **20**, 3516–3520.
- 46 O. V. Mikhnenko, H. Azimi, M. Scharber, M. Morana, P. W. M. Blom and M. A. Loi, *Energy Environ. Sci.*, 2012, **5**, 6960.
- 47 M. C. Scharber, D. Mühlbacher, M. Koppe, P. Denk, C. Waldauf, A. J. Heeger and C. J. Brabec, *Adv. Mater.*, 2006, **18**, 789–794.
- 48 C. Deibel and V. Dyakonov, *Rep. Prog. Phys.*, 2010, **73**, 096401.
- 49 G. Zhou, M. Zhang, Z. Chen, J. Zhang, L. Zhan, S. Li, L. Zhu, Z. Wang, X. Zhu, H. Chen, L. Wang, F. Liu and H. Zhu, *ACS Energy Lett.*, 2021, **6**, 2971–2981.
- 50 R. Jasiūnas, H. Zhang, J. Yuan, X. Zhou, D. Qian, Y. Zou, A. Devižis, J. Šulskus, F. Gao and V. Gulbinas, *J. Phys. Chem. C*, 2020, **124**, 21283–21292.
- 51 X. Li, R. Ma, T. Liu, Y. Xiao, G. Chai, X. Lu, H. Yan and Y. Li, *Sci. China: Chem.*, 2020, **63**, 1256–1261.
- 52 H. Yan, Z. Chen, Y. Zheng, C. Newman, J. R. Quinn, F. Dotz, M. Kastler and A. Facchetti, *Nature*, 2009, **457**, 679–686.
- 53 D. Trefz, Y. M. Gross, C. Dingler, R. Tkachov, A. Hamidi-Sakr, A. Kiriy, C. R. McNeill, M. Brinkmann and S. Ludwigs, *Macromolecules*, 2018, **52**, 43–54.
- 54 Y. M. Gross, D. Trefz, C. Dingler, D. Bauer, V. Vijayakumar, V. Untilova, L. Biniek, M. Brinkmann and S. Ludwigs, *Chem. Mater.*, 2019, **31**, 3542–3555.
- 55 H. Zhao, H. B. Naveed, B. Lin, X. Zhou, J. Yuan, K. Zhou, H. Wu, R. Guo, M. A. Scheel, A. Chumakov, S. V. Roth, Z. Tang, P. Muller-Buschbaum and W. Ma, *Adv. Mater.*, 2020, **32**, e2002302.
- 56 H. Fu, W. Gao, Y. Li, F. Lin, X. Wu, J. H. Son, J. Luo, H. Y. Woo, Z. Zhu and A. K. Y. Jen, *Small Methods*, 2020, **4**, 2000687.
- 57 Y. Qin, Y. Xu, Z. Peng, J. Hou and H. Ade, *Adv. Funct. Mater.*, 2020, **30**, 46.
- 58 Z. Wang, Z. Peng, Z. Xiao, D. Seyitliyev, K. Gundogdu, L. Ding and H. Ade, *Adv. Mater.*, 2020, **32**, e2005386.
- 59 W. Zhong, M. Zhang, G. Freychet, G. M. Su, L. Ying, F. Huang, Y. Cao, Y. Zhang, C. Wang and F. Liu, *Adv. Mater.*, 2022, **34**, e2107316.
- 60 R. Ma, T. Yang, Y. Xiao, T. Liu, G. Zhang, Z. Luo, G. Li, X. Lu, H. Yan and B. Tang, *Energy Environ. Mater.*, 2021, 1–9.

- 61 J. Zhan, L. Wang, M. Zhang, L. Zhu, T. Hao, G. Zhou, Z. Zhou, J. Chen, W. Zhong, C. Qiu, S. Leng, Y. Zou, Z. Shi, H. Zhu, W. Feng, M. Zhang, Y. Li, Y. Zhang and F. Liu, *Macromolecules*, 2021, **54**, 4030–4041.
- 62 S. Albrecht, K. Vandewal, J. R. Tumbleston, F. S. Fischer, J. D. Douglas, J. M. Frechet, S. Ludwigs, H. Ade, A. Salleo and D. Neher, *Adv. Mater.*, 2014, **26**, 2533–2539.
- 63 R. Ma, C. Yan, P. W.-K. Fong, J. Yu, H. Liu, J. Yin, J. Huang, X. Lu, H. Yan and G. Li, *Energy Environ. Sci.*, 2022, **15**, 2497.
- 64 X. Jiang, P. Chotard, K. Luo, F. Eckmann, S. Tu, M. A. Reus, S. Yin, J. Reitenbach, C. L. Weindl, M. Schwartzkopf, S. V. Roth and P. Müller-Buschbaum, *Adv. Energy Mater.*, 2022, **12**, 2103977.
- 65 M. Skompska and A. Szkulat, *Electrochim. Acta*, 2001, **46**, 4007–4015.
- 66 C. Enengl, S. Enengl, S. Pluczyk, M. Havlicek, M. Lapkowski, H. Neugebauer and E. Ehrenfreund, *ChemPhysChem*, 2016, **17**, 3836–3844.
- 67 J. Heinze, B. A. Frontana-Urbe and S. Ludwigs, *Chem. Rev.*, 2010, **110**, 4724–4771.
- 68 P. Li, G. Ingram, J.-J. Lee, Y. Zhao and Z.-H. Lu, *Commun. Phys.*, 2019, **2**, 1–7.
- 69 Y. Nakayama, S. Kera and N. Ueno, *J. Mater. Chem. C*, 2020, **8**, 9090–9132.
- 70 K. Ortstein, S. Hutsch, M. Hamsch, K. Tvingstedt, B. Wegner, J. Benduhn, J. Kublitski, M. Schwarze, S. Schellhammer, F. Talnack, A. Vogt, P. Bauerle, N. Koch, S. C. B. Mannsfeld, H. Kleemann, F. Ortmann and K. Leo, *Nat. Mater.*, 2021, **20**, 1407–1413.
- 71 K. Ortstein, S. Hutsch, A. Hinderhofer, J. Vahland, M. Schwarze, S. Schellhammer, M. Hodas, T. Geiger, H. Kleemann, H. F. Bettinger, F. Schreiber, F. Ortmann and K. Leo, *Adv. Funct. Mater.*, 2020, **30**, 2002987.
- 72 S. Duhm, G. Heimel, I. Salzmann, H. Glowatzki, R. L. Johnson, A. Vollmer, J. P. Rabe and N. Koch, *Nat. Mater.*, 2008, **7**, 326–332.
- 73 L. Zhu, J. Zhang, Y. Guo, C. Yang, Y. Yi and Z. Wei, *Angew. Chem., Int. Ed.*, 2021, **60**, 15348–15353.
- 74 M. B. Price, P. A. Hume, A. Ilina, I. Wagner, R. R. Tamming, K. E. Thorn, W. Jiao, A. Campbell, P. J. Conaghan, G. Lakhwani, N. J. L. K. Davis, Y. Wang, P. Xue, H. Lu, K. Chen, X. Zhan and J. M. Hodgkiss, Research Square.
- 75 S. N. Hood and I. Kassal, *J. Phys. Chem. Lett.*, 2016, **7**, 4495–4500.
- 76 L. Perdígón-Toro, L. Q. Phuong, F. Eller, G. Freychet, E. Saglamkaya, J. I. Khan, Q. Wei, S. Zeiske, D. Kroh, S. Wedler, A. Köhler, A. Armin, F. Laquai, E. M. Herzig, Y. Zou, S. Shoaee and D. Neher, *Adv. Energy Mater.*, 2022, **12**, 2103422.
- 77 I. N. Hulea, H. B. Brom, A. J. Houtepen, D. Vanmaekelbergh, J. J. Kelly and E. A. Meulenkaamp, *Phys. Rev. Lett.*, 2004, **93**, 166601.
- 78 T. Sueyoshi, H. Fukagawa, M. Ono, S. Kera and N. Ueno, *Appl. Phys. Lett.*, 2009, **95**, 183303.
- 79 S. Athanasopoulos, H. Bassler and A. Köhler, *J. Phys. Chem. Lett.*, 2019, **10**, 7107–7112.
- 80 U. Rau, *Phys. Rev. B: Condens. Matter Mater. Phys.*, 2007, **76**, 085303.
- 81 L. Perdígón-Toro, L. Q. Phuong, S. Zeiske, K. Vandewal, A. Armin, S. Shoaee and D. Neher, *ACS Energy Lett.*, 2021, **6**, 557–564.
- 82 Z. Tang, B. Liu, A. Melianas, J. Bergqvist, W. Tress, Q. Bao, D. Qian, O. Inganäs and F. Zhang, *Adv. Mater.*, 2015, **27**, 1900–1907.
- 83 M. Azzouzi, J. Yan, T. Kirchartz, K. Liu, J. Wang, H. Wu and J. Nelson, *Phys. Rev. X*, 2018, **8**, 031055.
- 84 N. A. Ran, S. Roland, J. A. Love, V. Savikhin, C. J. Takacs, Y. T. Fu, H. Li, V. Coropceanu, X. Liu, J. L. Bredas, G. C. Bazan, M. F. Toney, D. Neher and T. Q. Nguyen, *Nat. Commun.*, 2017, **8**, 79.
- 85 X. Chen, M. K. Ravva, H. Li, S. M. Ryno and J. L. Bredas, *Adv. Energy Mater.*, 2016, **6**, 1601325.
- 86 N. M. Kirby, S. T. Mudie, A. M. Hawley, D. J. Cookson, H. D. T. Mertens, N. Cowieson and V. Samardzic-Boban, *J. Appl. Crystallogr.*, 2013, **46**, 1670–1680.
- 87 J. Ilavsky, *J. Appl. Crystallogr.*, 2012, **45**, 324–328.
- 88 B. C. C. Cowie, A. Tadich and L. Thomsen, *AIP Conf. Proc.*, 2010, **1234**, 307–310.
- 89 E. Gann, C. R. McNeill, A. Tadich, B. C. Cowie and L. Thomsen, *J. Synchrotron Radiat.*, 2016, **23**, 374–380.
- 90 M. M. Nahid, E. Gann, L. Thomsen and C. R. McNeill, *Eur. Polym. J.*, 2016, **81**, 532–554.
- 91 X. Li, Q. Zhang, J. Yu, Y. Xu, R. Zhang, C. Wang, H. Zhang, S. Fabiano, X. Liu, J. Hou, F. Gao and M. Fahlman, *Nat. Commun.*, 2022, **13**, 2046.

4.1.4 Reprint Permission

Spectroelectrochemically determined energy levels of PM6:Y6 blends and their relevance to solar cell performance

D. Neusser, B. Sun, W. L. Tan, L. Thomsen, T. Schultz, L. Perdigón-Toro, N. Koch, S. Shoaee, C. R. McNeill, D. Neher and S. Ludwigs, *J. Mater. Chem. C*, 2022, **10**, 11565 DOI: 10.1039/D2TC01918C

To request permission to reproduce material from this article, please go to the [Copyright Clearance Center request page](#).

If you are **an author contributing to an RSC publication**, **you do not need to request permission** provided correct acknowledgement is given.

If you are **the author of this article**, **you do not need to request permission to reproduce figures and diagrams** provided correct acknowledgement is given. If you want to reproduce the whole article in a third-party publication (excluding your thesis/dissertation for which permission is not required) please go to the [Copyright Clearance Center request page](#).

4.2 Electrochemical Conductivity Tuning and its Structural Impact on Aligned Films of P(NDI2OD-T2)

4.2.1 Publication Data

Title: “Electrochemical Conductivity Tuning and its Structural Impact on Aligned Films of P(NDI2OD-T2)”

Status: Manuscript in preparation

Journal: Communication Style

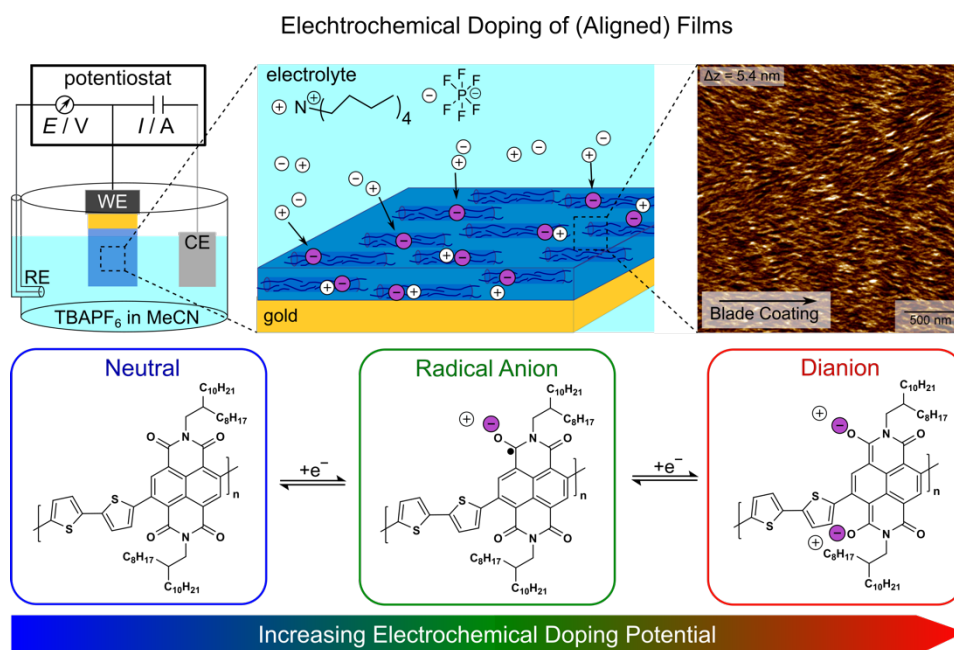
Publisher: -

DOI: -

Authors: David Neusser, Wen Liang Tan, Lars Thomsen, Christopher R. McNeill and Sabine Ludwigs.

Contributions: D. Neusser performed all experiments on the electrochemical doping and conductivity measurements. GIWAXS experiments were performed by W. L. Tan, L. Thomsen and C. R. McNeill. D. Neusser wrote the first version of the manuscript. All work was supervised by S. Ludwigs.

Scheme



4.2.2 Short Summary

Whereas previous chapters cover the electrochemical doping of p-type conducting polymers the next challenging step is to transfer the gained knowledge and expertise to n-type conducting polymers. Since the achievement of high conductivities in stable doped films is quite challenging for this material class, we selected the benchmark polymer P(NDI2OD-T2) (N2200) as promising material to understand basic concepts and identify challenges when doping n-type conducting polymers with our electrochemical doping approach. Results prove that it is possible to charge P(NDI2OD-T2) to different doping levels and transfer the generated charge carriers into the solid-state. The measured conductivities of spin coated films reach up to $2 \cdot 10^{-4} \text{ Scm}^{-1}$ which is around one order of magnitude lower than the highest conductivities achieved with chemical doping. Nevertheless, we are able to tune the conductivity over 3-4 orders of magnitude offering the possibility to adjust the desired conductivity. Overall, we observe a bell-shaped conductivity profile which differs significantly from the results obtained from P3HT underlining the classification of P(NDI2OD-T2) as conjugated redox polymer. As predicted from the mixed valence conductivity model highest conductivities are achieved at intermediate doping levels rather than reaching a high plateau of conductivity at highest doping levels.

Besides the study of the conductivity behavior, this manuscript tries to give insights into the impact of electrochemical doping on defined thin film morphologies. P(NDI2OD-T2) shows a strong tendency to aggregate and form lamellar morphologies in thin films which we exploit to produce highly aligned films by blade coating. When doping aligned films of P(NDI2OD-T2) we detect maximum conductivities that differ by a factor of 4.1 with higher conductivity for films that are aligned parallel to the direction of charge transport. Since electrochemical doping in solution leads to the introduction of counterions which compensate for the induced charge carriers on the polymer backbones, we performed *ex situ* GIWAXS measurements of films at different doping levels to examine the structural response to different degrees of doping and ion integration. Results show that ion integration definitely leads to a decrease of order, but the general configuration (face-on or edge-on) is being preserved.

4.2.3 Manuscript

Electrochemical Conductivity Tuning and its Structural Impact on Aligned Films of P(NDI2OD-T2)

David Neusser,^a Wen Liang Tan,^b Lars Thomsen,^c Chris R. McNeill^b and Sabine Ludwigs^a

^a IPOC – Functional Polymers, Institute of Polymer Chemistry, and Center for Integrated Quantum Science and Technology (IQST), University of Stuttgart, Germany

^b Department of Materials Science and Engineering, Monash University, Wellington Road, Clayton, Victoria, 3800 Australia

^c Australian Synchrotron, ANSTO, 800 Blackburn Road, Clayton, Victoria 3168, Australia

*sabine.ludwigs@ipoc.uni-stuttgart.de

The understanding of the doping process still remains the center of attention in the research surrounding conducting polymers. The control of the doping process on the fundamental level depicts the key technique when it comes to realizing highly conducting materials for an implementation in functional organic electronics devices.^{1,2} Since different applications require conducting polymers in either neutral or doped state, the ability to exactly tune the doping level is strongly desired.³ Whereas research in the field of doping of conjugated polymers is quite far in the case of p-type materials, n-type materials and their doping and conductivity behavior are still lagging behind.^{4,5}

One reason for that is the special synthetic attention that is required to stabilize large amounts of additional negative charge on the backbone of a conducting polymer. A structural unit that fulfills this criterion is the NDI (naphthalene-bis(dicarboximide)) unit, which is also one of the basic building blocks of the benchmark material P(NDI2OD-T2) (N2200).^{6,7} The NDI units strongly localize the additional negative charge, establishing an image where P(NDI2OD-T2) is often described as a sequence of isolated redox units.⁸⁻¹⁰ The localization of charge on the single repeating units leads to the classification as a redox polymer despite its conjugated backbone. Here, a difference to the model system P3HT can be drawn in which charges are delocalized over multiple repeating units,^{11,12} being one reason for the different conductivity mechanism and behavior thoroughly discussed in literature.^{13,14}

Besides the electronic properties, P(NDI2OD-T2) is known for its ability to show strong inter and intra chain aggregation in either segregated or mixed stacking configurations (polymorph I and II).¹⁵ The aggregation behavior is not only studied in the solid-state but can also be observed in solution drawing similarities to properties of liquid crystals.¹⁶⁻¹⁹ Special film coating methods like blade coating can take advantage of the aggregation in solution leading to film formation where fibers formed in solution are being aligned by shear forces during coating to produce thin films with anisotropic morphologies. This anisotropy has an influence not only on optical properties but also on charge transport and mobility as presented in the literature.^{20,21} Thin films with anisotropic electronic properties mark an interesting starting point for further experiments.

Typically, P(NDI2OD-T2) is being doped using a chemical doping approach based on dopants like 4-(2,3-dihydro-1,3-dimethyl-1H-benzimidazol-2-yl)-N,N-dimethylbenzeneamine (N-DMBI) and tetrakis(dimethylamino)ethylene (TDAE). Both dopants show a strong tendency for electron donation residing on a matching HOMO energy level that is able to donate electrons to the LUMO of P(NDI2OD-T2). A severe drawback of this chemical doping approach is that it typically suffers from low doping efficiencies due to aggregation of dopant molecules.¹ Additionally, the formation of locally bound charge transfer complexes disturbs integer charge transfer and limits the overall amount of accessible mobile charge carriers.²² Therefore, electrochemical doping depicts an alternative approach to charge conducting polymers inside an electrochemical setup where the doping level is linked to the applied electrochemical doping potential. This illustrates an inherent advantage of this method since the resulting doping level can be fine-tuned by simply choosing the desired electrochemical potential. The recently presented *ex situ* electrochemical doping study on P3HT is therefore extended to an n-type conducting polymer to overcome one of the main drawbacks of electrochemical doping which is the limitation of the electrochemical cell.^{23, 24} Following this approach, films can be charged in electrolyte to the desired doping level and then transferred into the solid-state. Counterbalancing ions are entering the film from the electrolyte while charges are being induced on the backbone of the polymer. The doping level can be assessed by spectroscopy which allows for the identification of characteristic charge carriers present at different doping levels. Tracking the conductivity in dependence of the doping potential offers the possibility to discuss the conductivity behavior and potential models of charge propagation. By using anisotropic films with controlled morphologies verified by AFM, the impact of different degrees of doping on the microstructure can be followed by *ex situ* GIWAXS and gives more insights into the doping process and possible locations where counterions reside. The following Figure (Figure 1) summarizes the approach and the different charged species of P(NDI2OD-T2) induced in anisotropic and aligned films.

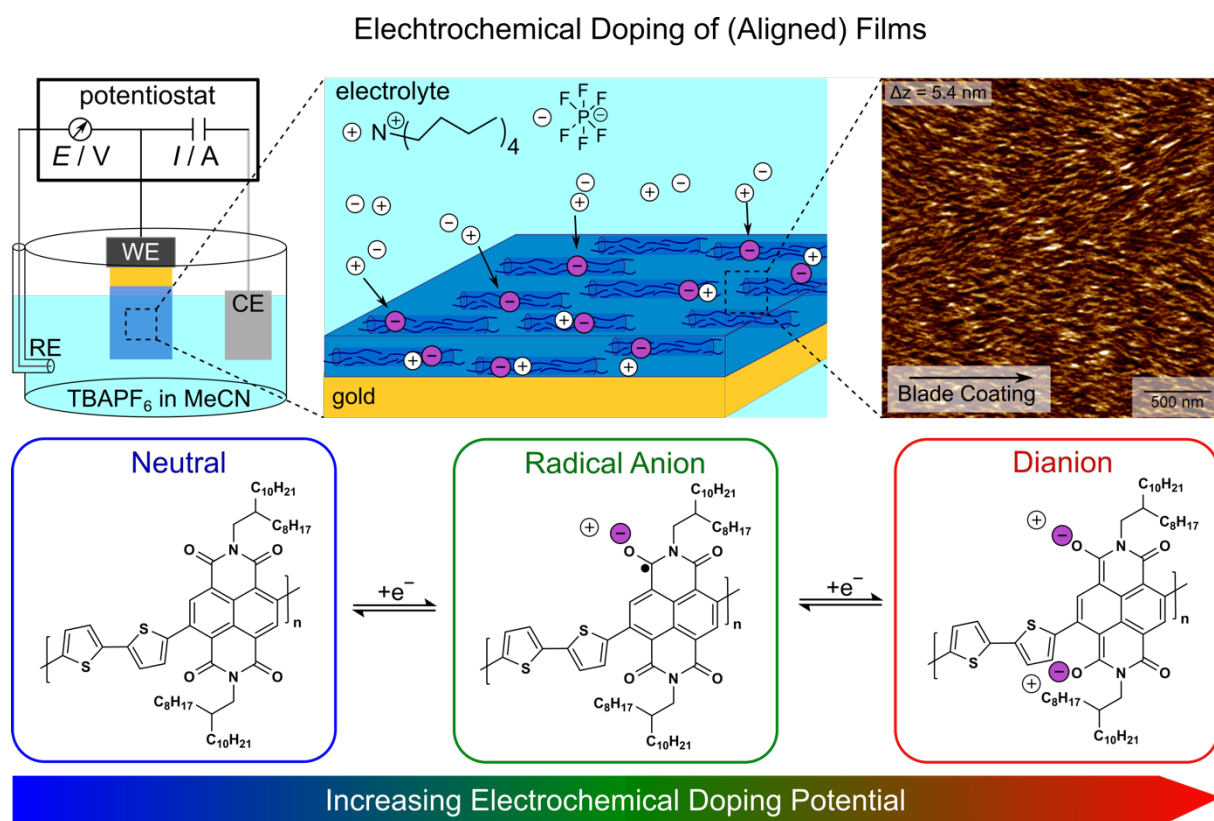


Figure 1: Schematic representation of our electrochemical bulk doping approach inside a three-electrode setup using 0.1 M TBAPF₆ in acetonitrile as electrolyte. Doped films are taken out of the setup under inert conditions and *ex situ* follow up experiments are conducted (conductivity measurements, UV-vis spectroscopy or GIWAXS). The blade coated films are anisotropic regarding the alignment of fibers which is verified by AFM. The bottom line presents the charged states of P(NDI2OD-T2) that can be exactly tuned and transferred into the solid-state.

When performing classical spectroelectrochemistry experiments, the occurrence of charged species of P(NDI2OD-T2) and the transfer from one into another species can be registered by UV-vis spectroscopy. Since this material allows for a two-step reduction on its NDI units, radical anions (one charge per repeating unit) and dianions (two charges per repeating unit) are created upon charging. This two-step process can be seen in the cyclic voltammogram (see Figure 2 a)) where two separated sets of redox waves are visible. An integration of the individual sets by Trefz et al.¹³ reveals the transferred charge and indicates a clear transition from neutral state into a dianion via a radical anion as intermediate state. This in-depth study of the CV of P(NDI2OD-T2) also highlights the influence of film morphology on shape and current ratio of the two peaks in the first reduction set of the CV. The characteristic spectral fingerprints of the charged species allow for a potential dependent identification of the creation of the individual charge carriers (see Figure 2 b)) during *in situ* absorption spectroscopy. The neutral state (blue spectra) has a high energy peak at 385 nm and a second peak at higher wavelengths at around 655 nm. When decreasing the electrochemical potential, a gradual change of the blue spectrum into the green spectrum is visible. The characteristic spectrum of the first reduced state (radical anion) shows absorption peaks at 370 nm, 490 nm, 700 nm and 800 nm. Especially the peak at 490 nm is distinct and correlates the presence of maximum radical anion species to an electrochemical potential of -1.34 V (vs.

Fc/Fc⁺). Further decreasing the potential below this value induces the transition into the second reduced state (dianion). This transition is accompanied by another significant change in the absorption spectrum with two new signals emerging at 392 nm and 704 nm (red spectrum). This charging behavior of P(NDI2OD-T2) is described in detail in literature of Trefz et al.¹³

Going beyond these fundamental studies, an advantage of our approach is to overcome the boundaries of the electrochemical cell, which means removing the doped samples from the electrolyte and transfer the induced charge carriers into the solid-state. The successful transfer, as shown in Figure 2 c) and d), is presented by results of the *ex situ* solid-state conductivity and spectroscopy experiments.

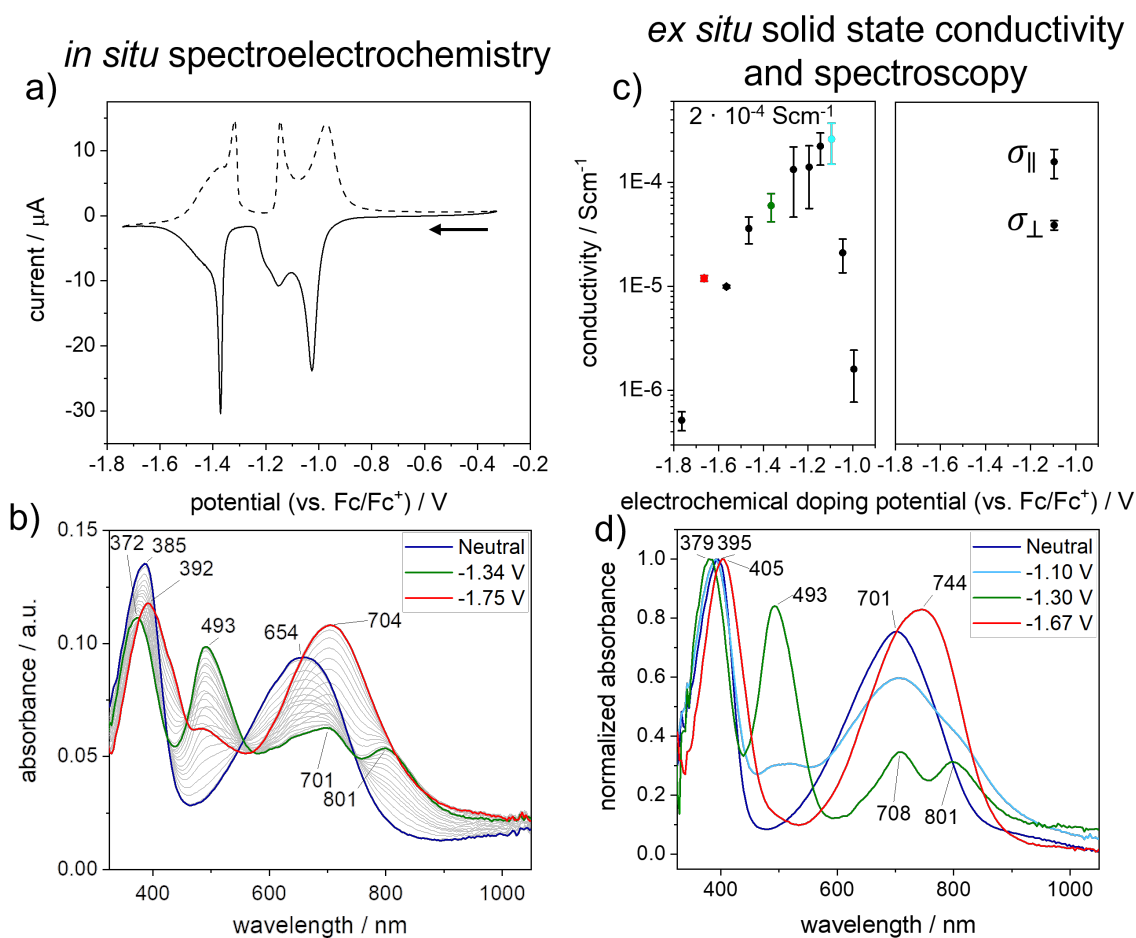


Figure 2: A cyclic voltammogram of a spin coated film of P(NDI2OD-T2) on a gold substrate is shown in a). *In situ* spectroelectrochemical measurement of a spin coated film of P(NDI2OD-T2) on an ITO substrate is given in b). Experiments are carried out on ITO substrates at a scan rate of 20 mVs^{-1} in $0.1 \text{ M TBAPF}_6/\text{acetonitrile}$ electrolyte. In c) the results of the *ex situ* measured conductivities of spin coated and blade coated films of P(NDI2OD-T2) at different electrochemical doping potentials in the solid-state are presented. Conductivities are measured on tailor-made gold electrodes in a four line probe geometry under inert conditions. Data points in c) are marked and corresponding UV-vis spectra are depicted in d) in the solid-state. UV-vis spectra are recorded of films spin coated and doped on ITO substrates under inert conditions.

Figure 2 c) shows the dependence of the solid-state conductivity on the potential applied during the electrochemical experiment. Due to the semiconducting nature of conjugated polymers, the neutral film (neutral state) has a very low conductivity that lies below the detection range of our experiment. By increasing the doping potential, the conductivity starts to rise until it develops a maximum at around -1.1 V (vs. Fc/Fc⁺) showing a conductivity of $2 \cdot 10^{-4} \text{ Scm}^{-1}$. A further increase of the doping potential

to more negative values leads to a gradual decrease of the conductivity with a low conductivity in the area of 10^{-6} Scm^{-1} at highest doping levels. Overall the conductivity behavior can be described as bell-shaped and therefore certainly differs from the plateau-like behavior, found for P3HT in previous works.^{23, 24} As mentioned previously P(NDI2OD-T2) can also be considered a molecular redox system where the charge transport mechanism is described in the mixed valence conductivity model.^{25, 26} Here, charge transport is governed by electron hopping between mixed charged redox sites. In the case of *in situ* experiments like *in situ* conductance this behavior has been proven for P(NDI2OD-T2) in literature.¹³ The bell-shaped behavior we found for the *ex situ* conductivity measurements can also be described when applying this model. A decrease in conductivity is explained by a saturation of redox sites with identical charge carriers (either radical anions or dianions). In our experiment the intermediate state with purely radical anion charge carriers cannot be resolved but the presence of more and more dianions at highest doping levels leads to a significant decrease of conductivity in our experiment.

To closer examine the present charge carriers in the solid-state, we conducted UV-vis spectroscopy measurements of our doped samples under inert conditions. Since we have detailed knowledge of the spectral fingerprints of the charged states from the *in situ* spectroelectrochemistry, an exact assignment of the bands in the solid-state was possible (see Figur 2 d)). The spectrum correlated to the highest conducting state (at -1.1 V, marked in light blue) shows absorption signals of both, the neutral and the radical anion state. The presence of mixed charged species at the highest conductivity fits into the context of the mixed valence conductivity model. The conductivity of this mixed state between neutral and radical cation is around one order of magnitude higher conducting than a purely radical anion state (at -1.35 V, marked in green). When charging to the purely dianion state (at -1.65 V, marked in red) a further decrease of the conductivity can be seen. The possibility to prepare a highly doped film in the dianion state demonstrates the variability of our approach. Regular chemical doping with N-DMBI or TDAE barely reaches the complete radical anion state as reported.²¹ For chemical doping the highest conductivities are found when neutral and radical anion species coexist in the doped films. Although our electrochemical doping approach allows for a reproducible conductivity tuning of 3-4 orders of magnitude, the reported chemical doping approach gives higher maximum conductivities of $7.7 \cdot 10^{-3} \text{ Scm}^{-1}$.²¹ Our maximum achievable conductivity with the electrochemical doping approach is around one order of magnitude lower at up to $2 \cdot 10^{-4} \text{ Scm}^{-1}$. A potential reason for the lower conductivity might arise from the technique itself, that involves taking the charged sample out of the electrolyte. A step that is highly susceptible to a loss of charge carriers and counterions. Although our spectroscopy implies that the charged state is being preserved to the largest extend, already a minor loss of charge carriers might lead to a significant lowering of the final conductivity in solid-state. In the end the final application must decide whether the focus is placed on maximum conductivity values or lower values that can be exactly tuned.

The doping experiments were also performed on aligned films prepared by blade coating. Following an approach established by Trefz, Gross et al.²⁰ highly concentrated solutions of P(NDI2OD-T2) are spread out across a substrate via blade coating. Here, it is assumed that aggregated chains in solution are being aligned by applying a certain directed shear force. Trefz et al. describe the aggregation in solution as liquid-crystalline mesophase which acts as starting point for oriented areas in the film. The alignment was checked by AFM (see Figure) at first, pointing out the surface alignment of fibers in the direction of blade coating. In a following step the bulk morphology of the neutral film is characterized (see Figure 3 a), neutral) using GIWAXS measurements. The neutral film shows distinct OOP lamellar peaks (h00) and an IP backbone (001) peak (black lines in b) and c) of Figure). These signals imply a majority edge-on configuration. The simultaneous presence of a lamellar (100) peak indicates a minority fraction that is oriented in face-on configuration. Additionally, the OOP lamellar peaks (h00) are visible up to the fifth order which is a result of the high degree of alignment in the blade coated films. It should be noted that a strong π - π stacking peak is absent which fits to findings in literature.^{27, 28} To probe the influence of the induced macroscopic alignment of the blade coated films on the conductivity behavior, four line gold electrodes (four parallel gold stripes separated by a defined channel distance) were coated in parallel and perpendicular direction relative to the channels. Since the measurement of conductivity (based on a classical four point probe measurement) suggests charge transport across the channels of the four line geometry, an alignment perpendicular to the channels results in a fiber orientation in the direction of the following conductivity measurement. By coating parallel to the channels, the fibers become oriented perpendicular to the direction of the conductivity measurement.

Maximum conductivities in the direction of alignment were similar to the spin coated samples with $\sigma_{\parallel} = 1.6 \pm 0.5 \cdot 10^{-4} \text{ Scm}^{-1}$ whereas the measurements perpendicular to the alignment showed significantly lower values of $\sigma_{\perp} = 3.9 \pm 0.4 \cdot 10^{-5} \text{ Scm}^{-1}$. The maximum conductivity values differ by a factor of 4.1 regarding the difference between parallel and perpendicular measurements. This shows the impressive influence of fiber alignment on the macroscopic conductivity also in the case of electrochemical doping. The reason why spin coated films perform equally good as aligned films in measurement direction certainly leaves room for interpretation. Spin coating distributes the material from the center of the substrate to the edges, producing films that typically show preferred alignment from the center of the substrate (radial). Due to the geometry of our samples and the position of the channels, this radial alignment is more similar to the parallel alignment by blade coating and therefore delivers values in the same range. In general, the anisotropy of conductivity in the electrochemically doped and aligned films, indicates that the morphology is being preserved during doping and the concomitant ion insertion. To examine the morphology changes during our *ex situ* electrochemical doping in a more precise way, we conducted *ex situ* GIWAXS measurements of our samples in different doped states (see Figure 3).

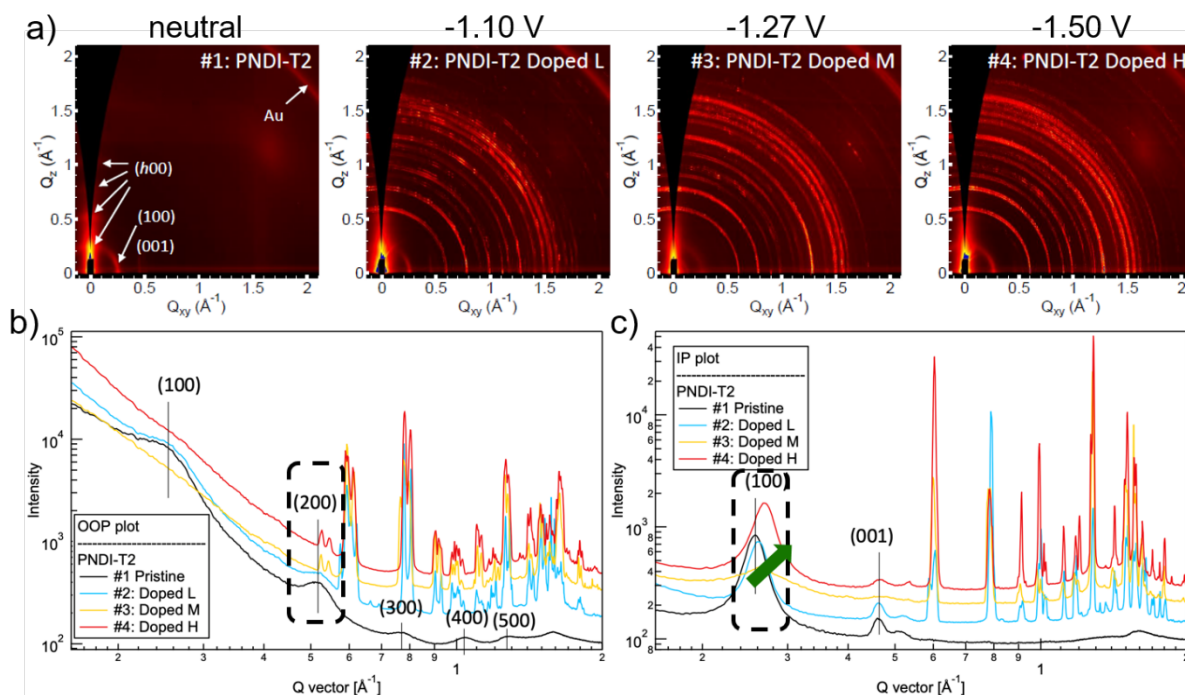


Figure 3: *Ex situ* measured GIWAXS data of aligned films of P(NDI2OD-T2) on gold substrates. Spectra are taken in neutral state and in three different doped states at different electrochemical doping potentials (referenced vs. Fc/Fc^+) in 0.1 M TBAPF₆/acetonitrile electrolyte. Samples are dried and transferred to the beam line under inert conditions. Line cuts IP and OOP are presented in b) and c). Doping states are listed as low (L, -1.10 V), medium (M, -1.27 V) and high (H, -1.50 V).

To assess the influence of electrochemical doping on the morphology of the aligned films, GIWAXS spectra are taken at a low (-1.10 V), medium (-1.27 V) and high doping level (-1.50 V, see Figure 3 a)). The doping potentials are chosen to correspond to three characteristic states (see Figure 2 d)). At the low doping potential, a mixture between neutral and radical anion is present which also depicts the highest conducting state in our experiment. The medium doped state corresponds to a mostly radical anion state and the highest doped state to a dianion state. Upon increasing the doping potential, additional sharp peaks appear which are most likely attributed to TBAPF₆ salt which remains in the film after electrochemical doping and leads to additional scattering signals which we suspect to increase with increasing doping level. In depth observation of the recorded spectra show that the OOP (h00) peaks are suppressed while the IP lamellar (100) peak remains stable. This indicates that the lamellar stacking order is affected stronger for the edge-on oriented chains, while the stacking remains stable for face-on oriented species. Reasons for a decrease in the overall order might be the intercalation of counterions from the electrolyte, which we suspect at increasing doping levels. When closely examining the IP (100) peak, a shift to higher q vectors can be noticed. This shift suggests a shorter lamellar stacking distance at high doping levels. This might sound counterintuitive since an uptake of ions that require a certain amount of space into the structure should lead to an increase in packing distance. In the case of chemical doping this behavior is reported in literature as well and in these cases explained by a change in backbone conformation.²¹

Concluding, these results offer an interesting approach to charge P(NDI2OD-T2) at distinct doping levels *in situ* and transfer the conducting films into the solid-state. The achieved conductivities can be tuned over 3-4 orders of magnitude helping to adjust the desired conductivity in spin coated films. Here, the highest conductivities are achieved at an intermediate doping level as it is predicted from the mixed valence conductivity model. Only the presence of mixed charged states allows for efficient charge transport in redox polymers like P(NDI2OD-T2). The strong tendency of this material to aggregate is used to produce highly aligned films by blade coating. Aligned films in the direction of charge transport show similar conductivity values as spin coated films being a factor of 4.1 higher than the conductivity of aligned films perpendicular to the direction of charge transport (anisotropic conductivity ratio). The question whether the aligned lamellar structure is still present after doping and ion introduction is being assessed by *ex situ* GIWAXS. These measurements suggest that ion integration decreases the overall order as expected, but the initially induced configuration (face-on or edge-on) can be found even after the doping process.

References

1. I. E. Jacobs and A. J. Moule, *Adv. Mater.*, 2017, **29**, 1703063.
2. B. Lüsse, M. Riede and K. Leo, *Phys. Status Solidi A*, 2013, **210**, 9-43.
3. K. A. Peterson, E. M. Thomas and M. L. Chabiny, *Annu. Rev. Mater. Res.*, 2020, **50**, 551-574.
4. J. Hynynen, D. Kiefer, L. Yu, R. Kroon, R. Munir, A. Amassian, M. Kemerink and C. Muller, *Macromolecules*, 2017, **50**, 8140-8148.
5. D. Kiefer, R. Kroon, A. I. Hofmann, H. Sun, X. Liu, A. Giovannitti, D. Stegerer, A. Cano, J. Hynynen, L. Yu, Y. Zhang, D. Nai, T. F. Harrelson, M. Sommer, A. J. Moule, M. Kemerink, S. R. Marder, I. McCulloch, M. Fahlman, S. Fabiano and C. Muller, *Nat Mater*, 2019, **18**, 149-155.
6. H. Yan, Z. Chen, Y. Zheng, C. Newman, J. R. Quinn, F. Dotz, M. Kastler and A. Facchetti, *Nature*, 2009, **457**, 679-686.
7. Y. M. Gross and S. Ludwigs, *Synth. Met.*, 2019, **253**, 73-87.
8. M. Caironi, M. Bird, D. Fazzi, Z. Chen, R. Di Pietro, C. Newman, A. Facchetti and H. Sirringhaus, *Adv. Funct. Mater.*, 2011, **21**, 3371-3381.
9. V. D'Innocenzo, A. Luzio, A. Petrozza, D. Fazzi and M. Caironi, *Adv. Funct. Mater.*, 2014, **24**, 5584-5593.
10. S. Wang, H. Sun, U. Ail, M. Vagin, P. O. Persson, J. W. Andreasen, W. Thiel, M. Berggren, X. Crispin, D. Fazzi and S. Fabiano, *Adv. Mater.*, 2016, **28**, 10764-10771.
11. M. Arvind, C. E. Tait, M. Guerrini, J. Krumland, A. M. Valencia, C. Cocchi, A. E. Mansour, N. Koch, S. Barlow, S. R. Marder, J. Behrends and D. Neher, *J. Phys. Chem. B*, 2020, **124**, 7694-7708.
12. C. E. Tait, A. Reckwitz, M. Arvind, D. Neher, R. Bittl and J. Behrends, *Phys. Chem. Chem. Phys.*, 2021, **23**, 13827-13841.
13. D. Trefz, A. Ruff, R. Tkachov, M. Wieland, M. Goll, A. Kiriya and S. Ludwigs, *J. Phys. Chem. C*, 2015, **119**, 22760-22771.
14. C. Malacrida, Y. Lu, K. Dirnberger, S. Gámez-Valenzuela, M. C. Ruiz Delgado and S. Ludwigs, *J. Mater. Chem. C*, 2020, **8**, 15393-15405.
15. M. Brinkmann, E. Gonthier, S. Bogen, K. Tremel, S. Ludwigs, M. Hufnagel and M. Sommer, *ACS Nano*, 2012, **6**, 10319-10326.
16. M. Li, H. Bin, X. Jiao, M. M. Wienk, H. Yan and R. A. J. Janssen, *Angew. Chem. Int. Ed. Engl.*, 2020, **59**, 846-852.
17. F. Panzer, H. Bassler and A. Kohler, *J. Phys. Chem. Lett.*, 2017, **8**, 114-125.
18. Y. Q. Zheng, Z. F. Yao, T. Lei, J. H. Dou, C. Y. Yang, L. Zou, X. Meng, W. Ma, J. Y. Wang and J. Pei, *Adv. Mater.*, 2017, **29**, 1701072.

19. M. M. Nahid, A. Welford, E. Gann, L. Thomsen, K. P. Sharma and C. R. McNeill, *Adv. Electron. Mater.*, 2018, **4**, 1700559.
20. D. Trefz, Y. M. Gross, C. Dingler, R. Tkachov, A. Hamidi-Sakr, A. Kiriy, C. R. McNeill, M. Brinkmann and S. Ludwigs, *Macromolecules*, 2018, **52**, 43-54.
21. Y. M. Gross, D. Trefz, C. Dingler, D. Bauer, V. Vijayakumar, V. Untilova, L. Biniek, M. Brinkmann and S. Ludwigs, *Chem. Mater.*, 2019, **31**, 3542-3555.
22. E. F. Aziz, A. Vollmer, S. Eisebitt, W. Eberhardt, P. Pingel, D. Neher and N. Koch, *Adv. Mater.*, 2007, **19**, 3257-3260.
23. D. Neusser, C. Malacrida, M. Kern, Y. M. Gross, J. van Slageren and S. Ludwigs, *Chem. Mater.*, 2020, **32**, 6003-6013.
24. L.-S. Hornberger, D. Neusser, C. Malacrida, L. G. Kaake and S. Ludwigs, *Appl. Phys. Lett.*, 2021, **119**, 163301.
25. D. Ofer, R. M. Crooks and M. S. Wrighton, *J. Am. Chem. Soc.*, 1990, **112**, 7869-7879.
26. A. Smie and J. Heinze, *Angew. Chem. Int. Ed.*, 1997, **36**, 363-367.
27. Y. M. Gross, D. Trefz, R. Tkachov, V. Untilova, M. Brinkmann, G. L. Schulz and S. Ludwigs, *Macromolecules*, 2017, **50**, 5353-5366.
28. K. Tremel, F. S. U. Fischer, N. Kayunkid, R. D. Pietro, R. Tkachov, A. Kiriy, D. Neher, S. Ludwigs and M. Brinkmann, *Adv. Energy Mater.*, 2014, **4**, 1301659.

5 Summary and Outlook

This thesis offers new insights and an in-depth understanding of electrochemical doping of semiconducting conjugated polymer films. To highlight the strength of this technique, a new approach has been developed that allows for transferring the doped films from the electrolyte into the solid-state where reliable conductivity values can be measured. The first publication starts with a systematic electrochemical *in situ* characterization of P3HT films and extends the gained knowledge to the *ex situ* doping approach leading to highly conducting P3HT films in the solid-state.

A combination of advanced electrochemical methods like spectroelectrochemistry and *in situ* conductance measurements give detailed information about occurring charged species and potential regions of high conductance. For P3HT films, the *in situ* spectroelectrochemical experiments identify three characteristic absorption spectra. By increasing the electrochemical potential, the spectrum of the neutral state (525 nm) shows decreasing intensity with a characteristic intermediate band rising at 805 nm. This marks the transition from the neutral state into polaronic charge carriers which starts at the onset of oxidation. A further increase of the potential gradually converts polarons into bipolarons, which is visible by a decrease of the polaron band at 805 nm and an increase at high wavelengths around 1600 nm. It is important to notice that the transitions between the individual charge carriers are gradual and suggest a presence of different charge carriers over the entire potential range. The *in situ* conductance experiment helps to connect the presence of different charge carriers to the point where the semiconducting material switches from a non-conducting ground state to a generally conducting state. In the case of P3HT, the conductance strongly increases when the onset of oxidation is reached and first polaronic charge carriers are being induced. At higher potentials a plateau of conductance forms, giving an overall sigmoidal shape of conductance as expected for conjugated polymers.^{15, 30} These results on the *in situ* study are the foundation for the following experiments for the *ex situ* electrochemical doping approach.

The *ex situ* experiments are performed on tailor-made four line gold electrodes that allow for both electrochemical doping in electrolyte and subsequent four line probe measurements in the solid-state to obtain reliable conductivity values. The *ex situ* electrochemical doping is performed by applying a distinct static doping potential followed by the extraction from the electrochemical cell under inert conditions. The dried doped film is then subjected to further experiments. Here, the critical question was if the doped films can be extracted from the electrochemical cell without a major loss of charge carriers which would severely harm the conductivity. UV-vis spectroscopy in solid-state after doping shows comparable results as the *in situ* spectroelectrochemistry and implies that the induced charge carriers are still present after transfer into the solid-state. Additionally, spin bearing polaronic charge carriers are detected by EPR spectroscopy after doping which supports the results from UV-vis spectroscopy.

Even at the highest doping levels, spins and therefore polarons were still present agreeing with our previous findings that mixed charge species (polarons and bipolarons) coexist over a wide potential range and are responsible for charge transport. Our highest conducting films reach conductivities up to 224 Scm^{-1} with charge carrier densities of 10^{21} holes per cm^3 . This equals to a maximum doping level of 40 % correlating to roughly two charges per five thiophene units. This fits to the image of mostly bipolarons at our highest doping level. Similar experiments performed with completely amorphous films of regiorandom P3HT give maximum conductivities of around 10 Scm^{-1} . This raises questions about the general impact of high crystallinity on the conductivity in conjugated polymer films. In our case we interpret this result as a demonstration of the importance of efficient aggregation and short-range interconnectivity as prerequisite of high conductivities. Here, additional experiments could clarify the image by examining highly crystalline P3HT films doped by an electrochemical doping approach. Different techniques could be applied to improve crystallinity like solvent vapor annealing or crystallization approaches in solution. Especially highly ordered structures like spherulites could act as interesting starting point for further experiments which focus more closely on the role of long-range order in the case of electrochemically doped P3HT films. Since the overall degree of order is strongly influenced by the molecular weight in these materials, a comparison regarding different molecular weights could be of interest as well.

To discuss the conductivity behavior in a wider context the results of P3HT are compared to the redox polymer PVPhCbz. Through electrochemical crosslinking of the carbazole side groups, connected bis(phenylcarbazole) moieties are formed, that act as highly localized redox centers in the following experiments. For this material a bell-shape conductivity profile can be obtained in the *in situ* conductance and *ex situ* doping approach. The existence of a local conductivity maximum and a decrease in conductivity at high doping levels is typically explained within the context of the mixed valence conductivity model.^{36,37} Here, an efficient hopping mechanism between the redox centers can only be guaranteed when mixed charged states with a maximum amount of isoenergetic states are present. With these results in mind, we interpret the results on P3HT as follows. The data shows a large plateau of high conductivity with a coexistence of mixed charge carriers over the entire potential range at the same time. Therefore, the plateau might be the consequence of many underlying conductivity maxima. The distribution of effective conjugation lengths in this polydisperse material can be seen as delocalized and extended redox systems with slightly different oxidation potentials resulting in a superposition of maxima and the formation of a plateau profile.

To extend the understanding of the electrochemical doping process in P3HT films, a second publication aims to understand the influence of the chosen salt in the electrolyte on the achievable solid-state conductivity. Therefore, the general performance of LiClO_4 , TBAPF_6 , LiTFSI and TBABF_4 salts in electrochemical experiments is being examined in sight of electrochemical reversibility and how charge trapping effects can impact the solid-state conductivity. Spectroelectrochemical studies imply entirely

reversible changes of the absorption spectra in the case of LiClO_4 and TBAPF_6 . For LiTFSI and TBABF_4 the documented absorption intensity significantly decreases upon cycling indicating much higher irreversibility for these two salts. The evaluation of the injected and released charges from the CV support this result and suggest a significant amount of trapped charges for LiTFSI and TBABF_4 . These trapped charges are known to appear naturally to a certain degree in charged organic semiconductors and are immobile ion/hole pairs that do not take part in any charge transport. This potentially harms the overall electronic conductivity. To extend the knowledge about the difference between the counterions regarding diffusion a set of scan rate dependent CV experiments is contained in this publication as well. Although all salts show general linear peak current sampling with increased scan rate, slight deviations are visible for LiTFSI and TBABF_4 , supporting the previously stated increased irreversibility of the electrochemical processes when using these salts. These insights are linked to the maximum achievable conductivity in the solid-state. Here, a similar trend can be found. Whereas LiClO_4 and TBAPF_6 give maximum conductivities around 200 Scm^{-1} , LiTFSI and TBABF_4 show values that are one order of magnitude lower. In general, a simple explanation purely based on ion size is not sufficient to explain our data but clearly, ion choice is a critical aspect. However, our results show an existing connection between the electrochemical reversibility and charge trapping phenomena both having a direct impact on the conductivity in the highly doped solid-state. Our main focus lies on the anion which we consider the important species due to its responsibility to compensate for created charges in the films. Follow up experiments could also focus on a potential role of the cation. Since a certain degree of passive swelling cannot be entirely ruled out and does also involve cations, there might be additional effects like cation expulsion during charging that are not considered in the present study. Another aspect that demands additional experiments and might help to explain the different degrees of charge trapping is the structural response of the P3HT films to different ions in the electrolyte upon charging. If certain ions induce a stronger or more disruptive restructuring during the electrochemical charging process, the resulting decrease in solid-state conductivity might also be a result of a more disrupted morphology. Here, techniques like GIWAXS can offer valuable information on the packing order and crystallinity before and after electrochemical cycling. Interesting experiments in this context have been presented by Sirringhaus et al.¹⁶⁰ A different aspect that can be considered for future studies is a transfer to water-based electrolytes. This might be generally interesting since it is the decisive step towards biological applications. It needs to be mentioned that the hydrophobicity of the P3HT film itself can depict a challenge for successful experiments and might only be overcome by the introduction of more hydrophilic side chains on the polymer backbone.^{152, 153}

The second part of this thesis is focused on electrochemical doping of current state-of-the-art materials in organic electronics and builds on the previously gained knowledge of the model system P3HT. The exact determination of the frontier orbital energies is a decisive parameter when it comes to designing new materials for successful applications. Here, the results from the electrochemical doping experiments

on P3HT films and the knowledge of the characteristic absorption bands upon charging is being used to locate and identify oxidation and reduction onsets. In this way, spectroelectrochemical experiments offer a powerful way of calculating HOMO and LUMO levels from the spectral onsets. An additional strength of this approach is the possibility to identify the absorption bands of individual compounds in a device relevant blend film. This is superior to neat material films for the determination of the energy levels since it places the experiment as close to the final device as possible. Following this approach, the energy levels of the conjugated polymer PM6 and the non-fullerene acceptor Y6 are in the focus of this publication. We discuss effects on the position of the energy levels arising from blending both materials and the impact of opposing blend morphologies which are a consequence of using different processing solvents (CF:CN and *o*-xylene). In the final device the blend morphology being face-on from CF:CN and edge-on from *o*-xylene (as examined by GIWAXS) proves to have a strong influence on the performance and reduces the V_{oc} from 0.83 V (face-on) to 0.77 V (edge-on). Interestingly, the calculated energy levels from our experiments are hardly different for the opposing morphologies giving HOMO/LUMO levels of -5.30 eV/-3.06 eV for PM6 and -5.63 eV/-3.90 eV for Y6 in blend films processed from CF:CN (face-on morphology in bulk). The results for the respective films from *o*-xylene (edge-on in bulk) show HOMO/LUMO levels of -5.31 eV/-3.07 eV for PM6 and -5.66 eV/-3.88 eV for Y6. From these frontier orbital energies the device relevant parameters HOMO offset and transport gap can be extracted. In this case the HOMO offset is 0.33 eV and the transport gap 1.4 eV for films from CF:CN and 0.35 eV and 1.43 eV for films from *o*-xylene, accordingly. The HOMO offsets can be confirmed from UPS measurements on blend films and yield 0.25 eV. Here, we like to point out that UPS measurements on neat films of PM6 and Y6 lead to HOMO offsets above 0.7 eV when the energy levels are calculated individually.¹⁶¹ We suggest electrostatic effects on the film surface, arising from introducing the second component in the blend films, to be one of the possible sources for the differing values. Once again this underlines the importance of measuring energy levels from blend films to generate exact results. To complete the image of device performance parameters besides the HOMO offsets and transport gaps are needed. Therefore, a singlet energy of Y6 in the blend can be calculated from the intersection of absorption and photoluminescence and yields 1.42 ± 0.02 eV. Subtracting this value from the bandgap of 1.73 eV from CF:CN and 1.78 eV from *o*-xylene results in the exciton binding energy of 0.33 ± 0.05 eV. Interestingly, the calculated exciton binding energy is in the same range as the HOMO offset in the blend film, strongly questioning the high efficiency of the blend, as it suggests nearly zero driving force for the generation of free charge carriers (exciton dissociation), as also observed by Wu et al.¹⁶²

A possible approach to nevertheless provide valuable explanations for the efficiency of the charge generation inside the blends, is to take the presence of sub-bandgap states into account.¹⁶³⁻¹⁶⁵ These sub-bandgap states are usually not detectable by our spectroscopy but can offer possible energies considerably below the energy of the singlet exciton of Y6 to locate the generated free electron hole

pair. This section is finalized by discussing reasons that cause the difference in V_{OC} between the two devices prepared from CF:CN (0.83 V) and o-xylene (0.77 V). We therefore focus on the main parameters defining the V_{OC} of the device, which is the radiative voltage limit and the non-radiative voltage loss ($V_{OC} = V_{OC}^{rad} - \Delta V_{OC}^{nr,rad}$). Whereas the radiative voltage limit shows no considerable variation between both blends due to its definition from the Y6 singlet exciton, differences can arise from non-radiative loss. The strongest contribution on the non-radiative loss is being delivered from vibronic couplings of the charge transfer state back into the ground state.^{166, 167} These couplings can be affected by molecular orientations in the blend and hence can differ for different blend morphologies.^{168, 169} Especially in light of the first two publications, a complete conductivity study with PM6 in future works would be very interesting and could give information about how the structural modifications coming from the model system P3HT to the advanced donor-acceptor structure of PM6 influences the performance regarding the solid-state conductivity.

The final part of this work aims at transferring the gained expertise on electrochemical doping of p-type organic semiconductors to n-type materials like the benchmark conjugated polymer P(NDI2OD-T2) (N2200) presented here. Electrochemical charging *in situ* and the following transfer into the solid-state shows the possibility to tune the doping level and the resulting solid-state conductivity over a region of 3-4 orders of magnitude. Maximum achievable conductivities in our experiments prove to situate in the area of $2 \cdot 10^{-4} \text{ Scm}^{-1}$. Compared to classical chemical doping the measured conductivities fall about one order of magnitude short but offer the inherent advantage of an easier way of adjusting the doping level and therefore the final conductivity value. In terms of doping level, an analysis of charge carriers by absorption spectroscopy in the solid-state shows that our electrochemical doping approach can produce highest doping levels with dianion charge carriers present in the solid-state as the predominant charge carrier. Alternative doping approaches based on prominent redox dopants like N-DMBI or TDAE can hardly induce bipolaronic charge carriers in films of P(NDI2OD-T2).⁹⁵ The final reason for the gap in conductivity between our electrochemical doping technique remains subject of future studies. Experiments using different electrolytes with different counterions could act as starting point to find a potentially more suitable electrolyte system for P(NDI2OD-T2). Maybe the reason for lower conductivity values remains the loss of charge during the extraction from the electrolyte. Here an alternative counterion could improve the stability of the charged species and reduce charge loss.

The mixed valence conductivity model, which was already established to explain previously published experiments like *in situ* conductance measurements, can also help to interpret the results of our *ex situ* conductivity profile appearing in a bell shape. Only redox states with mixed charge carriers offer high conductivities and good charge transport properties, due to the possibility for efficient hopping transport between the localized redox sites. The doping state with the highest conductivity in our experiments gives absorption spectra of the neutral and the radical anion state, fitting into the image of the mixed valence conductivity model with a decrease of conductivity towards purely bipolaronic doping states at

the highest doping levels. Further experiments on aligned films of P(NDI2OD-T2) are subject to understand relationships between morphology and charge transport properties. As results show, the impact of the direction of aligned fibers of P(NDI2OD-T2) in relation to the direction of charge transport is indeed significant. Conductivities alongside and perpendicular to the direction of charge transport prove to be $\sigma_{\parallel} = 1.6 \pm 0.5 \cdot 10^{-4} \text{ Scm}^{-1}$ and $\sigma_{\perp} = 3.9 \pm 0.4 \cdot 10^{-5} \text{ Scm}^{-1}$, differing by a factor of 4.1. Due to the highly defined morphology of our aligned films, they present an ideal platform to investigate the influence of electrochemical doping on thin film morphology. Therefore, we performed *ex situ* GIWAXS measurements in different doped states to examine different degrees of ion integration and the films structural response. First of all, edge-on and face-on oriented chains seem to be differently impacted regarding the order of lamellar stacking (stronger impact on edge-on chains). The general loss of order that becomes stronger upon increasing the doping level can be definitely interpreted as a consequence of ion intercalation which also intensifies when more charge carriers are being induced at high doping levels. In case of the IP (100) peak a counterintuitive shift to shorter stacking distance is observed for high doping levels although the integration of counterions would require space in between chains. Nevertheless, this effect has been observed in literature for chemical doping approaches before and is being explained by a change in backbone conformation.⁹⁵ Generally spoken, the ion intercalation upon electrochemical doping induces a decrease of overall order while maintaining the majority of the previously triggered order (face-on or edge-on). This measuring technique could also help to understand if different counterions from the electrolyte lead to a different morphological response upon electrochemical doping.

6 References

1. R. Pfaendner, *Polym. Degrad. Stab.*, 2006, **91**, 2249-2256.
2. S. C. Rasmussen, *Angew. Chem. Int. Ed. Engl.*, 2021, **60**, 8012-8016.
3. W. S. Wong and A. Salleo, eds., *Flexible Electronics: Materials and Applications*, Springer, 2009.
4. H. Ling, S. Liu, Z. Zheng and F. Yan, *Small Methods*, 2018, **2**, 1800070.
5. The Nobel Prize in Chemistry, 2000: Conductive polymers, nobelprize.org/uploads/2018/06/advanced-chemistryprize2000-1.pdf, (accessed 01.03.2022).
6. A. J. Heeger, *Angew. Chem.*, 2001, **113**, 2660-2682.
7. C. K. Chiang, M. A. Druy, S. C. Gao, A. J. Heeger, E. J. Louis, A. G. MacDiarmid, Y. W. Park and H. Shirakawa, *J. Am. Chem. Soc.*, 1978, **78**, 1013-1015.
8. C. K. Chiang, C. R. Fincher, Y. W. Park, A. J. Heeger, H. Shirakawa, E. J. Louis, S. C. Gau and A. G. MacDiarmid, *Phys. Rev. Lett.*, 1977, **39**, 1098-1101.
9. H. Shirakawa, E. J. Louis, A. G. MacDiarmid, C. K. Chiang and A. J. Heeger, *J. C. S. Chem. Comm.*, 1977, **474**, 578-580.
10. M. Rehahn, *Chem. Unserer Zeit*, 2003, **37**, 18-30.
11. A. J. Heeger, *Chem. Soc. Rev.*, 2010, **39**, 2354-2371.
12. J. L. Brédas, B. Thémans, J. G. Fripiat, J. M. André and R. R. Chance, *Phys. Rev. B.*, 1984, **29**, 6761-6773.
13. J. L. Bredas and G. B. Street, *Acc. Chem. Res.*, 1985, **18**, 309-315.
14. B. Lüssem, M. Riede and K. Leo, *Phys. Status Solidi A*, 2013, **210**, 9-43.
15. J. Heinze, B. A. Frontana-Urbe and S. Ludwigs, *Chem. Rev.*, 2010, **110**, 4724-4771.
16. R. R. Chance, J. L. Brédas and R. Silbey, *Phys. Rev. B.*, 1984, **29**, 4491-4495.
17. R. R. Chance, D. S. Boudreaux and J. L. Bredas, in *Handbook of Conducting Polymers*, ed. T. A. Skotheim, Marcel Dekker, New York, 1986.
18. G. Inzelt, *Monographs in Electrochemistry*, Springer, Berlin Heidelberg, 2008.
19. R. Gracia and D. Mecerreyes, *Polym. Chem.*, 2013, **4**, 2206.
20. T. M. Swager, *Macromolecules*, 2017, **50**, 4867-4886.
21. O. Yurchenko, J. Heinze and S. Ludwigs, *Chemphyschem*, 2010, **11**, 1637-1640.
22. O. Yurchenko, D. Freytag, L. zur Borg, R. Zentel, J. Heinze and S. Ludwigs, *J. Phys. Chem. B*, 2012, **116**, 30-39.
23. C. Malacrida, Y. Lu, K. Dirnberger, S. Gámez-Valenzuela, M. C. Ruiz Delgado and S. Ludwigs, *J. Mater. Chem. C*, 2020, **8**, 15393-15405.

24. D. Neusser, C. Malacrida, M. Kern, Y. M. Gross, J. van Slageren and S. Ludwigs, *Chem. Mater.*, 2020, **32**, 6003-6013.
25. K. Nakahara, K. Oyaizu and H. Nishide, *Chem. Lett.*, 2011, **40**, 222-227.
26. M. Suguro, S. Iwasa, Y. Kusachi, Y. Morioka and K. Nakahara, *Macromol. Rapid Commun.*, 2007, **28**, 1929-1933.
27. Z. Chen, Y. Zheng, H. Yan and A. Facchetti, *J. Am. Chem. Soc.*, 2009, **131**, 8-9.
28. V. D'Innocenzo, A. Luzio, A. Petrozza, D. Fazzi and M. Caironi, *Adv. Funct. Mater.*, 2014, **24**, 5584-5593.
29. S. Wang, H. Sun, U. Ail, M. Vagin, P. O. Persson, J. W. Andreasen, W. Thiel, M. Berggren, X. Crispin, D. Fazzi and S. Fabiano, *Adv. Mater.*, 2016, **28**, 10764-10771.
30. G. Salinas and B. A. Frontana-Uribe, *ChemElectroChem*, 2019, **6**, 4105-4117.
31. G. Schiavon, S. Sitran and G. Zotti, *Synth. Met.*, 1989, **32**, 209-217.
32. H. S. White, G. P. Kittlesen and M. S. Wrighton, *J. Am. Chem. Soc.*, 1984, **106**, 5375-5377.
33. E. F. Dalton, N. A. SurrIDGE, J. C. Jernigan, K. O. Wilbourn, J. S. Facci and W. Murray, *Chem. Phys.*, 1990, **141**, 143-157.
34. D. Lee and T. M. Swager, *J. Am. Chem. Soc.*, 2003, **125**, 6870-6871.
35. H. John, R. Bauer, P. Espindola, P. Sonar, J. Heinze and K. Mullen, *Angew. Chem. Int. Ed.*, 2005, **44**, 2447-2451.
36. D. Ofer, R. M. Crooks and M. S. Wrighton, *J. Am. Chem. Soc.*, 1990, **112**, 7869-7879.
37. A. Smie and J. Heinze, *Angew. Chem. Int. Ed.*, 1997, **36**, 363-367.
38. I. E. Jacobs and A. J. Moule, *Adv. Mater.*, 2017, **29**, 1703063.
39. B. Lussem, C. M. Keum, D. Kasemann, B. Naab, Z. Bao and K. Leo, *Chem. Rev.*, 2016, **116**, 13714-13751.
40. X. Crispin, F. L. E. Jakobsson, A. Crispin, P. C. M. Grim, P. Andersson, A. Volodin, C. van Haesendonck, M. Van der Auweraer, W. R. Salaneck and M. Berggren, *Chem. Mater.*, 2006, **18**, 4354-4360.
41. M. Modarresi, J. F. Franco-Gonzalez and I. Zozoulenko, *Phys. Chem. Chem. Phys.*, 2019, **21**, 6699-6711.
42. R. Noriega, J. Rivnay, K. Vandewal, F. P. Koch, N. Stingelin, P. Smith, M. F. Toney and A. Salleo, *Nat. Mater.*, 2013, **12**, 1038-1044.
43. E. F. Aziz, A. Vollmer, S. Eisebitt, W. Eberhardt, P. Pingel, D. Neher and N. Koch, *Adv. Mater.*, 2007, **19**, 3257-3260.
44. J. Hynynen, D. Kiefer, L. Yu, R. Kroon, R. Munir, A. Amassian, M. Kemerink and C. Muller, *Macromolecules*, 2017, **50**, 8140-8148.
45. D. Kiefer, R. Kroon, A. I. Hofmann, H. Sun, X. Liu, A. Giovannitti, D. Stegerer, A. Cano, J. Hynynen, L. Yu, Y. Zhang, D. Nai, T. F. Harrelson, M. Sommer, A. J. Moule, M. Kemerink, S.

- R. Marder, I. McCulloch, M. Fahlman, S. Fabiano and C. Muller, *Nat. Mater.*, 2019, **18**, 149-155.
46. J. Yamamoto and Y. Furukawa, *J. Phys. Chem. B*, 2015, **119**, 4788-4794.
47. M. T. Fontana, D. A. Stanfield, D. T. Scholes, K. J. Winchell, S. H. Tolbert and B. J. Schwartz, *J. Phys. Chem. C*, 2019, **123**, 22711-22724.
48. I. E. Jacobs, E. W. Aasen, J. L. Oliveira, T. N. Fonseca, J. D. Roehling, J. Li, G. Zhang, M. P. Augustine, M. Mascal and A. J. Moulé, *J. Mater. Chem. C*, 2016, **4**, 3454-3466.
49. J. D. Yuen, A. S. Dhoot, E. B. Namdas, N. E. Coates, M. Heeney, I. McCulloch, D. Moses and A. J. Heeger, *J. Am. Chem. Soc.*, 2007, **129**, 14367-14371.
50. D. Rawlings, E. M. Thomas, R. A. Segalman and M. L. Chabinye, *Chem. Mater.*, 2019, **31**, 8820-8829.
51. G. Tourillon and F. Garnier, *J. Electrochem. Soc.*, 1983, **130**, 2042-2044.
52. S. Ludwigs, ed., *P3HT Revisited - From Molecular Scale to Solar Cell Devices*, Springer, Berlin, Heidelberg, 2014.
53. R. D. McCulloch, *Adv. Mater.*, 1998, **10**, 93-116.
54. R. D. McCulloch and R. D. Lowe, *J. Chem. Soc. Chem. Commun.*, 1992, **1**, 70-72.
55. R. S. Loewe, S. M. Khersonsky and R. D. McCulloch, *Adv. Mater.*, 1999, **11**, 250-253.
56. M. C. Iovu, E. E. Sheina, R. R. Gil and R. D. McCulloch, *Macromolecules*, 2005, **38**, 8649-8656.
57. K. Müllen and G. Wegner, eds., *Electronic Materials: The Oligomer Approach*, Wiley-VCH, Weinheim, 1998.
58. A. F. Diaz, J. I. Castillo, J. A. Logan and W. Lee, *J. Electroanal. Chem.*, 1981, **129**, 115-132.
59. E. M. Genies, G. Bidan and A. F. Diaz, *J. Electroanal. Chem.*, 1983, **149**, 101-113.
60. C. K. Baker and J. R. Reynolds, *J. Electroanal. Chem.*, 1988, **251**, 307-322.
61. R. John and G. G. Wallace, *J. Electroanal. Chem.*, 1991, **306**, 157-167.
62. P. Audebert and P. Hapiot, *Synth. Met.*, 1995, **75**, 95-102.
63. L. Guyard, P. Hapiot and P. Neta, *J. Phys. Chem. B*, 1997, **101**, 5698-5706.
64. J. Heinze, C. Willmann and P. Bäuerle, *Angew. Chem. Int. Ed.*, 2001, **40**, 2861-2864.
65. P. Hapiot, D. Lorcy, A. Tallec, R. Carlier and A. Robert, *J. Phys. Chem.*, 1996, **100**, 14823-14827.
66. R. Kline, M. McGehee, E. Kadnikova, J. Liu, J. Fréchet and M. F. Toney, *Macromolecules*, 2005, **38**, 3312-3319.
67. J.-M. Verilhac, G. LeBlevenec, D. Djurado, F. Rieutord, M. Chouiki, J.-P. Travers and A. Pron, *Synth. Met.*, 2006, **156**, 815-823.
68. R. Zhang, B. Li, M. C. Iovu, M. Jeffries-EL, G. Sauvé, J. Cooper, S. Jia, S. Tristram-Nagle, D. Smilgies, D. Lambeth, R. D. McCulloch and T. Kowalewski, *J. Am. Chem. Soc.*, 2006, **128**, 3480-3481.

References

69. E. J. Crossland, K. Tremel, F. Fischer, K. Rahimi, G. Reiter, U. Steiner and S. Ludwigs, *Adv. Mater.*, 2012, **24**, 839-844.
70. E. J. W. Crossland, K. Rahimi, G. Reiter, U. Steiner and S. Ludwigs, *Adv. Funct. Mater.*, 2011, **21**, 518-524.
71. A. Zen, J. Pflaum, S. Hirschmann, W. Zhuang, F. Jaiser, U. Asawapirom, J. P. Rabe, U. Scherf and D. Neher, *Adv. Funct. Mater.*, 2004, **14**, 757-764.
72. B. Xu and S. Holdcroft, *Macromolecules*, 1993, **26**, 4457-4460.
73. T.-A. Chen, X. Wu and D. Rieke, *J. Am. Chem. Soc.*, 1995, **117**, 233-244.
74. P. J. Brown, D. S. Thomas, A. Köhler, J. S. Wilson, J.-S. Kim, C. M. Ramsdale, H. Sirringhaus and R. H. Friend, *Phys. Rev. B.*, 2003, **67**, 064203.
75. S. Wang, S. Fabiano, S. Himmelberger, S. Puzinas, X. Crispin, A. Salleo and M. Berggren, *Proc. Natl. Acad. Sci. USA*, 2015, **112**, 10599-10604.
76. K. Bruchlos, D. Trefz, A. Hamidi-Sakr, M. Brinkmann, J. Heinze, A. Ruff and S. Ludwigs, *Electrochim. Acta*, 2018, **269**, 299-311.
77. X. Jiang, Y. Harima, K. Yamashita, Y. Tada, J. Ohshita and A. Kunai, *Chem. Phys. Lett.*, 2002, **364**, 616-620.
78. M. Trznadel, A. Pron, M. Zagorska, R. Chrzaszcz and J. Pielichowski, *Macromolecules*, 1998, **31**, 5051-5058.
79. M. Trznadel, O. Chauvet, M. Lapkowski and A. Pron, *Synth. Met.*, 1999, **101**, 358.
80. M. Skompska and A. Szkurlat, *Electrochim. Acta*, 2001, **46**, 4007-4015.
81. M. Skompska, A. Szkurlat, A. Kowal and M. Szklarczyk, *Langmuir*, 2003, **19**, 2318-2324.
82. S. Thankaraj Salammal, S. Dai, U. Pietsch, S. Grigorian, N. Koenen, U. Scherf, N. Kayunkid and M. Brinkmann, *Eur. Polym. J.*, 2015, **67**, 199-212.
83. J. Clark, C. Silva, R. H. Friend and F. C. Spano, *Phys. Rev. Lett.*, 2007, **98**, 206406.
84. M. Chang, J. Lee, N. Kleinhenz, B. Fu and E. Reichmanis, *Adv. Funct. Mater.*, 2014, **24**, 4457-4465.
85. C. Enengl, S. Enengl, S. Pluczyk, M. Havlicek, M. Lapkowski, H. Neugebauer and E. Ehrenfreund, *Chemphyschem*, 2016, **17**, 3836-3844.
86. M. Arvind, C. E. Tait, M. Guerrini, J. Krumland, A. M. Valencia, C. Cocchi, A. E. Mansour, N. Koch, S. Barlow, S. R. Marder, J. Behrends and D. Neher, *J. Phys. Chem. B*, 2020, **124**, 7694-7708.
87. C. E. Tait, A. Reckwitz, M. Arvind, D. Neher, R. Bittl and J. Behrends, *Phys. Chem. Chem. Phys.*, 2021, **23**, 13827-13841.
88. M. Kern, L. Tesi, D. Neusser, N. Rußegger, M. Winkler, A. Allgaier, Y. M. Gross, S. Bechler, H. S. Funk, L. T. Chang, J. Schulze, S. Ludwigs and J. van Slageren, *Adv. Funct. Mater.*, 2020, **31**, 2006882.
89. M. Zhang, X. Guo, W. Ma, H. Ade and J. Hou, *Adv. Mater.*, 2015, **27**, 4655-4660.

90. H. Yan, Z. Chen, Y. Zheng, C. Newman, J. R. Quinn, F. Dotz, M. Kastler and A. Facchetti, *Nature*, 2009, **457**, 679-686.
91. D. Qian, L. Ye, M. Zhang, Y. Liang, L. Li, Y. Huang, X. Guo, S. Zhang, Z. a. Tan and J. Hou, *Macromolecules*, 2012, **45**, 9611-9617.
92. J. Yuan, Y. Zhang, L. Zhou, G. Zhang, H.-L. Yip, T.-K. Lau, X. Lu, C. Zhu, H. Peng, P. A. Johnson, M. Leclerc, Y. Cao, J. Ulanski, Y. Li and Y. Zou, *Joule*, 2019, **3**, 1140-1151.
93. L. Gao, Z. G. Zhang, L. Xue, J. Min, J. Zhang, Z. Wei and Y. Li, *Adv. Mater.*, 2016, **28**, 1884-1890.
94. D. Trefz, Y. M. Gross, C. Dingler, R. Tkachov, A. Hamidi-Sakr, A. Kiriy, C. R. McNeill, M. Brinkmann and S. Ludwigs, *Macromolecules*, 2018, **52**, 43-54.
95. Y. M. Gross, D. Trefz, C. Dingler, D. Bauer, V. Vijayakumar, V. Untilova, L. Biniek, M. Brinkmann and S. Ludwigs, *Chem. Mater.*, 2019, **31**, 3542-3555.
96. Fraunhofer ISE, *Photovoltaics Report*, 2022.
97. <https://www.nrel.gov/pv/cell-efficiency.html>, (accessed 03.05.2022).
98. B. Kippelen and J.-L. Brédas, *Energy Environ. Sci.*, 2009, **2**, 251.
99. K. A. Mazzio and C. K. Luscombe, *Chem. Soc. Rev.*, 2015, **44**, 78-90.
100. O. Doat, B. H. Barboza, A. Batagin-Neto, D. Bégué and R. C. Hiorns, *Polym. Int.*, 2021, **71**, 6-25.
101. O. V. Mikhnenko, H. Azimi, M. Scharber, M. Morana, P. W. M. Blom and M. A. Loi, *Energy Environ. Sci.*, 2012, **5**, 6960.
102. P. E. Shaw, A. Ruseckas and I. D. W. Samuel, *Adv. Mater.*, 2008, **20**, 3516-3520.
103. A. J. Heeger, *Adv. Mater.*, 2014, **26**, 10-27.
104. M. Hiramoto, H. Fujiwara and M. Yokoyama, *Appl. Phys. Lett.*, 1991, **58**, 1062-1064.
105. J. J. M. Halls, C. A. Walsh, N. C. Greenham, E. A. Marseglia, R. H. Friend, S. C. Moratti and A. B. Holmes, *Nature*, 1995, **376**, 498-500.
106. G. Yu, J. Gao, J. C. Hummelen, F. Wudl and A. J. Heeger, *Science*, 1995, **270**, 1789-1791.
107. Y. Huang, E. J. Kramer, A. J. Heeger and G. C. Bazan, *Chem. Rev.*, 2014, **114**, 7006-7043.
108. A. Mishra and P. Bauerle, *Angew. Chem. Int. Ed.*, 2012, **51**, 2020-2067.
109. R. C. Hiorns, R. de Bettignies, J. Leroy, S. Bailly, M. Firon, C. Sentein, A. Khoukh, H. Preud'homme and C. Dagron-Lartigau, *Adv. Funct. Mater.*, 2006, **16**, 2263-2273.
110. M. T. Dang, L. Hirsch and G. Wantz, *Adv. Mater.*, 2011, **23**, 3597-3602.
111. Y. Kim, S. A. Choulis, J. Nelson, D. D. C. Bradley, S. Cook and J. R. Durrant, *Appl. Phys. Lett.*, 2005, **86**, 063502.
112. J. Peet, J. Y. Kim, N. E. Coates, W. L. Ma, D. Moses, A. J. Heeger and G. C. Bazan, *Nat. Mater.*, 2007, **6**, 497-500.

References

113. F. S. U. Fischer, K. Tremel, A. K. Saur, S. Link, N. Kayunkid, M. Brinkmann, D. Herrero-Carvajal, J. T. L. Navarrete, M. C. R. Delgado and S. Ludwigs, *Macromolecules*, 2013, **46**, 4924-4931.
114. M. C. Scharber, M. Koppe, J. Gao, F. Cordella, M. A. Loi, P. Denk, M. Morana, H. J. Egelhaaf, K. Forberich, G. Dennler, R. Gaudiana, D. Waller, Z. Zhu, X. Shi and C. J. Brabec, *Adv. Mater.*, 2010, **22**, 367-370.
115. S. Albrecht, K. Vandewal, J. R. Tumbleston, F. S. Fischer, J. D. Douglas, J. M. Frechet, S. Ludwigs, H. Ade, A. Salleo and D. Neher, *Adv. Mater.*, 2014, **26**, 2533-2539.
116. Q. Fan, T. Liu, W. Gao, Y. Xiao, J. Wu, W. Su, X. Guo, X. Lu, C. Yang, H. Yan, M. Zhang and Y. Li, *J. Mater. Chem. A*, 2019, **7**, 15404-15410.
117. X. Xu, L. Yu, H. Yan, R. Li and Q. Peng, *Energy Environ. Sci.*, 2020, **13**, 4381-4388.
118. J. Wu, G. Li, J. Fang, X. Guo, L. Zhu, B. Guo, Y. Wang, G. Zhang, L. Arunagiri, F. Liu, H. Yan, M. Zhang and Y. Li, *Nat. Commun.*, 2020, **11**, 4612.
119. X. Wang, Q. Sun, J. Gao, X. Ma, J. H. Son, S. Y. Jeong, Z. Hu, L. Niu, H. Y. Woo, J. Zhang and F. Zhang, *Sol. RRL*, 2021, **5**, 2100007.
120. M. Zhang, L. Zhu, G. Zhou, T. Hao, C. Qiu, Z. Zhao, Q. Hu, B. W. Larson, H. Zhu, Z. Ma, Z. Tang, W. Feng, Y. Zhang, T. P. Russell and F. Liu, *Nat. Commun.*, 2021, **12**, 309.
121. Y. Zhang, K. Liu, J. Huang, X. Xia, J. Cao, G. Zhao, P. W. K. Fong, Y. Zhu, F. Yan, Y. Yang, X. Lu and G. Li, *Nat. Commun.*, 2021, **12**, 4815.
122. W. Peng, Y. Lin, S. Y. Jeong, Z. Genene, A. Magomedov, H. Y. Woo, C. Chen, W. Wahyudi, Q. Tao, J. Deng, Y. Han, V. Getautis, W. Zhu, T. D. Anthopoulos and E. Wang, *Nano Energy*, 2022, **92**, 106681.
123. J. Roncali, P. Leriche and P. Blanchard, *Adv. Mater.*, 2014, **26**, 3821-3838.
124. S. Roquet, A. Cravino, P. Leriche, O. Alévêque, P. Frère and J. Roncali, *J. Am. Chem. Soc.*, 2006, **128**, 3459-3466.
125. Y. Shirota, *J. Mater. Chem.*, 2005, **15**, 75-93.
126. G. Horowitz, D. Fichou, P. Xuezhou, X. Zhigang and F. Garnier, *Solid State Commun.*, 1989, **72**, 381-384.
127. J. Sakai, T. Taima and K. Saito, *Org. Electron.*, 2008, **9**, 582-590.
128. T. Taima, M. Shahiduzzaman, T. Ishizeki, K. Yamamoto, M. Karakawa, T. Kuwabara and K. Takahashi, *J. Phys. Chem. C*, 2017, **121**, 19699-19704.
129. J. C. Hummelen, B. W. Knight, F. LePeq and F. Wudl, *J. Org. Chem.*, 1995, **60**, 532-538.
130. P. H. Wöbkenberg, D. D. C. Bradley, D. Kronholm, J. C. Hummelen, D. M. de Leeuw, M. Cölle and T. D. Anthopoulos, *Synth. Met.*, 2008, **158**, 468-472.
131. A. Distler, T. Sauermann, H.-J. Egelhaaf, S. Rodman, D. Waller, K.-S. Cheon, M. Lee and D. M. Guldi, *Adv. Energy Mater.*, 2014, **4**, 1300693.
132. Y. M. Gross and S. Ludwigs, *Synth. Met.*, 2019, **253**, 73-87.

References

133. A. Wadsworth, M. Moser, A. Marks, M. S. Little, N. Gasparini, C. J. Brabec, D. Baran and I. McCulloch, *Chem. Soc. Rev.*, 2019, **48**, 1596-1625.
134. C. Yan, S. Barlow, Z. Wang, H. Yan, A. K. Y. Jen, S. R. Marder and X. Zhan, *Nat. Rev. Mater.*, 2018, **3**, 18003.
135. L. Zhu, M. Zhang, W. Zhong, S. Leng, G. Zhou, Y. Zou, X. Su, H. Ding, P. Gu, F. Liu and Y. Zhang, *Energy Environ. Sci.*, 2021, **14**, 4341-4357.
136. P. Meredith, W. Li and A. Armin, *Adv. Energy Mater.*, 2020, **10**, 2001788.
137. G. Forti, A. Nitti, P. Osw, G. Bianchi, R. Po and D. Pasini, *Int. J. Mol. Sci.*, 2020, **21**, 8085.
138. W. Zhao, D. Qian, S. Zhang, S. Li, O. Inganäs, F. Gao and J. Hou, *Adv. Mater.*, 2016, **28**, 4734-4739.
139. J. Zhan, L. Wang, M. Zhang, L. Zhu, T. Hao, G. Zhou, Z. Zhou, J. Chen, W. Zhong, C. Qiu, S. Leng, Y. Zou, Z. Shi, H. Zhu, W. Feng, M. Zhang, Y. Li, Y. Zhang and F. Liu, *Macromolecules*, 2021, **54**, 4030-4041.
140. R. Ma, G. Li, D. Li, T. Liu, Z. Luo, G. Zhang, M. Zhang, Z. Wang, S. Luo, T. Yang, F. Liu, H. Yan and B. Tang, *Sol. RRL*, 2020, **4**, 2000250.
141. Y. Lin, J. Wang, Z. G. Zhang, H. Bai, Y. Li, D. Zhu and X. Zhan, *Adv. Mater.*, 2015, **27**, 1170-1174.
142. K. Jiang, Q. Wei, J. Y. L. Lai, Z. Peng, H. K. Kim, J. Yuan, L. Ye, H. Ade, Y. Zou and H. Yan, *Joule*, 2019, **3**, 3020-3033.
143. Q. Wei, W. Liu, M. Leclerc, J. Yuan, H. Chen and Y. Zou, *Sci. China Chem.*, 2020, **63**, 1352-1366.
144. L. Perdigon-Toro, H. Zhang, A. Markina, J. Yuan, S. M. Hosseini, C. M. Wolff, G. Zuo, M. Stollerfoht, Y. Zou, F. Gao, D. Andrienko, S. Shoaee and D. Neher, *Adv. Mater.*, 2020, **32**, 1906763.
145. Q. Guo, Q. Guo, Y. Geng, A. Tang, M. Zhang, M. Du, X. Sun and E. Zhou, *Mater. Chem. Front.*, 2021, **5**, 3257-3280.
146. S. Inal, J. Rivnay, P. Leleux, M. Ferro, M. Ramuz, J. C. Brendel, M. M. Schmidt, M. Thelakkat and G. G. Malliaras, *Adv. Mater.*, 2014, **26**, 7450-7455.
147. S. Inal, G. G. Malliaras and J. Rivnay, *Nat. Commun.*, 2017, **8**, 1767.
148. J. K. Harris, B. Neelamraju and E. L. Ratcliff, *Chem. Mater.*, 2019, **31**, 6870-6879.
149. I. P. Maria, B. D. Paulsen, A. Savva, D. Ohayon, R. Wu, R. Hallani, A. Basu, W. Du, T. D. Anthopoulos, S. Inal, J. Rivnay, I. McCulloch and A. Giovannitti, *Adv. Funct. Mater.*, 2021, **31**, 2008718.
150. E. M. Thomas, M. A. Brady, H. Nakayama, B. C. Popere, R. A. Segalman and M. L. Chabinyc, *Adv. Funct. Mater.*, 2018, **28**, 1803687.
151. L. Kergoat, L. Herlogsson, B. Piro, M. C. Pham, G. Horowitz, X. Crispin and M. Berggren, *PNAS*, 2012, **109**, 8394-8399.

References

152. S. Inal, J. Rivnay, A. O. Suiu, G. G. Malliaras and I. McCulloch, *Acc. Chem. Res.*, 2018, **51**, 1368-1376.
153. A. Giovannitti, D. T. Sbircea, S. Inal, C. B. Nielsen, E. Bandiello, D. A. Hanifi, M. Sessolo, G. G. Malliaras, I. McCulloch and J. Rivnay, *PNAS*, 2016, **113**, 12017-12022.
154. J. C. Brendel, M. M. Schmidt, G. Hagen, R. Moos and M. Thelakkat, *Chem. Mater.*, 2014, **26**, 1992-1998.
155. J. Rivnay, R. M. Owens and G. G. Malliaras, *Chem. Mater.*, 2013, **26**, 679-685.
156. P. Gkoupidenis, N. Schaefer, B. Garlan and G. G. Malliaras, *Adv. Mater.*, 2015, **27**, 7176-7180.
157. J. Rivnay, S. Inal, B. A. Collins, M. Sessolo, E. Stavrinidou, X. Strakosas, C. Tassone, D. M. Delongchamp and G. G. Malliaras, *Nat. Commun.*, 2016, **7**, 11287.
158. M. Wieland, C. Dingler, R. Merkle, J. Maier and S. Ludwigs, *ACS Appl. Mater. Interfaces*, 2020, **12**, 6742-6751.
159. M. Berggren and A. Richter-Dahlfors, *Adv. Mater.*, 2007, **19**, 3201-3213.
160. I. E. Jacobs, G. D'Avino, V. Lemaure, Y. Lin, Y. Huang, C. Chen, T. F. Harrelson, W. Wood, L. J. Spalek, T. Mustafa, C. A. O'Keefe, X. Ren, D. Simatos, D. Tjhe, M. Statz, J. W. Strzalka, J. K. Lee, I. McCulloch, S. Fratini, D. Beljonne and H. Sirringhaus, *JACS*, 2022, **144**, 3005-3019.
161. S. Karuthedath, J. Gorenflot, Y. Firdaus, N. Chaturvedi, C. S. P. De Castro, G. T. Harrison, J. I. Khan, A. Markina, A. H. Balawi, T. A. D. Pena, W. Liu, R. Z. Liang, A. Sharma, S. H. K. Paleti, W. Zhang, Y. Lin, E. Alarousu, S. Lopatin, D. H. Anjum, P. M. Beaujuge, S. De Wolf, I. McCulloch, T. D. Anthopoulos, D. Baran, D. Andrienko and F. Laquai, *Nat. Mater.*, 2021, **20**, 378-384.
162. J. Wu, J. Lee, Y.-C. Chin, H. Yao, H. Cha, J. Luke, J. Hou, J.-S. Kim and J. R. Durrant, *Energy Environ. Sci.*, 2020, **13**, 2422-2430.
163. I. N. Hulea, H. B. Brom, A. J. Houtepen, D. Vanmaekelbergh, J. J. Kelly and E. A. Meulenkaamp, *Phys. Rev. Lett.*, 2004, **93**, 166601.
164. T. Sueyoshi, H. Fukagawa, M. Ono, S. Kera and N. Ueno, *Appl. Phys. Lett.*, 2009, **95**, 183303.
165. S. Athanasopoulos, H. Bassler and A. Kohler, *J. Phys. Chem. Lett.*, 2019, **10**, 7107-7112.
166. Z. Tang, B. Liu, A. Melianas, J. Bergqvist, W. Tress, Q. Bao, D. Qian, O. Inganas and F. Zhang, *Adv. Mater.*, 2015, **27**, 1900-1907.
167. M. Azzouzi, J. Yan, T. Kirchartz, K. Liu, J. Wang, H. Wu and J. Nelson, *Phys. Rev. X*, 2018, **8**, 031055.
168. N. A. Ran, S. Roland, J. A. Love, V. Savikhin, C. J. Takacs, Y. T. Fu, H. Li, V. Coropceanu, X. Liu, J. L. Bredas, G. C. Bazan, M. F. Toney, D. Neher and T. Q. Nguyen, *Nat. Commun.*, 2017, **8**, 79.
169. X. Chen, M. K. Ravva, H. Li, S. M. Ryno and J. L. Bredas, *Adv. Energy Mater.*, 2016, **6**, 1601325.

7 Appendix

7.1 SI to High Conductivities of Disordered P3HT Films by an Electrochemical Doping Strategy

Supporting Information to

High Conductivities of Disordered P3HT Films by an Electrochemical Doping Strategy

David Neusser¹, Claudia Malacrida¹, Michal Kern², Yannic Gross¹,Joris van Slageren² and Sabine Ludwigs¹¹IPOC – Functional Polymers, Institute of Polymer Chemistry, University of Stuttgart, Germany²Institute of Physical Chemistry, University of Stuttgart, Germany* sabine.ludwigs@ipoc.uni-stuttgart.de

1. In-situ CV studies of P3HT films

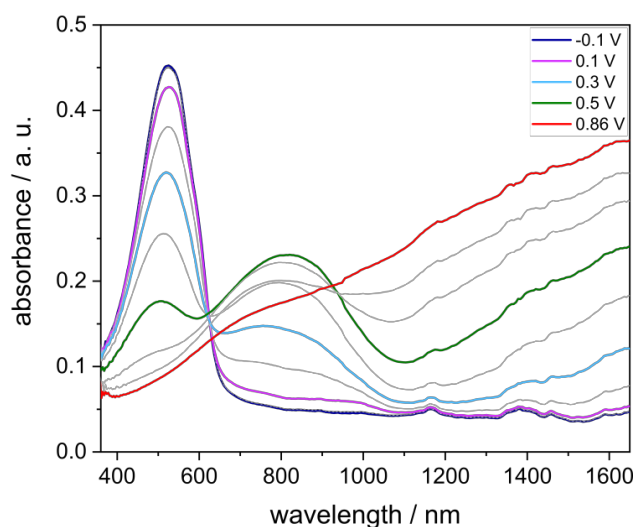


Figure S 1: Spectra for a regioregular P3HT film taken during the forward cycle of the CV experiment in Figure 1 in the main text. *In-situ* spectroelectrochemistry experiment in TBAPF₆/MeCN 0.1 M at 20 mVs⁻¹ on an interdigitated Pt electrode.

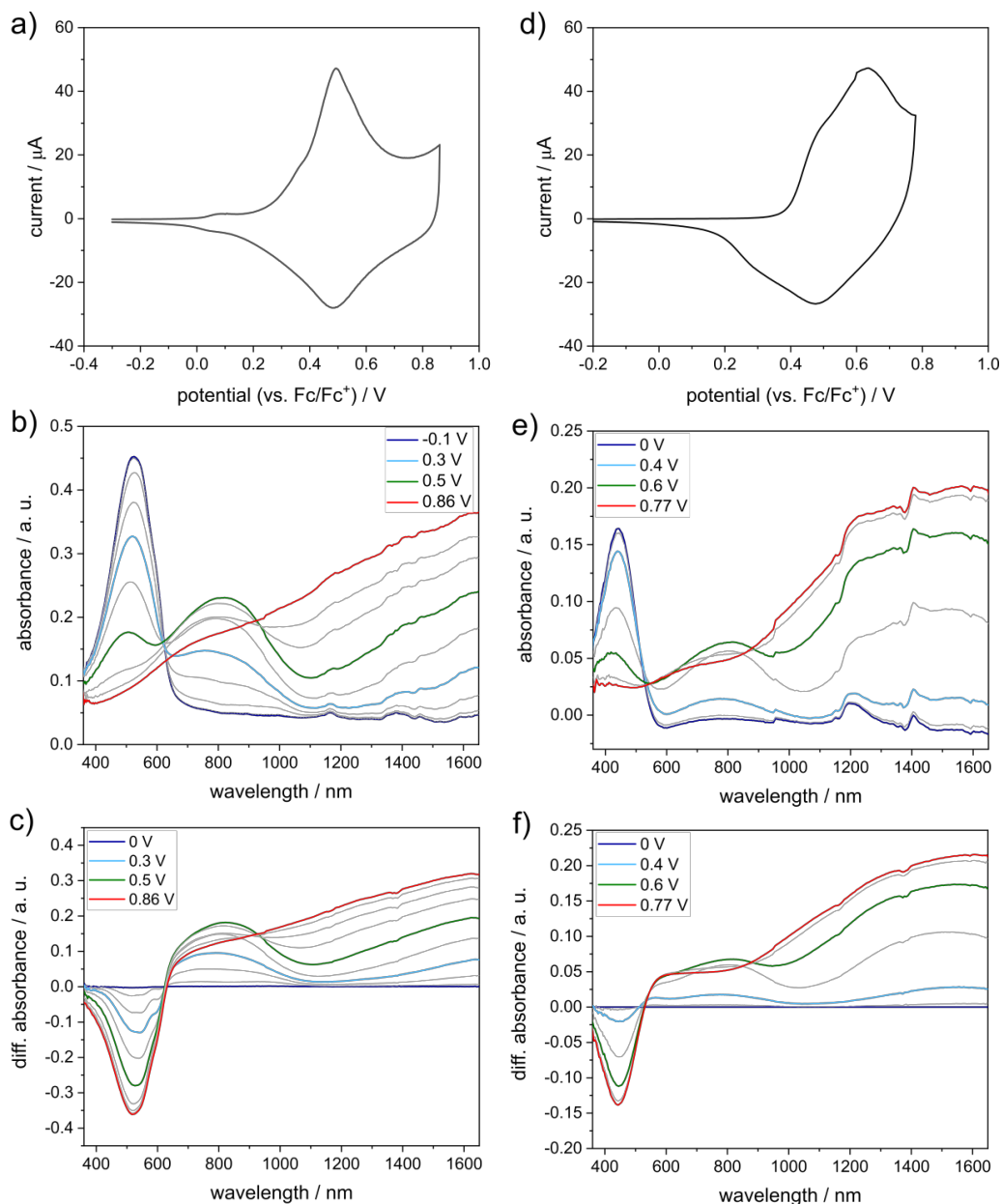


Figure S 2: Comparison of *in-situ* electrochemical studies of a regioregular P3HT film on the left side a) CV, b) UV-Vis-NIR spectra at the given potentials of the charge cycle and c) differential absorption of the spectra in b) and regiorandom P3HT on the right side d) CV, e) UV-Vis-NIR spectra at the given potentials of the charge cycle and f) differential absorption of the spectra in e). Both materials were spin coated from CHCl_3 solution and measured in 0.1 M $\text{TBAPF}_6/\text{MeCN}$ at a scan rate of 20 mVs^{-1} .

The visible shift of the onset of oxidation from $\sim 0 \text{ V}$ (regioregular P3HT) to $\sim 0.4 \text{ V}$ (regiorandom P3HT) can be explained by the completely amorphous nature of the regiorandom P3HT film. Although the crystallinity in the film of regioregular P3HT is very low, still a slight signal between 0.11 V and 0.13 V is visible induced by crystalline regions in the film.¹ These

regions are completely missing in the regiorandom P3HT film, thus leading to an onset of oxidation at higher potentials corresponding to the amorphous P3HT film. Besides the shift of the onset a different ratio of absorption maxima is visible when comparing the bands at 525 nm and 1600 nm in b) and e). This might be due to different extinction coefficients of the respective charged species in regioregular and regiorandom P3HT.

Comparing the spectra at highest doping levels one can see that the maximum absorption of the low energy band in the NIR-region is blue-shifted in the case of regiorandom P3HT (maximum around 1500 nm) in comparison to RR P3HT (maximum above 1600 nm). Schwartz et al attributed such phenomena due to less delocalization of the charged species.²

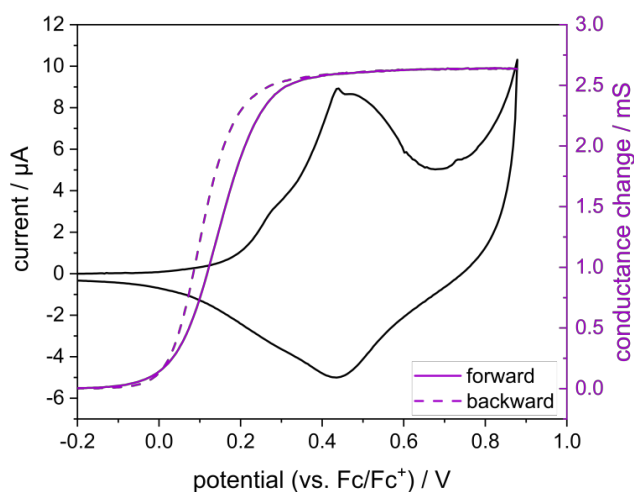


Figure S 3. Cyclic voltammetry (black) coupled with *in-situ* conductance measurements of a regioregular P3HT film (purple) measured in TBAPF₆/MeCN 0.1 M at 10 mVs⁻¹ on an interdigitated Pt electrode; forward cycle of conductance given in Figure 1 in the main text.

2. *Ex-situ* solid-state conductivities of electrochemically doped P3HT films

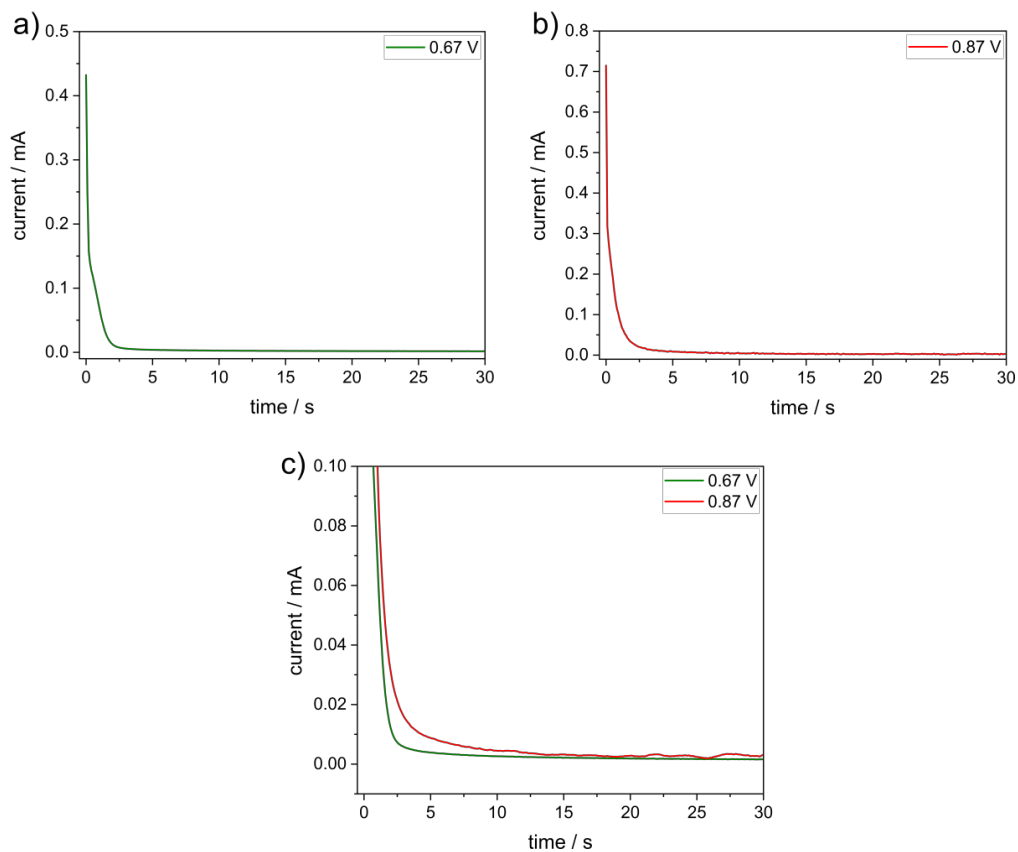


Figure S 4: Current-time graphs recorded during potentiostatic electrochemical doping for the conductivity measurements. Doping was performed in a three electrode setup using 0.1 M TBAPF₆ in acetonitrile as electrolyte on 4-line gold electrodes. A close up for comparison is depicted in c).

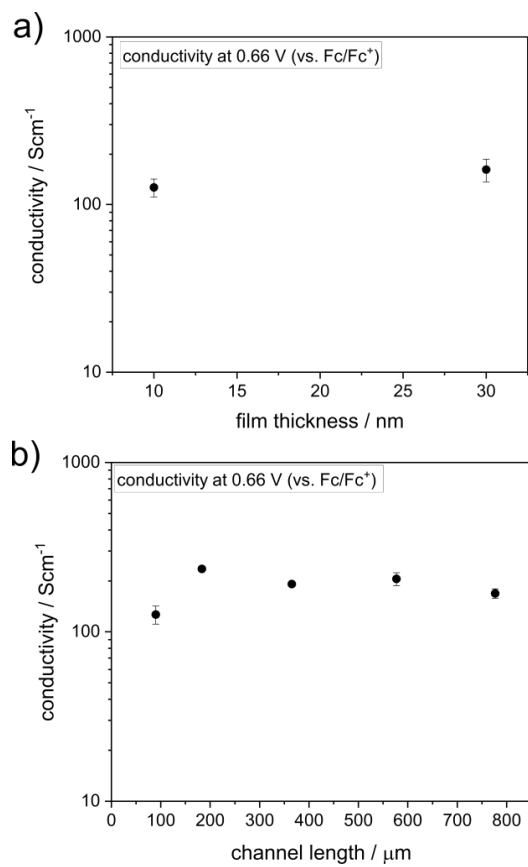


Figure S 5: Conductivity of doped P3HT films with different film thickness in a) and influence of different channel lengths b) on the conductivity of doped P3HT films with a thickness of 10 nm in b).

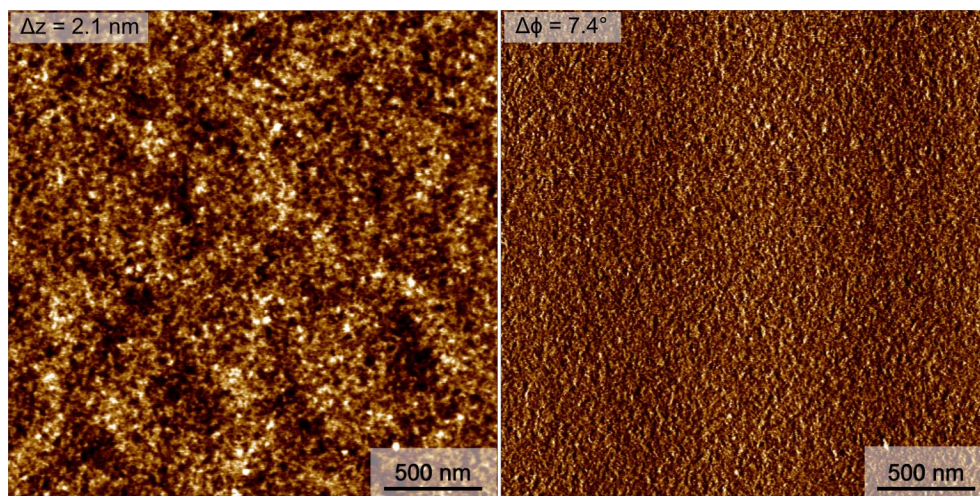


Figure S 6: AFM image of a P3HT film spin coated from toluene (3 gL^{-1}) on 4-line gold substrates. The image was taken inside the channel in between the gold bands.

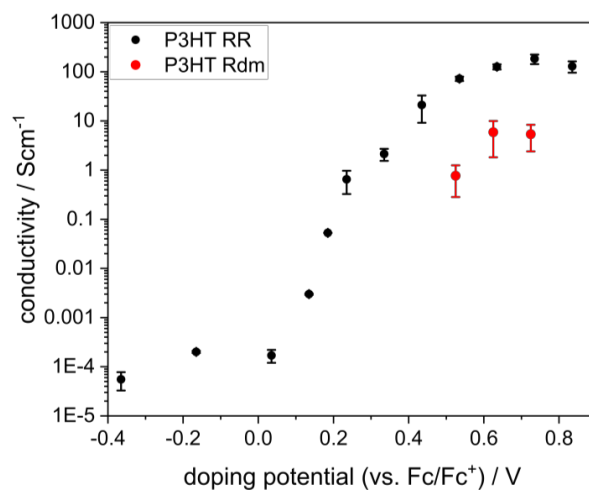


Figure S 7: *Ex-situ* measured solid-state conductivities of electrochemically doped films of regioregular (black) and regiorandom (red) P3HT on 4-line gold electrodes at different doping potentials.

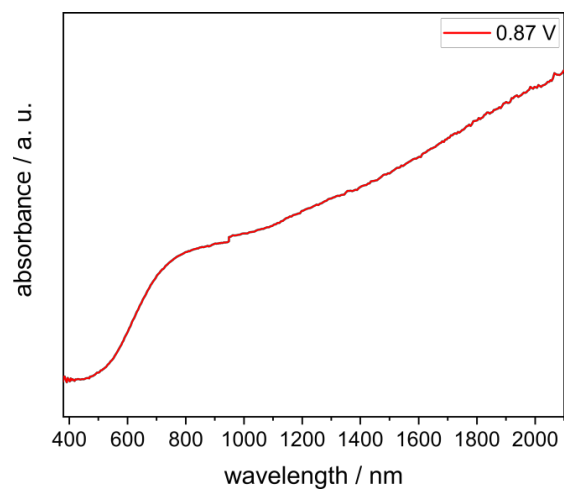


Figure S 8: Extended solid-state UV-Vis-NIR spectrum of a P3HT film electrochemically doped at a doping potential of 0.87 V (vs. Fc/Fc⁺), compare to Figure 2 b) in the main text.

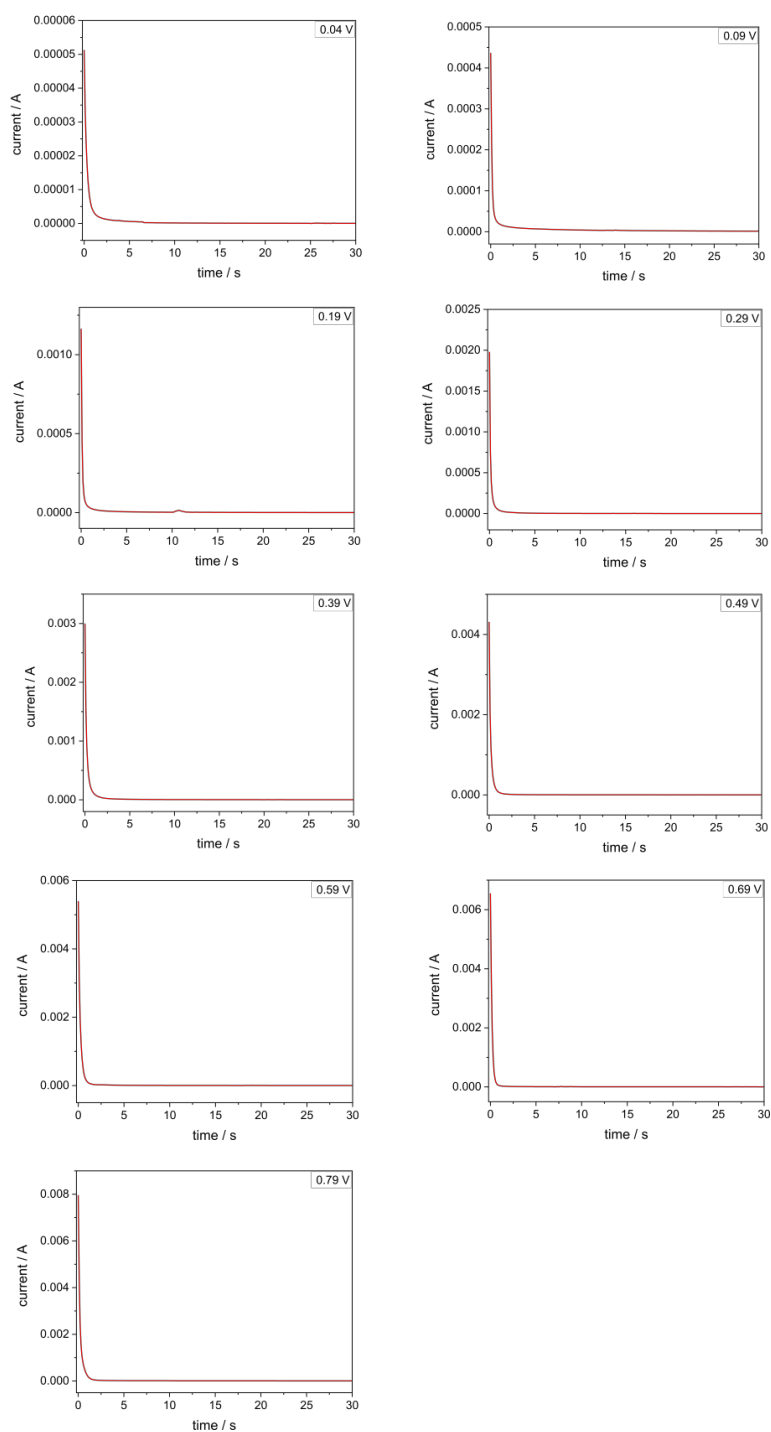


Figure S 9: Current-time graphs recorded during potentiostatic electrochemical doping for the EPR experiments. Experiments were performed in a three electrode setup using 0.1 M TBAPF₆ in acetonitrile as electrolyte on gold coated Kapton® foil as electrode.

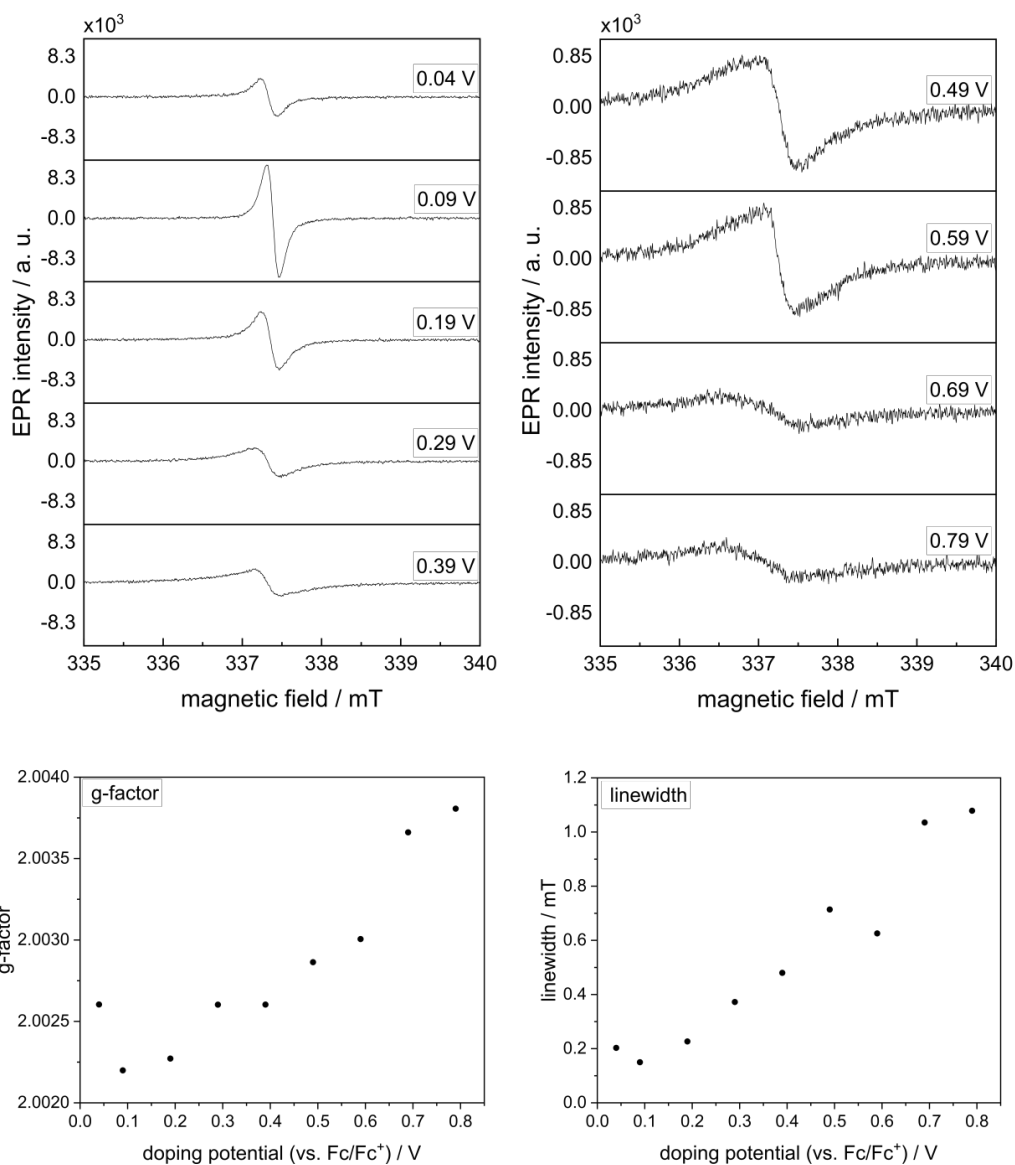


Figure S 10: EPR spectra of potentiostatically doped P3HT films on gold coated Kapton® foil at different doping potentials. The spectra recorded at higher doping potentials b) are scaled up to improve visibility. The extracted g-factor and linewidths from the EPR data is given underneath.

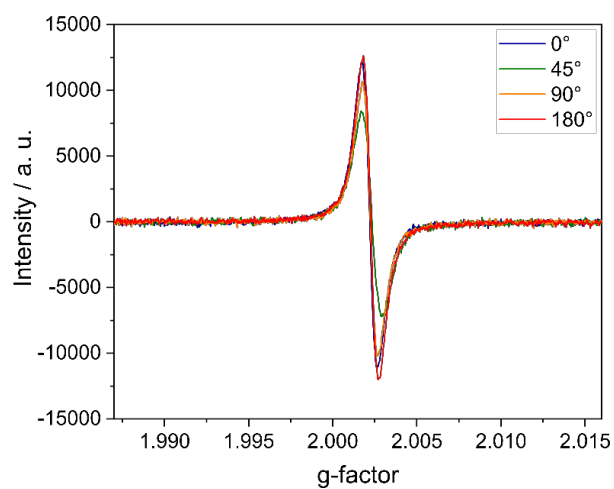


Figure S 11: Angular dependence of the EPR spectra of a sample doped at 0.09 V. The changes in intensity are most likely caused by different coupling of the MW radiation to the cavity at different orientations, as the sample pieces were not perfectly vertical and centered. Care was taken with subsequent samples to insert them in the same orientation for comparable quantification.

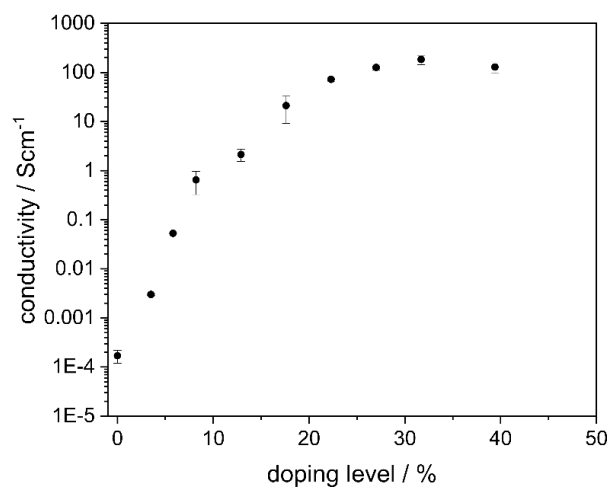


Figure S 12: Solid-state conductivity of electrochemically doped P3HT films as function of the doping level. The maximum doping level approaches 40 % at highest doping potentials. The doping level in % is calculated from the amount of injected charge during the doping procedure (see Figure 2 c)) and is the result from dividing the induced charges by the total number of thiophene units in the film. The doping level is then correlated to the measured conductivities in Figure 2 a).

3. Comparison of the results to a crosslinked poly(BCbz) film

Procedure to generate poly(BCbz) films from as-cast PVPhCbz films:

Films of PVPhCbz were spin coated from chloroform solutions ($c = 10 \text{ gL}^{-1}$, 1000 rpm for 180 s) giving a film thickness of $\sim 50 \text{ nm}$. These films were electrochemically crosslinked to generate poly(BCbz) films in an electrochemical setup by performing 5 complete cycles (see Figure S 13) following a procedure from literature on a comparable system.^{3,4} The first cycle shows the crosslinking process whereas all following cycles are identical and display a fully reversible two step oxidation process of the generated BCbz species from the neutral via the radical cation (BCbz^{+•}) to the dication (BCbz²⁺) species.

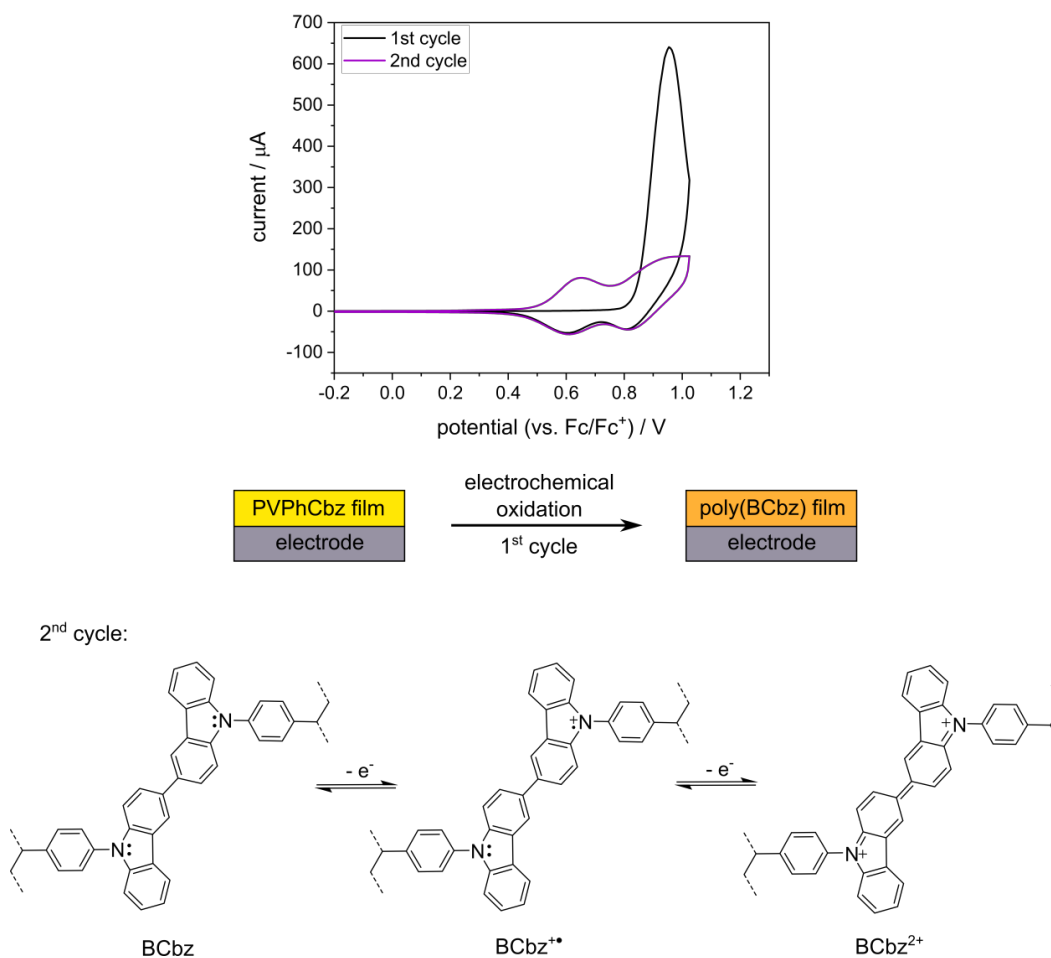


Figure S 13: First and second cycle of subsequently performed CVs of a spin coated film of PVPhCbz film on a gold substrate in TBAPF₆/MeCN 0.1 M at 20 mVs⁻¹. In the first cycle PVPhCbz is crosslinked, in the second cycle poly(BCbz) is reversibly oxidized and reduced.

The second cycle (purple) is representative for all following cycles. The mechanism of the occurring dimerization process follows the well-known dimerization of triphenylamine into tetraphenylbenzidine units.^{3,4}

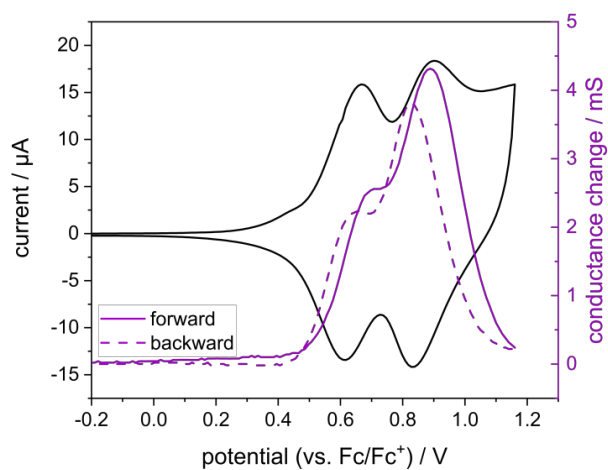


Figure S 14: *In-situ* conductance study (purple) of a poly(BCbz) film with underlying CV (black) measured in TBAPF₆/MeCN 0.1 M at 10 mVs⁻¹ on an interdigitated Pt electrode.

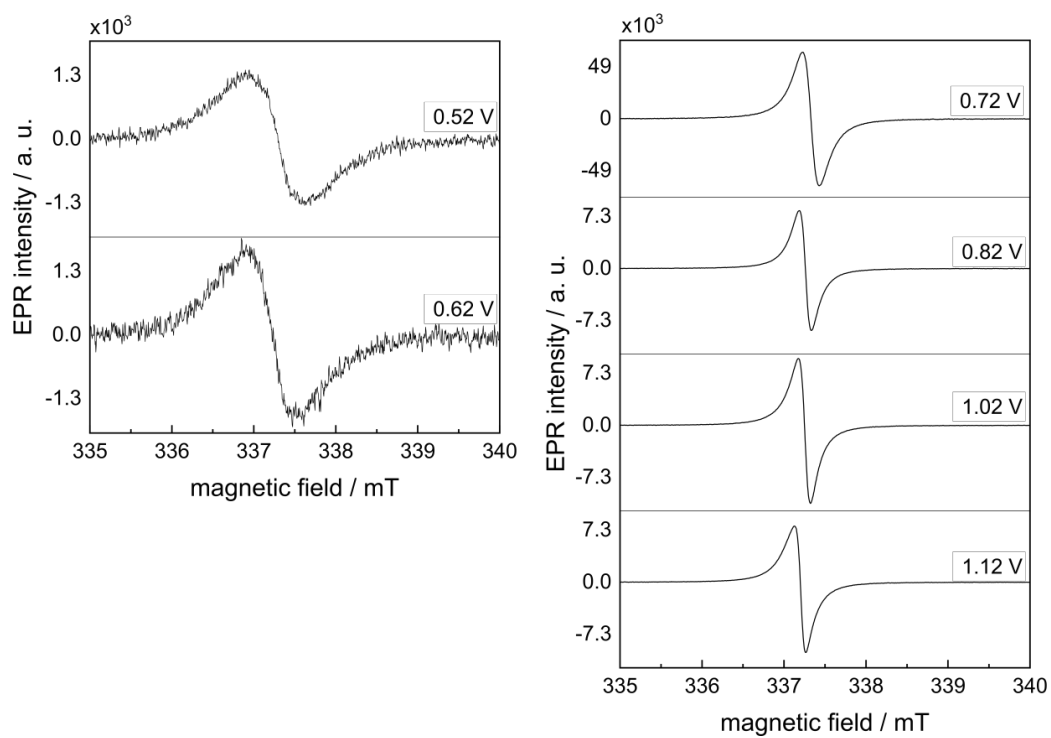


Figure S 15: EPR spectra of potentiostatically doped poly(BCbz) films on gold coated Kapton® foil at different doping potentials.

- (1) Bruchlos, K.; Trefz, D.; Hamidi-Sakr, A.; Brinkmann, M.; Heinze, J.; Ruff, A.; Ludwigs, S. Poly(3-hexylthiophene) Revisited – Influence of Film Deposition on the Electrochemical Behaviour and Energy Levels. *Electrochim. Acta* **2018**, 269, 299–311.
- (2) Aubry, Taylor J.; Winchell, K. J.; Salamat, Charlene Z.; Basile, Victoria M.; Lindemuth, Jeffrey R.; Stauber, Julia M.; Axtell, Jonathan C.; Kubena, Rebecca M.; Phan, Minh D.; Bird, Matthew J.; Spokoyny, Alexander M.; Tolbert, Sarah H.; Schwartz, Benjamin J. Tunable Dopants with Intrinsic Counterion Separation Reveal the Effects of Electron Affinity on Dopant Intercalation and Free Carrier Production in Sequentially Doped Conjugated Polymer Films. *Adv. Funct. Mater.* **2020**, 2001800.
- (3) Yurchenko, O.; Heinze, J.; Ludwigs, S. Electrochemically Induced Formation of Independent Conductivity Regimes in Polymeric Tetraphenylbenzidine Systems. *Chemphyschem* **2010**, 11, 1637–1640.
- (4) Yurchenko, O.; Freytag, D.; Zur Borg, L.; Zentel, R.; Heinze, J.; Ludwigs, S. Electrochemically Induced Reversible and Irreversible Coupling of Triarylaminines. *J. Phys. Chem. B* **2012**, 116, 30–39.

7.2 SI to How Charge Trapping affects the Conductivity of Electrochemically Doped Poly(3-Hexylthiophene) Films

Supporting Information to

How Charge Trapping affects the Conductivity of Electrochemically Doped Poly(3-Hexylthiophene) Films

Lea-Sophie Hornberger^{1,#}, David Neusser^{1,#}, Claudia Malacrida¹, Loren G. Kaake² and Sabine Ludwigs^{1,*}

¹ IPOC – Functional Polymers, Institute of Polymer Chemistry, and Center for Integrated Quantum Science and Technology (IQST), University of Stuttgart, Pfaffenwaldring 55, 70569 Stuttgart, Germany

² Department of Chemistry, Simon Fraser University, Burnaby BC, V5A 1S6, Canada

Authors contributed equally.

Correspondence should go to: sabine.ludwigs@ipoc.uni-stuttgart.de

1. Materials & Methods

Materials. Regioregular P3HT ($M_n = 46.6 \text{ kg mol}^{-1}$, PDI = 2.4) was purchased from Merck and used without further purification. Solvents in p. a. grade (toluene, chloroform and acetonitrile) and conducting salts (TBAPF₆, LiClO₄, LiTFSI and TBABF₄) were purchased from Sigma-Aldrich and used as received.

Film Preparation. For 10 nm thin films, P3HT was dissolved in toluene at concentrations of 3 g L⁻¹. For 50 nm films, P3HT was dissolved in chloroform at a concentration of 5 g L⁻¹. To ensure complete dissolving, the solutions were stirred overnight at 60 °C (toluene) and 40 °C (chloroform). Substrates were cleaned using ultrasonication in water, isopropanol and acetone. Thin films were spin coated onto the precleaned substrates under inert atmosphere. Different coating conditions for the 10 nm (2000 rpm for 120 s, then 4000 rpm for 15 s) and 50 nm (1500 rpm for 120 s, then 5000 rpm for 15 s) films were used. Film thicknesses were measured on a Bruker Dimension Iconic Atomic Force Microscope System.

In Situ Electrochemical Investigation of P3HT Thin Films. All CV measurements were performed under inert atmosphere using a Metrohm PGSTAT101 potentiostat with a three electrode setup. Pt sheet was used as counter electrode and Ag/AgCl wire as reference electrode.

The cell was placed under Ar atmosphere. Subsequently, it was filled up with electrolyte (0.1 M TBABF₆, LiClO₄, LiTFSI or TBABF₄ in acetonitrile). At the end of the measurements, the redox couple Fc/Fc⁺ was recorded as internal standard. For *in situ* spectroelectrochemistry ITO coated glass slides were used as substrates using the identical setup as for CV. The WE covered with the polymer film was positioned in the beam path of a diode array spectrometer. Optical fibers connected the setup with the modular Zeiss spectrometer system equipped with MCS611 2.2 and MCS621visII detectors and a halogen lamp (CLH600).

***Ex Situ* Electrochemical Investigation of P3HT Thin Films.** Electrochemical doping was done in an electrochemical three electrode setup under inert atmosphere. Each sample was potentiostatically doped holding the applied voltage for 30 s. The samples were extracted immediately and dried without further treatment. For 4-line probe conductivity measurements, tailor made 4-line gold electrodes with channel lengths of 100 μm and channel width of 1 cm were prepared. After electrochemical doping and transfer of the doped samples under inert conditions, 4-line probe conductivities were measured with a Keithley 2636 system source meter. The source meter was operated with a LabView interface. Custom-made 4-line gold electrodes with a channel width of 1 cm and a channel length of 800 μm were used for *ex situ* solid-state spectroscopy. The spin-coated films were equally prepared as for the 4-line probe. Every step was performed under inert conditions. The sample was positioned in the measuring chamber with the light path shining through one channel. Optical fibers were attached and connected with the modular Zeiss spectrometer system with diode array with MCS611 2.2 and MCS621visII detectors and a CLH600 halogen lamp.

2. *In Situ* Electrochemical Investigation of P3HT films

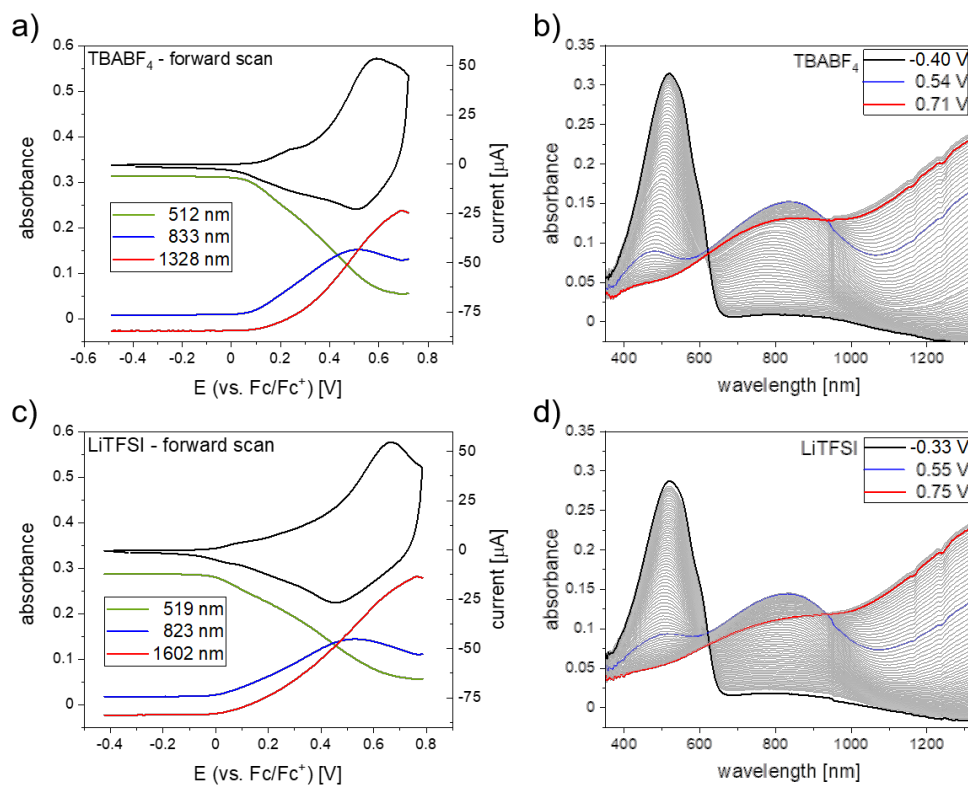


Figure S1: *In situ* UV-vis-NIR spectroelectrochemistry measurements of the second cycle of 10 nm thin P3HT films in 0.1 M TBABF₄ and LiTFSI in acetonitrile. CV and spectral development of selected bands in a) TBABF₄ and c) LiTFSI. *In situ* recorded absorbance during the forward scan of doping in b) TBABF₄ and d) LiTFSI.

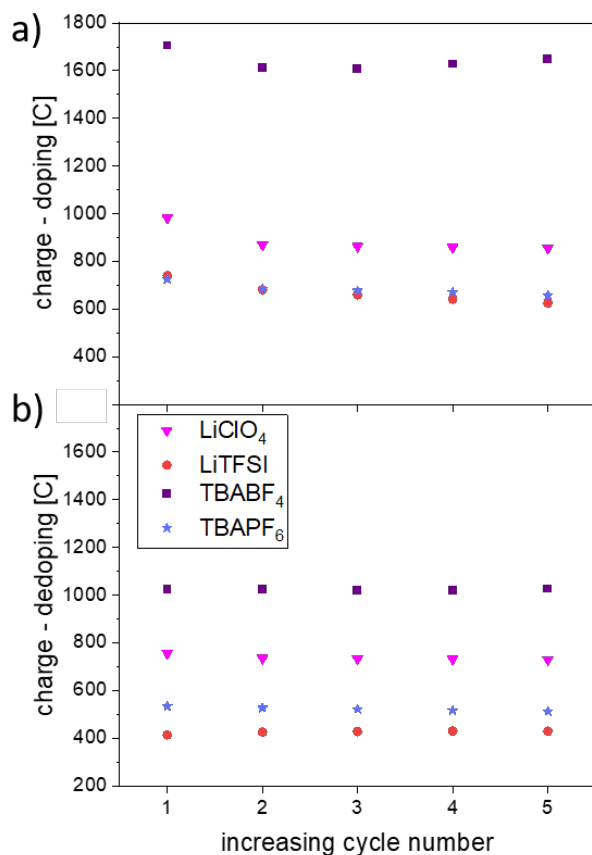


Figure S2: Calculated charge of the doping and dedoping process connected to the *in situ* absorbance measurement. The charge was calculated by integrating the area under the CV for the forward or backward scans, respectively, and dividing the number by the scan rate of 20 mV/s leading to the charge in Coulomb. The charges are shown separately as a function of the increasing cycle number for doping in a) and dedoping in b).

Figure S2 gives additional information about the injected and released charge in the CV experiments for the different electrolytes. The accumulated charge upon doping is calculated by integrating the forward cycle of the CV, whereas the charge from dedoping is the result of the integration of the CV during the backwards cycle. In an ideal and fully reversible system the injected and released charge should be the same since all redox processes are fully reversible and starting point and final point of the CV are identical. For our system this is not the case. The released charge is lower than the injected charge, leading to the conclusion that charges remain trapped in the film. Regarding the origin of these “traps”, natural defects in the material resulting from film preparation should be considered. Furthermore, performing a CV is connected with

swelling and deswelling of the film resulting in possibly unwanted modifications of morphologies. Side reaction initiated by oxygen are rather unlikely since the entire experiment is done under inert conditions. Electrochemical side reactions are avoided by choosing the correct potential window where the material remains stable.

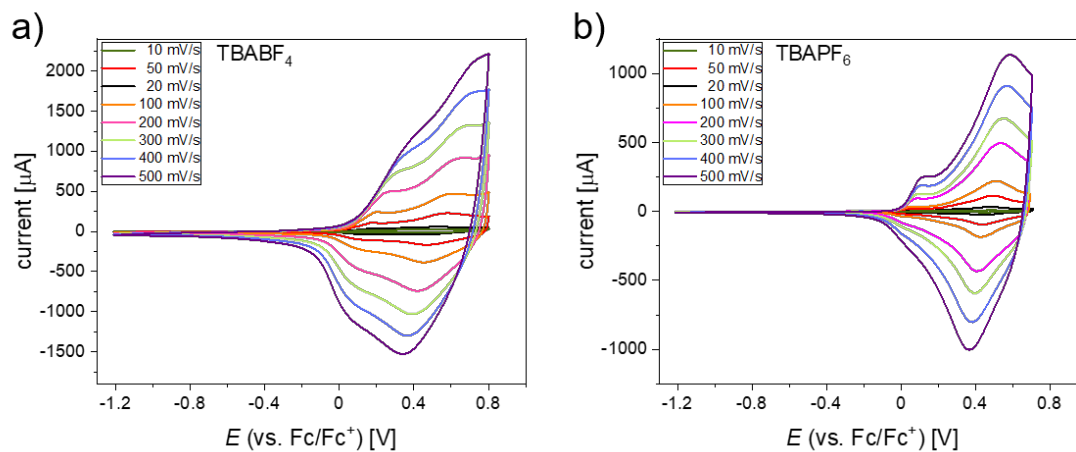


Figure S3: Scan rate dependent CV measurements of 50 nm thin P3HT films in different electrolytes: a) 0.1 M TBABF₄ in acetonitrile and b) 0.1 M TBAPF₆ in acetonitrile.

3. Ex Situ Investigations

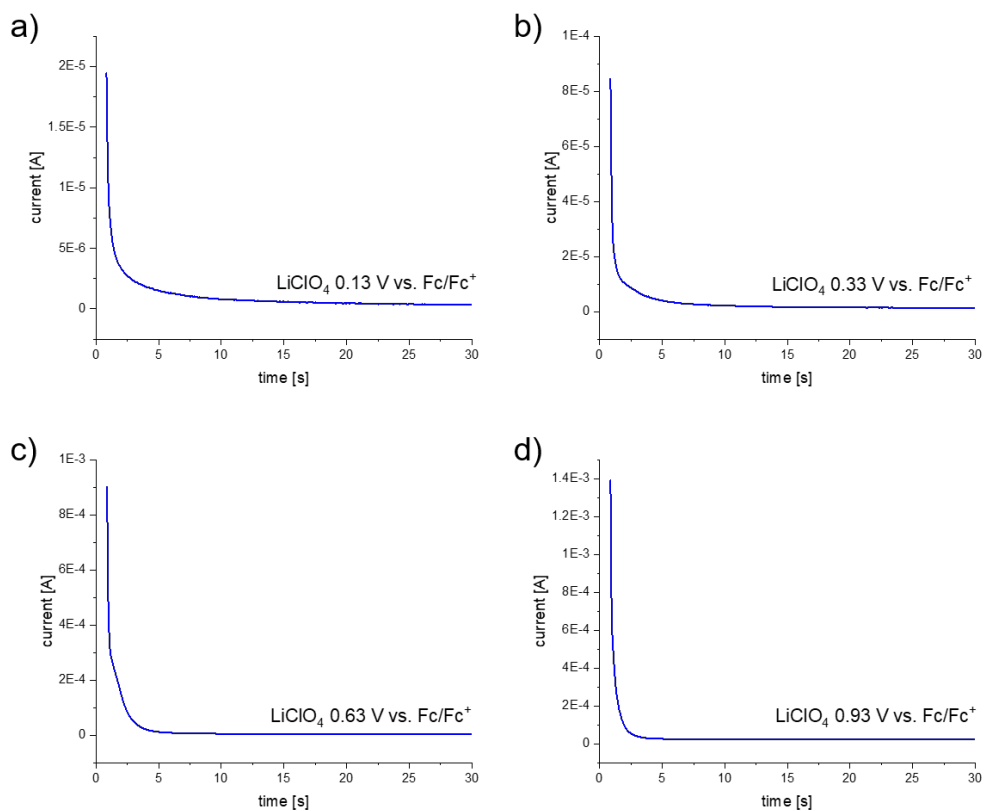


Figure S4: Current-time graphs of 10 nm thin P3HT films on tailor-made 800 μm four-line electrodes. All samples were doped in the three electrode set-up for 30 s in 0.1 M LiClO_4 in acetonitrile using the chosen potentials.

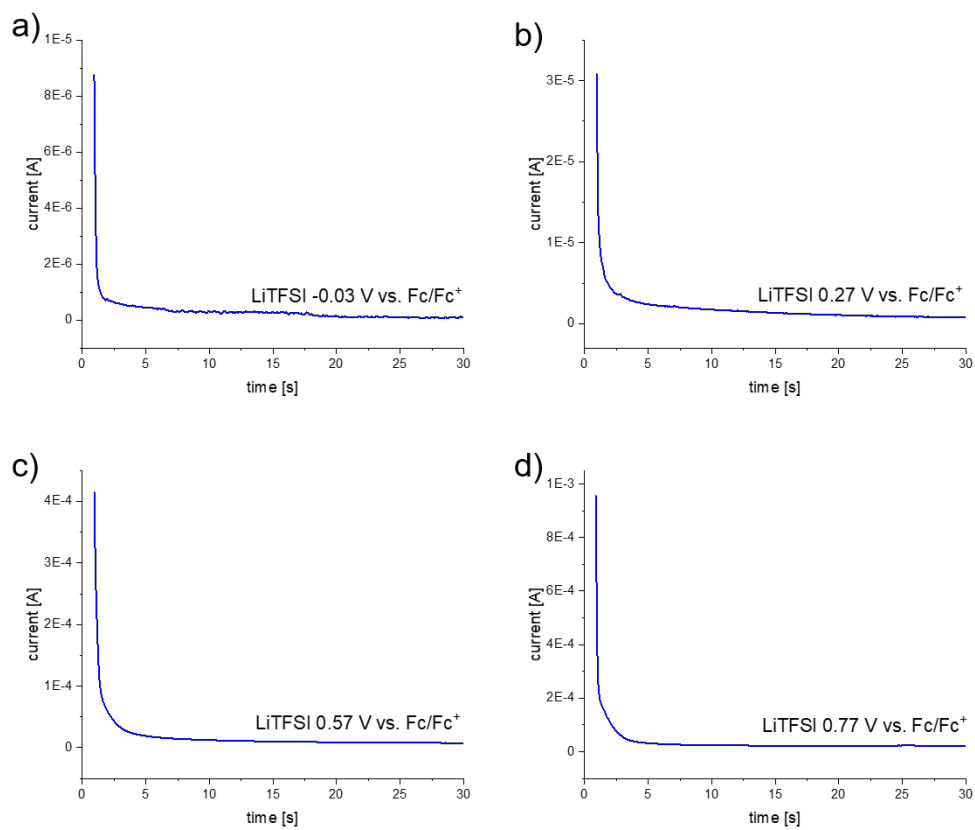


Figure S5: Current-time graphs of 10 nm thin P3HT films on tailor-made 800 μm four-line electrodes. All samples were doped in the three electrode set-up for 30 s in 0.1 M LiTFSI in acetonitrile using the chosen potentials.

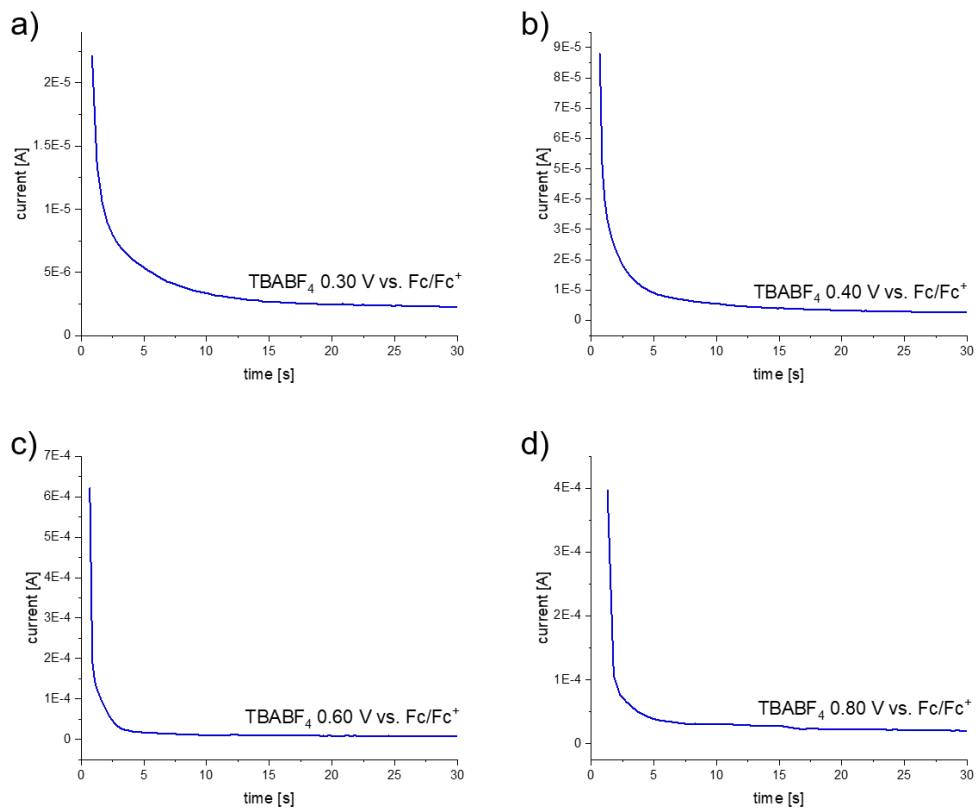


Figure S6: Current-time graphs of 10 nm thin P3HT films on tailor-made 800 μm four-line electrodes. All samples were doped in the three electrode set-up for 30 s in 0.1 M TBABF₄ in acetonitrile using the chosen potentials.

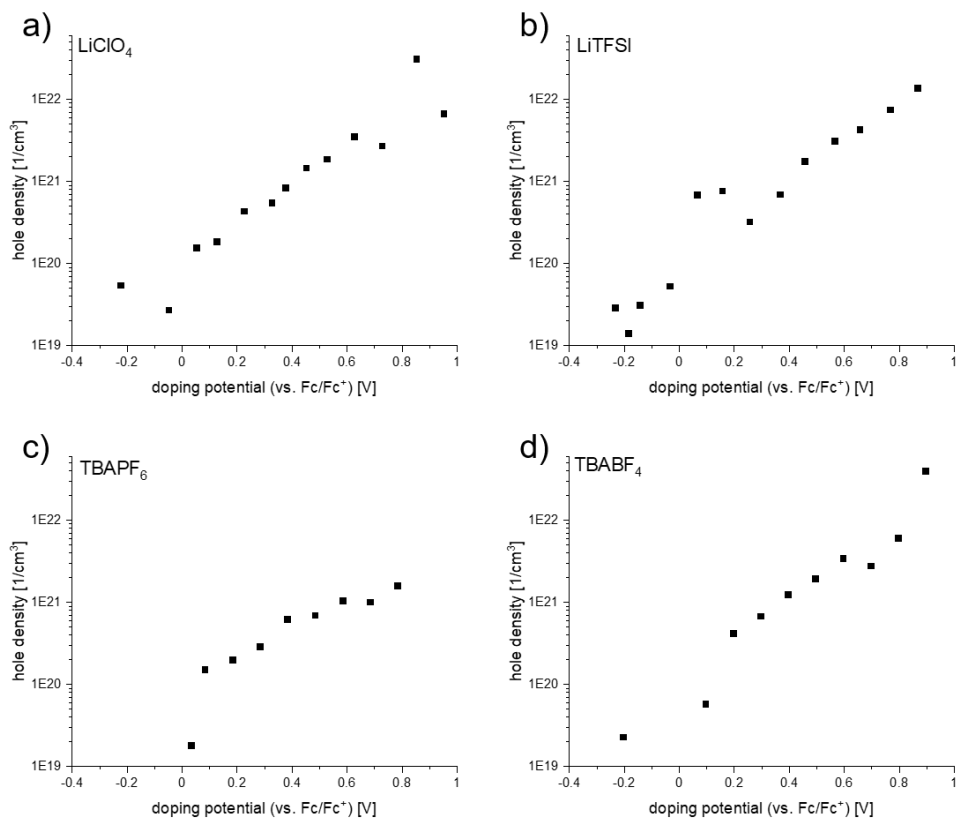


Figure S7: Calculated hole densities for the four-line conductivity measurements. Integrals under the current-time curves of 30 s of charging were determined and related to the volumes of the P3HT films for all electrolytes with a salt concentration of 0.1 M LiClO₄ a), LiTFSI b), TBAPF₆ c) or TBABF₄ d) in acetonitrile.

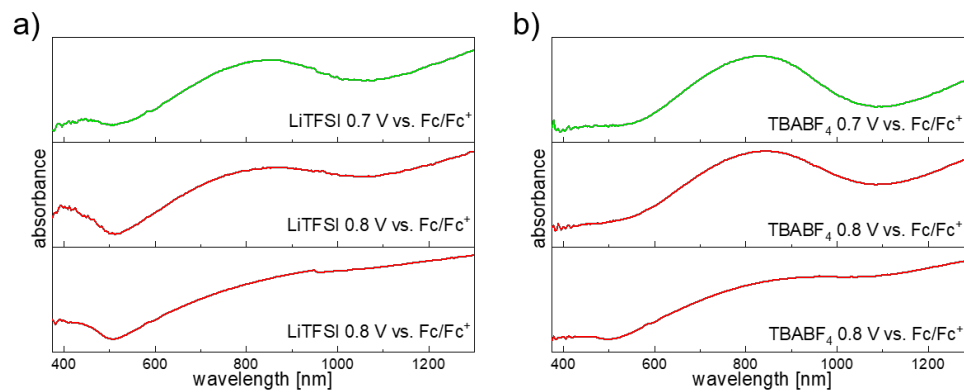


Figure S8: Solid state UV-vis-NIR spectroscopy measurements on 800 μm four-line electrodes after electrochemical doping in LiTFSI a) and LiClO₄ b). For every electrolyte, at least two 10 nm P3HT films were studied. Each sample was potentiostatically doped for 30 s at the given potentials and the corresponding absorbance was measured afterwards in solid-state. Top spectra (green): after doping with 0.7 V vs. Fc/Fc⁺. Middle and bottom: absorbance of the doped films in the solid state after doping with 0.8 V vs. Fc/Fc⁺ at different positions between the 4-line electrodes.

7.3 SI to Spectroelectrochemically Determined Energy Levels of PM6:Y6 Blends and their

Relevance to Solar Cell Performance

Supporting Information to

Spectroelectrochemically Determined Energy Levels of PM6:Y6 Blends and their Relevance to Solar Cell Performance

David Neusser,^a Bowen Sun,^b Wen Liang Tan,^c Lars Thomsen,^d Thorsten Schultz,^e Lorena Perdigón-Toro,^f Norbert Koch,^e Safa Shoaee,^b Christopher R. McNeill,^c Dieter Neher^{f,*} and Sabine Ludwigs^{a,*}

^a IPOC – Functional Polymers, Institute of Polymer Chemistry, University of Stuttgart, Germany

^b Optoelectronics of Disordered Semiconductors, Institute of Physics and Astronomy, University of Potsdam, Germany

^c Department of Materials Science and Engineering, Monash University, Wellington Road, Clayton, Victoria, 3800 Australia

^d Australian Synchrotron, ANSTO, 800 Blackburn Road, Clayton, Victoria 3168, Australia

^e Helmholtz-Zentrum Berlin für Materialien und Energie GmbH 12489 Berlin, Germany

^f Soft Matter Physics and Optoelectronics, Institute of Physics and Astronomy, University of Potsdam, Germany

*sabine.ludwigs@ipoc.uni-stuttgart.de

*neher@uni-potsdam.de

Table S1: Published HOMO and LUMO levels of PM6 and Y6 in the literature, determined by various experimental techniques from recent years. Electrochemical band gaps as well as the transport energy is given as well. If known, the correction factor for transferring the CV onset into the energy scale is given in brackets. Measurements performed on blend films are marked with an asterix.

PM6			Y6			$\Delta E_{HOMO} /$ eV	$E_{tr} /$ eV	method	Ref.
HOMO / eV	LUMO / eV	E_g^{EC} / eV	HOMO / eV	LUMO / eV	E_g^{EC} / eV				
-5.30	-3.05	2.25	-5.64	-3.92	1.72	0.34	1.38	spectroelectro-	our work
-5.30*	-3.06*	2.24*	-5.63*	-3.90*	1.73*	0.33*	1.40*	chemistry (4.8 eV)	
-5.56	-3.50	2.06	-5.65	-4.10	1.55	0.09	1.46	CV (4.36 eV)	1
-5.05	-3.59	1.46	-5.61	-4.10	1.51	0.56	0.95	CV (4.73 eV)	2
-5.45	-3.20	2.25	-	-	-	-	-	CV (4.8 eV)	3
-5.18	-	-	-	-	-	-	-	PESA	3
-5.54	-3.65	1.89	-5.62	-4.11	1.51	0.08	1.43	CV	4
-5.13	-3.28	-	-5.66	-4.29	-	0.53	0.84	UPS + opt. band gap CV	5
-5.45	-3.65	1.80	-	-	-	-	-	(4.71 eV) + opt. band gap CV	6
-5.50	-3.61	1.89	-	-	-	-	-	(4.29 eV)	7
-5.10	-3.10	-	-5.81	-4.10	-	0.71	1.00	UPS + IPES	8
-5.43	-3.47	1.96	-5.69	-3.96	1.73	0.26	1.47	CV	9
-5.53*	-	-	-	-3.92*	-	-	1.61*	CV	9
-5.50	-3.50	2.00	-	-	-	-	-	CV	10
-5.56	-3.48	2.08	-5.67	-4.08	1.59	0.11	1.48	CV (4.44 eV)	11
-	-	-	-5.65	-4.10	1.55	-	-	CV	12

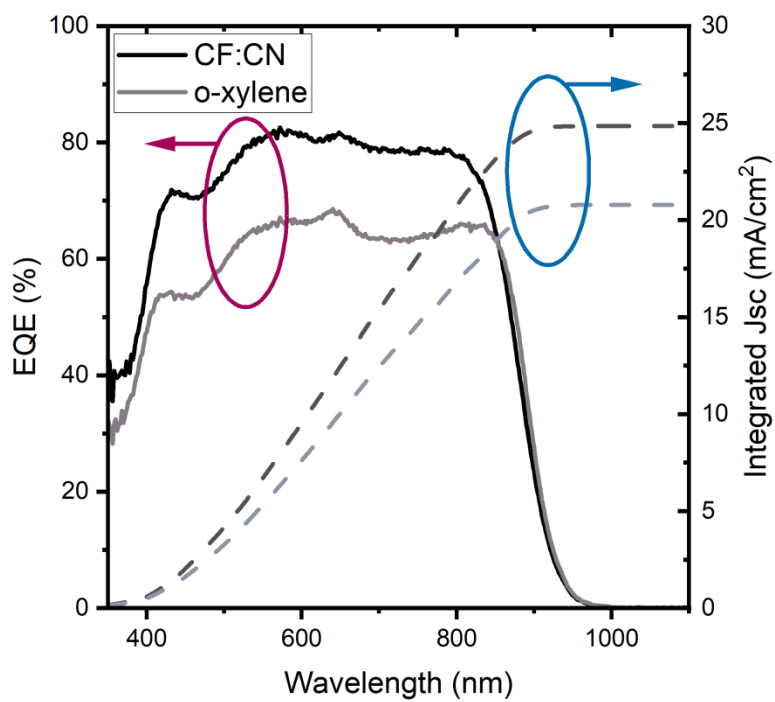


Figure S1: External quantum efficiency (EQE) spectrum of PM6:Y6 devices fabricated with CF:CN and o-xylene as the solvent for the active layer.

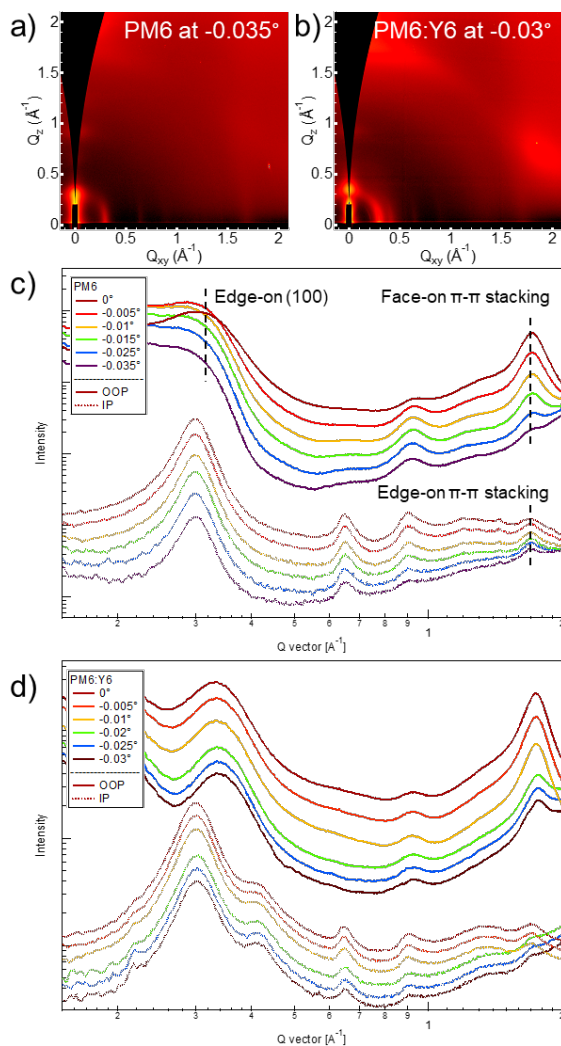


Figure S2: (a-b) 2D GIWAXS patterns and (c-d) the corresponding incident-angle-dependent 1D plots of neat PM6 films and PM6:Y6 blend films (1:1.2 wt%) spin-coated from CF + 0.5 v% CN solvent system. The angles of incidence are labelled relative to critical angle; the 0° data corresponds to the critical angle whereas negative values refer to measurements below the critical angle. In both neat and blend films, GIWAXS data collected at shallower incident angle observed weaker out-of-plane (OOP) π - π stacking peak relative to OOP (100) lamellar stacking peak and in-plane (IP) π - π stacking peak indicating the improved ratio of edge-on oriented PM6 crystallites, which is consistent with the NEXAFS findings. At -0.03° incident angle, the blend film observes stronger OOP π - π stacking peak than that in the neat film due to the π - π stacking order of face-on oriented Y6 crystallites.

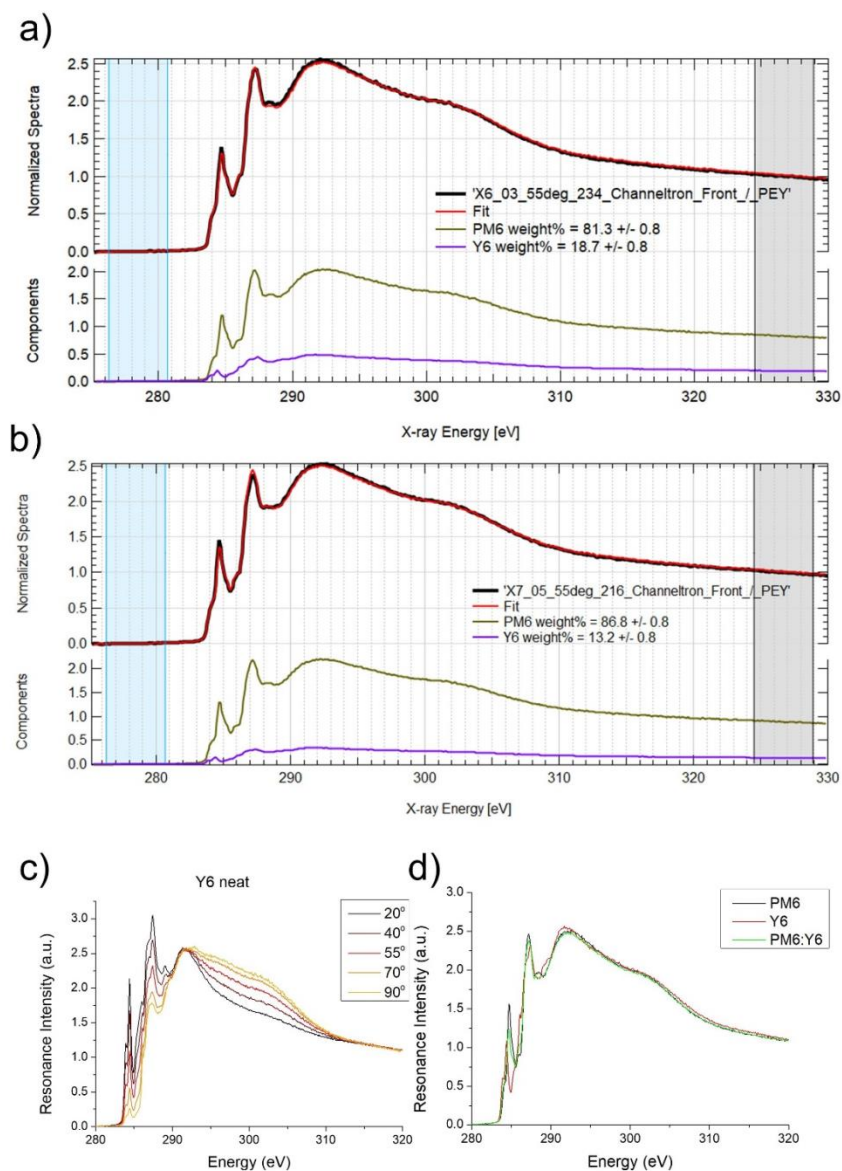


Figure S3: Angle-resolved NEXAFS spectra of PM6:Y6 blend films (1:1.2 wt%, 30 nm) processed from a) CF:CN (CF + 0.5 v% CN) and b) o-xylene solutions. Spectra of the neat compounds are given in c) and d).

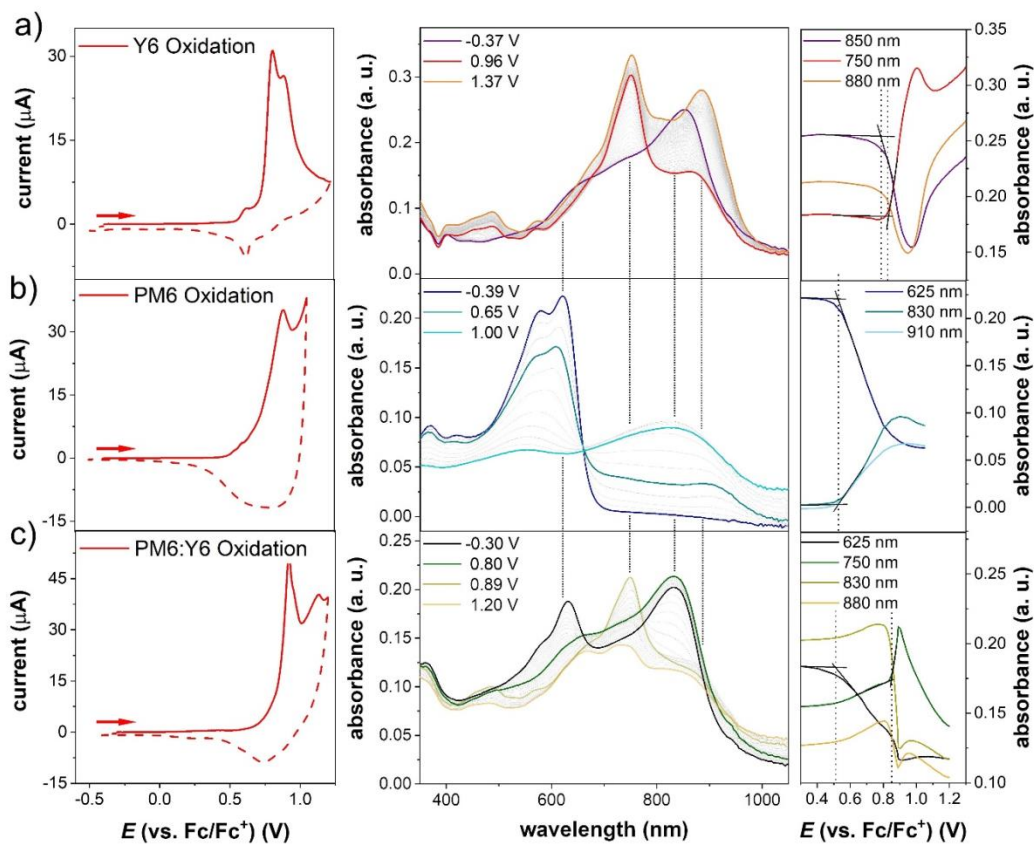


Figure S4: *In situ* CV measurements coupled with UV-vis spectroscopy of a) neat Y6, b) neat PM6 and c) a blend of PM6:Y6 (1:1.2 wt%) films, spin coated and annealed from *o*-xylene solutions. CVs are given on the left, the spectra of the charge half-cycle of the oxidation are presented in the center, completed with peak trends of significant bands on the right side. Spectral onsets of the oxidation are indicated by dotted lines and obtained via tangent method. Underlying CVs (1st cycles) are measured in 0.1 M TBAPF₆/MeCN at 20 mV s⁻¹ on ITO substrates.

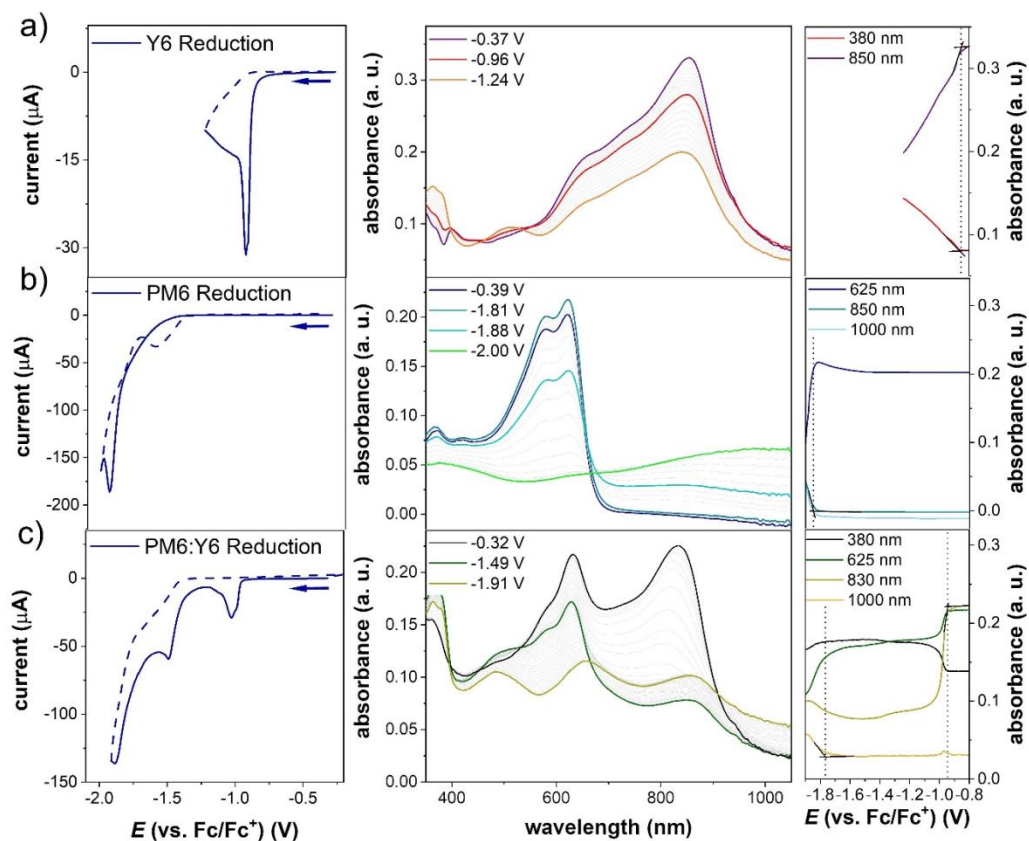


Figure S5: *In situ* CV measurements coupled with UV-vis spectroscopy of a) neat Y6, b) neat PM6 and c) a blend of PM6:Y6 (1:1.2 wt%) films, spin coated and annealed from *o*-xylene solutions. CVs are given on the left, the spectra of the charge half-cycle of the oxidation are presented in the center, completed with peak trends of significant bands on the right side. Spectral onsets of the reduction are indicated by dotted lines and obtained via tangent method. Underlying CVs (1st cycles) are measured in 0.1 M TBAPF₆/MeCN at 20 mV s⁻¹ on ITO substrates.

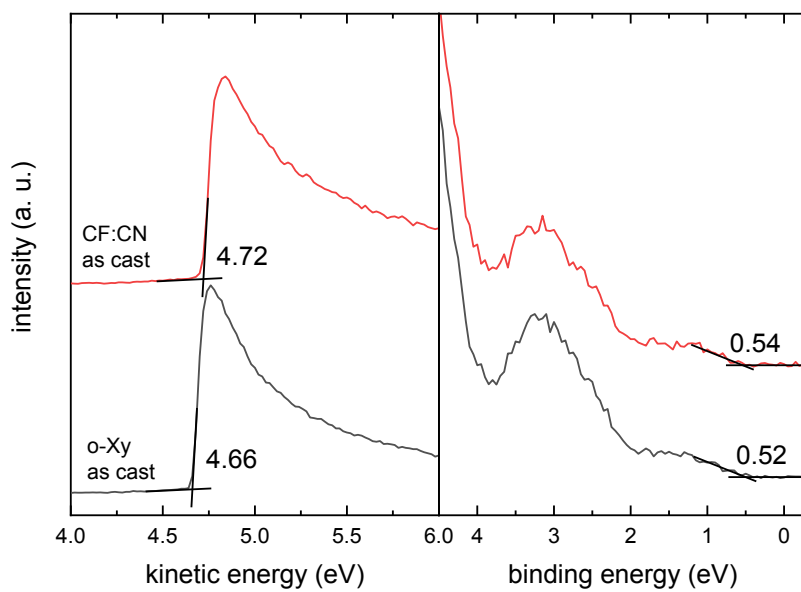


Figure S6: UPS spectra from PM6:Y6 blend films (1:1.2 wt%) processed from different solvent systems. Secondary electron cut-off (SECO) and valence band spectra of PM6:Y6 blend films prepared from CF:CN (0.5 wt%) and o-xylene.

Table S2: Voltage losses for PM6:Y6 devices fabricated with different solvents. The ELQY is measured at 1 sun injection condition ($J_{\text{int}} = J_{\text{SC}, 1 \text{ sun}}$)

Device	$J_{0,rad}$ [A/m^2]	V_{OC}^{rad} [V]	V_{OC} [V]	$\Delta V_{OC,calc}^{non-rad}$ [eV]	ELQY	$\Delta V_{OC,measured}^{non-rad}$ [eV]
PM6:Y6 (CF:CN)	2.81×10^{-16}	1.070	0.83	0.24	1.85×10^{-5}	0.28
PM6:Y6 (o-xylene)	2.36×10^{-16}	1.071	0.77	0.30	2.36×10^{-6}	0.34

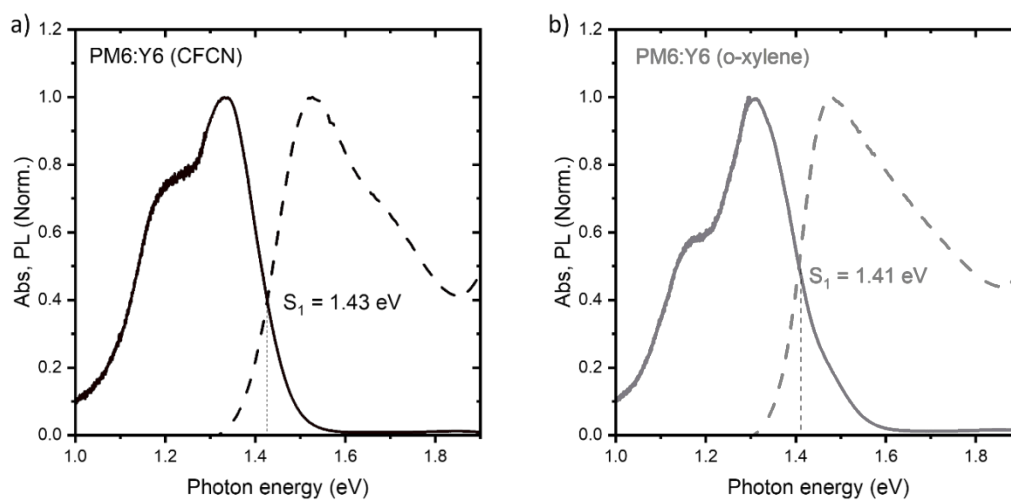


Figure S7: Normalized absorption and photoluminescence (PL) spectra of PM6:Y6 film fabricated with a) CF:CN and b) o-xylene as the solvent.

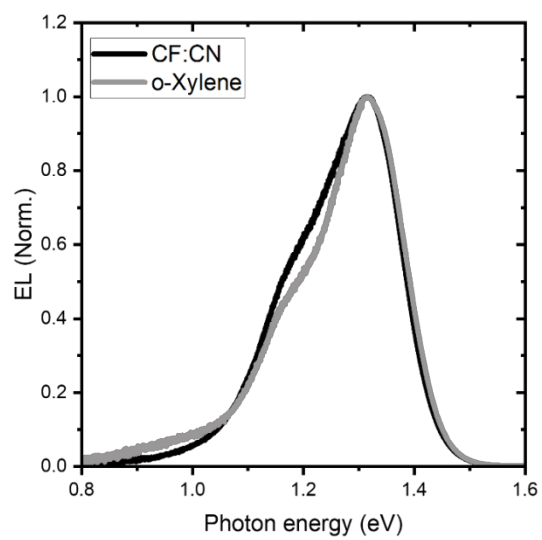


Figure S8: The normalized electroluminescence (EL) spectra of PM6:Y6 devices fabricated with CF:CN and o-xylene as the solvent for the active layer.

References

1. J. Yuan, Y. Zhang, L. Zhou, G. Zhang, H.-L. Yip, T.-K. Lau, X. Lu, C. Zhu, H. Peng, P. A. Johnson, M. Leclerc, Y. Cao, J. Ulanski, Y. Li and Y. Zou, *Joule*, 2019, **3**, 1140-1151.
2. J. Wu, G. Li, J. Fang, X. Guo, L. Zhu, B. Guo, Y. Wang, G. Zhang, L. Arunagiri, F. Liu, H. Yan, M. Zhang and Y. Li, *Nat. Commun.*, 2020, **11**, 4612.
3. W. Peng, Y. Lin, S. Y. Jeong, Z. Genene, A. Magomedov, H. Y. Woo, C. Chen, W. Wahyudi, Q. Tao, J. Deng, Y. Han, V. Getautis, W. Zhu, T. D. Anthopoulos and E. Wang, *Nano Energy*, 2022, **92**.
4. K. Li, Y. Wu, Y. Tang, M. A. Pan, W. Ma, H. Fu, C. Zhan and J. Yao, *Adv. Energy Mater.*, 2019, **9**.
5. M. Zhang, L. Zhu, G. Zhou, T. Hao, C. Qiu, Z. Zhao, Q. Hu, B. W. Larson, H. Zhu, Z. Ma, Z. Tang, W. Feng, Y. Zhang, T. P. Russell and F. Liu, *Nat. Commun.*, 2021, **12**, 309.
6. M. Zhang, X. Guo, W. Ma, H. Ade and J. Hou, *Adv. Mater.*, 2015, **27**, 4655-4660.
7. X. Li, R. Ma, T. Liu, Y. Xiao, G. Chai, X. Lu, H. Yan and Y. Li, *Sci. China Chem.*, 2020, **63**, 1256-1261.
8. S. Karuthedath, J. Gorenflot, Y. Firdaus, N. Chaturvedi, C. S. P. De Castro, G. T. Harrison, J. I. Khan, A. Markina, A. H. Balawi, T. A. D. Pena, W. Liu, R. Z. Liang, A. Sharma, S. H. K. Paleti, W. Zhang, Y. Lin, E. Alarousu, S. Lopatin, D. H. Anjum, P. M. Beaujuge, S. De Wolf, I. McCulloch, T. D. Anthopoulos, D. Baran, D. Andrienko and F. Laquai, *Nat. Mater.*, 2021, **20**, 378-384.
9. J. Wu, J. Lee, Y.-C. Chin, H. Yao, H. Cha, J. Luke, J. Hou, J.-S. Kim and J. R. Durrant, *Energy Environ. Sci.*, 2020, **13**, 2422-2430.
10. T. Liu, R. Ma, Z. Luo, Y. Guo, G. Zhang, Y. Xiao, T. Yang, Y. Chen, G. Li, Y. Yi, X. Lu, H. Yan and B. Tang, *Energy Environ. Sci.*, 2020, **13**, 2115-2123.
11. S. Tu, L. Zhang, X. Lin, L. Xiao, W. Wang and Q. Ling, *J. Mater. Chem. C*, 2022, **10**, 2026-2033.
12. Z. Wang, Z. Peng, Z. Xiao, D. Seyitliyev, K. Gundogdu, L. Ding and H. Ade, *Adv. Mater.*, 2020, **32**, e2005386.